



# THÈSE

En vue de l'obtention du  
**DOCTORAT DE L'UNIVERSITÉ DE TOULOUSE**  
Délivré par l'Université Toulouse 3 - Paul Sabatier

---

Présentée et soutenue par  
**Valentin SAUNIER**

Le 12 Mars 2021

**Microélectrodes nanocomposites implantables  
couplant enregistrement/stimulation neuronale et  
détection électrochimique de neurotransmetteurs**

---

Ecole doctorale : **GEET - Génie Electrique Electronique et Télécommunications :  
du système au nanosystème**

Spécialité : **MicroNano Systèmes**

Unité de recherche :

**LAAS - Laboratoire d'Analyse et d'Architecture des Systèmes**

Thèse dirigée par  
**Christian BERGAUD**

## Jury

**Mme Rosaria FERRIGNO**, Rapporteur  
**M. Pascal MAILLEY**, Rapporteur  
**Mme Catherine VILLARD**, Examinatrice (Présidente)  
**M. Stéphane MARINESCO**, Examineur  
**M. Emmanuel FLAHAUT**, Examineur  
**M. Ali MAZIZ**, Examineur



## Remerciements / Acknowledgements

*(language depend on mentioned people)*

Merci à Rosaria Ferrigno et Pascal Mailley pour leur travail dans le rôle de rapporteurs. Merci à Catherine Villard d'avoir accepté la présidence du jury lors de ma soutenance. Merci à Stéphane Marinesco pour son travail d'examineur. Enfin merci à Emmanuel, Ali et Christian. Merci à tous les membres du jury pour la discussion scientifique durant la soutenance et les ajouts à mon manuscrit.

A ma famille, ma mère, mon père, mon frère, ma sœur et mon grand cousin Jean-Pierre auxquels j'ajoute mes grands-parents partis trop tôt. Merci de m'avoir soutenu depuis la prépa et même avant, de ne m'avoir jamais dit de m'arrêter, que c'était peut-être assez. Merci pour tout et j'espère pouvoir vous rendre la pareil un jour.

To my team, particularly my mentor Christian BERGAUD, for his patience, his help, for trusting me and making me profit of his experience each time he could, thank you. To Ali MAZIZ, particularly for his help on the articles, and his vision on science and how to write about it. To Suresh, Asma, Clément, Vincent and Aarushee thank you for the team work. To Emmanuel Flahaut, even though you're not an actual member of the MEMS team, it's all the same to me and to a lot of us, thank you for your patience and your answers to my (very numerous) questions, for your help with the nanocarbon science and experiments. To the last that arrived in these troubled times of pandemics and mask-wearing lab hours, namely Refik, Elise, Yosr and Elodie, good luck to you!

A mon équipe, en particulier à Christian BERGAUD mon tuteur, un immense merci pour sa patience, son aide, sa confiance et son expérience dont il m'a fait profiter à chaque fois qu'il pouvait. A Ali, merci en particulier pour son aide sur les articles et nos débats sur la science. A Suresh, Asma, Clément, Vincent et Aarushee, merci pour le travail d'équipe et l'ambiance dans les labos. Merci à Emmanuel Flahaut, même si tu n'es pas officiellement un membre de l'équipe MEMS, tu l'es pour moi et pour beaucoup d'entre nous, merci pour ta patience et tes réponses à mes (très nombreuses) questions, pour ton aide dans la partie nanomatériaux de ma thèse, science et expériences. Aux derniers arrivés en ces temps troublés de pandémie et de masques, Refik, Elise, Yosr et Elodie, bonne chance et bonne continuation à vous !

A mes amis, merci pour leur amitié et leur soutien.

A Olivia, que j'ai à remercier pour bien trop de choses que je vais nécessairement en oublier. Merci de m'avoir accueilli chez toi après mes mésaventures de décembre 2019. Je t'en dois une que je ne peux pas encore te rendre mais je le ferai. Merci pour nos discussions à midi, autour de nos thés et cafés, pour nos débats touchant à tout et n'importe quoi. Merci pour ton aide et ton soutien au jour le jour depuis que tu es arrivée à Toulouse, pour les soirées chez toi, en ville etc... Et désolé de t'avoir fait aimer les bières noires. Mais bon maintenant à cause de toi maintenant j'aime les IPA, donc là-dessus on est quitte non ?

A Jean-Yves, merci de m'avoir aidé et sorti de chez moi au moment où j'étais le plus mal, de m'avoir soutenu. Merci pour la forge, pour les soirées, la bière, ta bonne-humeur... Je te rejoins à l'atelier de cuir et sur l'enclume dès que j'ai refait surface après ma soutenance, promis.

A JLo, merci pour ton aide et ton expérience de thésard, transmises autour d'une bonne bière (BiR session !) ou dans des conditions quelques peu inorthodoxes. Toi et tes Bam Baos auront définitivement joué un rôle important dans mon équilibre (pas le calorique, l'autre). Merci pour le GMM, est-ce que tu pourras faire un fest dans le coin un de ces jours ? Histoire qu'on puisse t'héberger. Et par pitié, laisse les autres payer un resto une fois de temps en temps.

A Guigui, pour ton aide et ton expérience de thésard toi aussi, tes bâtons lumineux, tes cure-dents et ton aide en toute circonstance toujours informée et pertinente. Merci pour tes tests pour la science et pour ta générosité pendant les soirées. Et tu es le meilleur scribe qu'on puisse espérer.

A Flo, d'abord merci pour ton aide pour mon déménagement qui s'est avéré...infernale et je reste mesuré je pense. Ta bonne étoile aura compensé ma poisse de l'année toute entière, je t'en dois une sacrée pour ça. Merci d'avoir payé ton appartement pour ces soirées à un million. Et pour ta collection de digestifs...

A Flo le véto, merci pour les soirées burger et jeux de société, pour le soutien entre californiens. Merci encore pour les marches interminables là-bas, ça reste dans mes meilleurs souvenirs. Et merci pour ton sourire permanent, et je sais que je pas le seul à le penser.

A Lucille, merci pour les cookies, tes histoires de chiens et tes photos.

A Clara, merci pour tes histoires de cailloux et de sous-marins perdus dans les arbres.

A mes collègues survivants des stagiaires (de l'open space ou non) de 2017, Mareva, Aymen, Vignesh, merci d'avoir été là les amis. Merci d'avoir constitué un crew solide le midi et d'avoir été là. Merci aux compagnons de table qui sont arrivés plus tard, Morgane, Sylvain, Benjamin et Ali pour avoir fait de même. Un merci particulier à Vignesh pour son aide avec les imprimantes 3D.

Merci à Julie et David de nous avoir accueilli avec le gang chez eux et de nous avoir amené à la rivière et félicitations pour votre petit !

Merci à Julie ma marraine de l'ENSCM pour avoir été toujours une amie fidèle et m'avoir accueilli à mon passage à Londres. J'espère te revoir vite sur Toulouse et qu'on pourra se remettre au billard.

Special thanks to the people from the C211 lab,

To the electrochemists, Suresh, Sai, Camille, Lofti, Asma, and Jensheer sorry if I bothered you with the reference electrodes and the ergonomics of the lab, thank you for the constant positive mood in the echem room and the perpetual help and solidarity. Please Sai stop using low-currents channels for battery cycling, it is kind of gross (wink). Asma, ne baisse pas les bras, Camille, désolé de pas avoir été là plus souvent pour t'aider, mauvais timing entre tes manips et ma rédaction.

Merci à notre grande cheffe à tous Sandrine pour sa patience et sa compréhension, ses bons conseils et son temps passé à endurer mes questions et mes suggestions.

Aux collègues de MILE, Paul, Baptiste, Lucie, Lyne et Zack, pour votre bonne humeur au PDMS, nos débats endiablés au travers de toute la C211. A Zack pour ta bonne humeur constamment positive et tes blagues constamment inattendues. A Baptiste, pour ta bonne humeur au second degré. A Paul pour sa souplesse dans les horaires pour les VSP240. A Lyne et Lucie pour avoir tenu tête à Baptiste.

Aux collègues de MH2F, Olivia et Ali principalement, ce n'est pas parce que vous êtes planqués dans la C211 que vous vous êtes planqués pour de vrai ni n'avez eu peur de nous les électrochimistes, merci pour ça.

Aux collègues de MPN, merci pour votre aide et pour les discussions au coin de votre incubateur aps stérile. Merci à Luca, arrivé en stage en même que moi, les deux vikings italiens (toi plus que moi j'avoue) qui bossent sur le cerveau (sans hache promis). A Inès, pour la bonne humeur en électrochimie et la motivation en salle blanche, je ne sais toujours pas comment tu fais mais c'est contagieux, merci pour ça. A Aziliz, dont j'ai repris les travaux, pour ses conseils au tout début de ma thèse par Skype et à la fin autour d'un café. Merci pour tous les docs que tu m'as transmis et qui m'ont beaucoup aidé. A Tiphaine pour les craquages autour d'une bière.

A Charline et Sandrine, merci pour votre patience, votre aide et votre disponibilité. Merci à Charline pour les manips pour les articles.

Mention spéciale à Alexiane, la seule ELIA qui bosse en C211 à portée de vue des électrochimistes.

Merci aux membres du Rugby : Chef, Olivia, Mathieu Chalnot le singe sportif et musclé, Lyne et son genou (tu me dois un demi-short au passage), Jérôme, Margot, Denis Arzelier et Thony (en espérant que ton genou se remette), Fanny, Gaël, Tim, Mareva (qui préfère la zumba au rugby) et ceux que j'oublie parce que je n'ai pas de mémoire, merci pour les matchs, les entraînement, sacrées bouffées d'air frais (parfois trop en janvier j'avoue). Merci à tous ceux qui ont organisés les match permanents vs non-permanents (hommage à Jean-Louis Sanchez), coordonné le tout et organiser les soirées qui suivaient. Merci aux gens du CIRIMAT qui ont joués avec nous un moment. Merci à Chef d'avoir repris les efforts de survie du club que j'avais fait dès son arrivée et l'avoir transformé en un vrai club. Et merci à Lyne pour avoir fait sa secrétaire, exploitée contre sa volonté qui venait jouer quand-même (wink).

Merci aux membres de l'équipe TEAM : Adrian et Laurent pour la photolitho, Adrian pour le parylene, David pour plein de trucs, David Colin et Pierre-Francois Calmon pour l'édition de masques, Benjamin pour la caractérisation (désolé pour les bêtises dans le S4800), Aurélie et Demba pour l'aide en gravure plasma, Ludo et Guillaume pour les dépôts par PVD, Jean-Baptiste pour la chimie, Samuel et Guy à l'assemblage, Julien Jonneau pour nos discussions techno et le Biergarten, Tom pour ton taf et ta servia-bilité, ta bonne humeur.

Merci aux électrochimistes de salle blanche, Lofti, Sai and Botayana, pour le soutien de galère en salle blanche après 18H30. Merci à David pour nous laisser squatter sa zone.

Merci aux occupants de la C112, en particulier Camille, Christophe et Botayana pour m'avoir accueilli dans votre open-space et pris part à nos débats.

Merci aux gens avec qui j'ai collaboré, Emmanuel FLAHAUT encore une fois, merci pour ton aide et pour m'avoir laissé utiliser ton labo. Lionel NOWAK, merci pour tes réponses à mes questions de néo-phyte en électrophysiologie, merci pour les expériences à ton labo, merci pour toutes nos discussions scientifiques très enrichissantes. Merci à Lionel et Gaëlle de l'ESIEE, à Blaise Yvert, et à toutes les personnes rencontrées par le consortium NeuroMeddle, pour les réunions toujours très intéressantes et instructives.

Merci à Liviu d'avoir créé le Conseil des doctorants au LAAS, dont j'ai fait partie de la 1<sup>ère</sup> génération, qui a permis de faire remonter nombres de problèmes et faciliter la vie des doctorants, merci à Roberto et Margot d'avoir fait un bouleau monstre pour animer ces conseils.

Merci à Xavier Dollat pour les impressions en 3D et les usinages de pièce à l'atelier mécanique. Merci aussi pour les discussions de musiques et autres.

Petite mention spéciale à toutes les personnes avec qui j'ai partagé un bureau, en l'occurrence Lucas à son passage en tant que stagiaire chez MEMS (félicitations encore pour la naissance de ta petite fille), Asma pour la majorité de ma thèse (jusqu'à la crise du CoVid), et Lucas recruté en CDD en à l'été 2020. Merci de m'avoir supporté, ma consommation de café et de thé, ma fâcheuse habitude d'avoir des écouteurs et de pas vous entendre et mon autre fâcheuse tendance à pas allumer la lumière. Promis je ferai plus de pancakes dès que j'ai fini ma thèse et je viens vous en offrir.

Petite pensée pour les anciens, partis trop vite : Adrien, Nico, Lucien, Gabriel, Matthieu, Fadhila, merci à vous tous pour votre aide.

Quelques mentions spéciales :

Merci à Nathalie de la prépa de l'INP de m'avoir accueilli en tant que DCCE à la prépa. Merci à toute l'équipe pédagogique là-bas, ne lâchez rien ! A Déborah, merci pour le tuilage sur les TPs. Bon courage à Alexandra qui doit reprendre nos enseignements.

Merci à Lya Fontaine pour sa présentation au congrès GEET et pour les rigolades à la JNRDM.

Merci à Olivier ROUX de Biologic pour toutes ses réponses et son aide pour comprendre commencer bien utiliser les potentiostat.

Merci à Vanessa pour son aide en électrophysiologie, en particulier sur le traitement de données.

Merci à Aude MALFAZ, elle saura pourquoi.

Thanks to Abhishek for his Youtube advices.

Merci aux Turbas pour la musique et les ambiances sur les médiévales.

Merci à Marie Estruga pour son aide dans les démarches d'inscription, particulièrement en ces temps de pandémie.

Merci aux gens du Biérographe, de l'Houblonnière et du Hopscotch, vous avez fait partie intégrante de ma thèse sans le savoir.

Merci à mon homonyme sirugéen, avec qui j'ai eu quelques bonnes barres de rires en jouant à Magic. Dommage que le Covid et nos études respectives nous aient empêchés de plus jouer ensemble, j'espère qu'on remettra ça vite.

Mention à toutes les personnes que j'ai déjà remercié pour mon stage :

De l'open Space: Jade GONZALES, Mégane TURPIN, Amin BENOUYCEF, Aymen, Akram, Frédéric, Grégory (Félicitations pour ton nouveau statut de fier papa). De l'équipe MEMS : Ali MAZIZ, Olivier LEPRETTE, Aarushee RANGRA, Fred (encore). Autres stagiaires : Carla BENASSIS, Elise BOU, Godfroi, Ben, Juliette, Akash, Benjamin. Collègues thésards/post-docs : Matthieu, Clara, Fadhila, Gabriel, Douglas, Angelo.

Amis : Julie et nos sorties en bar, Luca et nos sorties italiennes, Olivia pour nos discussions à base de rage, Joseph et nos craquages et sorties, Flo le Californien et nos marches interminables, Julie, David, Lulu, Poulet et Angélique pour nos Espaces Games et nos sorties plages.

The people from even before: Chris, the PhD from California who trained me in UC Davis, Pr Erkin Seker who host as an intern there, thank you to both of you, your trust in me when I was not much more than a science youngling in California was key for me.

## Table of content

LIST OF ACRONYMS .....	11
ABSTRACT.....	13
RESUME .....	14
GENERAL INTRODUCTION .....	17
CHAPTER I.....	19
IMPLANTABLE MICROELECTRODES FOR THE BRAIN: TOWARD COUPLED ELECTROPHYSIOLOGY AND NEUROCHEMICAL DETECTION .....	19
<b>1.1 Brain Role and Structure .....</b>	<b>19</b>
1.1.1 Brain Structure.....	19
1.1.2 Neurons .....	19
1.1.3 Neuroglial cells .....	20
1.1.4 Electrical activity of neurons.....	20
1.1.5 Synapse.....	22
1.1.6 Neurotransmitters .....	23
<b>1.2 Brain study methods .....</b>	<b>24</b>
1.2.1 Brain signals .....	24
1.2.1.1 Field potential due to network activity.....	24
1.2.1.2 Single units .....	25
1.2.2 Recording brain activity .....	25
1.2.2.1 Non-invasive (EEG) .....	25
1.2.2.2 Semi-Invasive (EcoG) .....	25
1.2.2.3 Invasive (Implanted microelectrodes).....	25
<b>1.3 Electrophysiology through implanted electrodes .....</b>	<b>26</b>
1.3.1 Examples of “historical” implantable microelectrodes .....	26
1.3.1.1 The glass cone .....	26
1.3.1.2 Wire-based probes: Microwires and Tetrodes .....	27
1.3.2 Microfabricated implantable probes .....	27
1.3.2.1 Utah MEAs and Michigan probe .....	27
1.3.2.2 Flexible polymer-based probes.....	28
1.3.2.3 Microelectrode modification for improved electrophysiology .....	29
1.3.3 Unsolved therapeutic challenges of electrophysiology.....	30
1.3.3.1 Epilepsy: toward seizures management?.....	30
1.3.3.2 Neurodegenerative diseases .....	31
1.3.3.3 Paradigm change: toward neurochemical detection .....	31
1.3.3.4 Combining electrophysiology and neurochemical detection .....	32
<b>1.4 Neurochemical detection .....</b>	<b>32</b>
1.4.1 Non-invasive techniques for neurochemical detection.....	32
1.4.1.1 Functional magnetic resonance imaging (fMRI) .....	32
1.4.1.2 Functional magnetic resonance spectroscopy (fMRS) .....	33
1.4.1.3 Positron-emission tomography (PET) .....	33
1.4.2 Invasive techniques for neurochemical detection .....	34

1.4.2.1	Microdialysis .....	34
1.4.2.2	Electroanalytical techniques.....	35
1.4.2.3	Technique choice for combined electrophysiology and neurochemical detection .....	35
<b>1.5</b>	<b>Neurochemical Electrode detection techniques.....</b>	<b>36</b>
1.5.1	Electrode detection principle .....	36
1.5.2	Chronoamperometry (CA) .....	38
1.5.3	Fast-scan cyclic voltammetry (FSCV) .....	38
1.5.4	In-vivo neurotransmitter electrode detection.....	39
1.5.5	Electrode detection integration.....	40
1.5.6	Working electrode modification.....	40
1.5.6.1	Conducting polymer and nanocarbon electrode modification .....	41
1.5.6.2	Electrochemistry at nanocarbon electrodes.....	41
1.5.6.3	Rapid review of PEDOT-Nanocarbon composites.....	43
<b>1.6</b>	<b>Aim of the thesis.....</b>	<b>44</b>
1.6.1	Electrode for combined electrophysiology and electrode detection.....	44
1.6.2	Electrode detection molecular targets for electrode detection.....	44
1.6.3	Final device, objectives and comparison to the state of the art.....	45
<b>CHAPTER II.....</b>		<b>53</b>
<b>MICROFABRICATION AND MODIFICATION OF DEVICES FOR COMBINED ELECTROPHYSIOLOGY AND NEUROCHEMICAL DETECTION. ....</b>		<b>53</b>
<b>2.1</b>	<b>Introduction to microfabrication.....</b>	<b>54</b>
2.1.1	Important microfabrication parameters.....	54
2.1.2	Device microfabrication for electrophysiology .....	54
2.1.3	Device microfabrication for electrode detection .....	54
2.1.3.1	Electrode material role in electrochemistry.....	55
2.1.3.2	Electrode-Solution interface role in electrochemistry.....	55
2.1.3.3	Passivation nature .....	57
<b>2.2</b>	<b>Microfabrication processes .....</b>	<b>57</b>
2.2.1	Multi-electrode array (MEA) microfabrication process .....	58
2.2.1.1	Overall process.....	58
2.2.1.2	Design choice .....	59
2.2.1.3	Dicing and packaging.....	59
2.2.1.4	Design evolution.....	60
2.2.2	Flexible implant microfabrication process .....	60
2.2.2.1	Overall process.....	60
2.2.2.2	Packaging.....	62
<b>2.3</b>	<b>Post-fabrication electrode modifications .....</b>	<b>62</b>
2.3.1	Electrochemical activation .....	63
2.3.2	PEDOT deposition on MEAs .....	65
2.3.2.1	PEDOT-PSS electrodeposition on MEAs.....	65
2.3.2.2	PEDOT-CNF nanocomposites on MEAs .....	68
2.3.3	PEDOT-CNF deposition on implants .....	72
<b>2.4</b>	<b>Conclusion .....</b>	<b>73</b>
<b>CHAPTER III.....</b>		<b>75</b>
<b>HIGH-PERFORMANCE PEDOT-CNF NEURAL ELECTRODES FOR RECORDING AND STIMULATION .....</b>		<b>75</b>



<b>3.1</b>	<b>Introduction .....</b>	<b>75</b>
3.1.1	Why the need of new, multifunctional, materials in neural interfaces? .....	75
3.1.2	Requirements for multifunctionality .....	75
3.1.2.1	In neural recording .....	75
3.1.2.2	In electrical stimulation .....	76
3.1.2.3	In sensing .....	76
3.1.2.4	How to trade-off? .....	76
3.1.3	Experimental plan .....	77
<b>3.2</b>	<b>Electrode characterization for electrophysiology .....</b>	<b>77</b>
3.2.1	Impedance measurements .....	78
3.2.1.1	Impedance measurements .....	79
3.2.1.2	Phase measurements .....	80
3.2.2	Electrodes Charge storage .....	81
3.2.3	Choice for integration on implants .....	83
<b>3.3</b>	<b>Charge injection for stimulation .....</b>	<b>84</b>
3.3.1	Current injection performance .....	84
3.3.2	CIL determination and stimulation performance .....	85
3.3.3	Comparison with the literature .....	87
<b>3.4</b>	<b>In-vitro cell culture assay .....</b>	<b>88</b>
3.4.1	MTT assay .....	88
3.4.2	Cell growth assay .....	89
3.4.3	Morphology and interfacing study .....	90
<b>3.5</b>	<b>Electrophysiological recordings and stimulation on implants .....</b>	<b>91</b>
3.5.1	Implant preparation .....	91
3.5.2	Setup and brain slice preparation .....	92
3.5.3	Brain slices recordings .....	93
3.5.3.1	Bandpassed recordings (300-3000Hz) .....	94
3.5.3.2	Wideband recordings (bandpass 0,1Hz-3000Hz) .....	94
3.5.3.3	SWRs frequency analysis and decomposition .....	96
3.5.4	Stimulation performances .....	98
<b>3.6</b>	<b>Conclusion &amp; Perspectives .....</b>	<b>99</b>
<b>CHAPTER IV .....</b>		<b>103</b>
<b>TOWARD NEUROTRANSMITTER ELECTRODETECTION ON PEDOT-MICROELECTRODES .....</b>		<b>103</b>
<b>4.1</b>	<b>Introduction .....</b>	<b>103</b>
4.1.1	Technical requirements .....	103
4.1.2	Electrodetection technique choice .....	103
4.1.2.1	Possible techniques for electrodedetection .....	103
4.1.2.2	Association of FSCV and CA .....	105
<b>4.2</b>	<b>Electrodetection Chronoamperometry .....</b>	<b>105</b>
4.2.1	Electrochemical characterization for faradaic currents .....	105
4.2.2	Chronoamperometric detection of dopamine .....	107
4.2.3	Conclusions for electrodedetection using chronoamperometry .....	110
<b>4.3</b>	<b>FSCV: Validation and deployment .....</b>	<b>111</b>
4.3.1	Focus on FSCV .....	111
4.3.1.1	Technique presentation .....	111
4.3.1.2	Background current (BC) management .....	113

4.3.1.3	FSCV modularity: Waveform manipulation .....	114
4.3.1.4	Experimental plan.....	117
4.3.2	FSCV sur CF $\mu$ E: Validation of the experimental setup and method .....	117
4.3.2.1	First tests: high DA concentrations.....	118
4.3.2.2	Further calibration: physiological concentrations .....	119
4.3.2.3	First tests conclusions .....	119
<b>4.4</b>	<b>PEDOT for FSCV: Validation and dopamine electrodedetection .....</b>	<b>120</b>
4.4.1	Electrode requirement for FSCV .....	120
4.4.1.1	Limitations of Carbon fiber microelectrodes.....	120
4.4.1.2	Translation to PEDOT requirements to perform FSCV .....	120
4.4.2	In-vitro calibration of FSCV on PEDOT-modified electrodes .....	121
4.4.2.1	Methodology.....	121
4.4.2.2	Stable FSCV signature.....	121
4.4.2.3	Fast electron transfer evaluation with Ferrocene-methanol.....	122
4.4.2.4	FSCV electrodedetection of dopamine on PEDOT-PSS.....	123
4.4.2.5	FSCV electrodedetection of dopamine on PEDOT-CNF.....	124
4.4.2.6	Performance comparison .....	125
4.4.2.7	Conclusions & Comparison for FSCV electrodedetection .....	126
<b>4.5</b>	<b>Conclusion for multifunctionality and perspectives.....</b>	<b>127</b>
4.5.1.1	Perspectives for FSCV at PEDOT microelectrodes .....	128
	<b>CONCLUSIONS AND PERSPECTIVES .....</b>	<b>132</b>
	<b>Outcome of the thesis .....</b>	<b>132</b>
	<b>Immediate to Short-term perspectives.....</b>	<b>133</b>
	<b>Futures developments: toward combined electrophysiology and electrodedetection .....</b>	<b>134</b>
	<b>Opportunities.....</b>	<b>136</b>
	<b>Technical and technological challenges toward long-term operation.....</b>	<b>138</b>
	<b>ANNEXES .....</b>	<b>142</b>
	<b>ANNEX 1: PUBLISHED MICROFABRICATED DEVICES USED FOR COMBINED ELECTROPHYSIOLOGY AND ELECTROCHEMISTRY IN-VIVO.....</b>	<b>143</b>
	<b>ANNEX 2: MEA MICROFABRICATION PROCESS SHEET .....</b>	<b>146</b>
	<b>ANNEX 3: MEA DESIGN EVOLUTION FOR MULTIPLE APPLICATIONS .....</b>	<b>147</b>
•	<b>MEA GEN1: Electrophysiologic recordings and PEDOT deposits .....</b>	<b>147</b>
•	MEA GEN2: Design modification for PEDOT-CNF deposition.....	147
•	MEA GEN3: Design modification for IrOx deposition .....	148
•	MEA GEN4: Design for microcell configuration optimization .....	148
•	Transition from MEA GEN1 to GEN4 .....	149

ANNEX 4: FLEXIBLE IMPLANT MICROFABRICATION PROCESS SHEET .....	152
ANNEX 5: CRITICAL ISSUES DURING FLEXIBLE IMPLANT MICROFABRICATION - PLASMA CLEANING & ADHESION PROMOTOR.....	154
• Plasma cleaning during microfabrication.....	154
• ParyleneC Adhesion Promotor (AP) use and interference with electrochemistry .....	156
ANNEX 6: SU8 ELECTROCHEMICAL DEGRADATION DURING MICROELECTRODE ACTIVATION .....	158
ANNEX 7: HIGH-PERFORMANCE FSCV ON PEDOT-MICROELECTRODES .....	161
ANNEX 8: IRIIDIUM OXIDE ELECTRODEPOSITION AND CHARACTERIZATION .....	164



# List of Acronyms

(in order of appearance, with redundancies)

## Chapter I

CNS – Central Nervous System  
PNS – Peripheral nervous system  
AP – Action potential  
GABA –  $\gamma$ -aminobutyric acid  
Ach – Acetylcholine  
Ad – Adenosine  
cAMP – Cyclic Adenosine Monophosphate  
Ser – Serotonin  
HT – Hydroxytryptamine  
HA – Histamine  
PLD – Phospholipase D  
NF- $\kappa$ B – Nuclear factor kappa-light-chain-enhancer of activated B cells)  
NE – Norepinephrine  
DA – Dopamine  
FP – Field potentials  
SU – Single Units  
EEG – Electroencephalogram  
ECoG – Electrocorticography  
LFP – Local field potential  
CSF – Cerebrospinal Fluid  
BCI – Brain Computer Interface  
DBS – Deep Brain Stimulation  
NGF – Neurotrophic factors  
SEM – Scanning electron microscopy  
W – Tungsten  
Pt – Platinum  
Ir – Iridium  
MEAs – Multi-electrode arrays  
Au – Gold  
AD – Alzheimer's disease  
PD – Parkinson's disease  
fMRI – Functional magnetic resonance imaging  
PET – Positron-emission tomography  
fMRS – Functional Magnetic Resonance Spectroscopy  
HPLC – High Performance Liquid Chromatography  
CF – Carbon fiber  
WE – Working electrode  
 $E_{eq}$  – Equilibrium potential (electrochemical)  
RE – Reference electrode  
CE – Counter electrode  
DP – Potential difference (for differentiation with Parkinson's disease)  
CA – Chronoamperometry  
FSCV – Fast-Scan Cyclic voltammetry  
CF $\mu$ E – Carbon fiber microelectrode

CV – Cyclic voltammetry  
iMEA – Implantable Microelectrode Array  
ATP – Adenosine Triphosphate  
CP – Conducting polymers  
CNT – Carbon Nanotube  
CSC – Charge Storage Capacity  
CIL – Charge Injection limit  
PEDOT – Poly EthyleneDiOxy-Thiophene  
GO – Graphene oxide  
PSS – Poly StyreneSulfonate  
MWCNT – MultiWall Carbon Nanotubes  
NH – NanoHorn  
CNF – Carbon Nanofiber  
PGNF – Platelet Graphene Nanofibers  
Ag/AgCl – Silver/Silver Chloride  
QRE – Quasi-reference electrode  
IrOx – Iridium Oxide  
PPy – PolyPyrrole

## Chapter II

MEA – Multi-Electrode Array  
SEM – Scanning electron microscopy  
PEDOT – Poly EthyleneDiOxy-Thiophene  
PSS – Poly StyreneSulfonate  
CNF – Carbon Nanofiber  
PDMS – Poly DiMethylSiloxane  
CV – Cyclic voltammetry  
EIS – Electrochemical Impedance Spectroscopy  
 $U_{\mu}Es$  – Ultra microelectrodes  
 $\mu Es$  – Microelectrodes  
PaC – ParyleneC  
PVD – Physical Vertical Deposition  
Ti/Au – Titanium/Gold  
KI/I<sub>2</sub> – Potassium Iodide/Diiodide  
HF – Hydrofluoric acid  
TA – Ambient Temperature  
DIW – De-Ionised Water  
N<sub>2</sub> – Nitrogen  
PVC – Poly VinylChloride  
Si – Silicon  
ICP-RIE – Inductively-Coupled Plasma Reactive Ion Etching  
DRIE – Deep Reactive Ion Etching  
SiP – Silicon-Phosphorus  
MW – MicroWave  
RF – Radio Frequency  
AP – Adhesion Promotor  
H<sub>2</sub>SO<sub>4</sub> – Sulfuric Acid  
IrOx – Iridium Oxide  
CA – Chronoamperometry

FSCV – Fast-Scan Cyclic voltammetry  
WE – Working electrode  
CE – Counter electrode  
CRE – Conformal Ring Electrode  
RoS – reactive oxygenated species  
RrS – reactive hydrogenated species  
UVP – Upper Vertex Potential  
LVP – Lower Vertex Potential  
UV – UltraViolet  
EDOT – Ethylene DiOxyThiophene  
CP – Chronopotentiometry  
SCE – Saturated Calomel Electrode  
PR – Polymerization rate  
HNO<sub>3</sub> – Nitric Acid  
NaPSS – Sodium Poly StyreneSulfonate  
IrCl<sub>4</sub> – Iridium (IV) tetrachloride  
H<sub>2</sub>O<sub>2</sub> – Hydrogen peroxide  
PBS – Phosphate Buffer Saline  
ITO – Indium Tin Oxide

## Chapter III

CSC – Charge Storage Capacity  
CIL – Charge Injection limit  
LOD – Limit of detection  
PEDOT – Poly EthyleneDiOxy-Thiophene  
PSS – Poly StyreneSulfonate  
CNF – Carbon Nanofiber  
CP – Chronopotentiometry  
CV – Cyclic voltammetry  
SCE – Saturated Calomel Electrode  
EIS – Electrochemical Impedance Spectroscopy  
SNR – Signal-to-Noise Ratio  
AC – Alternative current  
H<sub>2</sub>SO<sub>4</sub> – Sulfuric Acid  
CS – Charge Storage  
 $V_{max, neg}$  – maximum negative voltage  
 $V_a$  – access voltage  
 $V_{mc}$  – polarization potential  
EW – Electrolysis window  
CPE – Constant Phase Element  
MTT – bromide 3-(4,5-dimethylthiazol-2-yl)-2,5-diphenyl tetrazolium  
NADH – reduced Nicotinamide adenine dinucleotide  
DMSO – DiMethyl Sulfoxide  
aCSF – Artificial CerebroSpinal Fluid  
SWR – Sharp wave Ripples  
FFT – Fast Fourier Transform

## Chapter IV

CA – Chronoamperometry  
 FSCV – Fast-Scan Cyclic voltammetry  
 CV – Cyclic voltammetry  
 CP – Chronopotentiometry  
 CF $\mu$ E – Carbon fiber microelectrode  
 PEDOT – Poly EthyleneDiOxy-Thiophene  
 DPV – Differential Pulse Voltammetry  
 LOD – Limit of detection  
 PSS – Poly StyreneSulfonate  
 CNF – Carbon Nanofiber  
 EIS – Electrochemical Impedance Spectroscopy  
 KCl – Potassium Chloride  
 DA – Dopamine  
 SCE – Saturated Calomel Electrode  
 CNT – Carbon Nanotube  
 rGO – Reduced Graphene Oxide  
 PtNPs – Platinum NanoParticules  
 Ox-PPy – Oxidized Polypyrrole  
 GlutOx – Glutamate Oxidase  
 MPD – m-phenylenediamine  
 SWV – Squarewave voltammetry  
 Glut – Glutamate  
 L-Glu – L-Glucose  
 NE – Norepinephrine  
 PBS – Phosphate Buffer Saline  
 IIR – Infinite Impulse Response  
 HPF – High Pass Filter  
 UVP – Upper Vertex Potential  
 LVP – Lower Vertex Potential  
 Ag/AgCl – Silver/Silver Chloride  
 AD – Adenosine  
 GN – Guanosine  
 HCl – Hydrochloric Acid  
 NaOH – Sodium Hydroxide  
 $\mu$ E – microelectrode  
 WE – Working electrode  
 RE – Reference electrode  
 Pt – Platinum  
 CE – Counter electrode

BC – Background current  
 SR – scan rate  
 WF – Waveform Frequency  
 Erest – Rest potential  
 VLSR  
 IPA – IsoPropanol  
 DIW – De-Ionized Water  
 DA – Dopamine  
 NE – Norepinephrine  
 DOPAC - 3,4-Dihydroxy phenylacetic acid  
 H<sub>2</sub>O<sub>2</sub> – Hydrogen peroxide  
 EDOT – Ethylene DiOxyThiophene  
 FcMeOH – Ferrocene methanol  
 SV – Subtracted voltammograms  
 DQ – Dopamine Quinone  
 OTs – Tosylate  
 ClO<sub>4</sub> – Chlorate  
 PPF – Pyrolyzed Photoresist Film

#### Units

mV = millivolts  
 nm = nanometer  
 cm = centimeter  
 ms = milliseconds  
 mm = millimeter  
 nM = nanomolar  
 V/s = volt per second  
 $\mu$ m = micrometer  
 sccm = standard cubic centimeters per minute  
 $\mu$ bar = microbar  
 nC = nanocoulomb  
 nA = nanoampere  
 V = volt  
 mM = millimolar  
 $\mu$ M = micromolar  
 $\mu$ C = microcoulomb  
 $^{\circ}$ C = Celsius degree  
 h = hour  
 mbar = millibar  
 Hz = Hertz  
 k $\Omega$  = kiloOhm  
 $\mu$ A = microampere  
 cm<sup>2</sup> = centimeter square  
 mV/s = millivolt per second  
 $\mu$ V = micro volt  
 MHz = MegaHertz

## *Abstract*

---

### **Implantable nanocomposite microelectrodes for neural recordings and electrical stimulation combined with neurotransmitter electrochemical detection**

Electrophysiology is the physiology field that aims at recording the electrical activity of biological tissues. Using microelectrodes in or on the brain, electrophysiology helped make crucial advancements in the understanding of major neurological mechanisms like memory, language, learning by recording the brain electrical signals. Through these advances, it promised and helped develop treatments and therapeutic devices to cure the major neurological diseases like Parkinson's, Alzheimer's or epilepsy.

However, recently the need for other sources of information to combine with electrophysiological recordings has raised, as the research and therapeutic approaches over-relying on these recordings did mostly lead to dead-ends. As the brain electrical activity is molecularly supported by a class of molecules called neurotransmitters, their detection in real-time is proposed as a high-potential complementary brain study technique to integrate along with electrophysiological recordings during neural interfacing.

During this PhD, we developed a new generation of nanocomposite microelectrodes made of both PEDOT and oxidized carbon nanofibers to meet this combined integration. These electrodes displayed a key characteristics combination in-vitro, with low impedance, high charge injection limit, making them promising candidates for bidirectional electrophysiology, while being capable to detect dopamine (one key neurotransmitter) using two complementary techniques, chronoamperometry and fast-scan cyclic voltammetry. Moreover, these electrodes keep a sufficiently low spatial profile to interface with single cells, making them promising candidates for multifunctional neural interfacing, adding neurochemical detection to electrical recordings.

Integrated on flexible implants, these electrodes were first tested in-vivo in brain slices as recording and stimulating electrodes (realizing bidirectional electrophysiology). They showed high performances, being capable to record brain electrical signals on a wider frequency range than standard microelectrodes, with a higher Signal to Noise Ratio (SNR). They also allowed to electrically stimulate brain slices tissues, generating measurable outputs with low inputs compared to standard electrodes.

In conclusion, the modified electrodes developed in this thesis showed promising properties for multifunctional neural interfacing at a single cell level, enabling the coupling between electrophysiological recording and electrical stimulation of tissues in-vivo, while also being capable of neurotransmitter electrochemical detection in-vitro. Through these properties, they constitute meaningful candidates for long-term simultaneous recording of the brain electrical and neurochemical activities for research and therapeutic applications.

## *Résumé*

---

### **Microélectrodes nanocomposites implantables couplant enregistrement/stimulation neuronale et détection électrochimique de neurotransmetteurs**

L'électrophysiologie est le domaine de la physiologie qui vise à enregistrer l'activité électrique des tissus biologiques. En utilisant des microélectrodes implantées dans le cerveau, l'électrophysiologie a permis de réaliser des avancées décisives dans la compréhension des mécanismes neurologiques majeurs, comme la mémoire, le langage et l'apprentissage, grâce à l'enregistrement de l'activité électrique du cerveau. Ces avancées promettaient d'aider au développement de traitements et de dispositifs thérapeutiques pour les principales maladies neurologiques comme Parkinson, Alzheimer ou l'épilepsie.

Cependant, la nécessité d'obtenir des sources de signaux complémentaires aux enregistrements électrophysiologiques a récemment émergé, la recherche thérapeutique basée exclusivement sur l'utilisation de ces signaux électriques conduisant le plus souvent à des impasses. Ces signaux électriques étant portés par des molécules appelées neurotransmetteurs, leur détection en temps réel devrait être une source pertinente de signaux complémentaires à combiner aux signaux électrophysiologiques.

Durant cette thèse, de nouvelles microélectrodes nano-composites à base de PEDOT et de nanofibres de carbone oxydées ont été développées pour réaliser cette combinaison. Ces électrodes présentent d'excellentes caractéristiques in-vitro pour l'électrophysiologie bidirectionnelle, avec une faible impédance et une forte capacité d'injection de charge. Ces électrodes permettent également de détecter électrochimiquement la dopamine (un neurotransmetteur clé) grâce à deux techniques complémentaires, la chronoampérométrie et la voltammétrie cyclique rapide. De plus, ces électrodes modifiées gardent un profil spatial adéquat pour s'interfacer avec une cellule unique, ce qui ajouté à leurs autres caractéristiques en font des dispositifs adéquats pour l'interfaçage neuronal multifonctionnel, ajoutant la détection de neurotransmetteurs à l'enregistrement électrique.

Intégrées sur des implants flexibles, ces électrodes ont été testées in-vivo dans des tranches de cerveau de souris comme électrodes d'enregistrement et de stimulation électrique, réalisant de l'électrophysiologie bidirectionnelle. Leurs hautes performances ont permis d'enregistrer l'activité électrique du cerveau sur une plage de fréquences plus importante et avec un meilleur rapport Signal sur Bruit que celui obtenu avec des microélectrodes standard.



En conclusion, les performances des microélectrodes modifiées développées durant cette thèse sont très prometteuses pour l'interfaçage neuronal multifonctionnel au niveau de la cellule unique. Elles permettent en effet le couplage d'enregistrements électrophysiologiques et de stimulation électrique in-vivo, tout en permettant la détection électrochimique de neurotransmetteurs in-vitro. Ces propriétés en font des dispositifs de pointe pour la recherche et pour des applications thérapeutiques en neuroscience faisant appel à la fois à l'enregistrement des activités électrique et neurochimique.



## *General Introduction*

---

This PhD project lies in the context of biomedical engineering for neuroscience. More precisely, it concerns the specific field dealing with conception/fabrication of implantable devices, used to penetrate the brain tissue to interface with brain regions beneath its surface and record the electrical activity of neurons for brain research (neuroprosthetics, brain-computer interface...) and brain treatment research (epilepsy, Alzheimer's, Parkinson's...). These devices are already used for multiple studies and applications: from cochlear implants restoring hearing to neural probes used to connect people to a computer to communicate or control a machine (artificial arm for example).

However, these standard devices focusing on the electrical activity of the brain seem to reach a dead-end in terms of long-term therapeutic applications, particularly in epilepsy treatment and for most of neurodegenerative diseases (like Parkinson's and Alzheimer's). To overcome this limitation, it is proposed to add to these devices a new way of recording brain activity, to complement electrical recordings. As the brain activity is molecularly supported by the molecules ensuring neurotransmission, the neurotransmitters, their molecular detection is proposed as the most relevant source of information to help unravel the underlying mechanisms in neurological processes, both in the healthy and diseased brain.

To this purpose, the most indicated technique is neurotransmitter electro-detection, as it is technologically-compatible with devices already conceived and fabricated at LAAS, hence easy to integrate on the same device along with electrophysiology. Thus, this manuscript focuses on the development of a device compatible with implantation in free-moving patients that is also capable to perform high-performance bidirectional electrophysiological measurements (recordings and electrical stimulation) and neurotransmitter.

For that, collaborations with Emmanuel Flahaut from the CIRIMAT, Toulouse for nanocarbon engineering and with Lionel NOWAK from the CerCo, Toulouse for brain slices experiments have been conducted, to cover the entire path from the conception and fabrication of the device, to its test in brain slices, meant as easy-to-use model for brain, retaining most of the major characteristics of an actual brain. These collaborations, founded in 2010 as a Consortium, helped develop the local network of researchers already working on implantable devices for the brain to foster research development on neuroprosthetics in France. Other collaborations inside the NeuroMeddle ANR consortium were also conducted with ESIEE in Paris, INSERM in Grenoble and DIXI Medical in Besançon. This network of researchers and consortiums represent one of the key advantages of the technological and scientific environment in Toulouse, as it forms a very close and interactive organization capable of high-speed cross disciplinary exchanges of expertise.

The present manuscript is divided in four chapters.

**Chapter I** presents the scientific context in which the present thesis is being developed and the problematic it aims to answer. It begins by the description of the brain, its role and structure through the different cell types encountered in the brain and important to the objective of this thesis. Then, brain study methods are presented in accordance to the type of signals they are targeting and the devices they need to be recorded. A focus on part of the presented devices, the one that are implantable, is also presented. The limits of the approaches using these devices toward both epilepsy and neurodegenerative diseases are then presented and lead to the need of a new device, integrating neurochemical detection, which we propose to develop in this thesis. Subsequently, the different, already published, methodologies for neurochemical detection are described and a focus on the one that will be integrated on our device is done. The implications of its integration on the device design and the implied research effort are finally discussed.

Once given the scientific context of this work, the manuscript will split into three chapters:

- **Chapter II** deals with the microfabrication of our devices, what are the important parameters to master through microfabrication for their end application and what are the fabrication processes used during this thesis. Some critical issues during these processes are then discussed. The design evolution of the devices along the entire thesis and the post-fabrication device modifications aiming, both at making these devices meet different subsequent requirements, are finally presented. A new material composite is developed to modify the microelectrodes and improve their performances.
- The objective of **Chapter III** is to present the different characterizations aiming at assessing the performances of the modified electrodes as bidirectional interfaces. Namely, the characterization set is constituted of in-vitro impedance and charge storage measurements for recordings, and in-vitro charge storage capacity plus charge injection limit for stimulation. Also, cytotoxicity test of the device is assessed through the combination of a MTT and a cell growth assay completed with an SEM imaging study about morphology and interfacing of cells on modified microelectrodes. On a second hand, these electrodes are tested in brain slices for recording and stimulation in real condition.
- Finally, **Chapter IV** describes the use of the modified electrodes for electrodedetection in-vitro using chronoamperometry (CA) and fast-scan cyclic voltammetry (FSCV). First, CA is used as a simple, easy to implement electrodedetection technique. Electrodes are characterized toward electron transfer, as it is a different parameter than the ones already characterized in Chapter III. Then, FSCV is developed on the modified electrode, as a more complex technique, with a high degree of modularity and adaptability, and higher sensitivity and selectivity. These electrodes are ensured to be FSCV-compatible by the stability of their FSCV signature and possibility to realize high speed electron transfers.

## *Chapter I*

---

### *Implantable microelectrodes for the brain: toward coupled electrophysiology and neurochemical detection*

This chapter will develop the problematic that this PhD, meaning why the need of coupled electrophysiology and neurochemical detection is rising, and how it proposes to answer it. This chapter will go through the role of the brain and how both its electrical and neurochemical activities can be recorded, to finally conclude on a proposed way to record both using the same implantable microelectrodes.

#### **1.1 Brain Role and Structure**

##### **1.1.1 Brain Structure**

The brain is the center of the nervous system in the human body and forms with the spinal cord the central nervous system (CNS). The brain processes all the information coming from the external environment (images, sounds, sensations...) sensed by the peripheral nervous system (PNS), and is also responsible for the bidirectional transmission of information from the brain to the organs (and vice-versa)[1]. From this processing arises the possibility of interacting with the environment, having reflexes, and regulating metabolism for example.

Each region of the brain, which is split in two hemispheres themselves split in four lobes (frontal, temporal, parietal and occipital) is associated with a specific function (visual processing, coordination...). These lobes are completed by the cerebellum, brain stem and limbic system. All the information travels inside the brain through neurons, each one of them connected to thousand other neurons by synapses, all the brain areas being connected.

##### **1.1.2 Neurons**

Neurons are the fundamental unit of the nervous system. Their role is to ensure the transmission of information through the nervous system and information processing through spatial and temporal summation. Working in networks, neurons are specialized cells, electrically excitable, dedicated to the transport of electrical impulses called action potentials.

Neuron structure and characteristics reflect very much this specialization as they are composed of a soma containing the usual intracellular organelles (nucleus, Golgi apparatus, endoplasmic reticulum, mitochondrion...) and from this soma are propagating extensions called either dendrites or axons. Dendrites are short and thin, branched structures that receive action potentials from upstream neurons and propagate them to the cell soma, when axons are long (up to 1m in humans) thicker structures that propagate action potentials to downstream neurons.

There are multiple types of neuron forming the complex network that constitute the nervous system: sensory neurons (responding to stimuli), motor neurons (commanding muscular contractions according to received signals), interneurons (connecting neurons for local circuitry) and neurons can communicate with each other as well as with muscles and gland cells. These different neuron types ensure the communication with the whole body and its accurate control by the nervous system. Neurons are among the most polymorphic cells as their sizes and morphologies display a very high degree of diversity.

### 1.1.3 Neuroglial cells

Even though a human brain encompasses around 86 billion neurons (**Fig. 1**, right), neurons represent only for around half of the cells in the brain [2-4]. The other cells present in the brain are known as neuroglia. The neuroglia is composed of all non-neuronal cells (**Fig. 1**, left): astrocytes, microglia, oligodendrocyte.

Due to the high degree of specialization of the neuron, most functions outside the neurotransmission are at least partly done by the neuroglial cells like clearing the synapses from neurotransmitters (done by astrocytes [5]), supplying neurons with nutrients and oxygen to neurons, helping them grow [6], repairing them after injury, nutritifying neurons [7], ensuring myelination (done by oligodendrocytes in the CNS [8] and by Schwann cells in the PNS), destroying pathogens ...

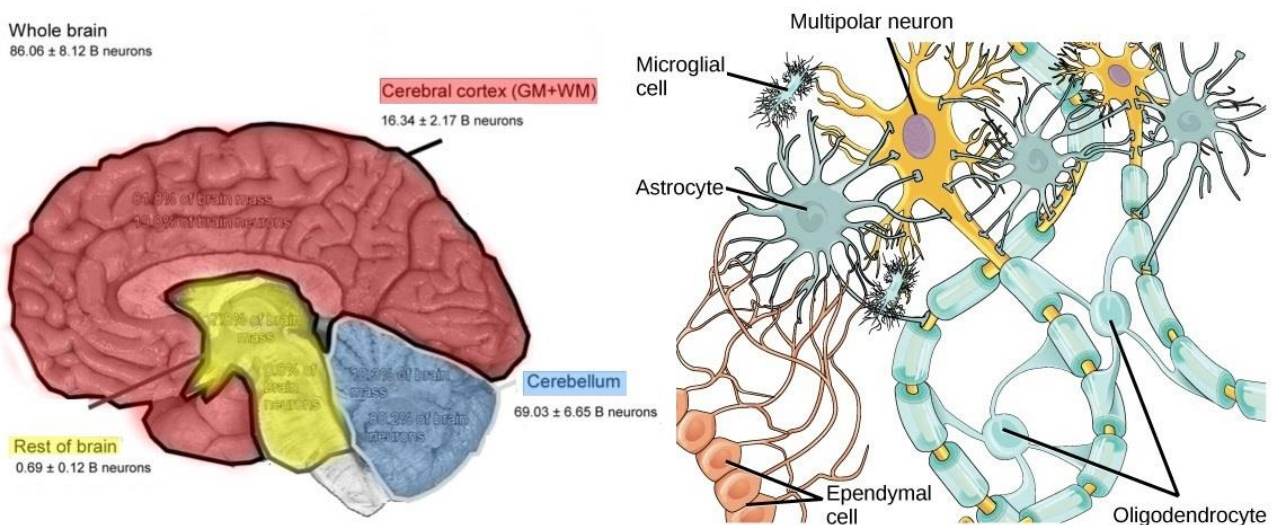


**Fig. 1: Brain overall and cellular morphology.** (Left) Neuronal vs non-neuronal cells distribution in the brain and (right) schematic representation of cells interactions between the different cell types in the brain, showing the interactions between some non-neuronal cells with neuron (Myelination done by oligodendrocytes...), reproduced from [2].

### 1.1.4 Electrical activity of neurons

As said before, neurons propagate the neural information under the form of action potentials. These actions potentials travel through their axons and neurons receive them through their dendrites. An action potential is a neuron membrane depolarization created through series of molecular events across the neuron membrane that propagate along the membrane. This propagation is done by membrane receptors (folded proteins which

3D-structure induces biological activity by creating specific sites) acting as catalysts for chemical reactions involved in biological functions or acting as binding sites for specific molecules for example. Receptors can be found both on cell membranes and in cell cytoplasm.

An action potential is the result of a neuron “firing” (depolarizing) induced when a neuron receives enough stimuli coming from upstream neurons, in the form of molecules released by these neurons. These molecules, called neurotransmitters, are “collected” by the downstream neuron through their binding on this neuron membrane receptors and when enough of them have been collected, the neuron fires. Thus, neuron firing is threshold-type phenomenon.

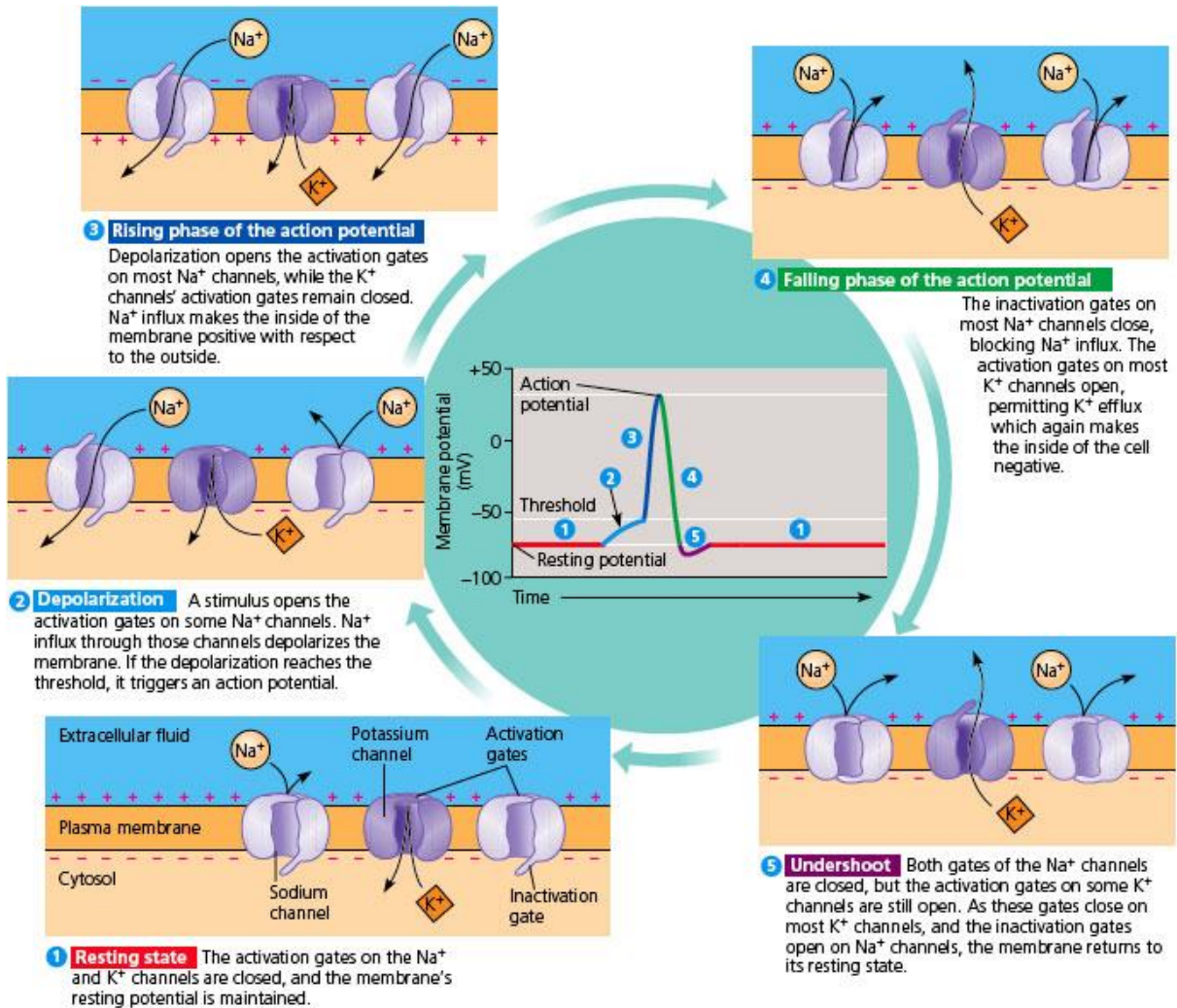


**Fig. 2: Electrical phases of a neuron firing** with ionic movements across the neuron membrane and the membrane polarity during each electrical phase (source: <http://biologytrialanderror.blogspot.com/2014/12/voltage-gated-channels-and-action.html>).

These neurotransmitters activate biochemical cascades inside the neuron which for example provoke the entry of  $\text{Na}^+$  ions (Fig. 2). This is called the depolarization of the membrane which always brings the membrane potential to the same value (+40mV) and propagate along the axon [9]. The neuron then repolarizes by rejecting  $\text{K}^+$  ions. After a firing, the neuron undergoes an over-polarization period, preventing to re-fire just after repolarization. 5ms are necessary before another firing. This all depolarization/repolarization cycle always follows the same temporal scheme and constitute an action potential.

When the depolarization reaches the end of one dendrite, it causes the release of neurotransmitters in a space called the synapse (cf. 1.1.5), which when they bind to the downstream neuron will activate new biochemical cascades and propagate further the information.

Locally, an action potential produces a very distinct potential variation (both in extra- and intra-cellular spaces) called a single unit. When several of these single units are generated by a group of neurons, in a synchronous manner, they produce a potential change constituted of the spatiotemporal sum of all these single units called a local-field potential (LFP).

### 1.1.5 Synapse

Synapses are the biological junctions (20-40nm sized cleft) between two neurons (or a neuron and a non-neuronal cell), allowing for action potential (AP) propagation. Most synapses convert it into a chemical signal and are called chemical synapses. They are the core points of neurotransmission, defined as the process by which neurotransmitters, carry the chemical message and transmit neural impulses.

At the end of an axon, the depolarization stimulus (the action potential) is converted into a chemical signal through the potential-induced (from the membrane depolarization) release of neurotransmitters into the synaptic cleft. These neurotransmitters then diffuse toward the post-synaptic neuron and bind to receptors onto this neuron membrane. This triggers new biochemical cascades, re-transforming the signal into an electrical one by inducing the depolarization of the post-synaptic neuron.

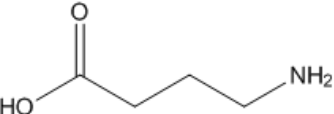
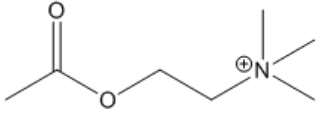
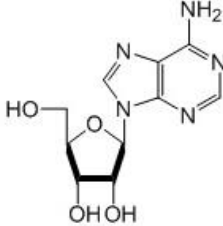
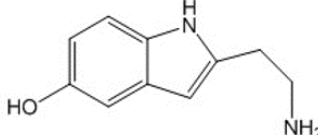
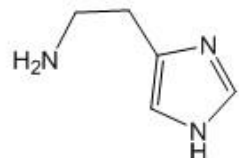
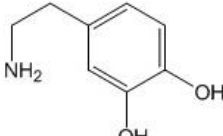
As each neuron is connected to thousands of other neurons, a downstream receives thousands of inputs at every instant. An input having either an excitatory (influence transmembrane ion flow to increase the probability of producing an AP) or inhibitory effect, the summation of all inputs at every instant (outside times when the considered neuron has already fired) is what defines if the neuron will fire. These inputs are binding of neurotransmitters coming from multiple upstream neurons on the considered downstream neuron and whether these bindings have an excitatory or an inhibitory effect is function of what type of receptors the neurotransmitter can bind. The same neurotransmitter could have antagonist effects by binding two different types of receptors (cf. 1.1.6).

It is important to note that release of some neurotransmitters can happen in the synapse without being triggered by an AP. Thus, a neurotransmitter can have a basal level in the synaptic cleft (and the extracellular media) and that level can have an influence on neurotransmission.

It is also important to note that chemical synapses co-exist with electrical synapses throughout the entire nervous system [10]. The two communicating cells in these synapse are much closer (about 4 nm from each other) and linked by gap junctions [11] channels crossing the membranes, with their cytoplasm connected. These synapses allow the direct and faster transfer of the action potential compared to chemical synapses, making these synapses part of brain processes like reflexes where rapid information propagation is critical. As these synapses do not involve neurotransmitters, the signal transmitted tends to be the same than the source one, signal modification, like gain, being less possible.



## 1.1.6 Neurotransmitters

Name	Structure	Receptor (not exhaustive)		Effect (not exhaustive)
		Metabotropic	Iontropic	
$\gamma$ -aminobutyric acid - GABA		GABA <sub>B</sub> receptors (inhibitory) [13]	GABA <sub>A</sub> and GABA- $\rho$ receptors	GABA <sub>B</sub> : Stimulate K <sup>+</sup> channels opening, lowering AP frequency. GABA <sub>A</sub> : bring the neuron potential closer to -75mV by either Cl <sup>-</sup> intake or rejection, impeding successful AP.
Acetylcholine ACh		Muscarinic ACh receptors [14]	Nicotinic ACh receptors	Depolarize post-synaptic neuron by non-selective positive ion intake (Na <sup>+</sup> , K <sup>+</sup> and Ca <sup>2+</sup> ). Involved in neuromuscular junctions, controlling muscle contraction.
Adenosine Ad		Adenosine receptors A <sub>1</sub> , A <sub>2A</sub> (in the brain) + A <sub>2B</sub> , A <sub>3</sub> [15]	-	A <sub>1</sub> : decrease vesicle release A <sub>2A</sub> : increase cAMP levels which decreases dopaminergic activity.
Serotonin Ser		5-HT (1 to 7 except 3) [16]	5-HT <sub>3</sub>	5-HT <sub>1</sub> : Decrease cellular levels of cAMP (inhibitory) 5-HT <sub>3</sub> : depolarizing plasma membrane (excitatory)
HA		Histamine receptors H (1 to 4) [17]	-	H <sub>1</sub> : activate PLD, promote NF- $\kappa$ B expression (inflammation) H <sub>3</sub> : decrease Ach, Ser and NE release
Dopamine DA		Dopamine receptors (D <sub>1</sub> to D <sub>5</sub> ) [18]	-	Increase intracellular levels of cAMP (D <sub>1</sub> and D <sub>5</sub> ) or decrease it (D <sub>2</sub> , D <sub>3</sub> and D <sub>4</sub> )
		TAAR1	-	Increase intracellular levels of cAMP and Ca <sup>2+</sup>

**Table 1: Main neurotransmitters** (name and structure) discussed in this thesis, with their corresponding receptors and possible effects.

Neurotransmitters are a category of molecules including all amino acids, peptides, amines, etc. that allow neurotransmission (**Table 1**). The exact number of neurotransmitters is unknown but more than 200 molecules having this role have been identified. Most neurotransmitters are simple molecules obtained by chemical modification (biosynthesis) of amino acids and other largely available molecules. Specifically, neurotransmitters are identified as molecules having an influence on the post-synaptic neuron membrane in a synapse and

molecules carrying functions influencing synapses or neurons (inducing a synapse reorganization for example), including molecules sending upstream messages that influence next firings.

Prior to their release, neurotransmitters are stocked in synaptic vesicles which are close to the synaptic cleft. After their release (which is action-potential induced), three mechanisms are involved in the synaptic space clearing: metabolization of the neurotransmitters by enzymes, reuptake to the pre-synaptic neuron or receptor binding on the post-synaptic. Most neurotransmitters have different roles or cause different reactions depending on their target receptors (ionotropic receptors or metabotropic receptors) on the post-synaptic neuron after release in the synapse.

On top of their role in a synapse, neurotransmitters can be present in the cerebral extracellular media and bind to different receptors than the ones they bind in a synapse.

This is well exemplified by dopamine, implicated in motor control and the reward neurological system. Dopamine signaling and effect is function of two phenomena: the phasic firing of dopaminergic neurons which produces a rapid and localized transient of dopamine and the basal level of extracellular dopamine (regulated by a tonic firing) [12]. The first is involved in direct neuron communication while the second influences the excitability of neurons for example.

## 1.2 Brain study methods

### 1.2.1 Brain signals

Brain signals that can be targeted are most of the time classified according to their nature, their amplitude and the number of cells needed for their generation. In that part, we will focus on field potentials (FP), raising from neuron network activity, and single units (SU), raising from the depolarization of a single neuron. Thus, they are other signals possible, raising from all intermediary neuron population from single neuron to the entire brain.

#### 1.2.1.1 Field potential due to network activity

A field potential (FP) is the signal coming from the electric current flowing from the neural network, resulting of the simultaneous activity of numerous postsynaptic potentials. FPs can be measured but the quality of the measurement is function of the distance between the recording device (EEG, ECoG or implanted electrode) and the signal source (**Fig. 3**). Furthermore, the local value of the potential at each monitored point of the brain is due to the spatial summation of all neuron firings at every moment, which implicates a high spatial and temporal variability. Implanted electrodes are able, for instance, to record local field potentials (LFP) resulting from smaller populations of neurons firing compared to larger populations recorded during EEG for example (better resolution).

### 1.2.1.2 Single units

Single-unit recordings are recordings of extracellular potential (due to the electric current flow around the neuron) of a single neuron using a microelectrode placed in the neuron vicinity. This technique is widely used in neuroscience (to create neuronal maps and link neuronal activity to behavior and study brain diseases like Parkinson's disease), using carefully placed metal (Platinum, Iridium, Tungsten...) microelectrodes or micro-pipettes-like electrodes to allow either intracellular or extracellular recordings with high spatial and temporal resolution.

## 1.2.2 Recording brain activity

As the different signals that can be targeted and recorded have different characteristics (amplitude, frequency, noise) depending on the size of the neuron population generating it, different devices have been developed to adequately interface with these populations and meet the different levels of recording possible. However, these devices need different levels of invasiveness to operate. For example, a single unit can be detected and recorded when the recording device is very close from the targeted neuron, that is to say from an implanted device in the brain structure. At a more macroscopic level, the activity of a whole population of neurons can be detected as brain oscillations by an electrode positioned on the scalp, therefore without the need to implant the recording device.

### 1.2.2.1 Non-invasive (EEG)

Electroencephalography (EEG) measures the electric activity of the brain via macro-electrodes placed on the scalp (**Fig 3A**). The electrical signal obtained is the result of large numbers of synchronous post-synaptic action potentials and thus must be conducted through several layers of the cerebral cortex, cerebrospinal fluid (CSF), pia mater, and arachnoid mater and finally the skull. Therefore, one drawback in this technique is the level of signal attenuation. Plus, the EEG signals encompass multiple simultaneously-ongoing brain processes, which would then need to be decorrelated. This means that the brain response to a single stimulus or event of interest is not usually visible in the EEG recording of a single trial.

### 1.2.2.2 Semi-Invasive (ECoG)

Electrocorticography (ECoG), or intracranial EEG, uses electrodes placed under the scalp on the surface on the brain to record electrical activity from the cerebral cortex, which places the procedure as a semi-invasive approach (**Fig. 3B**). Like EEG, ECoG signals are composed of synchronized postsynaptic potentials recorded from the exposed surface of the cortex but the signal is not attenuated by the low conductivity of bone. The spatial resolution of an ECoG is therefore much higher (of around 1cm) and a temporal resolution of approximately 5ms.

### 1.2.2.3 Invasive (Implanted microelectrodes)

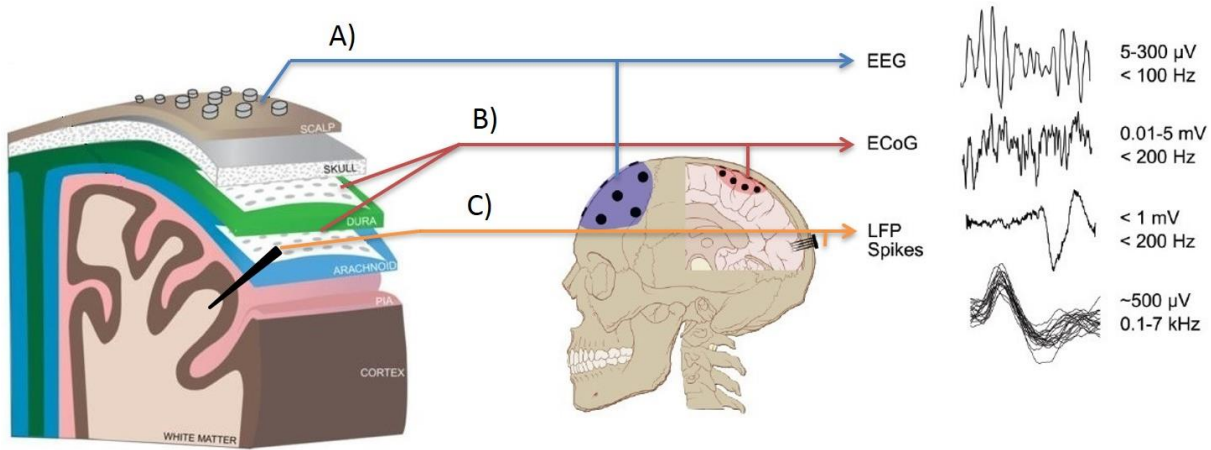


**Fig. 3: Possible signals (frequency and potential) in function of brain penetration depth. (A) EEG, (B) ECoG and (C) LFP spikes recordings showing relative quality of the signal recorded with each technique, reproduced from [19], [20].**

By using microelectrodes directly implanted into the brain tissue, these electrodes will detect electrical signals from smaller populations of neuron, with greater resolution as the signal source (the neuron) being closer (**Fig. 3C**). The applications of these electrodes range from pure neuroscience and electrophysiology research to epilepsy diagnostic and brain computer interfaces (BCI). Besides resolution, another advantage for implanted electrodes resides in the ability to record or stimulate cortical layers. For instance, deep brain stimulation (DBS) of buried hypothalamus layers has proven efficient for otherwise treatment-resistant movement and affective disorders such as Parkinson's disease, essential tremor, and dystonia, among others. The different existing cerebral microelectrodes and their use in neural interfaces is dealt further in the next section.

## 1.3 Electrophysiology through implanted electrodes

### 1.3.1 Examples of “historical” implantable microelectrodes

Multiple early designs of microelectrodes were produced in the early days of electrophysiology, that have been then modified to meet evolving requirements. New probe designs using microfabrication techniques were produced in the last decades to take advantages of microfabrication advantages (precision, reproducibility, access to new flexible materials...).

#### 1.3.1.1 The glass cone

The glass cone electrode is made of a 1-2mm long glass pipette containing conductive wires (**Fig. 4A**), coated with neurotrophic factors (such as NGF) to induce neurite outgrowth inside the cone after implantation where the wires can pick up electrical signals after axons connect to them. The total tissue growth is usually completed after a month after implantation. Even though it has shown to be completely biocompatible and robust (longevity superior to four years in human patient) and used as early as 1996 for implantation, the

necessary activation delay and the limited amount of information obtained by this type of electrode have made the need of new probe designs essential.

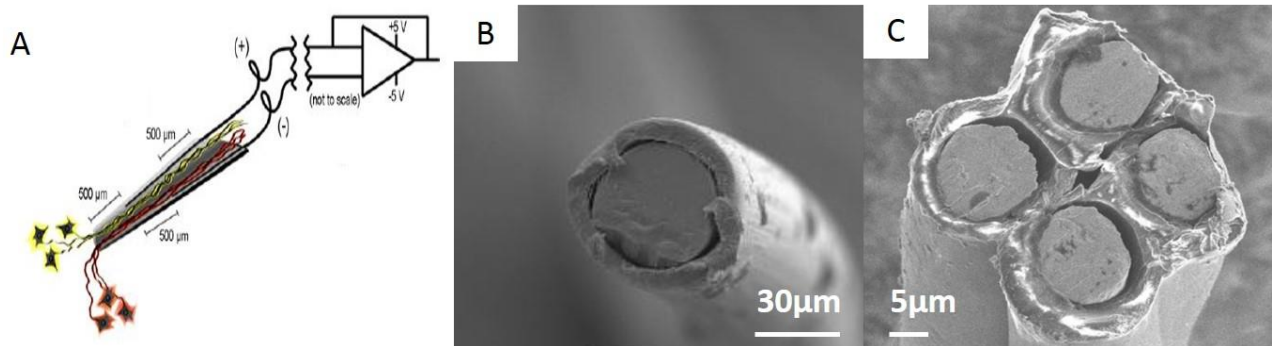


**Fig. 4: Historical implantable microelectrodes types.** Representation of a (A) neurotrophic electrode (Glass cone) [21], (B) Single wire insulated [22], (C) SEM picture of a tetrode made of four insulated Pt wires and of a single insulated Pt microwire [23].

### 1.3.1.2 Wire-based probes: Microwires and Tetrodes

Insulated metal wires made of Tungsten [24], Pt[22], Ir, Pt/Ir [25] (Fig. 4B) were used as early as in the 1950s as implanted microelectrodes to study the activity of individual neurons in awake, free-moving animals.

Even though these probes are well-established nowadays, easily fabricated, with the ability to record neural activity of large neuron groups, this type of device is unreliable for chronic implantation due to the delamination of the passivation layers and cracking risk. Tetrodes [23] are made of four wires attached to each other, as can be seen in Fig. 4C, and more precise because of the possibility of triangulation but suffer the same drawbacks.

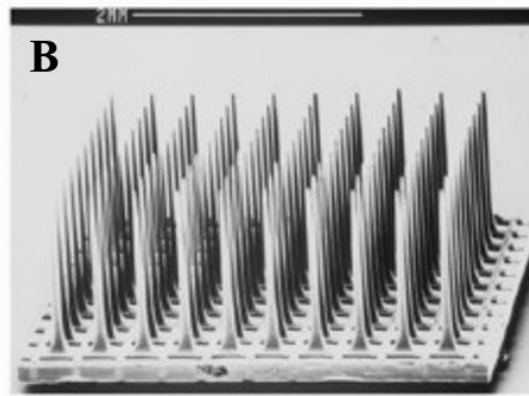
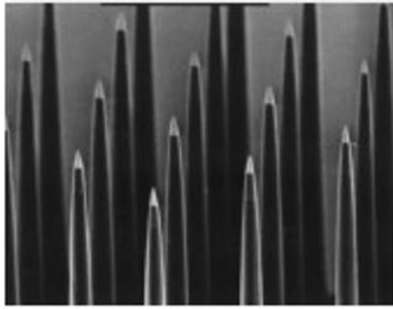
## 1.3.2 Microfabricated implantable probes

### 1.3.2.1 Utah MEAs and Michigan probe

Taking on tetrodes and using microfabrication techniques from the semiconductor industry, multi-electrode arrays (MEAs) were first produced in stiff materials like silicon. The two most iconic MEA types are the Utah array [26] (Fig. 5A&B), made of sharp insulated conductive tips arranged in a matrix, and the Michigan array (Fig. 5C&D), with microblades having multiple electrodes each.

These two MEAs tremendously help propel neuroscience research forward as they allowed recording from a high number of electrodes, arranged in a 2D/3D matrix which has impossible with unitary electrodes or with tetrodes.

### A) Utah Array



### C) Michigan Array

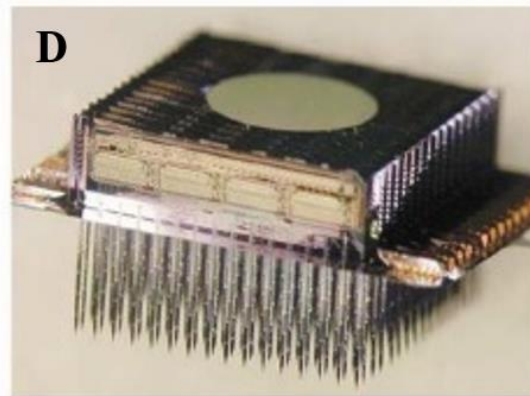


**Fig. 5: Historical implantable MEAs types.** (A) SEM picture of the recording tips of an Utah array, (B) SEM picture of the entire array, (C) Optical picture of two blades from a Michigan Array, (D) Optical picture of the entire array [27], [26] (modified), [28].

#### 1.3.2.2 Flexible polymer-based probes

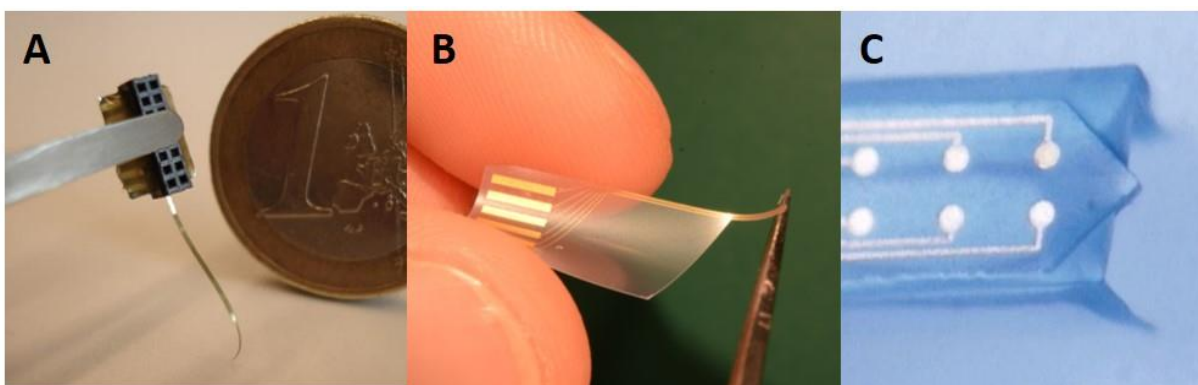


**Fig. 6: Flexible probes from the literature.** Pictures of (A) a bent polyimide-based implantable electrode, of (B) a Parylene C-based electrode developed at LAAS and of (C) its tip after stiffening by a silk deposit reproduced from [34], [35].

Flexible polymers (Polyimide [29], SU8 [30], Parylene C [31, 32], etc.) can be used both as dielectric insulator and backbone material for neural probes. By using a polymer material as backbone material, the implant becomes more flexible (Fig. 6A&B) and tissue-compliant. Thus, the strain due to the mechanical mismatch

at the electrode-tissue interface and to brain micromotions is greatly reduced [33]. That way the implant better mimics the brain tissue in terms of mechanical properties and minimize the inflammatory response due to the probe. These probes sometimes need stiffening to be able to pierce the brain tissue during implantation (Fig. 6C).

### 1.3.2.3 Microelectrode modification for improved electrophysiology

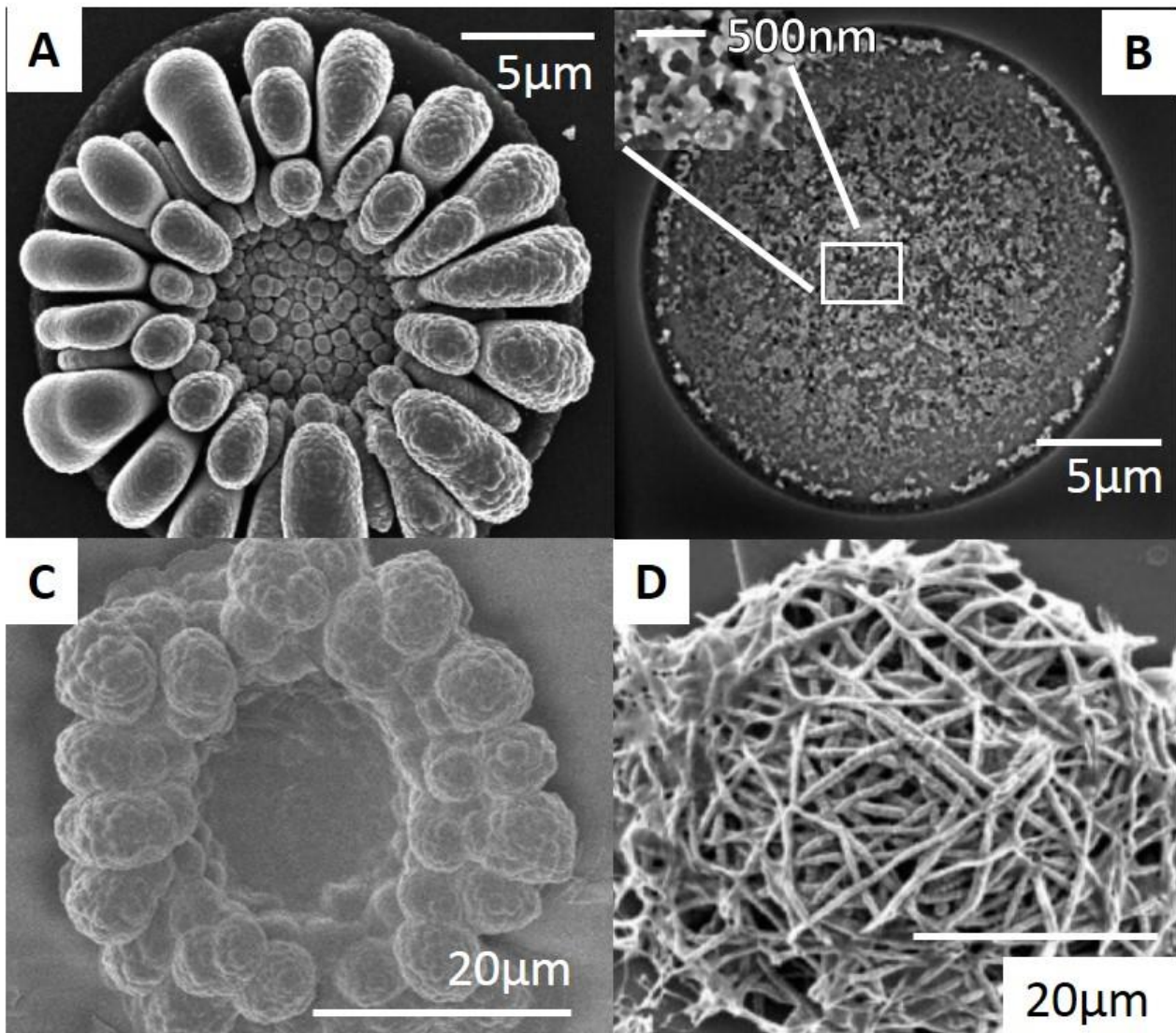


**Fig. 7: Modified microelectrodes examples from the literature.** (A) Sun flower-shaped nanostructured gold deposit on a gold 10µm-diameter microelectrode, reproduced from [36], (B) Gold nanoporous microelectrodes obtained after removal of a aluminum matrix by chemical etching [38], (C) PEDOT-PSS coating obtained using the protocol from [37] on a gold 20µm-diameter microelectrode. (D) Conducting polymer nanotubes grown on a metallic microelectrode from [39].

Most implantable microelectrodes produced by microfabrication are made out of noble metals (Au, Pt, Pt/Ir...) as conductive material, being biocompatible, inert and non-toxic. However, these metallic microelectrodes, when their characteristic dimension start being under around 50µm, present limiting characteristics

for recording and stimulation. In biomimicking media, they display very high impedances (roughly the electrode opposition to AC voltage/current going through it, at each probed AC frequency) in the frequency range of neural signals and very poor charge injection capability due to poor capacity (resulting in a low maximum current injectable through the electrode without tissue damage). These poor characteristics impede respectively the recording of neural electrical signals (which are potential variations  $<1\text{mV}$  most of the time) and electrical stimulation (current injection to generate depolarization) performances of these electrodes.

To overcome these limitations and achieve ideal properties, microelectrodes modification protocols have been developed, aiming at lowering the electrode impedances, enhancing the injection charge capability, etc. These protocols are either based on i) electrode structuration (without electrode material change), increasing the electrode surface by making it highly porous (**Fig. 7B**) and/or highly rough (**Fig. 7A**) [36], ii) electrode modification, changing the electrode material by adding another material like conductive oxides, conducting polymers [37] (**Fig. 7C**), carbon nanotubes (**Fig. 7D**) or graphene for example, on top of the original one, changing the characteristics of the electrode.

These electrodes helped to realize major technical advances and studies through electrophysiology, deploying both recording and stimulation at unreached scales (by the use of high-density multi-electrode arrays for example) compared to historical microelectrodes.

### **1.3.3 Unsolved therapeutic challenges of electrophysiology**

Since its practical achievement, electrophysiology has held many promises for the neurologists and the patients. Actually, it has shown to be a powerful tool for neuroscientists to study brain processes in both healthy and diseased brains. Major breakthroughs have been realized about motor control, reward-motivated behavior, memory and learning for example, as well as on Parkinson's disease and Alzheimer's disease. However, lately the better understanding brought by electrophysiology showed its limit as far as therapeutic applications and full understanding of brain processes are concerned, which leads to a lack of actual treatment development.

#### **1.3.3.1 Epilepsy: toward seizures management?**

Epilepsy is a spectrum of disorders defined by the occurrence of epileptic seizures, which are characterized by the abnormal firing of large populations of neurons [40]. Electrophysiology has proven to be a valuable tool in the case of pharmaco-resistant epilepsies, allowing through recordings and calculation to locate epileptic locus in patients, in prevision of surgery.

On another hand, it was assumed that EEG signals recorded in epileptic patients would, if an adequate processing is used, allow to detect incoming seizures. Computers models trained on one patient failed to treat multiple patients [40] and the personalized medicine approach consisting in using EcoG signals to train the



seizure detection worked on detecting seizures but with a high false alert rate [40]. Research in seizures detection is still vital as it holds the promise to stop seizures through adequate neurostimulation using a closed-loop system [40]. However, over-relying only on electrical signals to tackle seizure detection seems to be a dead-end after two decades of research.

Other signals sources must be considered, *and as the brain activity is molecularly-supported*, molecular studies on appropriate targets might allow to obtain complementary information on epileptic seizures, pre-ictal state, seizures molecular dynamics and molecular triggering and help understand the link of some already known phenomenon with epilepsy [41].

### 1.3.3.2 Neurodegenerative diseases

Electrophysiology has helped tremendously research about neurodegenerative diseases (mainly Parkinson's), as it showed pretty early the potential to unravel subtypes of symptoms like dementia in Parkinson's [42], quantify tissue damage due to the disease (measuring the loss of electrical activity in neuron populations), identify disease progression time-scales and schemes [43]. It also helped study patient symptom awareness [44]. Through these advances, it mainly helped about how to be the most effective with the current therapeutic tools already available to treat these diseases and diagnose them more accurately, as the diseases became more and more characterized. Also, brain stimulation is under development as therapeutic tool against Parkinson's. More speculatively, new electrophysiology-based approaches are still being proposed to expand Alzheimer's disease (AD) research, in combination with other techniques [45].

However, as these diseases are polymorphic and can be biologically multifactorial, the use of only one signal (the brain electrical activity) is too limiting and prevents electrophysiology to be used as a therapeutic tool. Having real-time molecular quantification/qualification of brain environment molecules would allow to study the impairments provoked and would help accurately diagnose and treat patients. Plus, it has been shown that common conditions like depression or serious diseases like schizophrenia and Parkinson's disease (PD) are at least partly induced by all causing brain chemistry dysfunctions [46], particularly at the synapse level [47, 48].

In the next paragraphs, we will develop the hypothesis that motivated this PhD work, as a mean to overcome these limitations and adapt to the feedback coming from past research (clinical and others) that imply the need for a paradigm change, to in the end develop a new device and new methodologies to achieve it.

### 1.3.3.3 Paradigm change: toward neurochemical detection

Therefore, studying brain chemistry at the single neuron-level in both healthy and malfunctioning neuron networks would provide a valuable additional information to unravel the underlying biological mechanisms and possibly find and study cures for the above-mentioned conditions.

Neurochemical detection studies have been conducted for decades, targeting the main neurotransmitters (dopamine, norepinephrine, adenosine...), and like electrophysiology, it also tremendously helped understand

the underlying molecular dynamics behind neurological mechanisms like memory, the reward system... It also helped discover that neurochemical activity impairments linked to some neurodegenerative diseases like Alzheimer's [49]. This further proves the interest to study the correlation between electrophysiological and neurochemical activity in both healthy and diseased brains.

However, neurochemical studies are rarely conducted simultaneously with electrophysiological studies (live animals [50], brains slices [51]). This combination is a cutting-edge topic in neuroscience, addressed only by a few groups (among them notably the The Mayo Clinic Neural Engineering Laboratory, founded by K.H. Lee and K.E. Bennet, which produced several proofs of concept in this field), and always bringing new insights and promising results. This is due to technical and technological difficulties, coming from both studying modes [52], and lack of adequate platforms, that are not translatable to free-moving patient studies most of the time.

#### **1.3.3.4 Combining electrophysiology and neurochemical detection**

Indeed, there is an unmet need for a way to record both the electrical activity and chemical activity of the brain (healthy or malfunctioning), to provide wider and correlated data sets and help understanding neurological processes and development of cures.

To meet this need, we propose to develop an adequate device would need to be capable to record both neural electrical activity and neurochemical activity simultaneously and in real-time. This device would also have to be both usable in free-moving animal models and translatable to patient, and so be operational on the long-term. To reach any population of neuron implicated in the targeted neurological processes, this device would also have to be implantable, hence chronically implantable.

## **1.4 Neurochemical detection**

As said before, neurochemical detection studies have been conducted in the past, using several different techniques, also classified according to their invasiveness levels. As for electrophysiology, they are all aiming at studying differently-scaled neuron populations and different signals.

### **1.4.1 Non-invasive techniques for neurochemical detection**

Non-invasive monitoring of neurochemical is mostly done by functional magnetic resonance imaging (fMRI) and Positron-emission tomography (PET). It is important to precise that some of these techniques are still at a development stage though, in order to adapt them for specific neurochemical monitoring objectives.

#### **1.4.1.1 Functional magnetic resonance imaging (fMRI)**

fMRI measures brain activity by detecting changes associated with blood flow using a magnetic field produce by a magnetic scanner (**Fig. 8A**). In its raw form, this technique does not actually detect neurotransmitters.

However, this technique allows a real-time mapping of the whole brain and does not require any surgery (**Fig. 8B**).

Alternative MRI-based techniques with a higher sensitivity and capable of detecting specific molecules are being recently developed and are promising. But they cannot be used on live human subjects as an injection of probes containing mutated proteins directly into the brain tissue is required [53] which represents a major biological risk.

#### 1.4.1.2 Functional magnetic resonance spectroscopy (fMRS)

As for MRI, MRS uses a magnetic field to study the brain regions (**Fig. 8C**) but resolves  $^1\text{H}$  spectra (Fig 8D) to detect chemicals (glutamate, amino acids etc.) present in these brain zones instead of providing brain images. Thus, this technique actually identifies molecules (and not blood flow) and would be more suitable for neurochemical detection. However, the fMRS temporal varies from 7 minutes to 5s according to the magnetic field strength and the minimal studied volume is  $1\text{cm}^3$  (**Fig. 8C**). On top of that, to be performed, fMRS needs very sophisticated data acquisition systems, quantification methods and interpretation of results as well as the access to very strong magnets (1.5T and higher).

#### 1.4.1.3 Positron-emission tomography (PET)

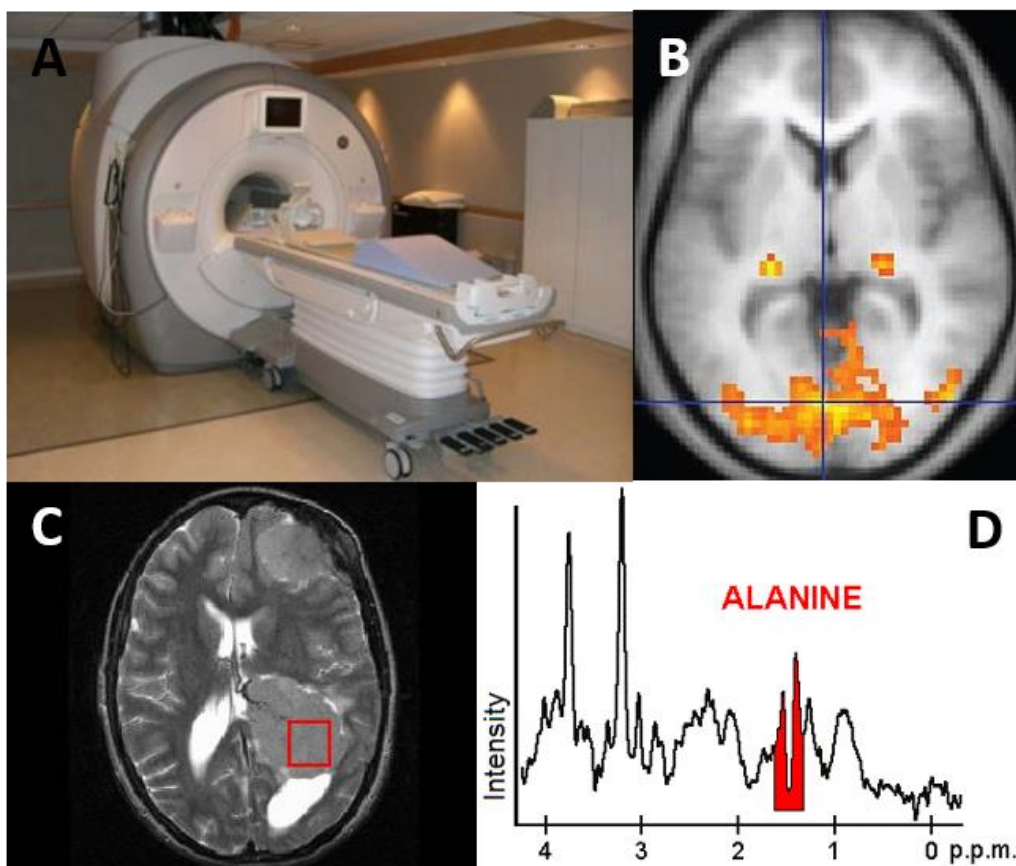


**Fig. 8: Non-invasive neurochemical detection.** (A) fMRI scanner (reproduced from SSC website), (B) fMRI scan (yellow areas = increased activity), (C) fMRS scan (red box shows the volume of interest which chemical information is extracted by MRS), (D) corresponding chemical displacement of chemical present in the volume of interest, with alanine highlighted.

PET works in conjunction with radioligand injected to the patient, which under radiation will emit gamma-rays detected by the machinery. This technique can be used to investigate different biological processes (metabolism with glucose-derived tracer for example) in the whole patient body, according to the probe (radioligand) used. PET combined with some specific probe can detect the activity of dopamine receptors which can then be correlated to dopamine neurotransmission [54]. However, both PET and fMRI/FMRS are quite unpractical for long-term neuroscience research as they do not allow for subject movement, have limited spatial resolution (2-3mm) and operational time, are relatively expensive (due to energy consumption) and require large equipment to be performed which make them impossible to integrate on an implantable platform.

Hence, a platform able to monitor neurochemicals on large-scale using this kind of non-invasive techniques is technologically impossible to produce if aiming at the patient everyday comfort and liberty of movement. Leading invasive techniques are therefore the only candidate for such an application, non-invasive techniques being primarily are mainly clinical tools, not compatible with patient.

## 1.4.2 Invasive techniques for neurochemical detection

The two most widely used direct neurotransmitters detection techniques are microdialysis and electrochemical sensors. These techniques have been widely developed in the last two decades. Several approaches supporting them have been employed and are undergoing intensive studies to obtain devices that could be commercialized as biomedical implants.

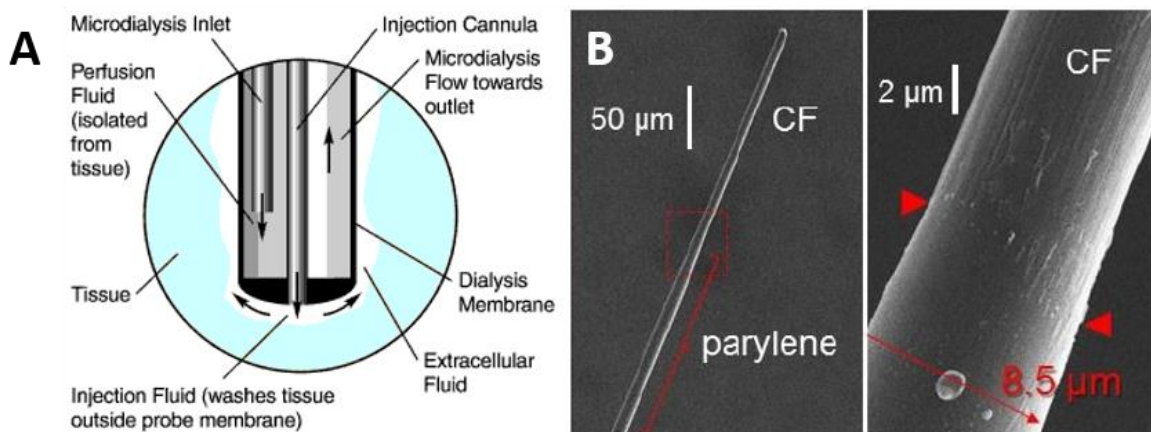


**Fig. 9: Carbon fiber and microdialysis electrodes.** (A) (Right) Microdialysis probe function reproduced from BASi website. (B) Carbon fiber (CF) microelectrode insulated with parylene, reproduced from [57].

### 1.4.2.1 Microdialysis

As can be seen in **Fig. 9A**, microdialysis works through the direct sampling of a fraction of the cerebral fluid that diffuses into the probe (constituted of a hollow tip covered with a semipermeable membrane). As this fluid then undergoes chemical analysis like HPLC, column chromatography, etc., microdialysis presents an excellent selectivity and quantification capability as it can identify various neurochemicals such as glutamate

[55] as well as dopamine [56]. However, as said the required diffusion (that highly increases sampling times which were over minutes per sample historically and can under 1min nowadays) and the required coupling with heavy equipment like HPLC hinders the possibility of real-time measurements.

#### 1.4.2.2 Electroanalytical techniques

Electroanalytical techniques are performed using electrically-conducting and biologically-inert microprobes (typically made in materials like Pt, Pt/Ir or carbon fiber as in **Fig. 9B**) with dimensions significantly lower than microdialysis probe (due to the absence of microfluidics), which greatly lower the insertion damage to the brain tissue. The electrode potential is then manipulated to induce chemical reactions generating electron transfer from molecules in the cerebral fluid to the electrode (creating a current), to detect electroactive molecules.

However, a lot of molecules of interest present in the cerebral media are not naturally electroactive. This limitation can be circumvented using specific enzyme-based coatings [52, 58], which convert non-electroactive species in electroactive molecule (as hydrogen peroxide for example) through enzymatic conversion, enabling their detection. In this kind of sensors, the electrode only plays the role of transducer. We will not consider enzyme-using sensors in the rest of this thesis, as enzymes have limited lifetime and lose their detection capabilities overtime, which is not compatible with our aim of long-term operational performance of our platform.

#### 1.4.2.3 Technique choice for combined electrophysiology and neurochemical detection

As these two techniques both directly sample the neurotransmitters (and allow patient freedom of movement), they offer both reliable quantification and continuous monitoring. However, only electrochemical detection (electrodetection) offers an adequate temporal and chemical resolution to study neurochemical dynamics in real-time (for dopamine for example, production peaks are tens of ms-long and range concentration-wise from 40 to 100nM). Moreover, electrochemical detection is technically fully compatible with microelectrodes (already present on microfabricated neural probes), which makes the integration and combined use of both electrochemical detection techniques and electrophysiologic measurements easier. On the contrary, microdialysis integration would be hard to realize as it implies multiple time-consuming additional microfabrication steps to integrate microfluidics on the probe.

Hence, to meet the need described before, the best choice is to combine electrophysiologic measurements and neurochemical electrochemical detection simultaneously and in real-time, on an implantable platform capable of both on the same electrode (with the possibility to alternate between both).

## 1.5 Neurochemical Electrode detection techniques

In this part, we will go through the electro detection principle, two examples of techniques usable for neurotransmitters detection and how their can be translated in-vivo to conclude on how we propose to integrate electro detection on our implantable platform.

### 1.5.1 Electro detection principle

Electro detection works through applying a potential to a working electrode (WE), following a certain potential excitative waveform (it can theoretically be applying a current to WE, however here we focus on potential). This potential change modifies the electrode surface energy level, allowing certain molecules to react to its surface (as a reaction energetic activation barrier is crossed) after diffusion. When a reaction occurs, electrons can be produced and transferred to the WE creating a flowing current (**Fig. 10**) whose measurement allows the source molecule to be detected. As all molecules start to react only at a certain potential, a data couple potential/current allows both the quantification and identification of a molecule.

However, to actually perform electro detection, at least two different electrodes are needed (as for electro-physiological recordings) to complete an electrochemical cell, as only a potential difference can be applied and the current induced by electron transfers needs a closed circuit to flow (**Fig. 11A**).

This potential difference is applied versus one of the cell electrodes called the reference electrode (RE), which is, in practice, an electrode maintaining a stable potential over the course of the experiment (thus, this electrode is non-polarizable). However, in this configuration, the reference electrode is used to close the circuit and so exposed to the current produced during the experiment. The risk is to damage it overtime, the electroactive material responsible for its stable potential being polarized which will eventually modify its nature by changing its potential (modifying the reference potential of the cell) or even by preventing to keep a stable potential afterwards.

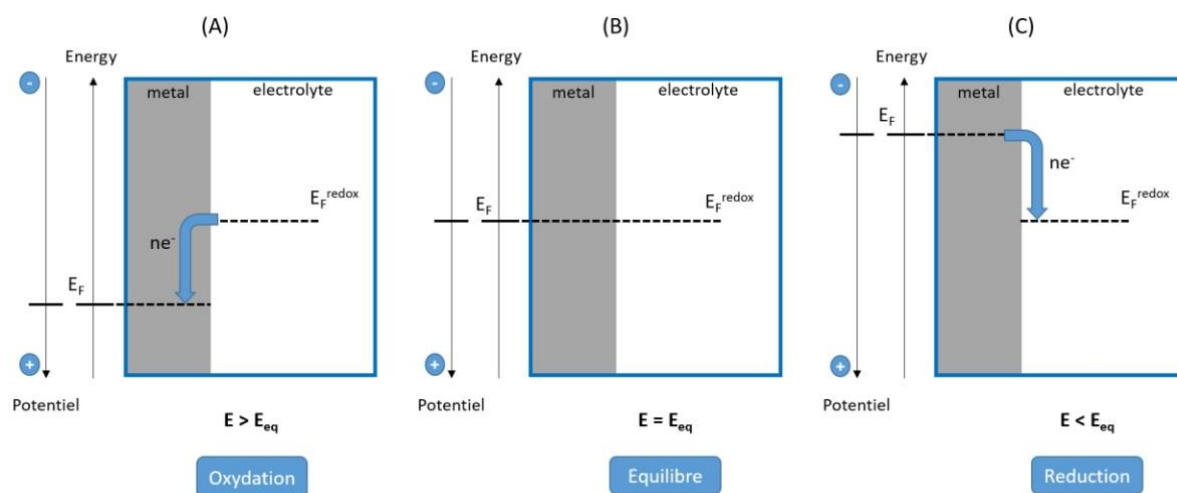


**Fig. 10: Electro detection working principle.** (A) The potential of the electrode (metal) is higher than the reaction potential of the redox couple in the electrolyte ( $E_F^{redox}$ ), the electrons are then flowing from the electrolyte (which is oxidized) to the electrode. (B) Both potentials are equal, no electron flux is observed. (C) Opposite to the first scenario, the electrons are then flowing from the metal to the electrolyte, which is reduced [59].

To prevent this phenomenon, another type of electrochemical cell can be used by adding a counter electrode (CE) as shown in **Fig. 11B**. This electrode is used to close the electrical circuit, which relieves the reference electrode of this role, monopolizing it for only its referencing role. The triad WE/RE/CE is called a three-electrode electrochemical cell and is preferred in practice as it provides better performance [60] and cell lifetime (the RE not being used to pass current, it does not get polarized and so degrades slowly).

The potential difference is applied by a potentiostat, a device capable of generating both an accurate potential difference (DP) or a current between two electrodes. It is impossible to both control the current and the DP between two electrodes as both are linked physically. Modern digitally-controlled potentiostats can be used to apply an excitative potential waveform, that can be constituted of combinations of potential step, ramp, sinus, etc. with a high accuracy.

The excitative waveform used to address the working electrode potential (polarization) plays a critical role in the possibility to selectively detect certain molecules and in the electro-detection performances in terms of temporal and chemical resolution, sensitivity and limit of detection.

Among all the techniques (each using one specific type of excitative waveform) existing, this influence is well demonstrated by the difference between chronoamperometry (CA) and fast-scan cyclic voltammetry (FSCV). The other techniques that could have been mentioned and considered are cyclic voltammetry (CV), square-wave voltammetry (SWV), pulse-based techniques like differential pulse voltammetry (DPV) for the main ones. These techniques could also theoretically match the requirements in this thesis however, they could not be thoroughly tested.

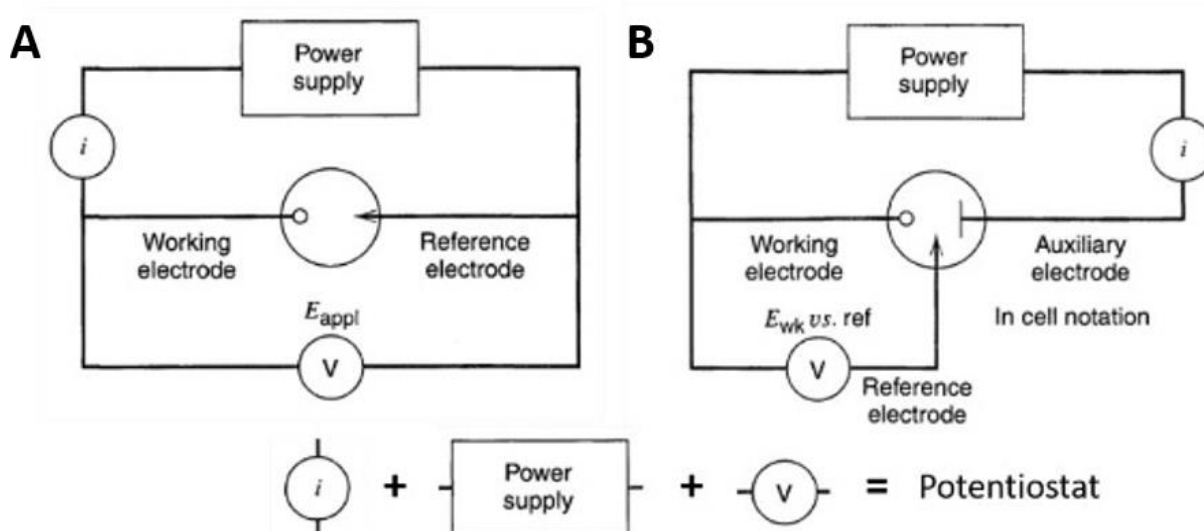


**Fig. 11: Two- and three-electrode electrochemical cell configuration with the potentiostat.** (Left) Two-electrode cell, with the WE and RE closing the circuit and the different functions of the potentiostat displayed in an equivalent circuit. (Right) Same circuit but with the counter electrode added as the third electrode [59].

## 1.5.2 Chronoamperometry (CA)

CA is a very easy electrochemical technique to perform, as it consists in only polarizing the working electrode to a constant potential. As the electrode surface energy level is modified, electron-transfers are induced (as their activation energies are lower than the electrode energy level) and the resulting current is monitored.

As this technique consists in applying a constant polarization to the electrode, the monitoring of the molecules that can react is continuous, which allows to follow quick concentration transients (only limited by the potentiostat sampling frequency) [61].

However, this technique can lack selectivity, as all molecules that can react due to the energy level of the WE react in the same time at its vicinity. Hence, the signal obtained is the sum of all currents produced by all electrochemical reactions at the electrode.

On top of its lack of selectivity, CA induces a constant electrostatic microenvironment perturbation over the experiment course as the electrode is maintained at a potential, which results in the WE fouling by charged biomolecules accumulating at its surface if the electrode stays polarized too long.

## 1.5.3 Fast-scan cyclic voltammetry (FSCV)

FSCV (and its use in-vivo) has been pioneered by Wightman *et al.*, as early as the 1980's, which leads the development of instrumentation and electrodes still used up to these days.

FSCV usually works by applying a triangle-shaped waveform to a microelectrode, typically a Carbon Fiber Microelectrode (CF $\mu$ E, **Fig. 11A**). The triangle scan is typically around 400 V/s (but can be up to 1200V/s or even 2400V/s [62]), with typical scan limits of -0.4 V to 1.3 V. The scans are typically applied every 100ms with the electrode holding at -0.4 V (being the lower vertex potential) in between scans. The current collected from a triangle scan is displayed as a cyclic voltammogram (CV), being a current=function(potential) graph, written  $I=f(E)$  in the rest of the manuscript.

The current obtained is the sum of the capacitive currents (charging of the electrical double layer, created by ions movements) and faradaic currents (the current created by electrons produced by redox reactions from interest species). To obtain the electrochemical FSCV signature of a targeted molecule, the capacitive currents (called background) must be subtracted, which makes this technique differential. This currents then must be measured beforehand without the molecule(s) of interest.

For example, an increase in dopamine (a common redox active neurotransmitter) in the electrode surrounding space yields the apparition of a current peak in the voltammogram at a certain potential (depending of the pH, the media, the scan rate, the electrode material...). A cyclic voltammogram of the current change due to this addition of dopamine is obtained by digitally subtracting the background current [63] from the signal with the dopamine.

These measurements are realized overtime at a given frequency (10Hz) and to display changes in concentration over time, the CVs are plotted in color maps where the y-axis is potential, x-axis is time, and current is



in false color [64] like in **Fig. 12B**. A trace taken along the x-axis (at one signature potential) indicates the changes in concentration of the corresponding analytes over the measurement time while a trace on the y-axis correspond to the concentration change at a potential, thus of one specific molecule like dopamine (**Fig. 12C**).

Thanks to high scan rates, FSCV displays a high sensitivity compared to other electrodedetection techniques (higher than CA for example, as faradaic currents increase with scan rate, CA being a “0V/s scan rate” technique) and the possibility to follow millisecond-transients. Moreover, the possibility to identify multiple molecules reacting at different potentials allows for a very high selectivity. These characteristics make FSCV a very effective technique for in-vivo electrochemical detection of neurotransmitters [65, 66].

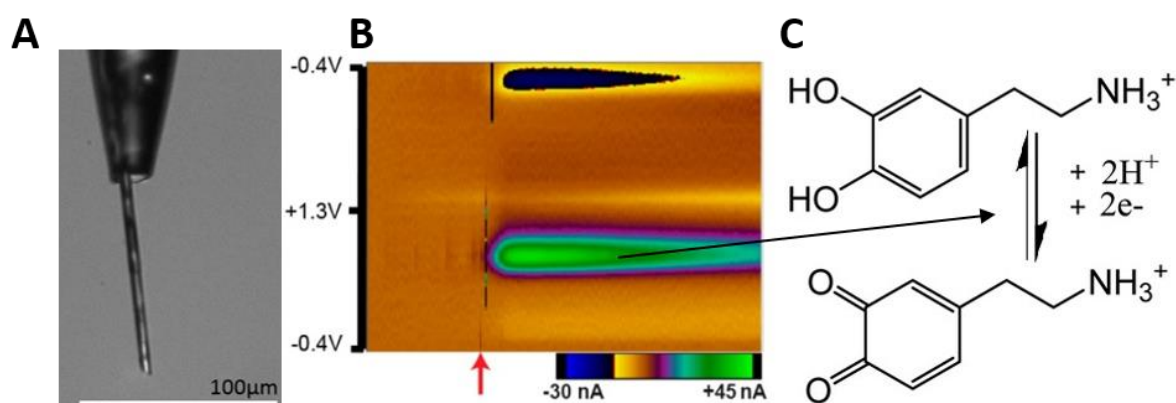


**Fig. 12: FSCV working principle.** (A) A carbon-fiber microelectrode, used as working electrode in FSCV experiments, where the electron exchange will take place, (B) Color plot of this electron transfer overtime, before and after the dopamine injection (red arrow), (C) Equation for the electrochemical reaction between dopamine in its reduced state (top) that is oxidized to form its o-quinone form, releasing the measured electron.

However, FSCV also has many disadvantages, mainly due to its differential nature. The need for background measurements done prior to implantation and then used to background subtract all data along the FSCV experiment makes this technique very sensitive to any background drift. This drawback has been the major motivation for research to overcome it by in-vivo calibration [67], recalibration [68] or post-measurement data detrending [69] for example. This also impedes FSCV to be easily used for long-term measurements (to detect slow-changing concentrations of some molecules for example) [70]. The potential rest value has also shown to have a great influence on the viability of the technique [71]. And finally, transients quicker than the time between two scans cannot be accurately followed with FSCV.

#### 1.5.4 In-vivo neurotransmitter electrodedetection

As the need is to detect neurotransmitters in-vivo, how it is performed in the literature?

In-vivo neurotransmitter electrodedetection is mostly performed by FSCV on single carbon fiber microelectrodes (CF $\mu$ Es) [72]. These electrodes are quite easily fabricated, have high surface with high surface electron transfer kinetics, making them the “gold standard” for this kind of study.

However, these electrodes must be implanted with at least a reference electrode (typically a chlorinated silver wire [73]) used both as a reference and a counter electrode to complete the electrochemical cell. The need for a double implantation to only get one working electrode is a major limitation of this kind of electrodes. Plus, CF $\mu$ Es are manufactured by hand [73], inducing a high discrepancy rate in between electrodes, which implies individual calibration to take into account individual electrode variation.

These limitations gave rise to research into ways to overcome them, by arraying them using microfabrication techniques for example. In the same time research into fully-microfabricated probes for in-vivo neurotransmitters detection [74] were conducted, to take advantage of microfabrication like better reproducibility.

However, for the time being, very few multi-electrode probes were fabricated and published for electrodedetection use, particularly using FSCV to detect neurotransmitters [74, 75].

### 1.5.5 Electrodedetection integration

Hence, electrodedetection will have to be integrated on multiple electrodes on the same device, to be able to study neuronal networks. Neurotransmitters electrodedetection will be performed using both FSCV for its high selectivity and sensitivity, more adequate to detection in complex media like brain microenvironments, and by CA to follow quick transients that could be missed with FSCV (due to its lower sampling frequency).

How to integrate electrodedetection on an electrode, in conjunction with electrophysiology? Electrodes with good electrophysiological measurement performances need low impedances to record small potential variations in their vicinity with high fidelity. However, for electrodedetection, electrodes need to have low electron transfer resistance and adequate surface chemistry for redox reactions.

### 1.5.6 Working electrode modification

As said before, after fabrication, the available microelectrodes on microfabricated devices are metallic microelectrodes. These electrodes need to be modified to fit their applications as recording electrodes, bare metallic microelectrodes having inadequate properties [76].

Electrode modification for electrophysiology employs a vast array of protocol, from electrode structuration (roughening, porosity enhancement...) to electrode modification through electrodeposition of conducting polymers (CPs), oxides, etc. or nanocarbon growth for example.

LAAS already has an expertise in conducting polymers electrodeposition (like Poly-EthyleneDiOxyThiophene "PEDOT" and PolyPyrrole) and CIRIMAT has an expertise in nanocarbon chemistry (synthesis, functionalization, etc.). As electrodes, these two materials can have adequate properties for electrophysiology. Thus, CP and nanocarbon will be the two materials considered for WE modification to yield an electrode capable of both electrophysiology and electrodedetection.

### 1.5.6.1 Conducting polymer and nanocarbon electrode modification

Conducting polymers (CPs) are organic polymers which molecular chain is made of conjugated atoms, allowing for charge carrying. Charge carriers in CPs are electronic deficiencies which need a counter ion to be stable.

Due to this structure, CPs reduce microelectrode impedance overall, improve charge storage capacity (CSC), charge injection limit (CIL) and present improved long-term stability. Conducting polymers can be deposited on surface by chemical or electrochemical polymerization. Direct electro-polymerization is the preferred choice for deposition on microelectrode, as it restrains the deposition on the microelectrode only. Plus, it allows to have an excellent control of total polymerization charge, morphology, counter ion integration and polymerization rate, allowing a tailoring of the deposited CPs for their targeted applications. Moreover, several molecules/polymers [37, 77-81] can be integrated (as dopants or not) in the CP matrix during its deposition, to obtain new properties (adhesion, surface chemistry, bioactive molecules release, biodegradability...) and further tailor the chemical, electrical and physical properties of the deposits. These properties make the use of CP electrodeposition a major asset to fabricate our target electrode. Among CPs, the most indicated is PEDOT, as it showed the best in-vivo performances.

One class of dopants that have been driving increasing interest is nanocarbon species like carbon nanotubes [82] (CNTs). They are conductive themselves and display extraordinary properties on all levels (mechanical, electrical, chemical...). They can be used as dopants for CPs if negatively-charged. Also, a big number of nanocarbon allotropes exist and can be integrated in CPs to produce multiple effects (templating, bulk integration for properties upgrade, mechanical reinforcement...). One key property for electro-detection is their exploitable surface electrochemistry for electro-detection, that promotes surface electron transfers by making them easier with the participation of the CNF surface electroactive functions (acting as “middles mans” for these electron transfer).

### 1.5.6.2 Electrochemistry at nanocarbon electrodes

Nanocarbon species are composed of mostly two types of carbon atoms:  $sp^3$  carbon which is the building block for graphene and diamond and  $sp^2$  carbon which is the building block graphene as it creates a conductive skeleton called the  $\pi$ -skeleton (due to  $sp^2$  carbon having  $\pi$ -orbitals, containing electrons, that align, allowing for electron travel). Any carbon species with specific dimensions below  $1\mu\text{m}$  can be considered as nanocarbon species.

Hence, the electrical properties of conductive nanocarbons are due to their  $\pi$ -skeleton. However, in solution with electrochemical probes (molecules that can exchange electrons at known potentials), their electrochemical properties are mainly determined to the edges of their skeleton. For example, graphene edges (**Fig. 13A**) show four orders of magnitude higher specific capacitance, much faster electron transfer rate and stronger electroactivity than those of graphene basal plane [83] (**Fig. 13B**). This is believed to rise from more adequate energy level at these edges for electron transfer and electrochemical interactions.

Considering perfect morphologies (without defects), the ideal nanocarbon species for electrochemistry (meaning the one with the best electrochemical properties and the higher surface electron transfer capabilities toward a considered target) would have the best ratio between its exposed graphene plan edges proportion and its unexposed conductive skeleton [84]. In that view, Platelet Graphene Nanofibers (PGNFs, **Fig. 13C**) would be the best nanocarbon allotropes to use to obtain an optimal nanocarbon containing electrode. PGNFs are nanofibers with a structure composed of parallel planes of graphene stacked (instead of rolled up like for CNT or tubular CNFs, **Fig. 13D**) on top of each other, exposing almost only graphene planes edges. They are quite similar to herringbone-carbon nanofibers (**Fig. 14E**), which are only differentiated by the angle made by the graphene layers in respect to the fiber axis.

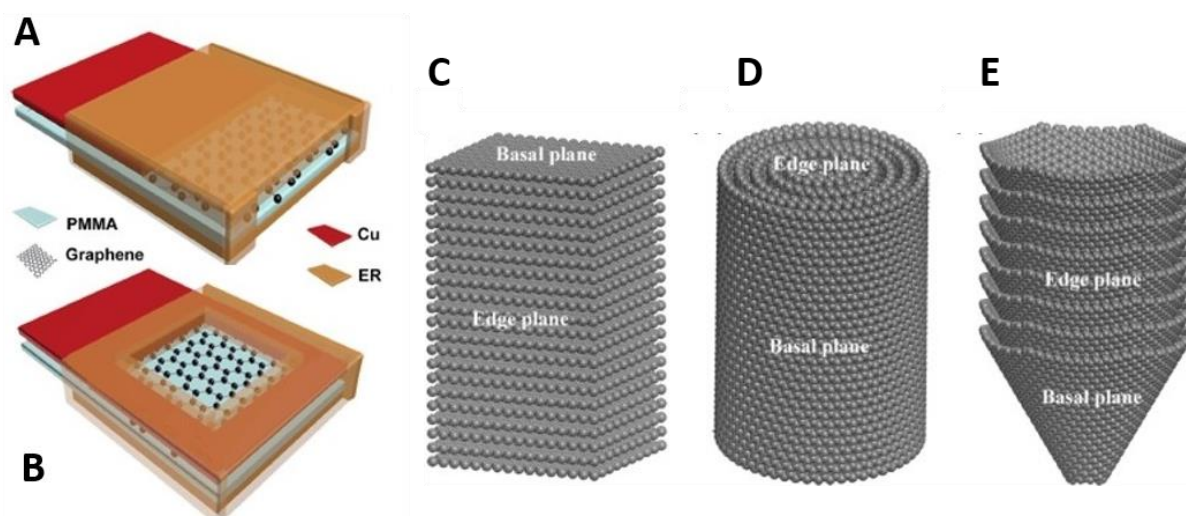


**Fig. 13: Surface electrochemistry at nanocarbons species.** Devices fabricated to study selectively both the electroactivity of the edge (A) and of the basal plane (B) of a graphene sheet [83]. Representation of three different type of organization graphene sheets inside nanocarbon allotropes with (C) graphene sheets stacked on top of each other into platelet graphene nanofibers (PGNFs), (D) rolled up into carbon nanotubes and (E) stacked up in conical configuration in herringbone carbon nanofibers.

It is important to note that carbon nanomaterials processing and conditioning can have major influence on the resulting nanocarbon electrodes and nanocomposites. Most nanocarbons are produced through synthesis catalyzed by metal particles/surfaces which can still be found in the resulting nanocarbon species in form of impurities and thus be responsible for some electrochemical behavior [85]. These impurities are commonly removed through chemical processing of the raw carbon material [86].

Carbon nanomaterials can be doped or functionalized to change their properties. Their surface chemistry can be tailored through molecules adsorption [87] or chemical/physical treatments resulting in functional groups grafting, porosity generation or defects creation. For example, carbon nanotubes chemical oxidation in strong oxidizing acids mixes (nitric acid and sulphuric acid) induce surface oxidation, grafting oxygenated groups on the tube sidewalls and ends, making it more hydrophilic. This makes the tubes easier to use through aqueous processes, and enhance hydrogen bonding of other molecules on the tube surface. This kind of chemical

treatment also generates surface defects that have similar reactivity that graphene edges (they are sometimes called “edge-like defects”).

Considering all these factors influencing the electrochemical behavior of nanocarbon species, the high electron transfer kinetics of CF $\mu$ Es can be explained by their high proportion of defects along the exposed tubular carbon surface, their high specific surface (tens of  $\mu\text{m}$  of length exposed) and the in-solution pre-conditioning, necessary for their use in-vivo, which further induces surface defects.

However, exploitation of these interesting electrochemical properties is made impossible on polymer-based flexible implants, as the nanocarbon synthesis conditions are incompatible with such polymers (high temperatures, pyrolysis, hydrogen exposure...). To circumvent this critical limitation, a nanocomposite of PEDOT and nanocarbon is proposed as candidate for multifunctional electrode.

### 1.5.6.3 Rapid review of PEDOT-Nanocarbon composites

**Table 3: References from the literature of PEDOT composite presenting nanocarbon species and their subsequent application.**

Ref	Composite <sup>a</sup>	Electrode material	Electrode diameter	Application
[82]	PEDOT-CNT	Gold	25 $\mu\text{m}$	Sensing <sup>b</sup> electrode
[88]	PEDOT-CNT	Carbon paste	NA	Sensing electrode
[89]	PEDOT-GO	T650 CF $\mu$ E	7 $\mu\text{m}$	Sensing electrode
[22]	PEDOT-PSS-MWCNT	Gold microspheres	50 $\mu\text{m}$ (Pt*)	Recording electrode
[90]	PEDOT-NHs	Nanostructured Au	60 $\mu\text{m}$	Recording <sup>b</sup> /Stimulating electrode
LAAS	PEDOT-CNF	Gold	20 $\mu\text{m}$	Recording/Stimulating/Sensing

\*: starting microelectrode surface, electrode modified before PEDOT-nanocarbon deposition, <sup>a</sup>: please refer to the abbreviation list for material name, <sup>b</sup>: sensing is meant as used for electrodedetection and recording for used in electrophysiology recordings

As PEDOT needs a counter ion (that can be called dopant) during both its electrodeposition and use, any molecules/nano-objects with negative charges can be integrated in the PEDOT matrix during polymerization. As can be seen in **Table 3**, numerous nanocarbon allotropes have already been used with PEDOT, from CNTs to Graphene (Gr), to construct multiple types of electrodes. These allotropes have typical dimensions of a few  $\mu\text{m}$  or even smaller, which makes their integration a full encapsulation, resulting in a composite having a higher specific surface area and capacitance for example but not exploiting the surface properties after PEDOT deposition.

## 1.6 Aim of the thesis

### 1.6.1 Electrode for combined electrophysiology and electrodedetection

Exploiting LAAS' already existing expertise in CPs microelectrodes, we propose to develop a PEDOT-nanocarbon electrode to modify the WEs of a microfabricated device, making them multifunctional. The combination of nanocarbon specific surface electrochemistry and properties and advantages of CPs like PEDOT would help obtain microelectrodes both suitable for electrophysiology and neurotransmitter electrodedetection.

For the WE, to mimic CF $\mu$ Es, a PEDOT-CNF nanocomposite is chosen as the best candidate. As we have seen before, PGNFs are the best theoretical nanocarbon allotrope for electrochemistry. However, PGNFs are not commercially available and no reachable expertise in their synthesis was present in LAAS's network. CNFs are widely commercially available, at low cost and have already shown interesting electrochemical properties for detection [91]. This is due to their high edge proportion when they have a herringbone morphology. They can easily be modified by chemical oxidation to induce surface defects when having a tubular morphology without critical damage risk (due to the tens graphene sheets constituting their tube).

Furthermore, PGNFs when deposited electrochemically with PolyPyrrole (PPy) [92] tend to be easily encapsulated in the resulting film. Thus, taking advantage of their surface electrochemical properties rely mostly on the porosity of the film. CNFs, as they have high factor ratio (high length to small diameter), they will not be easily fully encapsulated, allowing to expose their surface directly to the target media.

Hence, we choose to integrate PEDOT-CNF-modified microelectrode as multifunctional electrodes, taking advantage of nanocarbon surface properties for both electrophysiology and electrodedetection, to detect neurotransmitters.

### 1.6.2 Electrodedetection molecular targets for electrodedetection

As said before, more than 200 molecules have been identified as neurotransmitters and could be targeted. However, only a handful are naturally electrodedetectable (capable of exchanging electrons). Thus, only naturally electroactive molecules will be targeted in this thesis. The main target for this work will be dopamine. Dopamine is one of the most widely studied and documented neurotransmitters [12, 63, 66, 70, 75, 93-97], over multiple animal/cellular models (in-vitro, in-vivo, in mice, rats...), allowing any new data about its activity and its correlation with electrophysiology to be compared with already existing literature. Plus, dopamine electrodedetection has also already been studied in multiple groups and animal/cell models. On top of dopamine, adenosine and histamine will also be considered as potential targets for their respective molecular role,

but these molecules are known to be less electroactive, needing higher potentials to trigger electron exchange, thus are harder targets.

Adenosine plays a critical role in cellular metabolism (as a modulator, a sub product of cellular metabolism/ATP consumption), is ubiquitously-produced in biological tissues and play a role in neurotransmission and in epilepsy [98], making it a high-value target for our studies. As it has already been studied through FSCV, it will be possible to compare results with the literature [99-102]. It has also been shown that a correlation between adenosine transients frequency and events like ischemia [102] and seizures [98].

Finally, histamine FSCV electrodedetection is less documented [103-105], particularly in-vivo, which makes any new data more difficult to compare with existing literature, it is however a high value target as HA is implicated in a plethora of brain biochemical processes such as in inflammatory processes [106]. Thus, HA monitoring could allow for real time monitoring of the foreign body response around the implant after implantation for example. Furthermore, HA seems to be a neuroprotective molecule, as high levels of HA have been known to suppress seizures for over 20 years [107].

### **1.6.3 Final device, objectives and comparison to the state of the art**

We propose to develop a flexible implant with electrodes capable of both real-time long-term electrophysiology and neurotransmitter electrodedetection, compatible with both a therapeutic and research end applications. This implant will be fabricated in clean room using standard microfabrication technologies. Then the electrodes will be modified using electrodeposition of a new PEDOT-CNF nanocomposite. These electrodes are meant as multifunctional electrodes, due to the use of a selected nanomaterial, the CNFs, which integration is not compatible otherwise with flexible devices. This will allow these electrodes to be capable of electrophysiological recordings, electrical stimulation and electrochemical sensing, both in-vitro and in-vivo. Electrodedetection will be performed by CA to follow quick transients and FSCV to monitor multiple interest species selectively. The proposed device is compared to other published device aiming at combined electrophysiology and neurochemical detection in-vivo.

The advantages of microfabrication are numerous:

- Multiple electrodes can be integrated on each device, allowing for studies on multiple neurons (networks) in the same time;
- both kinds of electrodes (recording and detecting) will be integrated in the same time in the fabrication process, keeping the fabrication process simple;

- these base microelectrodes used for electrodeposition will have reproducible configuration and characteristics, ensured by microfabrication, largely eliminating the discrepancy from device to device;
- both kinds of electrodes will be integrated separately, allowing their simultaneous use in the end;
- microfabrication also ensures a certain ease for prototyping the device;

Based on previous work and results from the LAAS MEMS group, this implant will be fabricated on a soft substrate to prevent any long-term mechanical mismatch between the implant and the brain tissue. This soft substrate will be ParyleneC [35, 108, 109], an inert, microfabrication-compatible, flexible and biocompatible material already used in the LAAS. This will prevent long-term electrophysiological measurements fail due chronic inflammation maintained [110-112] at the insertion site by this mismatch (ending in scarring of the tissue around the device, phenomenon called foreign body response). This inflammation is usually due to brain micromotion around the implant [113-115], which adds to the inevitable acute trauma due to the implantation itself [112, 116, 117] (basically equivalent to a stab wound for the brain tissue [118-120]).

Finally, our devices will be tested in brain slices, as promising models to study both healthy and diseased brain, which are also easy to access for more relevant biological studies [121] than cell culture.

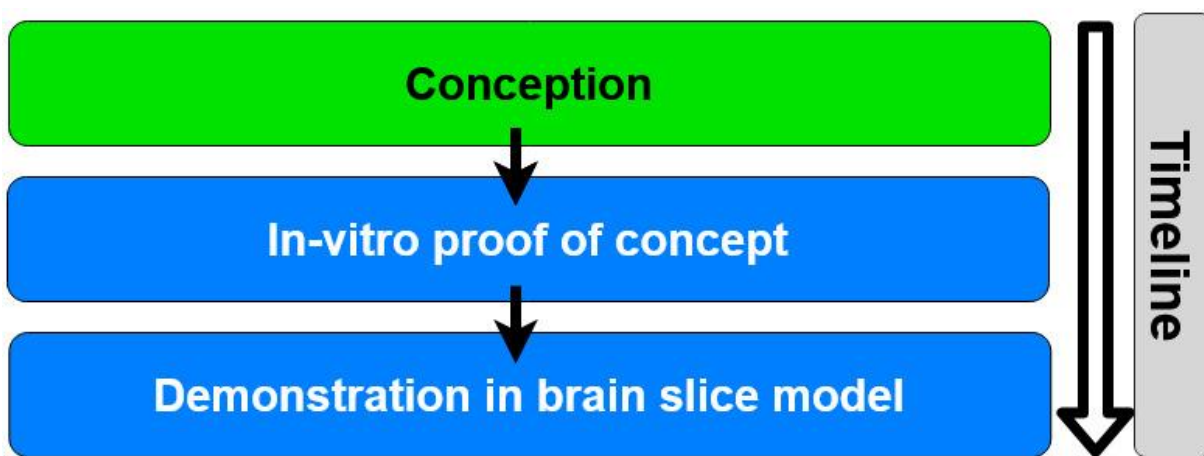


**Fig. 14:** Proposed theoretical time line of the present thesis, from the conception of the device to its use in brain slices.



1. Deco, G. and M.L. Kringelbach, *Hierarchy of Information Processing in the Brain: A Novel 'Intrinsic Ignition' Framework*. *Neuron*, 2017. **94**(5): p. 961-968.
2. Azevedo, F.A., et al., *Equal numbers of neuronal and nonneuronal cells make the human brain an isometrically scaled-up primate brain*. *J Comp Neurol*, 2009. **513**(5): p. 532-41.
3. Herculano-Houzel, S., *The human brain in numbers: a linearly scaled-up primate brain*. *Front Hum Neurosci*, 2009. **3**: 31.
4. Herculano-Houzel, S., *The glia/neuron ratio: how it varies uniformly across brain structures and species and what that means for brain physiology and evolution*. *Glia*, 2014. **62**(9): p. 1377-91.
5. Edwards, R.H., *The neurotransmitter cycle and quantal size*. *Neuron*, 2007. **55**(6): p. 835-58.
6. Ferguson, T.A. and S.S. Scherer, *Neuronal cadherin (NCAD) increases sensory neurite formation and outgrowth on astrocytes*. *Neurosci Lett*, 2012. **522**(2): p. 108-12.
7. Belanger, M., I. Allaman, and P.J. Magistretti, *Brain energy metabolism: focus on astrocyte-neuron metabolic cooperation*. *Cell Metab*, 2011. **14**(6): p. 724-38.
8. Lee, S., et al., *A culture system to study oligodendrocyte myelination processes using engineered nanofibers*. *Nat Methods*, 2012. **9**(9): p. 917-22.
9. Fain, G.L., *Molecular and Cellular Physiology of Neurons (2nd Edition)*, 2014.
10. Pereda, A.E., *Electrical synapses and their functional interactions with chemical synapses*. *Nat Rev Neurosci*, 2014. **15**(4): p. 250-63.
11. Evans, W.H. and P.E. Martin, *Gap junctions: structure and function (Review)*. *Mol Membr Biol*, 2002. **19**(2): p. 121-36.
12. Atcherley, C.W., et al., *The coaction of tonic and phasic dopamine dynamics*. *Chem Commun (Camb)*, 2015. **51**(12): p. 2235-8.
13. Wu, C. and D. Sun, *GABA receptors in brain development, function, and injury*. *Metab Brain Dis*, 2015. **30**(2): p. 367-79.
14. Brown, D.A., *Acetylcholine and cholinergic receptors*. *Brain and Neuroscience Advances*, 2019. **3**.
15. Borea, P.A., et al., *Pharmacology of Adenosine Receptors: The State of the Art*. *Physiol Rev*, 2018. **98**(3): p. 1591-1625.
16. Carhart-Harris, R.L. and D.J. Nutt, *Serotonin and brain function: a tale of two receptors*. *J Psychopharmacol*, 2017. **31**(9): p. 1091-1120.
17. Bhowmik, M., R. Khanam, and D. Vohora, *Histamine H3 receptor antagonists in relation to epilepsy and neurodegeneration: a systemic consideration of recent progress and perspectives*. *Br J Pharmacol*, 2012. **167**(7): p. 1398-414.
18. Beaulieu, J.M. and R.R. Gainetdinov, *The physiology, signaling, and pharmacology of dopamine receptors*. *Pharmacol Rev*, 2011. **63**(1): p. 182-217.
19. Jorfi, M., et al., *Progress towards biocompatible intracortical microelectrodes for neural interfacing applications*. *J Neural Eng*, 2015. **12**(1): 011001.
20. Lecomte, A., *Conception and characterization of flexible microelectrodes for implantable neuroprosthetic development*. 2016, Université Fédérale de Toulouse Midi-Pyrénées.
21. Bartels, J., et al., *Neurotrophic electrode: method of assembly and implantation into human motor speech cortex*. *J Neurosci Methods*, 2008. **174**(2): p. 168-76.
22. Castagnola, E., et al., *pHEMA Encapsulated PEDOT-PSS-CNT Microsphere Microelectrodes for Recording Single Unit Activity in the Brain*. *Front Neurosci*, 2016. **10**: p. 151.
23. Ferguson, J.E., C. Boldt, and A.D. Redish, *Creating low-impedance tetrodes by electroplating with additives*. *Sens Actuators A Phys*, 2009. **156**(2): p. 388-393.
24. Prasad, A., et al., *Comprehensive characterization and failure modes of tungsten microwire arrays in chronic neural implants*. *J Neural Eng*, 2012. **9**(5): 056015.
25. Prasad, A., et al., *Abiotic-biotic characterization of Pt/Ir microelectrode arrays in chronic implants*. *Front Neuroeng*, 2014. **7**: p. 2.
26. Normann, R.A. and E. Fernandez, *Clinical applications of penetrating neural interfaces and Utah Electrode Array technologies*. *J Neural Eng*, 2016. **13**(6): p. 061003.
27. HajjHassan, M., V. Chodavarapu, and S. Musallam, *NeuroMEMS: Neural Probe Microtechnologies*. *Sensors (Basel)*, 2008. **8**(10): p. 6704-6726.
28. Wise, K.D., et al., *Wireless Implantable Microsystems: High-Density Electronic Interfaces to the Nervous System*. *Proceedings of the IEEE*, 2004. **92**(1): p. 76-97.
29. Xiang, Z., et al., *Ultra-thin flexible polyimide neural probe embedded in a dissolvable maltose-coated microneedle*. *Journal of Micromechanics and Microengineering*, 2014. **24**(6): 065015.

30. Altuna, A., et al., *SU-8 based microprobes for simultaneous neural depth recording and drug delivery in the brain*. Lab Chip, 2013. **13**(7): p. 1422-30.
31. Huanan Zhang, P.R.P., Zhixing Xie, Scott D. Swanson, Xueding Wang, and Nicholas A. Kotov, *Tissue-Compliant Neural Implants from Microfabricated CNT Multilayer Composite*, ACS Nano, 2013.
32. Castagnola, V., et al., *Parylene-based flexible neural probes with PEDOT coated surface for brain stimulation and recording*. Biosens Bioelectron, 2015. **67**: p. 450-7.
33. Weltman, A., J. Yoo, and E. Meng, *Flexible, Penetrating Brain Probes Enabled by Advances in Polymer Microfabrication*. Micromachines, 2016. **7**(10): p. 180.
34. Metallo, C., R.D. White, and B.A. Trimmer, *Flexible parylene-based microelectrode arrays for high resolution EMG recordings in freely moving small animals*. J Neurosci Methods, 2011. **195**(2): p. 176-84.
35. Lecomte, A., et al., *Silk and PEG as means to stiffen a parylene probe for insertion in the brain: toward a double time-scale tool for local drug delivery*. Journal of Micromechanics and Microengineering, 2015. **25**(12): 125003.
36. Raeyoung, K., H. Nari, and N. Yoonkey, *Gold nanograin microelectrodes for neuroelectronic interfaces*. Biotechnol J, 2013. **8**(2): p. 206-214.
37. Castagnola, V., et al., *Morphology and conductivity of PEDOT layers produced by different electrochemical routes*. Synthetic Metals, 2014. **189**: p. 7-16.
38. Wesche, M., et al., *A nanoporous alumina microelectrode array for functional cell-chip coupling*. Nanotechnology, 2012. **23**(49): 495303.
39. Abidian, M.R., et al., *Conducting-polymer nanotubes improve electrical properties, mechanical adhesion, neural attachment, and neurite outgrowth of neural electrodes*. Small, 2010. **6**(3): p. 421-9.
40. Bernard, C., *Understanding and Predicting Epilepsy*. IEEE Signal Processing Magazine, 2016. **33**(4): p. 90-95.
41. Kubista, H., S. Boehm, and M. Hotka, *The Paroxysmal Depolarization Shift: Reconsidering Its Role in Epilepsy, Epileptogenesis and Beyond*. Int J Mol Sci, 2019. **20**(3).
42. Goodin, D.S. and M.J. Aminoff, *Electrophysiological differences between demented and nondemented patients with parkinson's disease*. Annals of Neurology, 1987. **21**(1): p. 90-94.
43. Arabia, G., et al., *Clinical, electrophysiological, and imaging study in essential tremor-Parkinson's disease syndrome*. Parkinsonism Relat Disord, 2018. **56**: p. 20-26.
44. Bargiotas, P., et al., *Sleepiness and sleepiness perception in patients with Parkinson's disease: a clinical and electrophysiological study*. Sleep, 2019. **42**(4).
45. Babiloni, C., et al., *What electrophysiology tells us about Alzheimer's disease: a window into the synchronization and connectivity of brain neurons*. Neurobiol Aging, 2020. **85**: p. 58-73.
46. Young, A.B., *Four Decades of Neurodegenerative Disease Research: How Far We Have Come*. The Journal of Neuroscience, 2009. **29**(41): p. 12722-12728.
47. Selkoe, D.J., *Alzheimer's disease is a synaptic failure*. Science 2002. **298**.
48. Lu, B., et al., *BDNF-based synaptic repair as a disease-modifying strategy for neurodegenerative diseases*. Nat Rev Neurosci, 2013. **14**(6): p. 401-16.
49. Pan, X., et al., *Dopamine and Dopamine Receptors in Alzheimer's Disease: A Systematic Review and Network Meta-Analysis*. Front Aging Neurosci, 2019. **11**: p. 175.
50. Zhang, Y., et al., *High frequency stimulation of subthalamic nucleus synchronously modulates primary motor cortex and caudate putamen based on dopamine concentration and electrophysiology activities using microelectrode arrays in Parkinson's disease rats*. Sensors and Actuators B: Chemical, 2019. **301**: 127126.
51. Kirkpatrick, D.C., et al., *Expanding neurochemical investigations with multi-modal recording: simultaneous fast-scan cyclic voltammetry, iontophoresis, and patch clamp measurements*. Analyst, 2016. **141**(16): p. 4902-11.
52. B., B., *Technological Barriers in the Use of Electrochemical Microsensors and Microbiosensors for in vivo Analysis of Neurological Relevant Substances*. Current Neuropharmacology, 2012. **10**: p. 197-211.
53. Shapiro, M.G., et al., *Directed evolution of a magnetic resonance imaging contrast agent for noninvasive imaging of dopamine*. Nat Biotechnol, 2010. **28**(3): p. 264-70.
54. Koeppe, M.J., et al., *Evidence for striatal dopamine release during a video game*. Letters to Nature, 1998. **393**.

55. Fell, M.J., et al., *Glutamatergic regulation of brain histamine neurons: In vivo microdialysis and electrophysiology studies in the rat*. *Neuropharmacology*, 2015. **99**: p. 1-8.
56. Jaquins-Gerstl, A. and A.C. Michael, *A review of the effects of FSCV and microdialysis measurements on dopamine release in the surrounding tissue*. *Analyst*, 2015. **140**(11): p. 3696-708.
57. Schwerdt, H.N., et al., *Subcellular probes for neurochemical recording from multiple brain sites*. *Lab Chip*, 2017. **17**(6): p. 1104-1115.
58. Fan, X., et al., *In Situ Real-Time Monitoring of Glutamate and Electrophysiology from Cortex to Hippocampus in Mice Based on a Microelectrode Array*. *Sensors (Basel)*, 2016. **17**(1).
59. Lemercier, G., *Conception et réalisation de microdispositifs électrochimiques, pour l'analyse de l'activité bioénergétique de mitochondries isolées, dans le cadre de la mise au point de traitements innovants des leucémies aiguës myéloïdes*. 2018, LAAS-CNRS (UPR-8001) & CRCT-INSERM (UMR-1037).
60. Bard, A.J. and L.R. Faulkner, *Bard Electrochemical methods. Fundamentals and applications (2ed)*.
61. Miller, E.M., et al., *Simultaneous glutamate recordings in the frontal cortex network with multisite biomorphic microelectrodes: New tools for ADHD research*. *J Neurosci Methods*, 2015. **252**: p. 75-9.
62. Keithley, R.B., et al., *Higher sensitivity dopamine measurements with faster-scan cyclic voltammetry*. *Anal Chem*, 2011. **83**(9): p. 3563-71.
63. A. Hermans, R.B.K., J.M. Kita, L.A. Sombers, and R. Mark Wightman, *Dopamine Detection with Fast-Scan Cyclic Voltammetry Used with Analog Background Subtraction*, *Analytical Chemistry*, 2008. **80**(11): p. 4040-4048.
64. Michael, D., E.R. Travis, and R.M. Wightman, *Color Images for Fast-Scan CV*. *Analytical Chemistry News & Features*, 1998: p. 586-592.
65. Schmidt, A.C., et al., *Multiple scan rate voltammetry for selective quantification of real-time enkephalin dynamics*. *Anal Chem*, 2014. **86**(15): p. 7806-12.
66. Park, J., P. Takmakov, and R.M. Wightman, *In vivo comparison of norepinephrine and dopamine release in rat brain by simultaneous measurements with fast-scan cyclic voltammetry*. *J Neurochem*, 2011. **119**(5): p. 932-44.
67. Roberts, J.G., et al., *In situ electrode calibration strategy for voltammetric measurements in vivo*. *Anal Chem*, 2013. **85**(23): p. 11568-75.
68. Johnson, J.A., C.N. Hobbs, and R.M. Wightman, *Removal of Differential Capacitive Interferences in Fast-Scan Cyclic Voltammetry*. *Anal Chem*, 2017. **89**(11): p. 6166-6174.
69. DeWaele, M., et al., *A baseline drift detrending technique for fast scan cyclic voltammetry*. *Analyst*, 2017. **142**(22): p. 4317-4321.
70. Dengler, A.K. and G.S. McCarty, *Microfabricated Microelectrode Sensor for Measuring Background and Slowly Changing Dopamine Concentrations*. *J Electroanal Chem (Lausanne)*, 2013. **693**: p. 28-33.
71. Oh, Y., et al., *Monitoring In Vivo Changes in Tonic Extracellular Dopamine Level by Charge-Balancing Multiple Waveform Fast-Scan Cyclic Voltammetry*. *Anal Chem*, 2016. **88**(22): p. 10962-10970.
72. Lama, R.D., et al., *Ultrafast detection and quantification of brain signaling molecules with carbon fiber microelectrodes*. *Anal Chem*, 2012. **84**(19): p. 8096-101.
73. Bledsoe, J.M., et al., *Development of the Wireless Instantaneous Neurotransmitter Concentration System for intraoperative neurochemical monitoring using fast-scan cyclic voltammetry*. *J Neurosurg* 2009. **111**: p. 712-723.
74. Ngermsutivorakul, T., T.S. White, and R.T. Kennedy, *Microfabricated Probes for Studying Brain Chemistry: A Review*. *Chemphyschem*, 2018. **19**(10): p. 1128-1142.
75. Zachek, M.K., et al., *Microfabricated FSCV-compatible microelectrode array for real-time monitoring of heterogeneous dopamine release*. *Analyst*, 2010. **135**(7): p. 1556-63.
76. Yakushenko, A., et al., *On-chip fast scan cyclic voltammetry for selective detection of redox active neurotransmitters*. *physica status solidi (a)*, 2014. **211**(6): p. 1364-1371.
77. Wang, K., et al., *Covalent bonding of YIGSR and RGD to PEDOT/PSS/MWCNT-COOH composite material to improve the neural interface*. *Nanoscale*, 2015. **7**(44): p. 18677-85.
78. Xiao, Y., et al., *Incorporation of collagen in poly(3,4-ethylenedioxythiophene) for a bifunctional film with high bio- and electrochemical activity*. *J Biomed Mater Res A*, 2010. **92**(2): p. 766-72.
79. Boehler, C., et al., *Actively controlled release of Dexamethasone from neural microelectrodes in a chronic in vivo study*. *Biomaterials*, 2017. **129**: p. 176-187.

80. Chen, C.H. and S.C. Luo, *Tuning Surface Charge and Morphology for the Efficient Detection of Dopamine under the Interferences of Uric Acid, Ascorbic Acid, and Protein Adsorption*. ACS Appl Mater Interfaces, 2015. **7**(39): p. 21931-38.
81. Kim, R. and Y. Nam, *Polydopamine-doped conductive polymer microelectrodes for neural recording and stimulation*. J Neurosci Methods, 2019. **326**: 108369.
82. Samba, R., et al., *Application of PEDOT-CNT Microelectrodes for Neurotransmitter Sensing*. Electroanalysis, 2014. **26**(3): p. 548-555.
83. Yuan, W.e.a., *The edge- and basal-plane-specific electrochemistry of a single-layer graphene sheet*, Sci. Rep, 2013. **3**, **2248**.
84. Ambrosi, A., S. Toshio, and P. Martin, *Platelet Graphite NFs for Electrochemical Sensing and Biosensing : The Influence of Graphene Sheet Orientation*, Chem. Asian J, 2010(5): p. 266-271.
85. V., M., et al., *Ultrapure Graphene Is a Poor Electrocatalyst: Definitive Proof of the Key Role of Metallic Impurities in Graphene-Based Electrocatalysis*. ACS Nano, 2019. **13**(2): p. 1574-1582.
86. Bortolamiol, T., et al., *Double-walled carbon nanotubes: Quantitative purification assessment, balance between purification and degradation and solution filling as an evidence of opening*. Carbon, 2014. **78**: p. 79-90.
87. Ambrosi, A. and M. Pumera, *Nanographite impurities dominate electrochemistry of carbon nanotubes*. Chemistry, 2010. **16**(36): p. 10946-49.
88. Xu, G., B. Li, and X. Luo, *Carbon nanotube doped poly(3,4-ethylenedioxythiophene) for the electrocatalytic oxidation and detection of hydroquinone*. Sensors and Actuators B: Chemical, 2013. **176**: p. 69-74.
89. Taylor, I.M., et al., *Enhanced dopamine detection sensitivity by PEDOT/graphene oxide coating on in vivo carbon fiber electrodes*. Biosens Bioelectron, 2017. **89**(Pt 1): p. 400-410.
90. Carli, S., et al., *Single walled carbon nanohorns composite for neural sensing and stimulation*. Sensors and Actuators B: Chemical, 2018. **271**: p. 280-288.
91. Wu, L., X. Zhang, and H. Ju, *Amperometric glucose sensor based on catalytic reduction of dissolved oxygen at soluble carbon nanofiber*. Biosens Bioelectron, 2007. **23**(4): p. 479-84.
92. Scott, C.L., G. Zhao, and M. Pumera, *Stacked graphene nanofibers doped polypyrrole nanocomposites for electrochemical sensing*. Electrochemistry Communications, 2010. **12**(12): p. 1788-1791.
93. Castagnola, E., et al., *In Vivo Dopamine Detection and Single Unit Recordings Using Intracortical Glassy Carbon Microelectrode Arrays*. MRS Adv, 2018. **3**(29): p. 1629-1634.
94. Ishida, A., et al., *A novel biosensor with high signal-to-noise ratio for real-time measurement of dopamine levels in vivo*. J Neurosci Res, 2017.
95. M.A. Makos, Y.-C.K., K-A. Han, M.L. Heien, and Andrew G. Ewing, *In Vivo Electrochemical Measurements of Exogenously Applied Dopamine in Drosophila*, Anal Chem, 2009. **81**(5): p. 1848-1854.
96. Meier, A.R., et al., *Rapid Voltammetric Measurements at Conducting Polymer Microelectrodes Using Ultralow-Capacitance Poly(3,4-ethylenedioxythiophene):Tosylate*. Langmuir, 2016. **32**(32): p. 8009-18.
97. Jackowska, K. and P. Krysinski, *New trends in the electrochemical sensing of dopamine*. Anal Bioanal Chem, 2013. **405**(11): p. 3753-71.
98. Tescarollo, F.C., et al., *Role of Adenosine in Epilepsy and Seizures*. Journal of Caffeine and Adenosine Research, 2020.
99. Xu, Y. and B.J. Venton, *Microelectrode Sensing of Adenosine/Adenosine-5'-triphosphate with Fast-Scan Cyclic Voltammetry*. Electroanalysis, 2010. **22**(11): p. 1167-1174.
100. Ross, A.E. and B.J. Venton, *Sawhorse waveform voltammetry for selective detection of adenosine, ATP, and hydrogen peroxide*. Anal Chem, 2014. **86**(15): p. 7486-93.
101. Cryan, M.T. and A.E. Ross, *Scalene Waveform for Codetection of Guanosine and Adenosine Using Fast-Scan Cyclic Voltammetry*. Anal Chem, 2019. **91**(9): p. 5987-5993.
102. Ganesana, M. and B.J. Venton, *Early changes in transient adenosine during cerebral ischemia and reperfusion injury*. PLoS One, 2018. **13**(5): e0196932.
103. Denno, M.E., et al., *Quantification of Histamine and Carcinine in Drosophila melanogaster Tissues*. ACS Chem Neurosci, 2016. **7**(3): p. 407-14.
104. Hashemi, P., et al., *In vivo electrochemical evidence for simultaneous 5-HT and histamine release in the rat substantia nigra pars reticulata following medial forebrain bundle stimulation*. J Neurochem, 2011. **118**(5): p. 749-59.

105. Samaranayake, S., et al., *In vivo histamine voltammetry in the mouse premammillary nucleus*. Analyst, 2015. **140**(11): p. 3759-65.
106. Rocha, S.M., et al., *Histamine: a new immunomodulatory player in the neuron-glia crosstalk*. Front Cell Neurosci, 2014. **8**: 120.
107. Scherkl, R., A. Hashem, and H.-H. Frey, *Histamine in brain - its role in regulation of seizure susceptibility*. Epilepsy Res., 1991. **10**: p. 111-118.
108. Lecomte, A., et al., *Biostability Assessment of Flexible Parylene C-based Implantable Sensor in Wireless Chronic Neural Recording*. Procedia Engineering, 2016. **168**: p. 189-192.
109. Lecomte, A., et al., *Deep plasma etching of Parylene C patterns for biomedical applications*. Microelectronic Engineering, 2017. **177**: p. 70-73.
110. McConnell, G.C., et al., *Implanted neural electrodes cause chronic, local inflammation that is correlated with local neurodegeneration*. J Neural Eng, 2009. **6**(5): 056003.
111. Saxena, T., et al., *The impact of chronic blood-brain barrier breach on intracortical electrode function*. Biomaterials, 2013. **34**(20): p. 4703-13.
112. Potter, K.A., et al., *Stab injury and device implantation within the brain results in inversely multiphasic neuroinflammatory and neurodegenerative responses*. J Neural Eng, 2012. **9**(4): 046020.
113. Gilletti, A. and J. Muthuswamy, *Brain micromotion around implants in the rodent somatosensory cortex*. J Neural Eng, 2006. **3**(3): p. 189-95.
114. Spencer, K.C., et al., *A three dimensional in vitro glial scar model to investigate the local strain effects from micromotion around neural implants*. Lab Chip, 2017. **17**(5): p. 795-804.
115. Michael Polanco, H.Y., and Sebastian Bawaba, *Micromotion-induced dynamic effects from a neural probe and brain tissue interface*. Journal of Micro/Nanolithography, MEMS, and MOEMS, 2014. **13**(2): 023009.
116. Hammer, D.X., et al., *Acute insertion effects of penetrating cortical microelectrodes imaged with quantitative optical coherence angiography*. Neurophotonics, 2016. **3**(2): 025002.
117. Biran, R., D.C. Martin, and P.A. Tresco, *Neuronal cell loss accompanies the brain tissue response to chronically implanted silicon microelectrode arrays*. Exp Neurol, 2005. **195**(1): p. 115-26.
118. Kozai, T.D., et al., *Reduction of neurovascular damage resulting from microelectrode insertion into the cerebral cortex using in vivo two-photon mapping*. J Neural Eng, 2010. **7**(4): 046011.
119. Nolte, N.F., et al., *BBB leakage, astrogliosis, and tissue loss correlate with silicon microelectrode array recording performance*. Biomaterials, 2015. **53**: p. 753-62.
120. Kozai, T.D., et al., *In vivo two-photon microscopy reveals immediate microglial reaction to implantation of microelectrode through extension of processes*. J Neural Eng, 2012. **9**(6): 066001.
121. Cho, S., A. Wood, and M.R. Bowlby, *Brains Slices as Models for Neurodegenerative Disease and Screening Platforms to Identify Novel Therapeutics*. Current Neuropharmacology, 2007. **5**(1): p. 19-33.



## Chapter II

### ***Microfabrication and modification of devices for combined electrophysiology and neurochemical detection.***

As said in Chapter I, the main goal of this thesis is to develop an implantable platform allowing both electrophysiology and electro-detection to be realized simultaneously in-vivo. With this aim in view, flexible implants will be modified using a PEDOT-CNF nanocomposite.

However, these flexible implants are not ideal samples for material development. Microfabrication of implants is time consuming, with long packaging time for each device while providing only 4 microelectrodes per implant. This makes them inadequate platforms for this PEDOT-CNF material development as the research effort requires a high number of electrodes, easy and quick to access (conditioned and ready).

To circumvent such experimental lock, Multi-Electrode Arrays (MEAs) will be developed as a “test system”. For this purpose, microelectrodes similar to the ones on implants are reproduced on a MEA, presenting a higher microelectrode number, quicker microfabrication and packaging.

Such MEAs are well-known tools [1], developed decades ago, with fabrication guidelines already existing [2], and already having multiple designs for a wide array of applications: electrochemical detection of pollutants, in-vitro studies, impedance spectroscopy monitoring of tissue, DEP particle manipulation, etc.

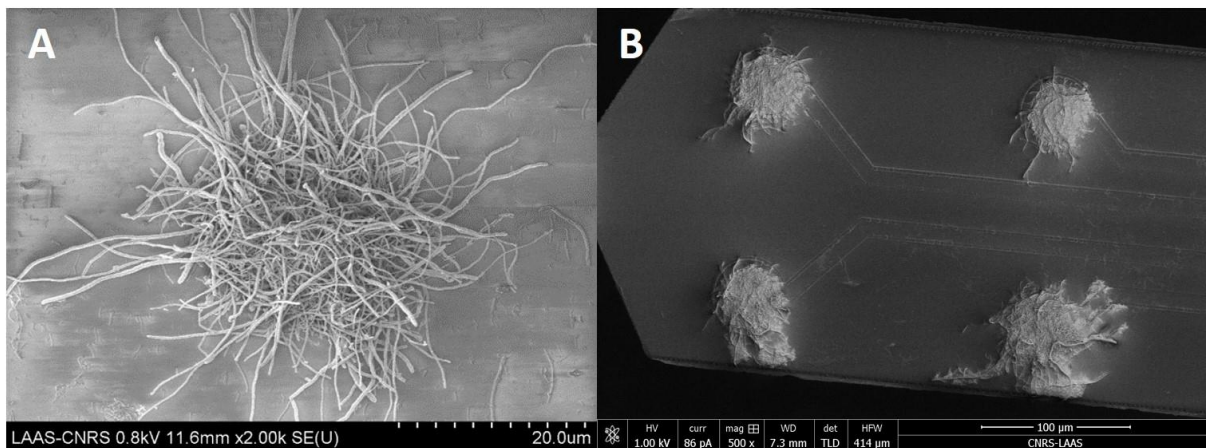


**Fig. 1: PEDOT-CNF on MEAs and implant.** A) PEDOT-CNF on 20 $\mu$ m-diameter microelectrode on a MEA, B) Implant with its four microelectrodes modified with PEDOT-CNF.

In this chapter, the microfabrication of both Multi-Electrode Arrays (MEAs) and Flexible implants will be described. The microfabrication of neural probes for electrophysiology (microfabrication process development, material choices, characterization...) has already been discussed in a previous thesis and some articles [1, 3, 4], that one should read as only additional insight is discussed on this point in this thesis. The modification post-fabrication of both devices is also presented, with emphasis of some critical technological

parameters/steps for good functioning of these devices. After development on MEAs (**Fig. 1A**), PEDOT-CNF electrodeposition is transferred on implants (**Fig. 1B**).

## **2.1 Introduction to microfabrication**

### **2.1.1 Important microfabrication parameters**

Here will be discussed the important basic parameters that need to be addressed through microfabrication. Particularly, the requirements raising from the search of multifunctionality (for both electrophysiology and electrodedetection). This imposes limitations for the couple electrode/passivation [5], their interactions in the fabricated device and with the media, to lead to operational devices with the adequate properties.

### **2.1.2 Device microfabrication for electrophysiology**

As electrophysiology aims at recording the electrical activity of a living tissue, all surfaces (electrode and passivation) must be biocompatible, to be interfaceable with the tissue without harming it. The passivation acts as an electrical barrier defining the microelectrode contour (and possibly recess) and isolating the rest of the metal tracks.

Thus, it must be structurally robust to i) prevent track exposure to the medium [6] ii) prevent signal/noise pickup from sources outside the microelectrode vicinity and iii) maintain the electrode contouring during all the device preparation and recording duration. The efficiency of such passivation can be estimated through CV, EIS and electrical noise measurements [7], even though no absolute methodology seems to exist on that specific point. The electrode must be i) biocompatible, as said before, that is to say that the electrode material does not trigger any immune reaction (with cells or tissue), ii) robust, meaning that it does not degrade due to the interfacing, and iii) conductive, to have an impedance low enough to allow electrical signals to be recorded.

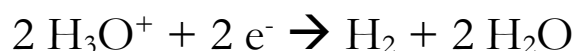
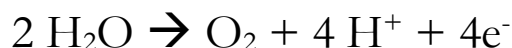
Hence, the specifically targeted application (electrophysiological experiments) and desired characteristics of the final device dictate the microfabrication process (material choices for electrode and passivation, material thickness, technological steps order, etc.). For example, a thin passivation layer will allow a closer interfacing between the targeted cell/tissue and the electrode but will be less robust on the long-term, both chemically and mechanically, and perhaps have reduced barrier properties.

### **2.1.3 Device microfabrication for electrodedetection**

Some requirements are common between electrophysiology and electrodedetection: the passivation must still define the contour of the microelectrode and isolate the metal tracks. The electrode material must still be conductive. However, the main differences between electrode requirements for electrochemistry compared to electrophysiology raises from the paradigm change: for electrophysiology, electrodes are passive elements (not meant for sensing), only recording potentials (exception made of experiments involving tissue electrical stimulation), when for electrodedetection, the electrodes are polarized, making them “active elements”, sensing the interface with a perturbation as input and a current as an output.



Hence, electrode interfacing with media and/or tissue is no longer a passive phenomenon, but an active one as the polarization perturbs the surface energy levels of the electrode and its interface with solutions/tissues, which in turn trigger chemical reactions at its surface. These reactions can be used to probe the interfaced system/tissue (cf. chapter I) for example, but can also be harmful to the tissue if for instance they produce toxic byproducts, like during water electrolysis (**cf. Equation 1**)



**Equation 1: Water electro-oxidation (top) and electro-reduction (bottom) reactions.** Under sufficient potential, the water can be oxidized to produce oxygen (and release protons and electrons) or reduced into hydrogen (by consuming electrons and protons).

### 2.1.3.1 Electrode material role in electrochemistry

The electrode material will dictate its response to the polarization in a certain media and fix the usable potential window in this considered medium for further electrochemical experiments like characterization, deposition, detection, etc. (contained within the medium electrolysis window or the electrode material degradation potential window).

For example, Platinum is a material known to have the property to reduce dissolved oxygen in aqueous media within water electrolysis window where gold cannot. This property can be used to measure oxygen with Pt electrodes for example. Another striking example would be diamond, which is known to have a very large safe electrochemical window in water as its electrolysis is highly inhibited at a diamond surface and needs very high potentials to be triggered, allowing to access more redox reactions as a larger array of potentials is accessible on diamond electrodes [8].

### 2.1.3.2 Electrode-Solution interface role in electrochemistry

The electrode interface with any solution/tissue is defined, as said before, by the combination of both its surface exposed and spatial configuration toward the solution/tissue (recess, etc.). In electrochemistry, these two parameters dictate the molecular paths of the moving electroactive molecules toward the electrode, which in turn dictate the electro-detection performance, i.e. the maximum current collected by the electrode when redox reactions are generated by the electrode polarization.

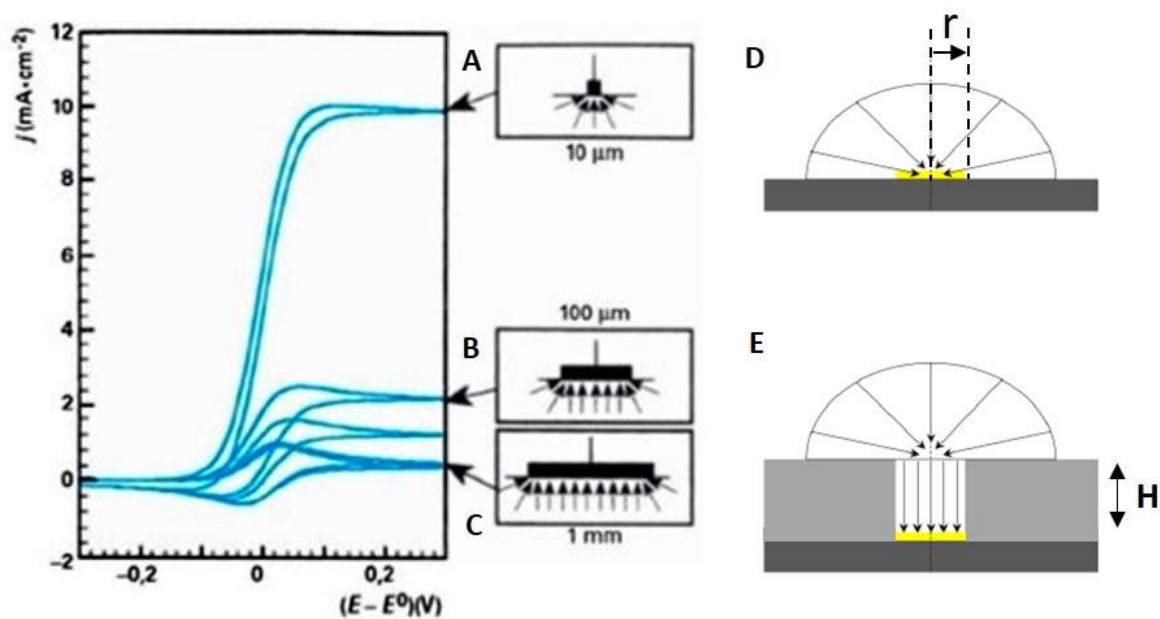


**Fig. 2: Influence of the electrode size and passivation thickness on the migration mechanisms toward the electrode.** A) Ultramicroelectrode (with 10 $\mu\text{m}$  diameter), with almost only radial migration; B) Microelectrode (with 100 $\mu\text{m}$  diameter) with mixed linear/radial migration; C) Electrode (with a 1mm diameter), with mostly linear migration happening as radial migration is only happening on the edges; D) Influence of the radius  $r$  on the migration toward an unrecessed microelectrode; E) Influence of the microelectrode recess due to the passivation thickness  $H$  on the migration. Graph from [9] and reworked for clarity.

In an un-agitated solution, the fueling of electroactive molecules at an electrode is ensured by two transportation mechanisms (not counting convection): migration and diffusion. Migration is defined in electrochemistry as motion (of an ion, a charged particle) triggered an electric field gradient when diffusion is triggered by a concentration gradient.

Considering a theoretical, perfectly flat un-recessed, polarized (thus creating a local electrical field) circular electrode, the migration of species from an interfaced solution (containing charged and neutral species) can first be thought (in an oversimplified description) to follow the shortest path toward the electrode while not interfering with the rest of the matter flux toward the electrode (Fig. 2D). This leads to the migration toward each point of the electrode perimeter being “provisioned” from the solution volume shaped as a quarter of a circle centered in that point, phenomenon called “radial migration”. On the other hand, each point from the rest of the electrode is “provisioned” only by the perpendicular path to the electrode surface reaching this point, called “linear migration”. The same logic is applied to diffusion.

Thus, radial mass transfer to an electrode point is inherently more efficient than linear one to bring electroactive/charged molecules to the electrode, but only happens on a very limited part of the electrode. This has repercussions as the electrode becomes smaller, the total current observed during electro-detection decreasing (as the total migration volume also decreases, hence the number of molecules being brought at the electrode surface and reacting) while the current density increases (Fig. 2A-C) as the part of radial migration becomes more important in the molecular flux toward the electrode, making the overall mass transfer density more

efficient. This directly impacts the growth of electrodeposited polymers for example, but also performances in electrodedetection.

Electrodes that take advantage of this phenomenon in electrodedetection are referred as Ultramicroelectrodes (U $\mu$ Es). These electrodes are defined as electrodes having at least one (critical) dimension smaller than 25 $\mu$ m, like the diameter. This leads them to have multiple advantages: i) they can enter stationary state without convection as the migration of active species toward the electrode is mainly assured by radial diffusion (making them particularly interesting for analysis in unstirred medium like brain tissue), ii) their reduced inherent capacitive current compared to bigger electrode, as their surface is smaller, making the sensing response time of the electrode smaller (scan rates in CV can be increased compared to bigger electrodes), iii) their ohmic drop is also reduced, making them more accurate electrodes to use in electroanalysis, iv) due to their small current, such U $\mu$ Es can be used in resistive media while being less impacted performance-wise by the media resistivity. It is important to note that these advantages are true only in a specific set of conditions where ultramicroelectrodes are used, for example in a certain set of scan rate during potential sweeps. For means of simplicity, for the rest of the manuscript, such electrode will be referred as “microelectrodes” ( $\mu$ Es), before and after their modification.

However, reducing one electrode surface can lead to problems of surface inhomogeneity and irreproducibility [10] and will eventually lead to currents too small to measure. It is also important to note that these migration mechanisms are disturbed by electrode rugosity, the presence of path blockers (like cells), the recess of microelectrodes induced by the passivation thickness (**Fig. 2E**).

### 2.1.3.3 Passivation nature

As for electrophysiology, accurate electrochemistry can be performed only if the passivation maintains its barrier properties over all the desired device lifetime, in the corresponding operational conditions (medium, temperature...) [11, 12]. The passivation material should then be carefully chosen according to the application targeted, particularly taking into account the effect of the polarization, which can damage the passivation and its implementation into fabrication processes carefully realized, to preserve its barrier properties [11-14]. A somewhat vast choice of possible passivation is accessible, like silicon dioxide, SU8, all parylene (N, C, D etc.), polyimide.

It is important to note that strategies to enhance barrier properties exist (plasma treatment [15], thermal annealing [15, 16]), in case bare materials do not have the adequate properties, like for paryleneC or SU8.

## 2.2 Microfabrication processes

In this section will be described the clean room process used for microfabrication of MEA and Implants. As said before, MEAs are meant as “test systems” for the implant, reproducing the implant electrode configuration (diameter, passivation thickness, electrode material), which allows for easier research effort for electrode

modification (deposition, characterization) and qualification for further applications (calibration) while preventing the need for long (three additive steps and one subtractive for MEAs vs five additive steps and three subtractive for implants) and expensive (dry etching and thick resist) microfabrication process. After electrode modification protocols have been optimized, they are transferred on newly fabricated implants for further use.

Also, MEAs are easier and quicker to package to be experiment-ready when implants need unitary packaging, including a pretty long process.

### 2.2.1 Multi-electrode array (MEA) microfabrication process

Multi-electrode arrays (called MEAs for the rest of the manuscript if not stated otherwise) were meant as “test devices” in replacement of implants for all development phases (**Fig. 3A**). They consist in 60 metal tracks sandwiched between a glass wafer and a SU8 passivation opened like for implants, on the microelectrode tip (**Fig. 3C**) of the metal track and on the contact pad.

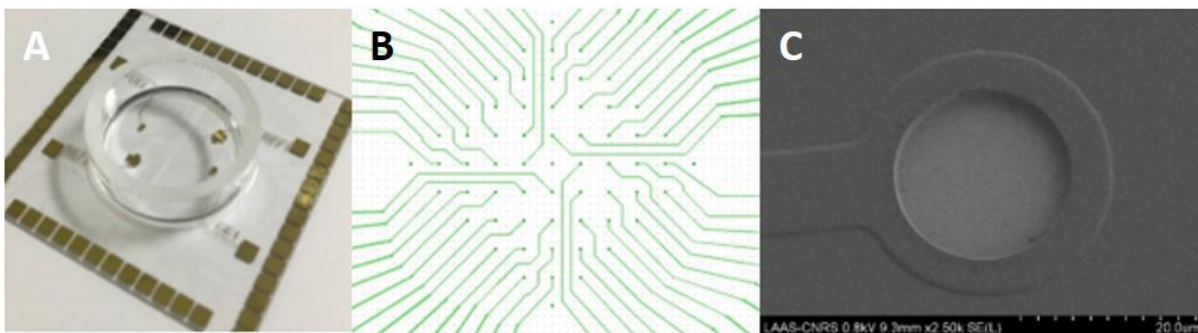


**Fig. 3: MEA fabricated in this thesis.** A) Picture of a completed MEA after dicing and PDMS well gluing; B) Microelectrode matrix in the center of the MEA; C) SEM image of a gold microelectrode passivated by Parylene C after plasma etching.

As can be seen on **Fig. 3A-B**, they present a high electrode density (56 working microelectrodes/device within first designs), are rigid devices as they are built on glass wafer, and require less microfabrication time, leading to easier prototyping. Plus, they only require well gluing as packaging before use (**Fig. 3A**), which is not time consuming (1h long) and allow for the packaging of 56 electrodes at once (vs 4 per implant), and can be used for biology tests in-vitro.

Here is described the microfabrication of these MEAs, step by step, and their packaging.

#### 2.2.1.1 Overall process

As depicted in **Fig. 4**, MEAs are fabricated by Physical Plasma Deposition (PVD) of a Ti/Au bilayer on a glass wafer masked with a photopatterned, 5 $\mu$ m-thick NLoF resist which after lift-off leaves a patterned metal constituting of the tracks/pads and microelectrodes for the MEA. Subsequently, a 1.5 $\mu$ m-thick SU8 resist is spin-coated on the wafer and photopatterned to leave a passivation layer opened on the pads and microelectrodes. Finally, the SU8 layer is hard-baked to enhance its mechanical and chemical stability and

remove solvents traces that could be detrimental to further experiments (cytotoxicity and electrochemistry pollution). All process steps are described in *Annex n°2*.

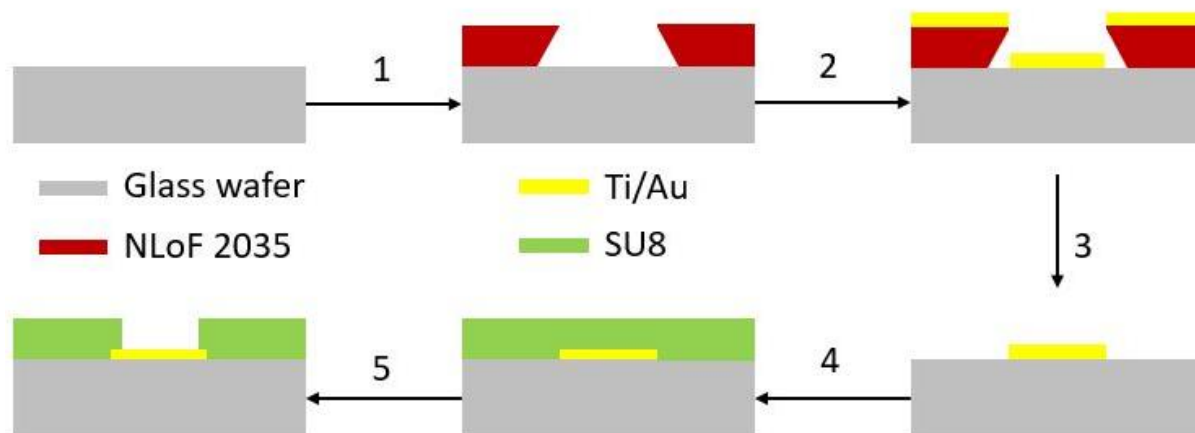


**Fig. 4: Microfabrication steps of the fabrication of MEAs.** 1=NLoF photopatterning, 2=PVD metallization with Ti/Au, 3=Lift-off for metal patterning, 4=SU8 spin coating for passivation, 5=SU8 photopatterning for passivation definition.

It is important to note that metal patterning has also been performed by metal wet etching. In that case, the glass wafer is used bare for the PVD of the Ti/Au bilayer, an ECI photoresist is then spin-coated on the metal and photopatterned to be used as mask for the following wet etching with KI/I<sub>2</sub> and HF.

### 2.2.1.2 Design choice

As described before, the MEAs produced for this thesis present 20 $\mu$ m-diameter microelectrodes, which are ultramicroelectrodes. This allows to take advantages of this microelectrode types. Also, these electrodes are made out of gold, which is a conductive biocompatible material (only under passive conditions, without current injection).

Finally, the MEA passivation layer is hard-baked SU8, with a thickness less than 2 $\mu$ m, here 1.5 $\mu$ m, which is adequate for PEDOT deposition and electrochemistry (being similar to the implants previously used for PEDOT modification).

### 2.2.1.3 Dicing and packaging

After hard-bake, a 10 $\mu$ m-thick AZ4562 resist is spin-coated of the entire wafer to protect it from glass dust generated by wafer dicing, necessary for MEA separation.

This protective layer is then stripped by a double acetone bath. MEAs are removed from the gluing support necessary for dicing and immersed 10min in a first acetone bath at ambient temperature (TA) in order to remove the bulk of the dicing resist. They are then rinsed for 10s with running acetone and immersed in a second acetone bath, upside down the electrodes pointing down (to prevent any residues to redeposit of the electrode surface like for lift-off). After 1h under orbital agitation, the MEAs are rinsed with running DIW, 30s each and then dried by a N<sub>2</sub>-stream.

To be usable with solutions, MEAs must be completed by gluing a well on their surface, isolating electrically the connecting pads from the electrodes and keeping the solutions only on the electrodes. This well can be made of either glass or PVC (glass is preferred for any cell-based experiments) and is glued to the MEA with a thin PDMS layer (used for its biocompatibility and ease of use/preparation).

#### 2.2.1.4 Design evolution

Multiple designs of MEA were produced and fabricated during this thesis, to adapt to research requirements (electrophysiology, electrode modification with multiple materials, electrophysiology combination with electro-detection, etc.) and are presented in *Annex n°3*.

### 2.2.2 Flexible implant microfabrication process

The microfabrication process for flexible has already been developed by previous PhD students (A.LECOMTE [4] & V.CASTAGNOLA [3]).

These implants consist of 4 to 6 metallic tracks (**Fig. 5A-B**) sandwiched between two flexible paryleneC (**Fig. 5B**) layers (one thick used as the implant backbone, one thin used for passivation), with openings for the contact pads and microelectrodes (**Fig. 5C**). That architecture leads them to have a high biocompatibility and flexibility, and showed high performance in-vivo after PEDOT-PSS modification for electrophysiological measurements on long-term in mouse [17] (**Fig. 5D**). This architecture will be kept for the implants presented in this thesis, but to reach their new goal, they will be redesigned to match new requirements for brain slices. In this thesis, only 4-electrodes implants were used.

#### 2.2.2.1 Overall process

As can be seen on **Fig. 6**, the process starts on a Si wafer used as substrate for the implant microfabrication. The first layer of parylene of 25 $\mu\text{m}$  is deposited, followed by a photopatterned 5 $\mu\text{m}$ -thick NLoF resist, its metallization by PVD and lift-off to obtain the desired patterned metal tracks. The second parylene of 1.5 $\mu\text{m}$  is conformally deposited on top of the metal tracks and then opened by ICP-RIE using a 5 $\mu\text{m}$ -thick AZ4562 photoresist mask. The implant contour is then obtained by DRIE using a 50 $\mu\text{m}$ -thick BPN mask, which is stripped to release the implants. A more detailed description of the fabrication process is presented in *Annex n°4*. Several problems were met during implant microfabrication. The two main ones are presented in the *Annex n°5*. One is related to the use of an adhesion promotor, polluting the parylene and interfering with the subsequent electrochemistry necessary for electrode modification and electro-detection. The other is related to the use of microwave-plasma treatment for microfabrication, reacting with metal microelectrodes and degrading the parylene.

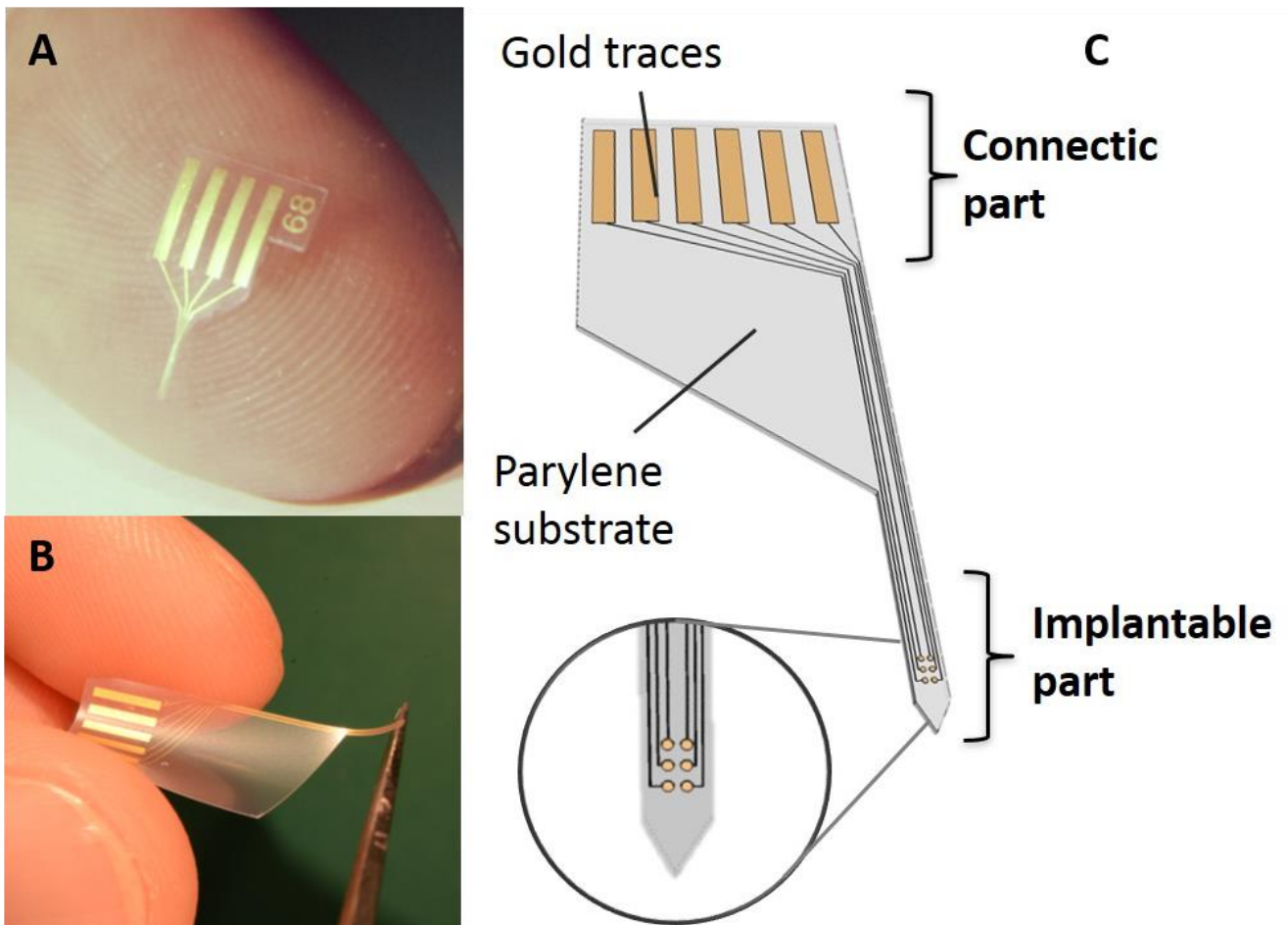


**Fig. 5: Implants already fabricated in LAAS.** A) 4-electrodes implant design for chronic recordings *in vivo* in mice hippocampi, B) 6-electrodes implant design for single acute recordings with stimulation electrode *in vivo* in mouse hippocampus, C) Global architecture of an implant [4].

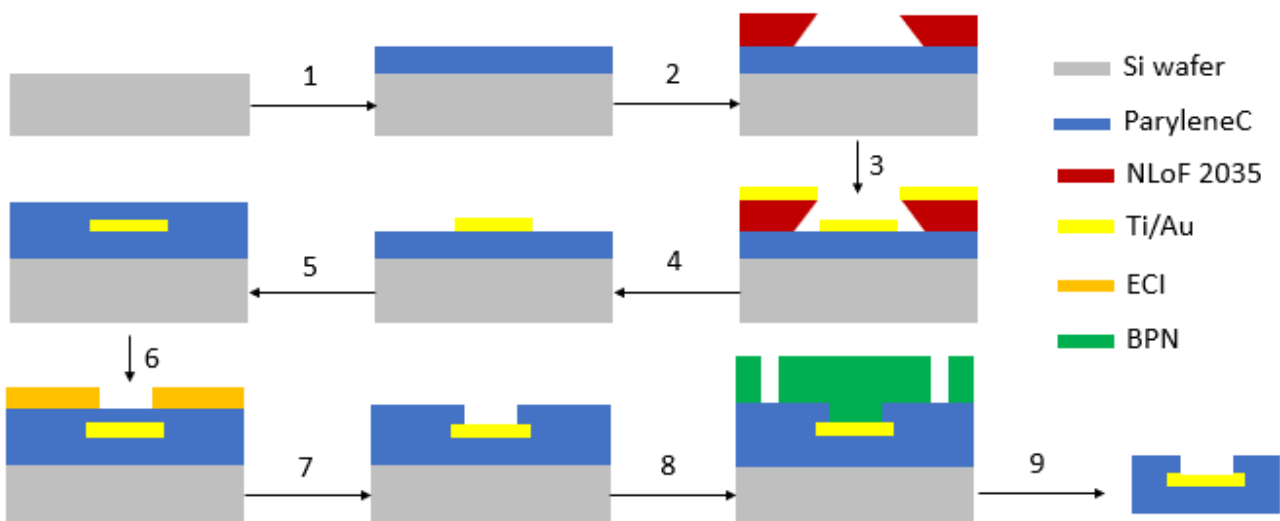


**Fig. 6: Microfabrication steps of the fabrication of flexible implants.** 1=Backbone parylene layer deposition on a Si wafer, 2=NLoF photopatterning, 3=PVD metallization with Ti/Au, 4=Lift-off for metal patterning, 5=Passivation parylene layer deposition, 6=ECl photopatterning, 7=Passivation plasma etching and ECl stripping, 8=BPN photopatterning, 9=Implant contour etching by DRIE and implant release.

Then, the final flexible implants consist in four  $40\mu\text{m}$ -diameter gold microelectrodes sandwiched between two thermally-annealed paryleneC layers, with a passivation of  $1.3\mu\text{m}$  (**Fig. 7**). Like MEAs, this passivation is biocompatible and adequate with PEDOT deposition. Electrodes are slightly bigger than those on MEAs, due to masks differences and technical issues in the clean room (maintenances, closings, etc.) during this thesis.

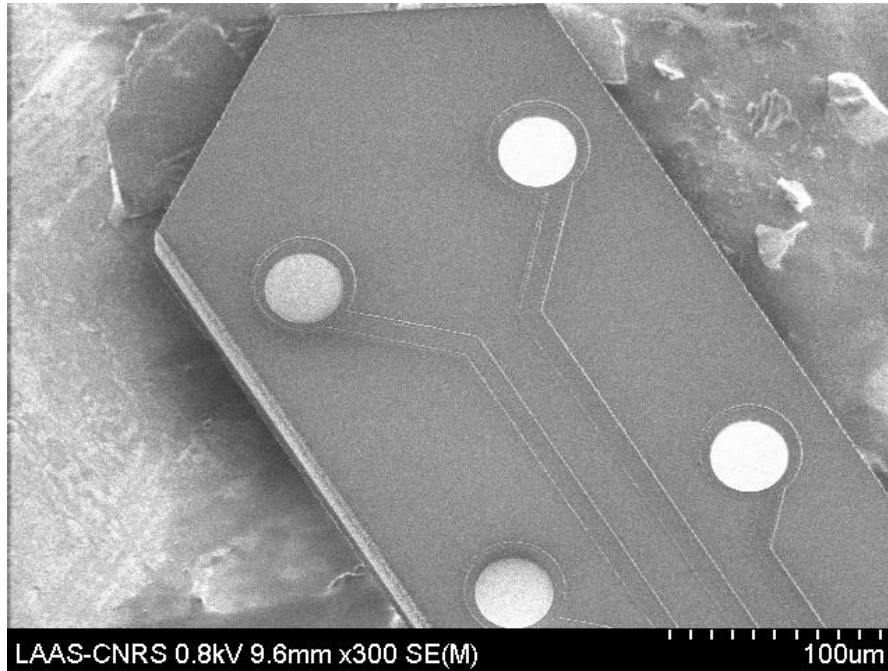


**Fig. 7:** SEM picture of the implant needle end, with the four microelectrodes clearly opened (bright area on SEM picture) and the implant contour well defined by DRIE.

#### 2.2.2.2 Packaging

The final packaging of the implants has already been previously described by A.LECOMTE. It involves the bonding of an implant to a flexible cable by soldering using an asymmetrically-conducting glue [4].

### 2.3 Post-fabrication electrode modifications

After completion of their microfabrication in clean room, the device electrodes (MEA and flexible implant) must be modified to meet requirements for further use as recording, stimulation or sensing devices, both in-vitro and in-vivo. To that purpose, the standard protocol used in the thesis is as follows: i) electrodes are first activated (meaning cleaned and primed) before deposition, ii) electrode are modified through electrochemical deposition of a new material on their surface, iii) electrodes are characterized to verify their successful modification. Steps i) and ii) of this protocol are presented in this chapter II. The characterization of these electrodes is presented in chapter III to preserve balance between chapters.



All electrochemical procedures described in this chapter were realized in a three-electrode cell, using a Pt-macroelectrode (1cm<sup>2</sup>) as a counter electrode and either a SCE (Saturated Calomel Electrode) reference electrode or an Ag/AgCl quasi-reference, in an unstirred solution.

### 2.3.1 Electrochemical activation

The aim of electrochemical activation is to clean and roughen the electrode. The cleaning is mainly aimed at removing any potential pollutants from the surface of a microelectrode (organic molecules coming from microfabrication and ions). The advantages of such cleaning protocol are: i) the possibility to clean one electrode specifically (no multiple cleaning of unused electrodes like with chemical cleaning), ii) no use of further chemical other than the medium used, iii) the modularity of the cleaning protocol (cycle number can be increased to reach stable state), iv) the accuracy of the cleaning effect evaluation (height and shape of the peaks, presence of additional peaks...). However, this kind of cleaning is not efficient to remove inorganic pollutions (like the adhesion promotor pollution described in *Annex n°5*).

The working principle of electrochemical cleaning is based on three phenomena:

- 1) polarization of the electrode surface to create surface state change (energy levels, oxidation state, electrostatic lines), which induce the desorption of ions and adsorbed molecules;
- 2) hydrolysis induction to create reactive species, oxygenated (RoS=reactive oxygenated species) and hydrogenated (RrS=reactive hydrogenated species) ones, that etch the organic residues and break them, allowing their removal by bubbling.
- 3) Selective electrochemical etching of some crystalline planes on the microelectrode surface [18].

Two protocols were used for electrochemical activation: one using CV at 4V/s derived from the literature [19-21] and the other potential pulses in H<sub>2</sub>SO<sub>4</sub> 0.5M. Their step sequencing and aim are gathered and explained in **Table 1**.

**Table 1: Activation protocols steps.**

<i>Potential pulses (CA) protocol</i>		<i>CV protocol</i>	
<i>Steps</i>	<i>Aim</i>	<i>Steps</i>	<i>Aim</i>
<i>CV at 200mV/s, between -0.4 and 1.5V, 2 cycles</i>	<i>Probe the starting state of the <math>\mu E</math> and desorb low attached molecules/ions.</i>	<i>CV at 200mV/s, between -0.4 and 1.5V, 2 cycles</i>	<i>Probe the starting state of the <math>\mu E</math> and desorb low attached molecules/ions.</i>
<i>10 cycles of two CA: 2V for 250ms and 0V for 1s</i>	<i>Produce high number of reactive species (RoS) and bubbling</i>	<i>CV at 4V/s between -0.9 and 1.8V for 100 cycles**</i>	<i>Produce short "pulses" of both RoS and RrS at the electrode and small bubbling***</i>
<i>CV at 200mV/s, between -0.4 and 1.5V, X cycles*</i>	<i>Probe the state of the <math>\mu E</math> after activation and desorb RoS from its surface</i>	<i>CV at 200mV/s, between -0.4 and 1.5V, X cycles*</i>	<i>Probe the state of the <math>\mu E</math> after activation and desorb RoS from its surface</i>

\*: number of cycles needs to be adapted to reach stable state (CV stable), \*\*: Potential and number of cycles can be decreased or increased depending of the starting state of the electrode, CV must be stable during cycling at 4V/s, \*\*\*: can be increased if the current passed during this step near the Upper Vertex Potential (UVP) and Lower Vertex Potential (LVP) is high.

Activation through series of CA, following the described protocol, is quicker but harsher for the microelectrodes, than the one by CV, which can result in the formation of a bubble on the electrode, preventing electrical connection with the medium and demanding manual intervention to remove the bubble. CVs at 4V/s are less aggressive and so need a longer activation time to result in a clean microelectrode (longer cycling time than pulsing time) and longer time to reach a stable state after cycling at 4V/s. However, it does produce reducing species without bubbling most of the time (which is not true when CA at for example -1.5V are used).

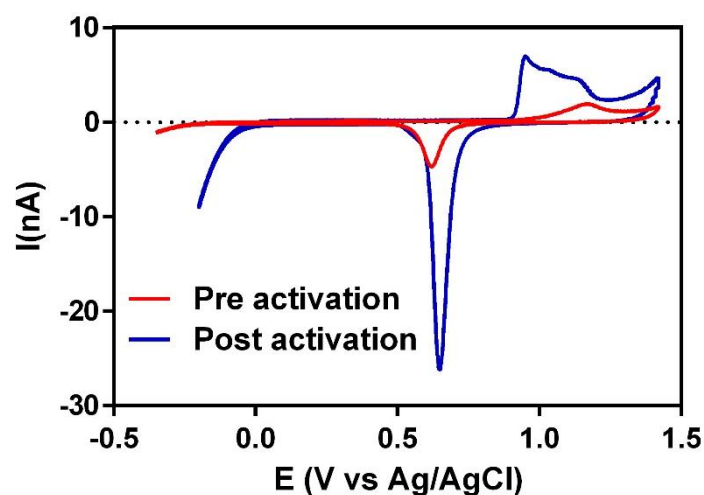


**Fig. 8:** Cyclic voltammetry in  $H_2SO_4$  (0.5M) before and after activation by CA. CV at 200mV/s, between -0.4 (red trace)/-0.25V (blue trace) and 1.5V, of a gold microelectrode (20 $\mu$ m diameter) before and after activation (10 cycles of CA at 2V for 250ms and 0V for 1s).

The cleaning of the electrode can be observed through multiple changes in the CV as shown in **Fig. 8:** i) by the shift toward the right of the reduction peak (which is also more resolved), meaning that less energy is necessary to gold oxide reduction, and by the higher reduction current observed, ii) by the apparition of multiple oxidation peaks on the forward scan, more resolved than the starting one, and their shift toward the left, meaning less energy is necessary for gold oxide generation, iii) by the increase of current at 1.5V, meaning that more hydrolysis is happening, and that the exposed surface has increased, iv) by the apparition of the hydrogen sorption current at higher potentials, with a quicker increase, meaning the electrode state is compatible with hydrogen sorption on the electrode, phenomenon known to be inhibited by organic pollution.

It is important to note that activation of the microelectrode has to be tailored to the device (electrode material, passivation nature and thickness, etc.), as it is quite a harsh treatment, with active chemical production. For example, SU8 can be degraded by electro-oxidation, when exposed to high potentials (2V with our setup) for duration higher than 250ms (issue discussed in Annex n°6).

## 2.3.2 PEDOT deposition on MEAs

As said before in Chapter I, PEDOT is a biocompatible, flexible polymer, well described in the literature as neural electrodes which showed high performances in-vivo (low impedances and high charge storage). Furthermore, PEDOT capability to incorporate several types of molecules as dopants make it a key ally for engineering of multifunctional electrodes capable of both electrophysiology and electro-detection, as desired in this thesis.

In the following paragraphs, electrodeposition of two PEDOT-based materials on microelectrodes is described. The first is PEDOT-PolyStyreneSulfonate (PSS) and the second PEDOT-CNF. Electrodeposition was chosen as deposition method for multiple reasons: its modularity and adaptability, its capability to deposit PEDOT-coatings selectively on microelectrodes in a controlled manner, etc.

### 2.3.2.1 PEDOT-PSS electrodeposition on MEAs

PEDOT electrodeposition works through electro-oxidation of its monomer in a solution (aqueous or non-aqueous) and is very well described procedure in the literature. During its oxidation, EDOT forms a cation-radical that needs to be stabilized by a counter-anion (that will then act as a dopant), in order to be able to polymerize. This allows for incorporation of almost any negatively-charged molecule in an electrodeposited PEDOT-coating, which is a major advantage for electrode engineering.

To trigger EDOT electro-oxidation and polymerization, one must manipulate current or potential at the target electrode to trigger these reactions by creation of an oxidative potential or current. It is important to note that the polymerization of two EDOT monomers produce or need a fixed number of electrons (4). Hence, the chosen manipulation will dramatically influence the properties of deposited PEDOT-coating (in terms of morphology, conductivity, electrochemical properties, dopant ratio, etc.). Theoretically, there are four modes usable for such manipulation, two manipulating the potential at the electrode: potentiostatic (electrode fixed at a potential high enough to trigger the polymerization), potentiodynamic (potential changing during deposition) and two manipulating the current: galvanostatic (current fixed at a value) and galvanodynamic (current value changing).

Here, PEDOT-PSS was deposited according to two protocols: i) Deposition by Cyclic voltammetry (CV) as a potentiodynamic deposition method, ii) Deposition by ChronoPotentiometry (CP) in galvanostatic mode (also CC in the literature for “constant current”). Both these methods are employed in an objective of exploration of the best condition to yield an electrode meeting the aim of the thesis described in chapter I.

In CV, the potential is cycled back and forth between two values at a certain scan rate for a certain number of cycles. Here, these parameters were chosen in accordance with work already published by our team with potential being cycled between 1V (called the upper vertex potential UVP) and -0.7V (called the lower vertex potential LVP), at 10mV/s for 2 cycles. This protocol allows for a smooth and slow nucleation during the scan when potential reach adequate value and allows for a control of the oxidation/reduction degree of the polymer through the UVP and LVP values. However, it does neither allow for a control of the charge if a

number of cycles is fixed nor for a control of the polymerization rate (as current is not controlled). In CP (in this thesis), the current at an electrode is instantaneously brought to its resting value at  $10\text{pA}/\mu\text{m}^2$  (resulting in a current of  $3.14\text{nA}$  on  $20\mu\text{m}$ -diameter microelectrodes). This protocol triggers a quick nucleation and allows for a control of the polymerization rate (as the oxidation current is fixed). The oxidation state of the polymer is not controlled though as potential evolves only according to the polymerization.

Vastly different morphologies were obtained according to the deposition protocol used, and these were similar to work already published by our group [3, 22], with a cauliflower-like morphology obtained by CV and a very flat morphology by CP.

This morphology difference is due to polymerization rate (PR) being widely different during CV and CP deposition. In the first, as the current is not fixed and potential scanned up to  $1\text{V}$  vs SCE (Saturated Calomel Electrode), the PR is higher (leading to the consumption of all EDOT molecules brought by diffusion in the microelectrode vicinity) and nucleation of new polymers chains is promoted, leading to more expanded deposits. While in CP, the current and then the PR are fixed, here at a particularly low value, leading to low PR (and only partial consumption of the EDOT molecules available) and potential, which results in a denser, flatter deposits, as more time is left for the polymer chains to grow and organize themselves.

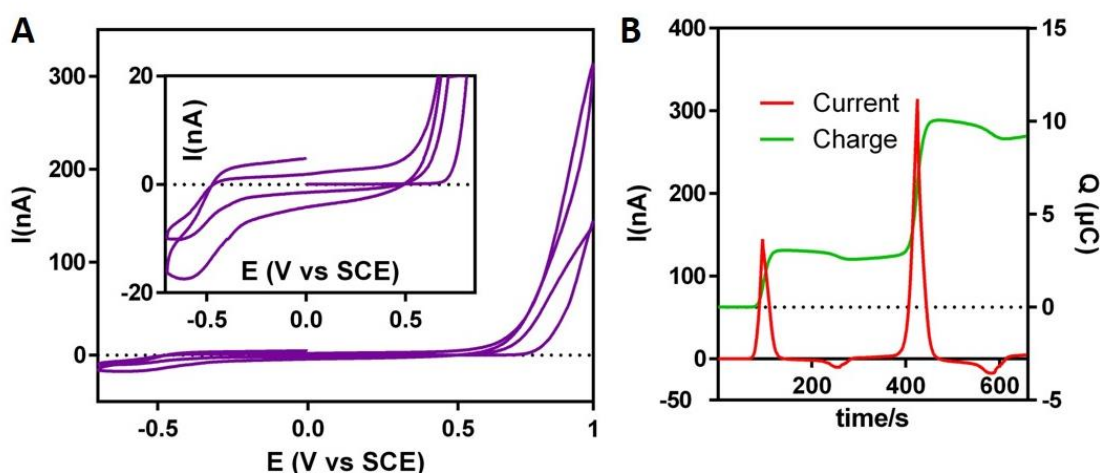


**Fig. 9: Electrodeposition data for PEDOT-PSS CV deposition.** A) Voltammograms of a 2-cycle deposition, between  $-0.7$  and  $1\text{V}$  vs SCE in a  $10\text{mM}$  EDOT and  $0.7\%$  (w/v) NaPSS, (inset) Zoom on the polymerization onsets and reduction waves between  $20\text{nA}$  and  $-20\text{nA}$ , (B) Current and charge vs time curves during CV deposition.

We can see in **Fig. 9A** that PEDOT-PSS deposition by CV consists in a first cycle with an onset in polymerization shown by a current increase around  $0.7\text{V}$  which reaches  $150\text{nA}$  at  $1\text{V}$ . On the returning part of the cycle, the current is higher than on the forward part. The reduction of the deposited polymer is found to take place at around  $-0.55\text{V}$  in the reverse-going part of the scan. The second cycle shows a polymerization onset earlier at  $0.5\text{V}$ , with a current raising up to  $300\text{nA}$ , with the reduction of the polymer still occurring around  $-0.55\text{V}$ . The final deposition charge ends up at around  $9.6\mu\text{C}$  (**Fig. 9B**), with most of this charge being created in two sharp increases around the UVP during the two scans. This deposition leads to a deposit having a cauliflower-like morphology, as can be seen in **Fig. 10**.

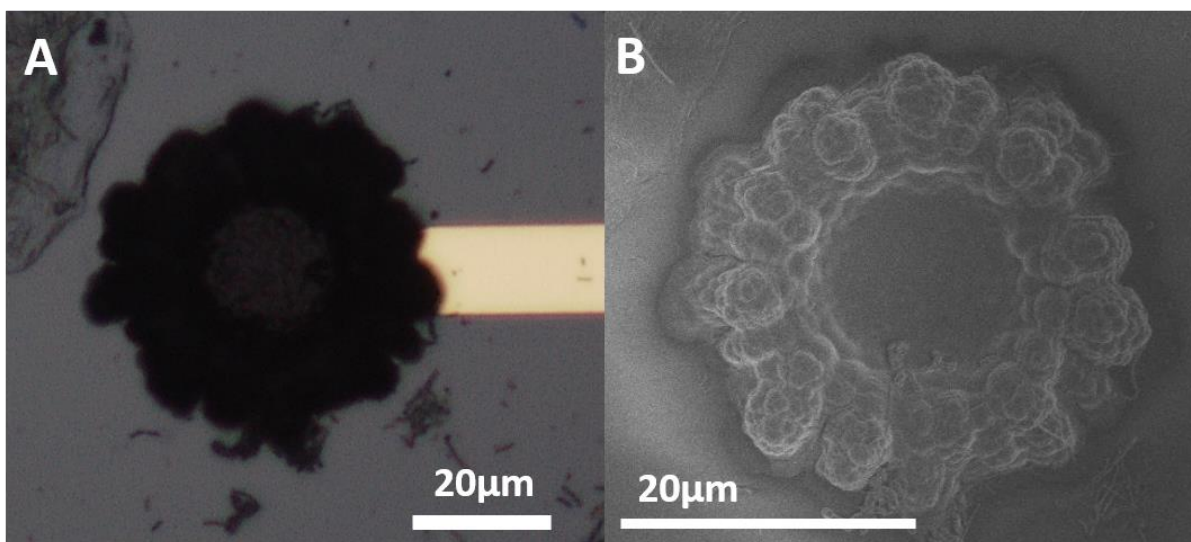


**Fig. 10: PEDOT-PSS electrodeposits.** A) Optical picture and B) SEM picture of deposits made by CV between -0.7 and 1V vs SCE, 2 cycles.

On the other hand, the deposition of PEDOT-PSS by CP consists in an initial sharp increase (usually within 0.5s) of the potential, constituting the nucleation peak, up to around 0.75V (**Fig. 11A**), followed by a decrease of the potential, synonym of polymerization, during 360s.

As the current is fixed and controlled, the charge increases linearly during all the deposition (**Fig. 11B**), to finally reach the set value of 1200nC. Comparatively to deposition in CV, the deposition profile by CP presents very different features, with a low polymerization rate and low deposition charge, leading to a more controlled and precise deposition (**Fig. 12**).

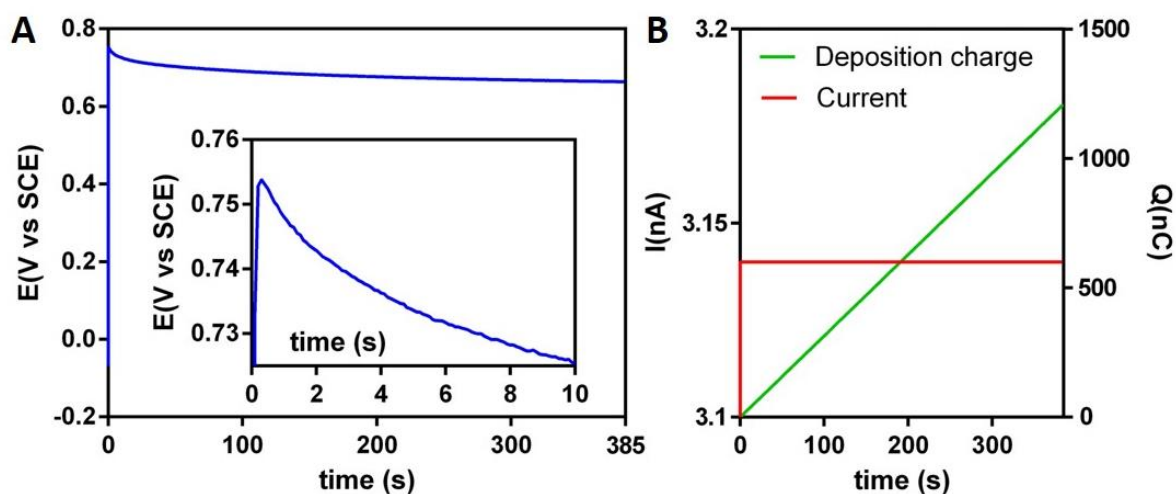


**Fig. 11: Electrodeposition data for PEDOT-PSS during CP deposition.** A) Potentiometric time measurements during a deposition at 3.14nA in a 10mM EDOT and 0.7%(w/v) NaPSS, (inset) Zoom in the region between 0 and 10s during coating nucleation, (B) Current and charge vs time curves during CP deposition.

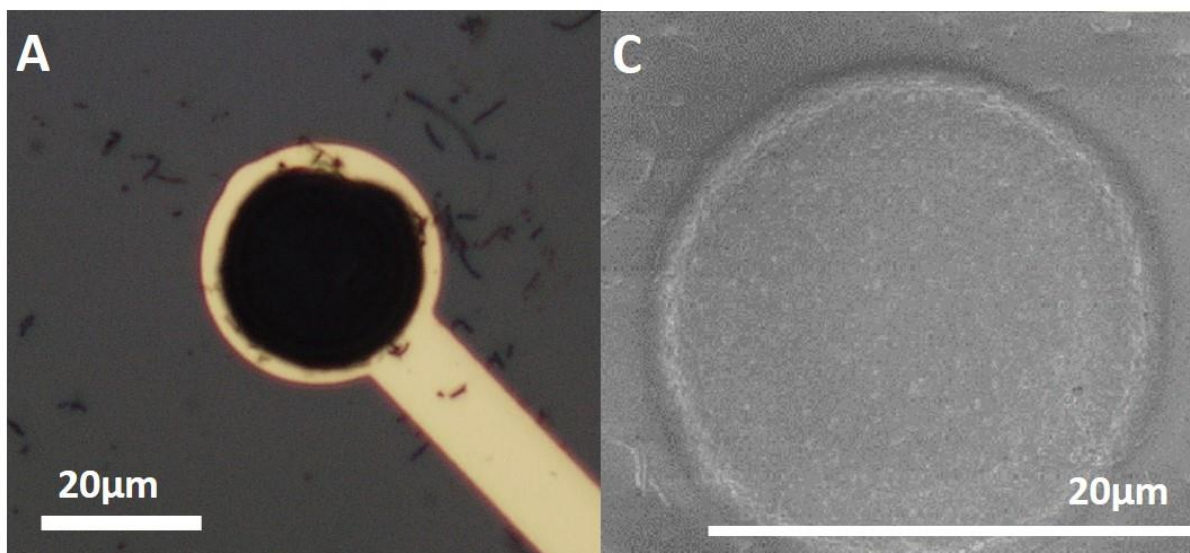


**Fig. 12: PEDOT-PSS electrodeposits.** A) Optical picture and B) SEM picture of deposits made by CP at 3.14nA with a deposition charge of 1200nC.

### 2.3.2.2 PEDOT-CNF nanocomposites on MEAs

As described in Chapter I, a PEDOT-CNF nanocomposite is proposed as a multifunctional material for implantable microelectrodes.

First tests to obtain PEDOT-CNF composite by electrodeposition were conducted on macroelectrodes (pieces of 1cm<sup>2</sup> of gold metallized wafers). Concentrations of raw CNFs were tested up to 2mg/mL in aqueous dispersions (**Fig. 13A&B**) but could not allow the incorporation of a high enough density of CNF in a PEDOT matrix. Also, the deposition solution could not be kept in an adequate state for deposition, as raw CNFs did precipitate within minutes, even after extensive (more than 2h) horn sonication.

To solve this issue, CNFs were chemically oxidized in a strong acid mix (3:1, v/v, H<sub>2</sub>SO<sub>4</sub> 96%/HNO<sub>3</sub> 18M), 2h at reflux at 70°C. The obtained material is filtered with deionized water until the water stays clear passing through the filter cake.

The oxidation process has multiple beneficial effects: i) it oxidizes and introduces negatively charge oxygenated functions on the CNF surface, increasing their dispersibility in water; ii) it shortens the CNFs, further increasing their dispersibility; iii) it oxidizes the residual amorphous carbon, turning it into either gas (CO and CO<sub>2</sub>) or into oxidized carbon fragments, which in turn can help disperse the CNFs; iv) it opens the ends and the walls of the CNF, exposing more of their surface (increased specific area), creating defects and removing metal traces (catalyst from the CNF synthesis), which make them adequate for electrochemistry.

CNFs were kept humid after filtration to be easily re-dispersed. To accurately use them in known concentrations for further experiments, the yield of this treatment was calculated through the drying (50°C at 200mbar for 24h) of a small known part of the total mass obtained, to determine the mass of oxidized CNFs and water content.

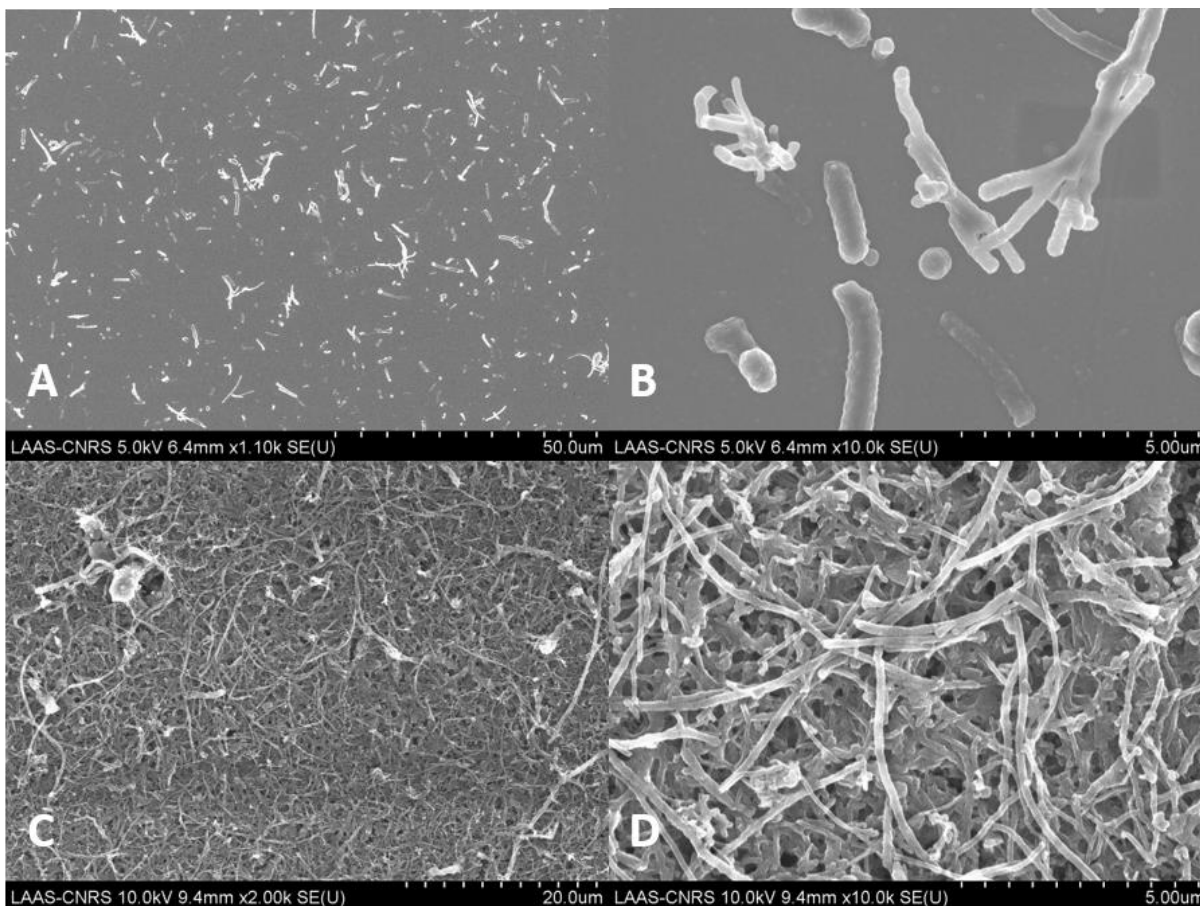


**Fig. 13: SEM pictures of PEDOT-CNF composites on macroelectrodes ( $10\text{pA}/\mu\text{m}^2$ ).** A&B) PEDOT-CNF composite obtained with 10mM EDOT and 2mg/mL raw CNFs; C&D) PEDOT-CNF composite with 10mM EDOT and 1mg/mL oxidized CNFs.

After this treatment, oxidized CNFs (called CNFs for the rest of the manuscript) could be dispersed easily in water at 2mg/mL concentration. Deposition solution could be prepared by mixing EDOT (97%) with CNFs in DIW, bath sonication and vortex. Such solutions were prepared 24h before use. Just after mix, they were vortexed for 2h and then kept at 4°C in the dark. Before use, they were sonicated (pulse, 10min) and vortexed (15min) to ensure a total dispersion of both EDOT and CNF. No sign of sedimentation/precipitation could be observed, even 4h after conditioning for deposition. These solutions were not used more than 48h after preparation. They allowed to obtain PEDOT-CNF composite on macroelectrodes by electrodeposition with good CNFs content (**Fig. 13C&D**).

The use of CNFs as PEDOT counter-ion, instead of NaPSS, leads to drastically different morphologies compared to PEDOT-PSS and PEDOT-CNF on macroelectrodes. Using the same deposition parameters used for PEDOT-PSS deposition, deposition by CP (**Fig. 14 A&C**) leads to a fibrous, porous, quasi-fractal network of CNFs entrapped on the microelectrode, quite confined, with no visible trace of a PEDOT bulk matrix or coverage, implying that CNFs are in quasi-pristine state in the deposit.

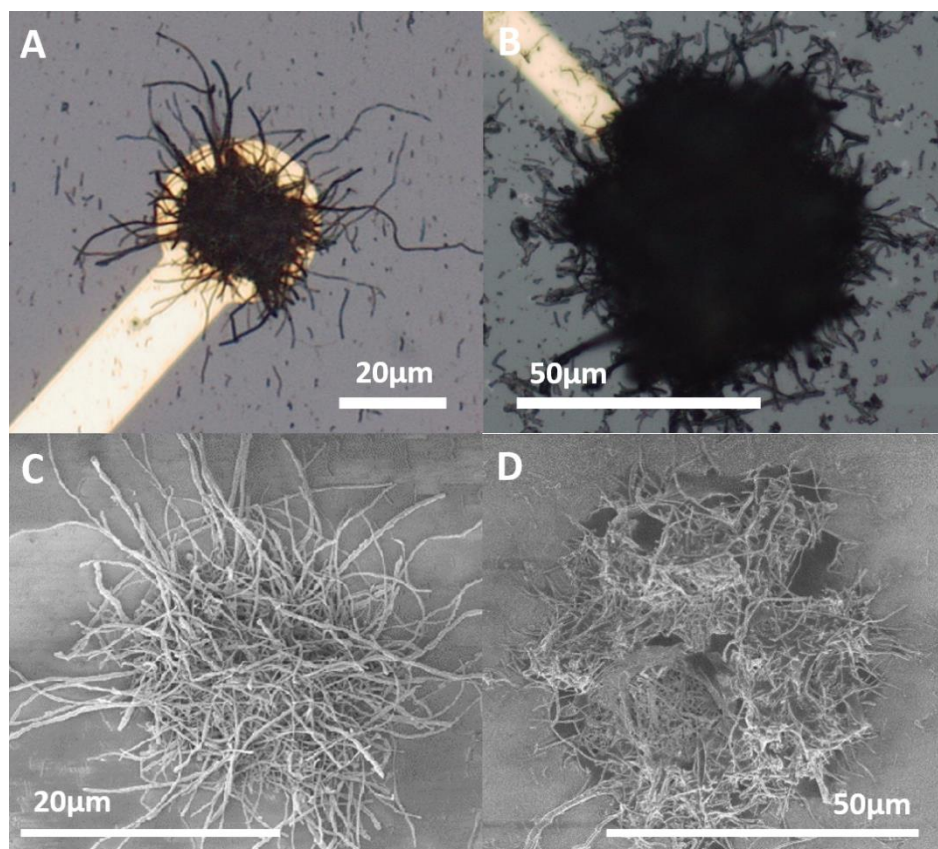


**Fig. 14: PEDOT-CNF electrodeposits.** Optical picture of deposits obtained from a 10mM EDOT, 1mg/mL CNF solution by A) CP at 3.14nA, 1200nC, B) CV between -0.7 and 1V vs SCE, 2 cycles; C and D) SEM pictures of the corresponding deposits.

CV deposition leads to PEDOT-CNF deposits with a 50 $\mu$ m-diameter (due to no control over the total charge injected during deposition), with a very high proportion of CNFs tightly encapsulated in its structure, in a webbed skein-like morphology (**Fig. 14 B&D**). Small or even no PEDOT coverage was observed on the fiber length, only polymer drapes can be observed connecting fibers, which also implies that most of the fibers are encapsulated in a quasi-pristine-like state in the deposit.

This might show that CNFs are too big to be fully integrated in PEDOT coatings on microelectrodes. Their size might prevent their surface to entirely act as a counter-anion as the polymerization might not reach all negative charges on the CNFs surface, letting them at least partly exposed after deposition.

The morphology differences (between macro- and microelectrodes) are believed to be due to the difference in EDOT and CNFs diffusion toward the electrode. The smaller surface of the electrode implies a higher CNF concentration at the electrode vicinity (due to radial diffusion being predominant at this electrode scale) during the polymerization which prevents them to fully act as templating agents (the entire surface of the CNFs being not covered), the EDOT to CNF ratio being low enough to let part of the fibers exposed.



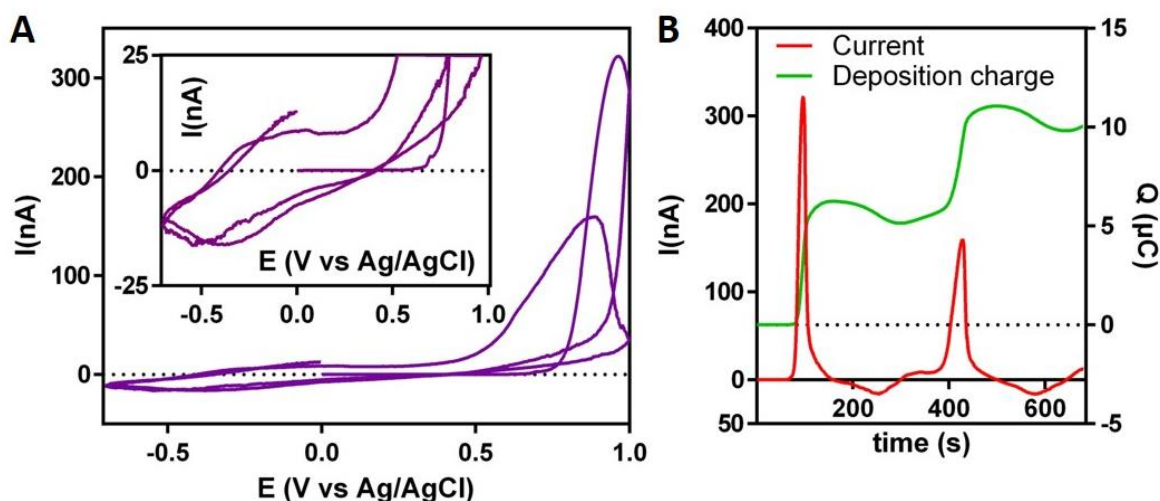


**Fig. 15: Electrodeposition data for PEDOT-PSS CV deposition.** (A) Voltammograms of a 2-cycle deposition, between -0.7 and 1V vs SCE in a 10mM EDOT and 1mg/mL CNF, (inset) Zoom on the polymerization onsets and reduction waves between 25nA and -25nA, C) Current and charge vs time curves during CV deposition.

The voltammograms obtained during CV deposition of PEDOT-CNF are quite different than the ones for PEDOT-PSS. The onset of polymerization is later, and the current reached values superior to 300nA at the first cycle, with an oxidation peak (**Fig. 15A**). On the return part of the scan, the current is smaller than on the forward scan. Reduction of the polymer happened around -0.5V, with some little instabilities (**Fig. 15B**). On the second cycle, the polymerization onset happens at 0.5V, followed by an oxidation peak at 0.8V, with a lower current of 150nA. Reduction of the polymer on the reverse part of the scan happens at a higher potential of -0.4V but with no actual increase of the reduction current. The final charge ends up at around 10µC (vs 9.6µC for PEDOT-PSS). Taken together, these cues tend to reveal that the polymerization mechanisms are quite different. Possibly, the main polymerization would take place during the first cycle, while the polymer is partly re-oxidized during the second cycle, with a slight increase of the polymer content (**Fig. 15C**).

For CP deposition, the potential sharply increases to peak at 0.725V (within 1.5s, **Fig. 16 A&B**) and then decreases to around 0.52V (**Fig 16A**), which is globally the same features than PEDOT-PSS deposition. As for PEDOT-PSS, deposition charge increases linearly (**Fig. 16C**).

Globally, for both CV and CP deposition, aside from difference features-wise, PEDOT-CNF deposition was less reproducible value-wise from deposit to deposit (larger variation) than PEDOT-PSS deposition, with more noise in the data. The final deposition parameters are gathered in the following **Table 2**.

**Table 2: PEDOT microelectrodes deposition parameters.**

<b>Material</b>	<b>PEDOT-CNF</b>		<b>PEDOT-PSS</b>	
	<b>CV</b>	<b>CP</b>	<b>CV</b>	<b>CP</b>
<b>Technique</b>				
<b>Protocol</b>	-0.7 to 1V vs SCE, 10mV/s, 2 cycles	10pA/µm <sup>2</sup>	-0.7 to 1V vs SCE, 10mV/s, 2 cycles	10pA/µm <sup>2</sup>
<b>Charge (µC)</b>	10	1,2	9,6	1,2

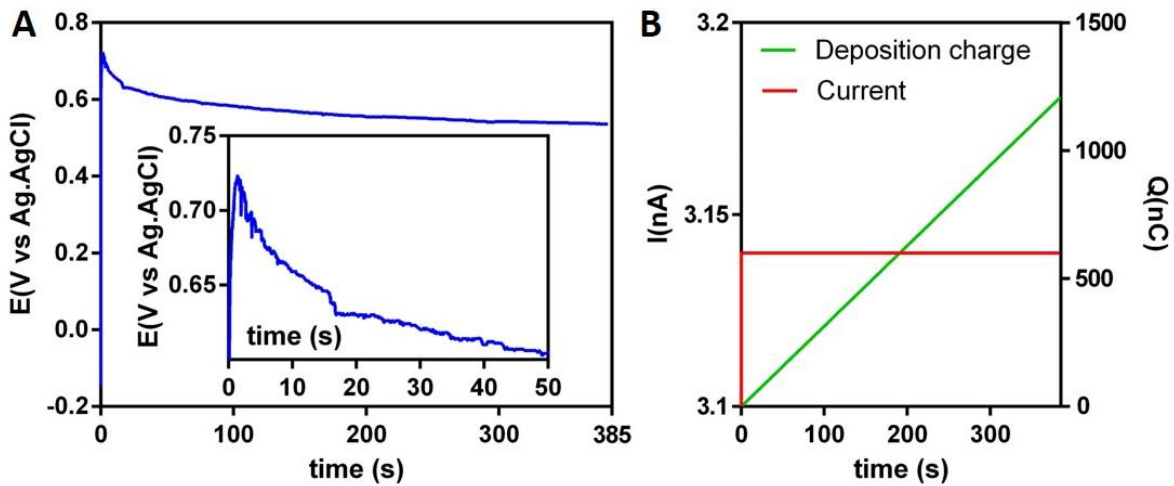


**Fig 16: Electrodeposition data for PEDOT-CNF CP deposition.** (A) Potentiometric time measurements during a deposition at 3.14 nA in a 10 mM EDOT and 1 mM CNF, (inset) Zoom in the region between 0 and 50 s, (C) Current and charge vs time curves during CP deposition.

### 2.3.3 PEDOT-CNF deposition on implants

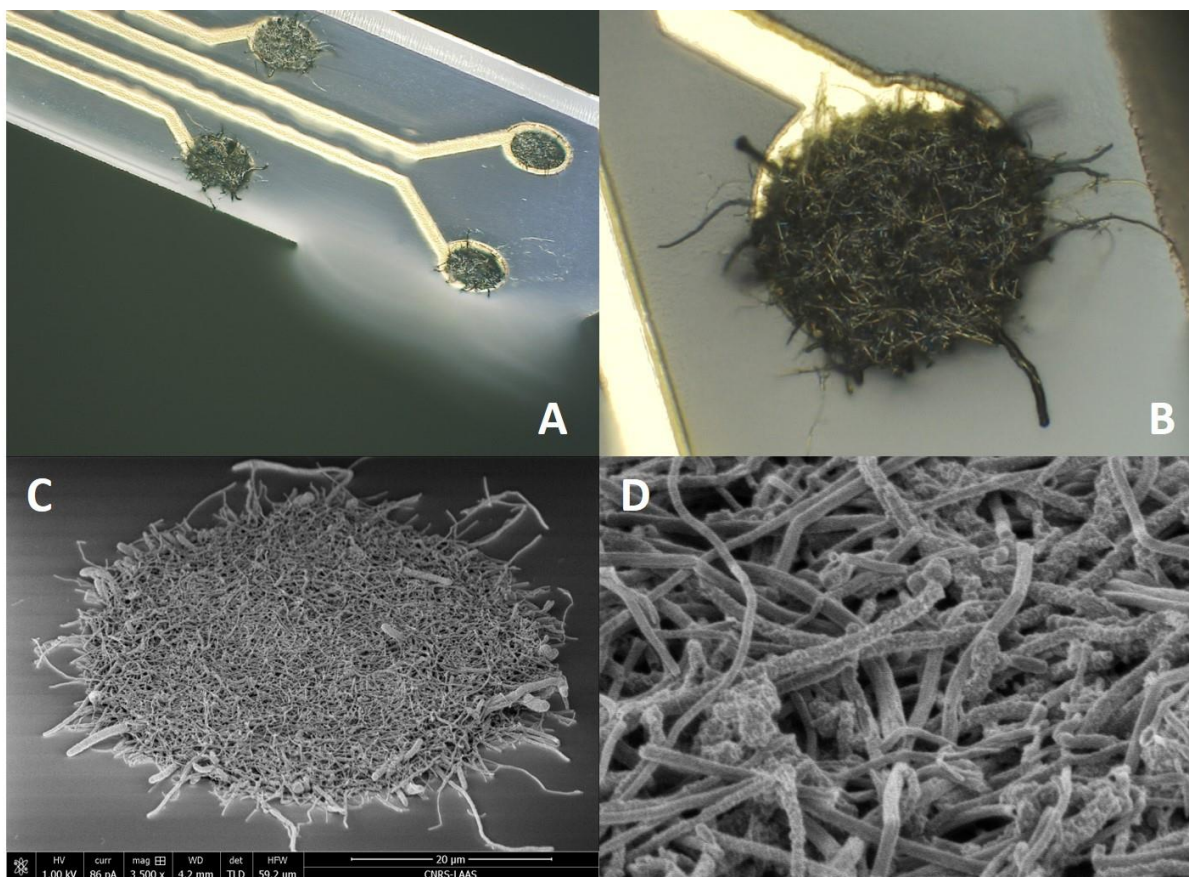


**Fig. 17: PEDOT-CNF microelectrodes on flexible implants.** A) Multi-focus picture of a flexible implant with its four electrodes modified with PEDOT-CNF at various deposition charge, B) Multi-focus picture of one PEDOT-CNF microelectrode ( $3.82 \text{ nC}/\mu\text{m}^2$ ), C) SEM image of a PEDOT-CNF microelectrode with a  $45^\circ$  tilt, D) Zoom in on the electrode surface.

After development on MEAs, PEDOT-CNF microelectrodes were transferred on flexible implants (**Fig. 17A&B**) with the same current density ( $10\text{pA}/\mu\text{m}^2$ ) and deposition charge density ( $3.82\text{nC}/\mu\text{m}^2$ ). As the electrode diameter was increased from 20 to  $40\mu\text{m}$ , the deposit morphology was similar (**Fig. 17C**), with a high number of CNFs integrated in the deposit (**Fig. 17D**). However, it can clearly be seen that some CNFs are encapsulated in PEDOT and other are not, making the surface heterogeneous.

## 2.4 Conclusion

We described new and revisited protocols for the microfabrication of two types of device: rigid MEAs built on glass and flexible implants built from paryleneC. MEAs were then used to develop a new electrode material, PEDOT-CNF, which was electrodeposited on gold microelectrodes using oxidized CNFs as PEDOT counter-anions. Two electrodeposition techniques were explored and yielded different electrode morphologies that will be characterized in Chapter III for exploitation as multifunctional electrodes. This new electrode material was then transferred on flexible implants.

1. Huang, X.J., A.M. O'Mahony, and R.G. Compton, *Microelectrode arrays for electrochemistry: approaches to fabrication*. Small, 2009. **5**(7): p. 776-88.
2. Said, N.A.M., et al., *Fabrication and characterization of microfabricated on-chip microelectrochemical cell for biosensing applications*. 2017. **1808**: 020032.
3. Castagnola, V., *Implantable microelectrodes on soft substrate with Nanostructured Active Surface for Stimulation and Recording of Brain Activities*, 2014.
4. Lecomte, A., *Conception and characterization of flexible microelectrodes for implantable neuroprosthetic development*. 2016, Université Fédérale de Toulouse Midi-Pyrénées.
5. Wellman, S.M., et al., *A Materials Roadmap to Functional Neural Interface Design*. Advanced Functional Materials, 2017: 1701269.
6. Faßbender, F., et al., *Optimization of passivation layers for corrosion protection of silicon-based microelectrode arrays*. Sensors and Actuators B, 2000. **68**: p. 128-133.
7. Kim, Y.H., et al., *Optimisation of bi-layer resist overhang structure formation and SiO<sub>2</sub> sputter-deposition process for fabrication of gold multi-electrode array*. RSC Advances, 2015. **5**(9): p. 6675-6681.
8. Torz-Piotrowska, R., et al., *Electrochemical properties of undoped CVD diamond films*. Journal of Physics and Chemistry of Solids, 2011. **72**(11): p. 1225-1229.
9. Lemercier, G., *Conception et réalisation de microdispositifs électrochimiques, pour l'analyse de l'activité bioénergétique de mitochondries isolées, dans le cadre de la mise au point de traitements innovants des leucémies aiguës myéloïdes*. 2018, LAAS-CNRS (UPR-8001) & CRCT-INSERM (UMR-1037).
10. Dutta, G., et al., *The effect of electrode size and surface heterogeneity on electrochemical properties of ultrananocrystalline diamond microelectrode*. Journal of Electroanalytical Chemistry, 2015. **756**: p. 61-68.
11. Vanhove, E., et al., *Final capping passivation layers for long-life microsensors in real fluids*. Sensors and Actuators B: Chemical, 2013. **178**: p. 350-358.
12. Beshchasna, N., et al., *Influence of Artificial Body Fluids and Medical Sterilization Procedures on Chemical Stability of Parylene C*. Electronic Components and Technology Conference, 2010: p. 1846-1852.
13. Temiz, Y., et al., *A comparative study on fabrication techniques for on-chip microelectrodes*. Lab Chip, 2012. **12**(22): p. 4920-8.
14. Mokni, M., et al., *Improvement of chemical, physical, and electrical properties of parylene-D deposited by chemical vapor deposition by controlling the parameters process*. Materials Chemistry and Physics, 2017. **186**: p. 598-611.
15. Kim, B.J. and E. Meng, *Micromachining of Parylene C for bioMEMS*. Polymers for Advanced Technologies, 2016. **27**(5): p. 564-576.
16. Hassler, C., et al., *Characterization of parylene C as an encapsulation material for implanted neural prostheses*. J Biomed Mater Res B Appl Biomater, 2010. **93**(1): p. 266-74.
17. Castagnola, V., et al., *Parylene-based flexible neural probes with PEDOT coated surface for brain stimulation and recording*. Biosens Bioelectron, 2015. **67**: p. 450-7.
18. Qiang, L., et al., *Highly sensitive and reusable Pt-black microfluidic electrodes for long-term electrochemical sensing*. Biosens Bioelectron, 2010. **26**(2): p. 682-8.
19. Ma, W., et al., *Investigating electron-transfer processes using a biomimetic hybrid bilayer membrane system*. Nat Protoc, 2013. **8**(3): p. 439-50.
20. Han, D., et al., *A regenerative electrochemical sensor based on oligonucleotide for the selective determination of mercury(II)*. Analyst, 2009. **134**(9): p. 1857-62.
21. Zhang, J., et al., *A gold nanoparticle-based chronocoulometric DNA sensor for amplified detection of DNA*. Nat Protoc, 2007. **2**(11): p. 2888-95.
22. Castagnola, V., et al., *Morphology and conductivity of PEDOT layers produced by different electrochemical routes*. Synthetic Metals, 2014. **189**: p. 7-16.

## Chapter III

# *High-performance PEDOT-CNF neural electrodes for recording and stimulation*

## 3.1 Introduction

### 3.1.1 Why the need of new, multifunctional, materials in neural interfaces?

As said in chapter I of this thesis, there is an unmet need for technological solutions for combined electrophysiology and electrochemistry studies, both at the platform level and the electrode level.

In the two next chapters, we will focus on how it is to possible to solve this problem at the electrode-level, using multifunctional materials, particularly the PEDOT-CNF nanocomposite microelectrode developed at LAAS which synthesis has been described in the Chapter II of the present manuscript.

### 3.1.2 Requirements for multifunctionality

#### 3.1.2.1 In neural recording

For electrophysiology, electrodes need to have low impedances in the adequate frequency range for neural signals recording (between 0.1Hz and 2kHz mainly, up to 50kHz) and low intrinsic noise [1-4]. To measure single units and interface with tissue at the single cell level, the spatial electrode footprint needs to be kept in the range of the standard neuron size, as electrodes with diameter superior to 20 $\mu$ m tend to record a spatio-temporally averaged value of several spikes, coming from multiple cells, without the possibility to discriminate one among the others [2].

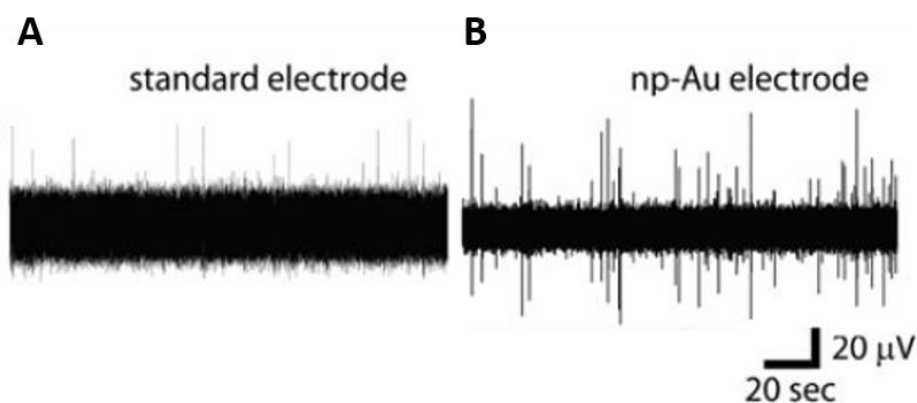


**Fig. 1: Electrophysiological measurement on a hippocampal brain slice.** (A) Measurements with a standard gold microelectrode and (B) a nanoporous gold microelectrode, showing the reduced noise and higher number of spikes recorded, reproduced from [4].

This can be done by having electrodes with high surfaces and/or high conductivities. It is also important to note that such microelectrodes, with low impedance/high surface yet having a small spatial footprint, exhibit

lower noise and can record more spikes [4]. This can be seen in **Fig. 1**, in which a standard, flat, electrode is compared with a nanoporous gold electrode.

### **3.1.2.2 In electrical stimulation**

For stimulation, to be operational on the long run for both research and therapeutic applications, electrodes need to display high charge injection limits (CIL)/ charge storage capacity (CSC) to have good performances. They also need to have long-term stability to current injection [5-7]. Both these parameters are contributed to by a high electrode surface, while on top of that, high charge storage can be obtained through a high capacitance. High charge injection capabilities can be achieved through the access to multiple, efficient charge exchange mechanisms (like ion discharge, material de-doping) at the electrode-tissue interface, preventing charge to be transmitted to the interface tissue by water electrolysis.

Hence, a theoretical material with highly inhibited water electrolysis at its surface would have access to a wider potential window during current injection, without triggering water electrolysis. Developing a high electrode surface helps charge transfer by accessing higher exchange capabilities, and so to a higher number of ions to discharge the applied current. High capacitance allows the electrode to stock charge (multiple mechanisms possible), that will be released upon current injection. In practice, most electrodes used for clinical tissue stimulation are metallic electrode presenting high surfaces due to high rugosity (roughness factors of 100s to 1000s [8]).

### **3.1.2.3 In sensing**

Finally, for molecular sensing by electrodedetection, electrodes need high sensitivities, low response times, high selectivity and low detection limits, while still having a small footprint to measure concentrations in a small volume. Electrodedetection is negatively impacted by charge storage (CS), as increasing CS increases response time (as electrons time of travel becomes higher) and increases the inherent noise (increasing the LOD). Selectivity can be enhanced using heterogeneous materials, that can differentiate multiple molecules through different surface redox mechanisms. Finally, sensitivity can be improved by surface increase, developing more reactions sites...

### **3.1.2.4 How to trade-off?**

In summary, high stimulation performance involves microelectrodes with high surfaces and charge storage capacities and thus, a higher capacitance while this induces adverse effects for electrodedetection. Electrodes with high capacitances can have increased response times in electrodedetection or higher background current, which is detrimental for real-time molecular monitoring, particularly of low concentrations. Also, good stimulation performances are commonly reached by the use of rather big electrodes (with dimensions of 100s of  $\mu\text{m}$  for example), with a footprint incompatible with single cell interfacing for both electrodedetection and electrophysiology.

On top of all these constraints for multifunctionality, the electrode material must be biocompatible and flexible to prevent any mechanical mismatch with the surrounding tissue and immune reactions (acute and chronic).

To circumvent the necessary trade-off between all these constraints, the use of nanostructures materials provides key advantages, mainly the possibility to obtain high surface electrodes with small footprints. The use of a composite, to have the better of both worlds, provide the remaining necessary properties for such applications.

### 3.1.3 Experimental plan

As said in Chapter I, we propose to use PEDOT-CNF microelectrodes as multifunctional electrodes. The point of this composite is to combine the advantages of PEDOT and CNF to create an electrode that has adequate electrochemical properties for electroredetection. Among these advantages, PEDOT is known to be biocompatible, have appropriate properties for recording, electrical stability, and CNF is known for having surface templating capabilities, high electrochemical stability, adequate size and electrochemical properties for our targeted applications. On top of that, PEDOT have a high degree of modularity (multiple dopants possible, multiple synthesis/deposition techniques, already exploited for multiple applications, (solar cells, biomedical electrodes, [2]). The synthesis of PEDOT-CNF nanocomposites microelectrodes is described in Chapter II, aside with their PEDOT-PSS counterparts, meant as comparison materials for our results.

The properties of the composite will be evaluated by electrochemical characterization through impedance, current charge, already published PEDOT composite, PEDOT-PSS.

In a first part, we will focus on evaluating the best modified microelectrodes in terms of both impedance, capacitance and size factor, as best candidates for in-vivo, neural interfacing at the single cell level. Then, performances of the selected microelectrodes used to perform electrical stimulation of tissue will be evaluated in-vitro. Finally, the non-toxicity of these microelectrodes is assessed by cell culture on modified microelectrodes and neural recordings are performed on brain slices.

Electroredetection using modified electrodes will be discussed in Chapter IV.

## 3.2 Electrode characterization for electrophysiology

Here, we will compare the performances of both composites, each deposited by the two deposition protocols, CP or CV presented in Chapter II.

CP deposition refers to chronopotentiometry deposition at a current of  $10\text{pA}/\mu\text{m}^2$  with a total charge of  $1200\text{nC}$ , while CV deposition refers to deposition by cyclic voltammetry between  $-0.7$  and  $1\text{V}$  vs SCE at  $10\text{mV/s}$  for 2 cycles. Modified electrodes are also compared to bare gold microelectrodes.

First, characterization of the depositions realized on MEAs (on 20 $\mu\text{m}$ -diameter microelectrodes, **Fig. 2**) and then transferred on implants. Characterizations were performed with the three-electrode system described in Chapter II. Then the same characterizations were transferred on the depositions on implants. These electrodes are then validated as high-performance neural electrodes in brain slices, for the recording and stimulation.

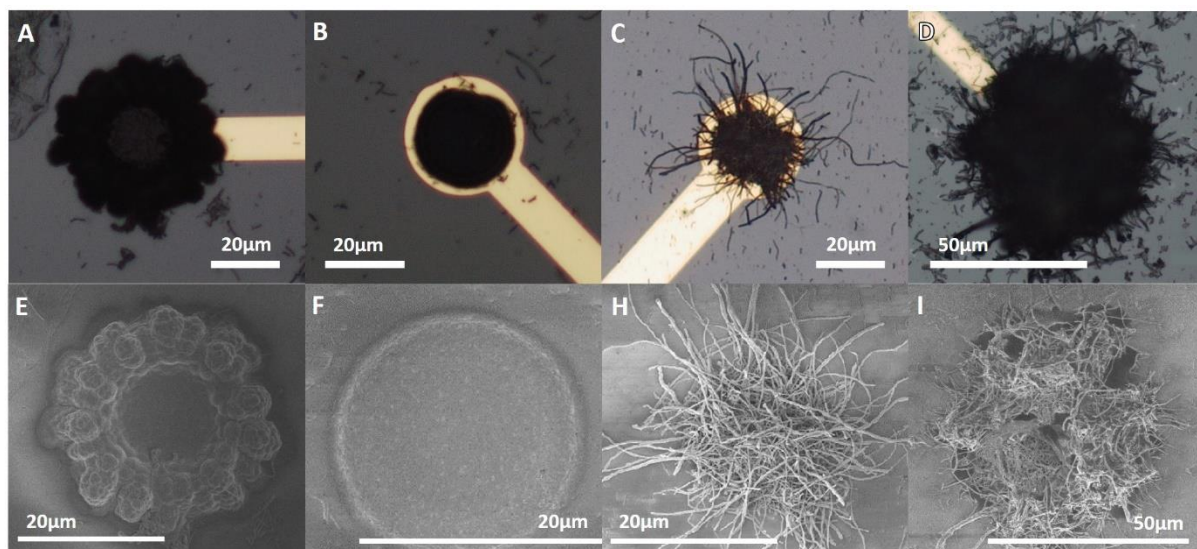


**Fig. 2: PEDOT-PSS and PEDOT-CNF electrodeposits.** (A-D) Optical pictures and (E-I) SEM pictures of PEDOT deposits. (A&E) PEDOT-PSS and (D&I) PEDOT-CNF deposits made by CV between  $-0.7$  and  $1\text{V}$  vs SCE, 2 cycles. (B&F) PEDOT-PSS and (C&H) PEDOT-CNF made by CP at  $3.14\text{nA}$ ,  $1200\text{nC}$ .

### 3.2.1 Impedance measurements

First, the electrodes performances were probed by Electrochemical Impedance Spectroscopy (EIS), to both extract their impedance and phase behavior and correlate them to their foreseen performances in neural recordings.

As presented previously, a low impedance is key for high-quality neural recordings, allowing a high signal-to-noise ratio (SNR) during these recordings and thus, allowing the discrimination of spikes.

Impedance refers to the behavior of a system to which is applied an AC-signal. For neural electrodes, interfaced with tissue in a liquid media (or just media), it is measured by a potentiostat through electrochemical impedance spectroscopy (EIS) experiments, consisting at passing a sinusoidal potential through the probed system, with sinus frequency being varied over a certain frequency range.

The measurement obtained is the sum of all resistance (charge movement limitation), capacitance (charge storage) and inductance (formally the energy storage into the induced magnetic field, generating an opposing voltage) effects in the probed circuit. It is a complex number, its magnitude being the ratio between the voltage difference and the current difference and its angle being the phase between the current and voltage. From these two characteristics, the resistance of the electrode at all frequency can be extracted, along with all other electrical properties of the electrode, in a given media, at a given potential.



### 3.2.1.1 Impedance measurements

EIS can be used to obtain Bode plots ( $|Z| = f(\text{frequency})$ ) plots, usually represented in log-log) of microelectrodes among other data. These plots allow to quantify the impedance of the microelectrodes at each frequency used during the measurements. These plots are displayed in **Fig. 3 and 4** for both PEDOT-CNF and PEDOT-PSS microelectrodes, CV and CP-deposited.

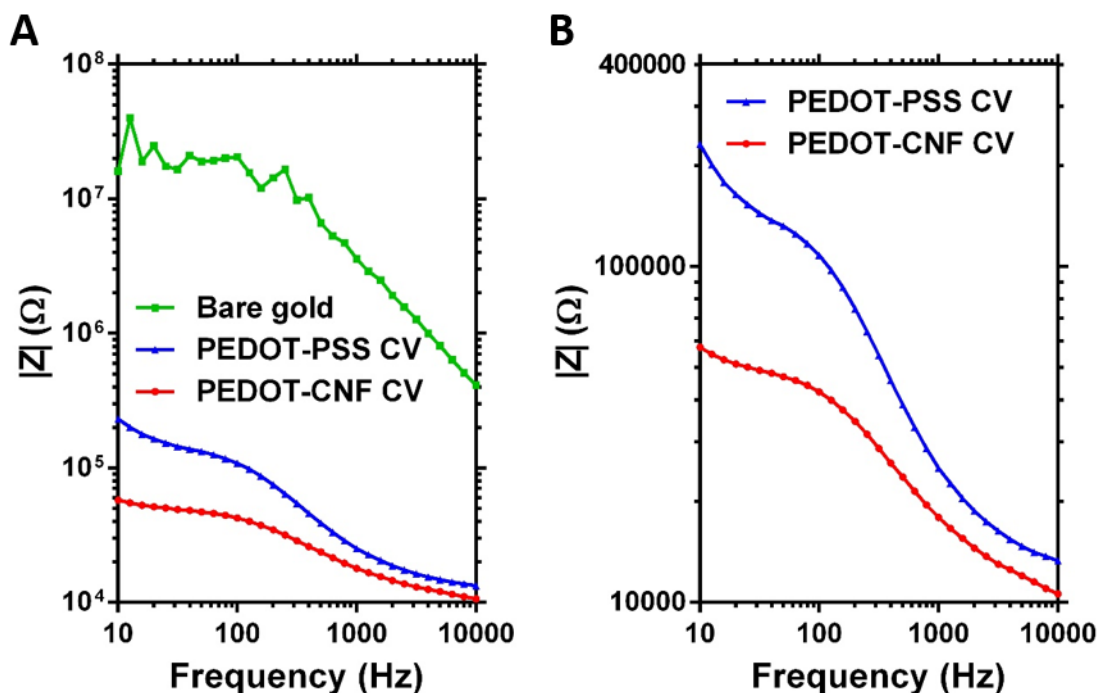


**Fig. 3:** EIS characterization of CV-modified PEDOT-CNF and PEDOT-PSS and unmodified gold microelectrodes. EIS measurements over a frequency range of 10Hz-10kHz in  $H_2SO_4$  (0.5M) at 0V vs SCE A)  $|Z|$  vs frequency and (B) Focus on the modified electrodes only.

As expected, modified electrodes always have impedances below unmodified electrodes (**Fig. 3A & 4A**). As we can see from **Fig. 3 and 4**, CP-deposition leads to lower impedance than CV-deposition for both PEDOT-PSS and PEDOT-CNF electrodes. This is due to lower polymerization rate and polymer oxidation, allowing more time to polymer chains to organize themselves in conductive domains, with longer chains and less conduction defects due to oxidation.

CV-deposited PEDOT-PSS displays impedance values higher than PEDOT-CNF over the 10Hz-10kHz frequency range (**Fig. 3B**), showing the superior doping behavior of CNFs over PSS. This is believed to be due to both the inherent conductivity of CNFs and their templating role during deposition, leading to a higher conductive surface for PEDOT-CNF electrodes. Indeed, the final electrode had an equivalent diameter of 50 $\mu$ m after PEDOT-CNF modification while only a 25- $\mu$ m diameter after PEDOT-PSS modification.

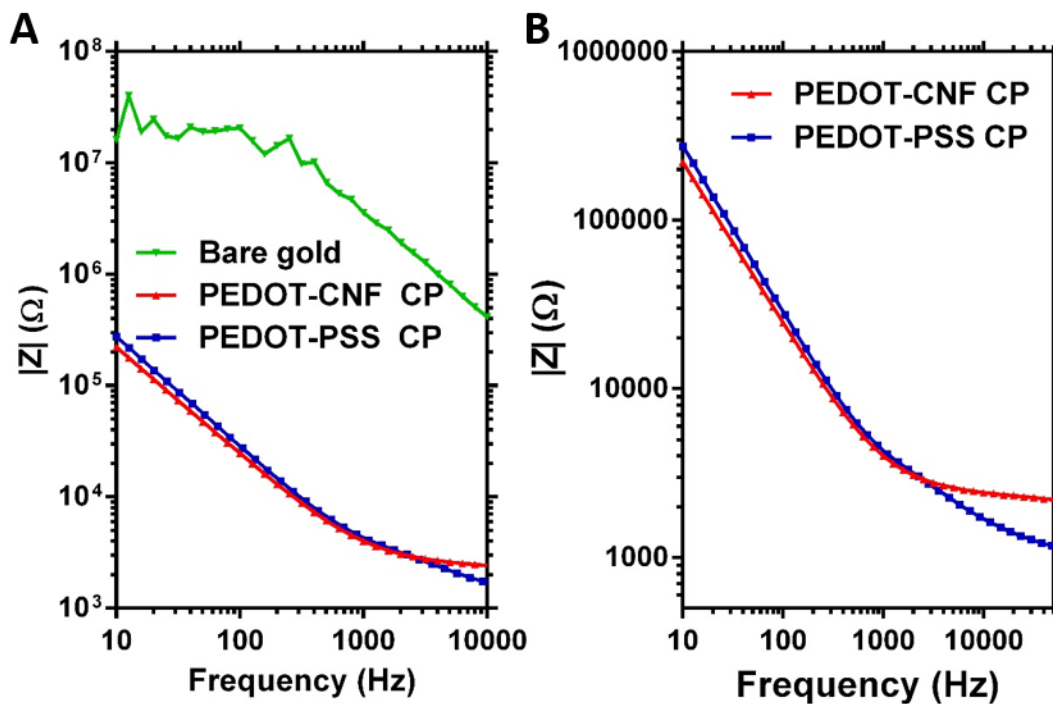


**Fig. 4: Impedance characterization of CP-modified PEDOT-CNF and PEDOT-PSS and unmodified gold microelectrodes.** A)  $|Z|$  vs frequency over a frequency range of 10Hz-10kHz in  $H_2SO_4$  (0.5M) at 0V vs SCE; (B) Focus on the modified electrodes only.  $H_2SO_4$  was used for comparison sakes. It will be change to physiological media later in the manuscript.

CP-deposited electrodes (**Fig. 4B**) display very similar behavior in the 10Hz-2kHz range with PEDOT-CNF electrodes having higher impedances than PEDOT-PSS ones in the 2kHz-10kHz range.

At 1kHz (standard values for neural interfaces comparison), PEDOT-CNF modified electrodes have lower impedance ( $4.1 \pm 2.2k\Omega$  for CP and  $18.9 \pm 1.0k\Omega$  for CV) than their PEDOT-PSS counterparts ( $4.3 \pm 0.3k\Omega$  for CP and  $25.7 \pm 1.3k\Omega$  for CV).

### 3.2.1.2 Phase measurements

Absolute values for phase angle are used for the rest of the manuscript. The phase plot of CP-deposited PEDOT-CNF and PEDOT-PSS was capacitive in the low frequency range (10 Hz), with a phase angle around  $80-90^\circ$  (**Fig. 5A**). The phase angle decreased for the PEDOT-CNF coated microelectrodes in the frequency range of 10 Hz-2 kHz to  $\approx 20^\circ$ , while the phase angle of bare gold was about  $90^\circ$  and PEDOT-PSS increased quickly from  $90^\circ$  to  $45^\circ$  between 10Hz and 2kHz and then to  $30^\circ$  at 10kHz. The shift in the phase of the impedance for modified microelectrodes suggests an increase in effective surface area from PEDOT-PSS to PEDOT-CNF. Such changes were consistent with previous findings where carbon nanotubes were incorporated in the PEDOT matrix as a single composite material [10-12]. These results show that PEDOT-CNF acts as a capacitive material for frequencies lower than 2 kHz and as a more-resistive material for frequencies higher than 2 kHz.

As can be seen in **Fig. 5B**, the phase behavior of CV-deposited PEDOT-PSS and PEDOT-PSS actually displays a radically different profile when compared to their CP-deposited counterparts. For PEDOT-CNF, phase starts to 15° at 1Hz, then increases to reach a minimum of 31° around 500Hz and slowly re-increases after to 18° at 10kHz. PEDOT-PSS deposited by CV follows the same profile, only with a starting point at -33°, a minimum of 52.5° and a final value of 17.6°.

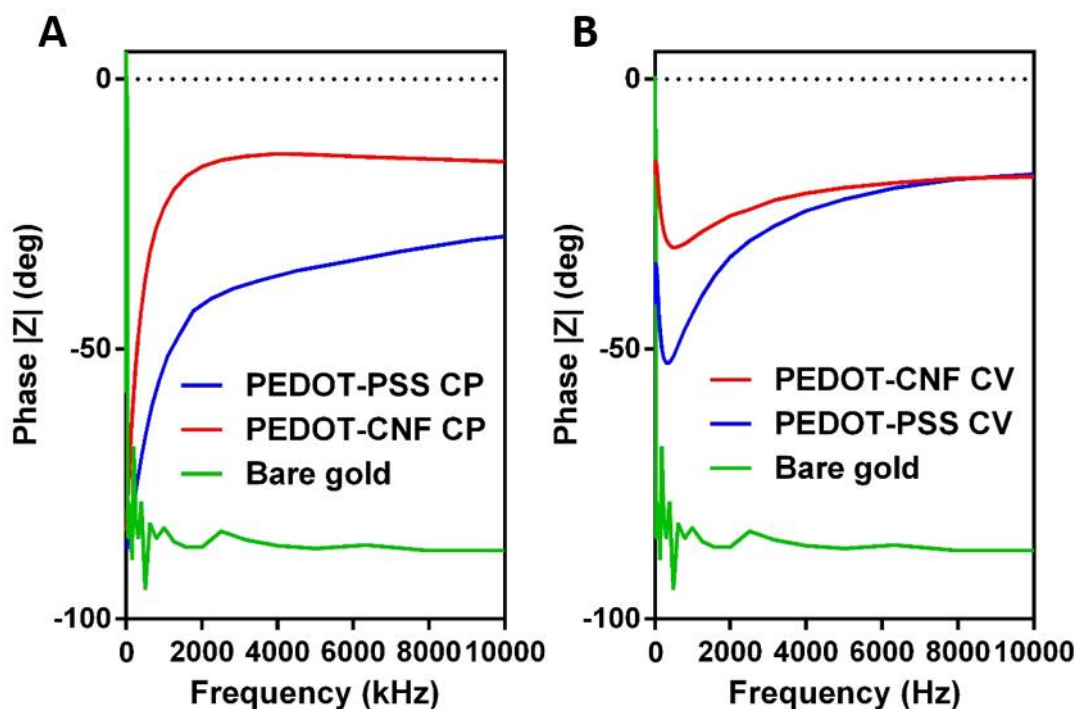


**Fig. 5: Phase during EIS measurements.** Phase over frequency measurements obtained by EIS measurements on (A) CP- and (B) CV-modified PEDOT-CNF and PEDOT-PSS microelectrodes and unmodified gold microelectrodes over a frequency range of 10Hz-10kHz in  $H_2SO_4$  (0.5M) at 0V vs SCE.

Even though impedance and phase behaviors are similar between PEDOT-PSS and PEDOT-CNF, the differences observed are due to diameter and developed surfaces differences, due to counter-anion change from PSS to CNF. The intrinsic properties differences of PSS and CNFs (mechanical rigidity, conductivity, etc.) could also have influence in these impedance and phase behaviors changes.

Taken together, these features show that the PEDOT-modified electrodes have low impedances and conduction profiles, that would induce high SNR neural recordings.

### 3.2.2 Electrodes Charge storage

Charge storage (CS) can be estimated by CV while the actual capacitance of a considered microelectrode is extracted from EIS measurements by circuit fitting. However, circuit fitting to extract the capacitance is a time consuming process (find the good circuit to fit on the data and treat all data obtained, and finally verify the model) and somewhat hard to use for comparison sake (as a lot of models have been published for such circuit fitting [1, 13, 14]).

Thus, CV measurements were preferred, as a more straight-forward and quick process, yet it is not as precise as circuit fitting. To measure the CS capacities (which is roughly equivalent to a capacitance), a cycling in a reversible (no major disymetry), purely capacitive (no faradaic peak observed) region of the electrode voltamograms have to be performed. After integration of the anodic current obtained, the CS capability (the capacity of the material to retain charge in the probed potential window) can be extracted.

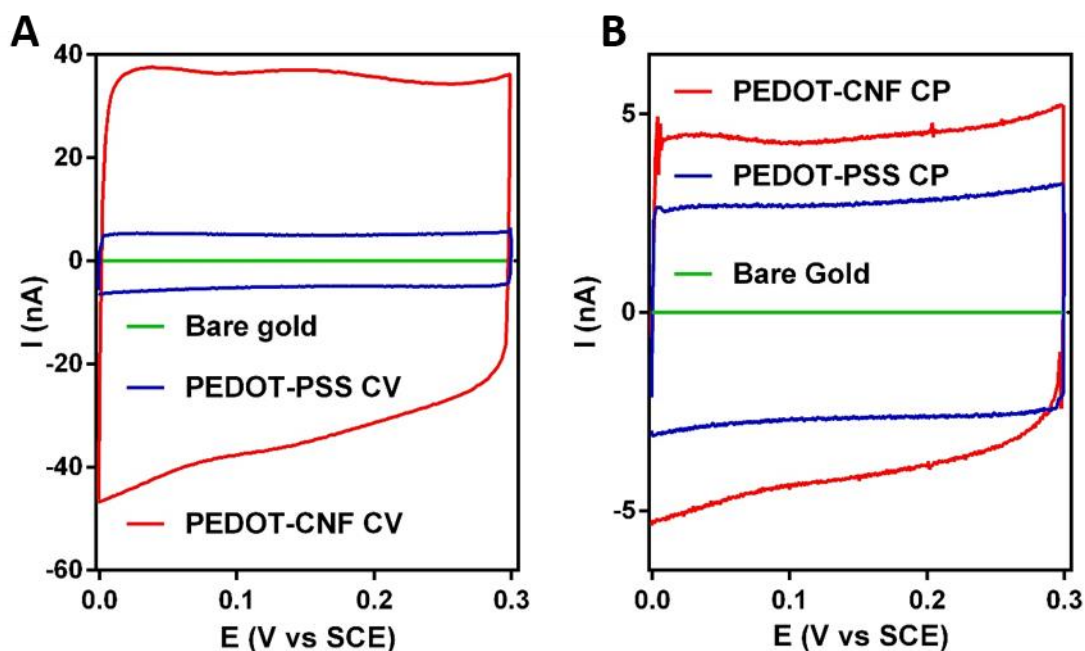


**Fig. 6: Capacitive measurements by CV.** (A) Cyclic voltammetry in  $H_2SO_4$  (0.5M) at 50mV/s between 0 and 0.3V vs SCE on CV-modified and unmodified electrode. (B) Cyclic voltammetry in  $H_2SO_4$  (0.5M) at 50mV/s between 0 and 0.3V vs SCE on CP-modified and unmodified electrode.

As for impedance, modified electrodes displayed dramatically higher CS than unmodified ones (data not displayed,  $0.1\text{mC}/\text{cm}^2$ , **Fig. 6A&B**). This increase is explained by higher surface, allowing higher proportions of ions to diffuse at the electrode-electrolyte interface, and to the transformation of the electrode material into a redox active polymer, capable of storing/releasing charges through redox reactions. For PEDOT-PSS, it is important to note that an important part of its observed CS raises from the bulk of the material, through ion/hole movement at PEDOT and PSS chains interfaces [15].

CV deposition of PEDOT-CNF resulted in a CS almost 6 times higher than the corresponding PEDOT-PSS electrodes (**Fig. 7A**). CP-deposited electrode had a less dramatic difference in CS as can be seen in **Fig. 7B**, PEDOT-CNF electrodes only displayed a 17% CS increase compared to their PEDOT-PSS counterparts ( $7.89\text{mC}/\text{cm}^2$  vs  $6.55\text{mC}/\text{cm}^2$ ).

Taken together, these observations lead to explain the dramatic CS increase of CV-deposited PEDOT-CNF electrodes mostly by the storage surface increase (as deposition charge are similar with PEDOT-PSS deposits). The symmetry of the CVs of both types of PEDOT-PSS and PEDOT-CNF indicates a high reversibility of the charge storage/release (doping/dedoping) phenomena, making these materials good candidates for ionic-to-electronic transducers.

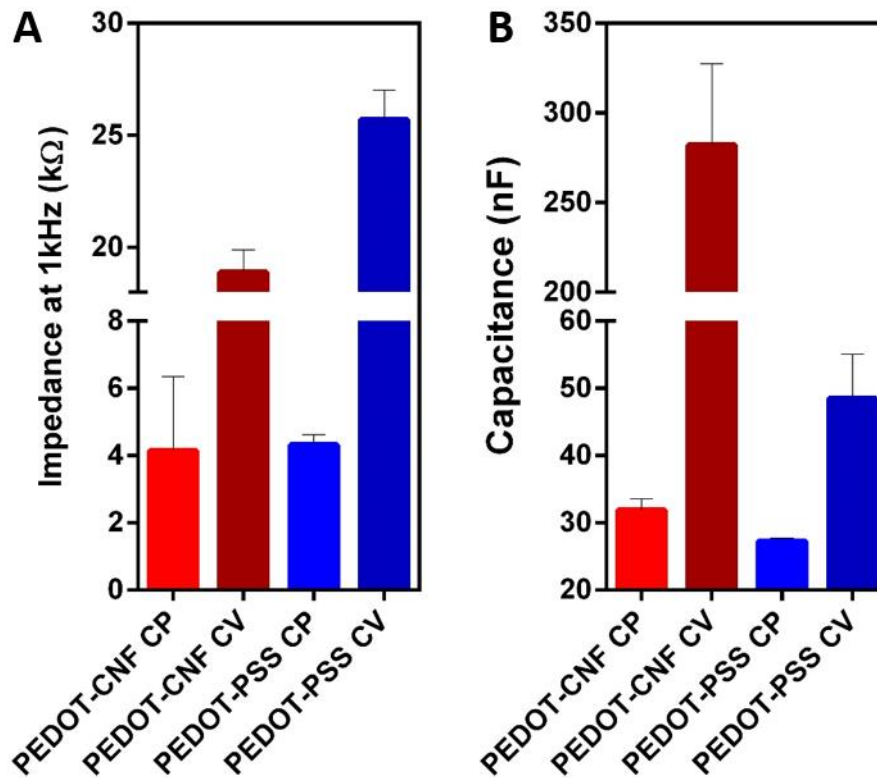


**Fig. 7: Impedance and charge storage values in function of the modification protocol.** (A) Impedance values at 1kHz; (B) CS values calculated from cyclic voltammetry data in Fig. 6.

All these electrochemical measurements show that PEDOT-CNF composites have adequate properties for neural interfacing. Even though the high CS, compared to standard electrodes used for neural recordings (W, Ti, PtIr, etc.), might wash out part of the signals of small amplitudes, this should not prevent to record valuable signals. However, for stimulation applications, CS measurements cannot be considered relevant to estimate the electrodes performances in terms of current injection. For such applications, charge injection tests using current pulses will have to be performed, as a more specific characterization.

### 3.2.3 Choice for integration on implants

Taken together, the deposition and characterization results showed that only CP-deposited electrodes have adequate properties for both electrophysiology and electrodedetection, with lower impedances and capacitances (hence, lower response time). Moreover, CV-deposited electrodes display an equivalent diameter too high (50μm) to still take advantages of microelectrodes. In the light of these points, only PEDOT-PSS and PEDOT-CNF deposited by CP were considered for further characterization and used in our experiments.

### 3.3 Charge injection for stimulation

The previously calculated charge capacity values are not totally relevant for neural stimulation, as it measures the total charge capacity of the electrodes when subjected to a slow voltage ramp in a given potential window. However, for neural stimulation, voltage ramps are not used for charge transfer to the tissue. For such applications, biphasic current (cathodal-first) pulses are used for effective, quick stimulation of neural tissue [5, 6, 16].

Hence, most of the time, only a small fraction of the total charge capacity is available at each pulse, the electrodes needing to conduct numerous millisecond pulses to inject a given charge [17]. To properly estimate microelectrode stimulation performance, we measured the voltage transient responses of our modified microelectrodes to millisecond biphasic current pulses.

#### 3.3.1 Current injection performance

For current injection by a current pulse, an adequate electrode should generate lower electrode voltage transients, to prevent bio-environment perturbation and electrochemical reactions triggering.

Starting with a series of small pulses ( $\pm 1\text{pA}/\mu\text{m}^2$ , 10Hz, for a total 10s of pulses, **Fig. 8A**), corresponding to  $0.4\text{mC}/\text{cm}^2$ , the highest cathodic voltage transient was observed for non-coated gold microelectrode, producing maximum negative voltage  $V_{\text{max,neg}}$  of  $-1.92\text{V}$  (**Fig. 8B**). Under the same stimulation conditions, the amplitude of voltage transient is much less in PEDOT-CNF coated microelectrode producing  $V_{\text{max,neg}}$  of  $-0.067\text{V}$ , when compared to PEDOT-PSS control ( $V_{\text{max,neg}}$  of  $-0.14\text{V}$ , **Fig. 8C**). These maximum values  $V_{\text{max,neg}}$  are the sum of two voltages across the electrode-electrolyte interface: the negative potential excursion  $V_{\text{mc}}$  and the access voltage ( $V_a$ ), associated with the ohmic resistance of the electrolyte. These two voltages appear successively on voltage excursions, with first the access voltage (sharp drop) followed by the polarization (more gradual decrease). For PEDOT-CNF and PEDOT-PSS, polarizations values of  $-37\text{mV}$  for PEDOT-CNF and  $-90\text{mV}$  for PEDOT-PSS [18] were estimated while the voltage drops  $V_a$  observed for PEDOT-CNF and PEDOT-PSS were of  $29\text{mV}$  and  $47\text{mV}$  respectively. It is important to note that gold microelectrodes displayed access voltage of around  $1\text{V}$  (absolute value) and polarization of  $-0.95\text{V}$ , already hitting potentials well beyond their water electrolysis potential (as displayed in CVs in chapter II, water reduction happens at potentials lower than  $-0.25\text{V}$  on gold microelectrodes).

This result would be in accordance with the electrochemical CV characterization that exhibited a higher electroactive surface area (to be characterized thoroughly) for PEDOT-CNF with respect to PEDOT-PSS and bare gold controls. Due to increased charge carriers at the interface, less polarization is seen at the PEDOT-CNF interface compared to PEDOT-PSS and gold microelectrodes.

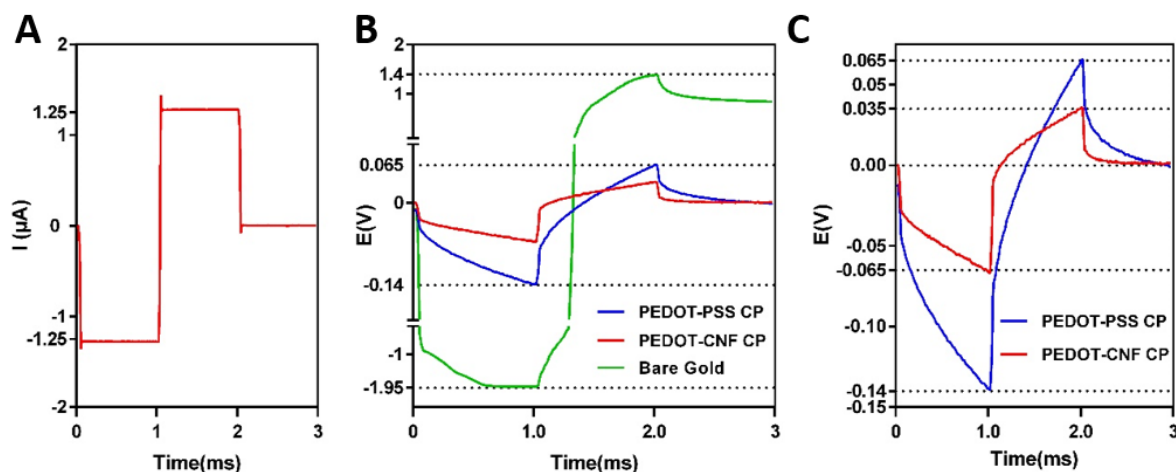


**Fig. 8: Stimulation characterization at low charge injection.** (A) Biphasic excitation current waveform ( $\pm 1 \mu\text{A}/\mu\text{m}^2$ , 1ms-long pulses) tested *in vitro* in Tris buffer 1X, cathodic pulse first. (B) Voltage responses of CP-modified PEDOT-CNF microelectrodes and bare gold microelectrode. (C) Voltage transient of PEDOT-CNF microelectrodes only.

### 3.3.2 CIL determination and stimulation performance

The charge injection limit (CIL) is defined by the charge at which the electrode polarization potential is equal to the potential at which the electrolysis of the media is triggered on the electrode material (water electrolysis can be triggered by both water oxidation into dioxygen and reduction into dihydrogen [19]).

Hence, one material can achieve high CIL by having a high surface, a highly inhibited media electrolysis at its surface (leading to high potential applicable) and an adequate combination of electrical properties (like ionic conductivity, high speed charge release, etc.).

First, the water electrolysis window (EW) of the modified microelectrodes in Tris buffer was determined using CV at 200mV/s (Fig. 9A). Even though, PEDOT-PSS and PEDOT-CNF microelectrodes displayed quite similar behavior toward electrolysis with onset of the reaction at potentials lower than -1V vs Ag/AgCl, EW low frontiers were -1.4V for PEDOT-CNF and -1.3V for PEDOT-PSS (values defined as the inflexion points of the electrolysis onset). Upper HW frontiers were found to be around +0.7V for PEDOT-PSS and +0.6V for PEDOT-CNF.

Following, modified microelectrodes were submitted to increasing current pulses until the polarization potential of the electrode hits these potentials values. As can be seen in **Fig. 9B** and as have been explained before, the polarization potential ( $V_{mc}$ ) can be calculated after removing the access potential ( $V_a$ ) from the total voltage excursion of the electrode submitted to the current pulse. Maximum current injectable before reaching the negative electrolysis frontier was found to be  $31.5 \pm 3.4 \mu\text{A}$  (**Fig. 9B&C**) and  $24.0 \pm 0.1 \mu\text{A}$  for PEDOT-CNF and PEDOT-PSS respectively corresponding to a CIL of  $10.0 \pm 1.1 \text{mC}/\text{cm}^2$  and  $7.6 \pm 0.1 \text{mC}/\text{cm}^2$ .

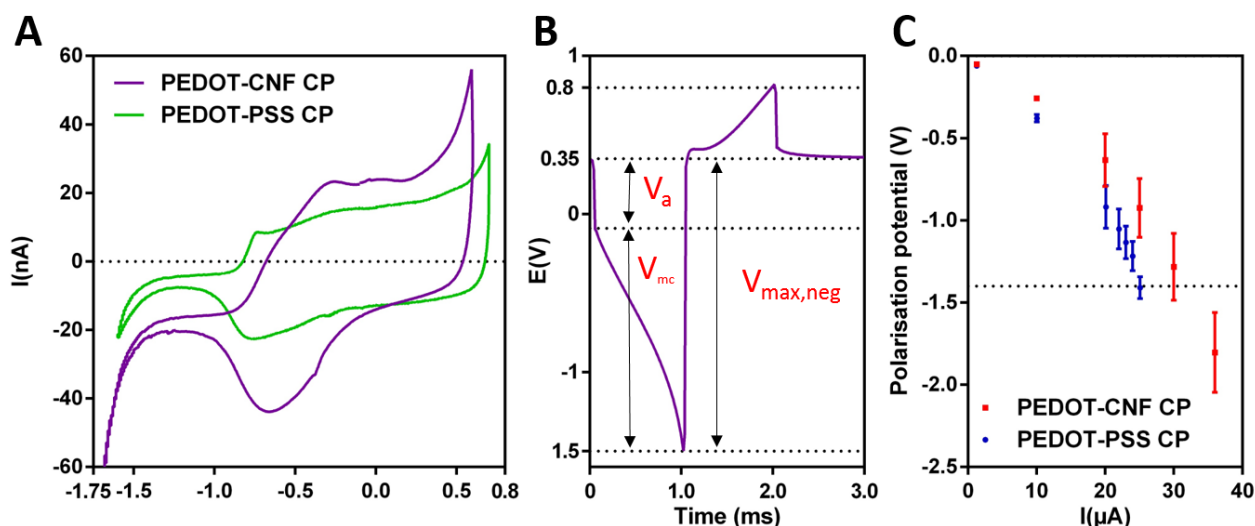


**Fig. 9: Charge injection limit (CIL) characterization.** (A) Cyclic voltammetry of CP-modified PEDOT-PSS and PEDOT-CNF microelectrodes in Tris buffer 1X, at 200mV/s. (B) Voltage transient of a PEDOT-CNF-modified microelectrode at 31.5 $\mu$ A injection, when reaching the CIL. (C) Polarization potentials measured under different current pulse amplitudes for both modified microelectrode types.

Finally, the stability of the modified electrodes used during continuous stimulation was evaluated. CIL was measured on one electrode as described before and then, the electrode was continuously submitted to current pulsing at CIL/10, at 1Hz in PBS. EIS at 0V, between 10Hz and 7MHz was performed every 1000 cycles to measure the electrode degradation through its Bode and Nyquist plots changes overtime.

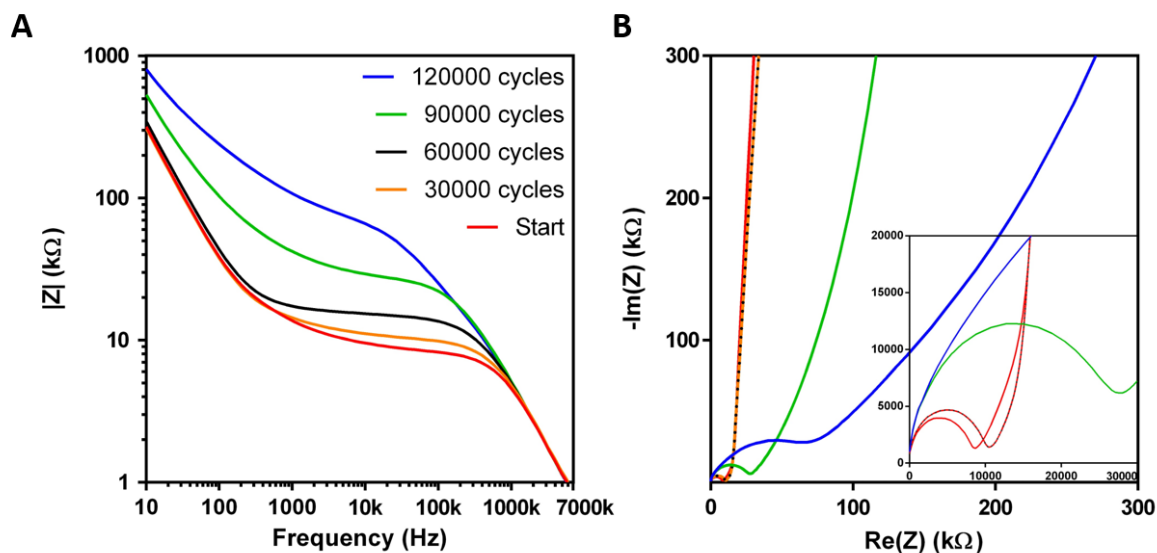


**Fig. 10: EIS monitoring of a PEDOT-CNF microelectrode during in-vitro stimulation, pulsing at CIL/10 ( $\approx 3,15\mu$ A), at 1Hz in PBS (pH=7,2).** EIS realized at 0V vs SCE, with a 10mV sinus, between 10Hz and 7MHz. A) Bode plot change and B) Nyquist plot change in function of number of cycles passed through the electrode.

As can be seen in **Fig. 10**, both Bode and Nyquist plots change drastically overtime. At start, impedance at 1kHz was around 10k $\Omega$  (**Fig. 10A**), to increase to almost 100k $\Omega$  after 120 000 cycles. Impedance value at



1kHz did show little change after 60 000 cycles, only reaching 19k $\Omega$ . These impedances changes are most likely due to the increasing collapse of the porous developed surface of the electrode, lowering the access to supporting electrolytes, and degradation of the charge conductive backbone.

More drastic changes were observed on the Nyquist plots (**Fig. 10B**). The starting Nyquist plot presented standard features with a semi-circle in the high frequency domain and a sharp sloped tail in the low frequency domain. With increasing cycles number, the semi-circle diameter increases from 10k $\Omega$  up to almost 100k $\Omega$  after 120 000 cycles. Also, the angle between the semi-circle axis and the X-axis increases overtime. This corresponds to the apparition and growth of a Constant Phase Element (CPE), meaning that the electrode surface properties are becoming more inhomogeneous with non-ideal capacitive properties (possibly due to exposition of the underneath metal microelectrode), which is consistent with composite electrode surface degradation, as both PEDOT and CNF degrade by different mechanisms and at different paces. Also, the angle between the low frequency domain (tail) and the Y-axis increases, going from a slope of 19 (close to a theoretical Warburg T element after its linear portion, suggesting that the electrode is constituted of a thin film in which ions are capable to diffuse) to a close to 1 (which would suggest a standard Warburg element which would correspond to an electrode in which the charge carrier cannot reach the entire diffusion layer in its structure). This is consistent with perturbed mass transfer diffusion mechanisms as the electrode degrades, becoming less conductive and more oxidized, with its structure collapsing and becoming less penetrable to ions.

### 3.3.3 Comparison with the literature

PEDOT-CNF and PEDOT-PSS performances in terms of geometric surface area of the microelectrodes, specific impedances and charge injection limit were compared to relevant references extracted a review [19] and then plotted in 3D manner constituting the **Fig. 11**. As it can be seen from their placement in this graph, our PEDOT-PSS and PEDOT-CNF microelectrode among the best 3 references selected (for their similar configurations), with a clear advantage to PEDOT-CNF microelectrodes over their PEDOT-PSS counterparts.

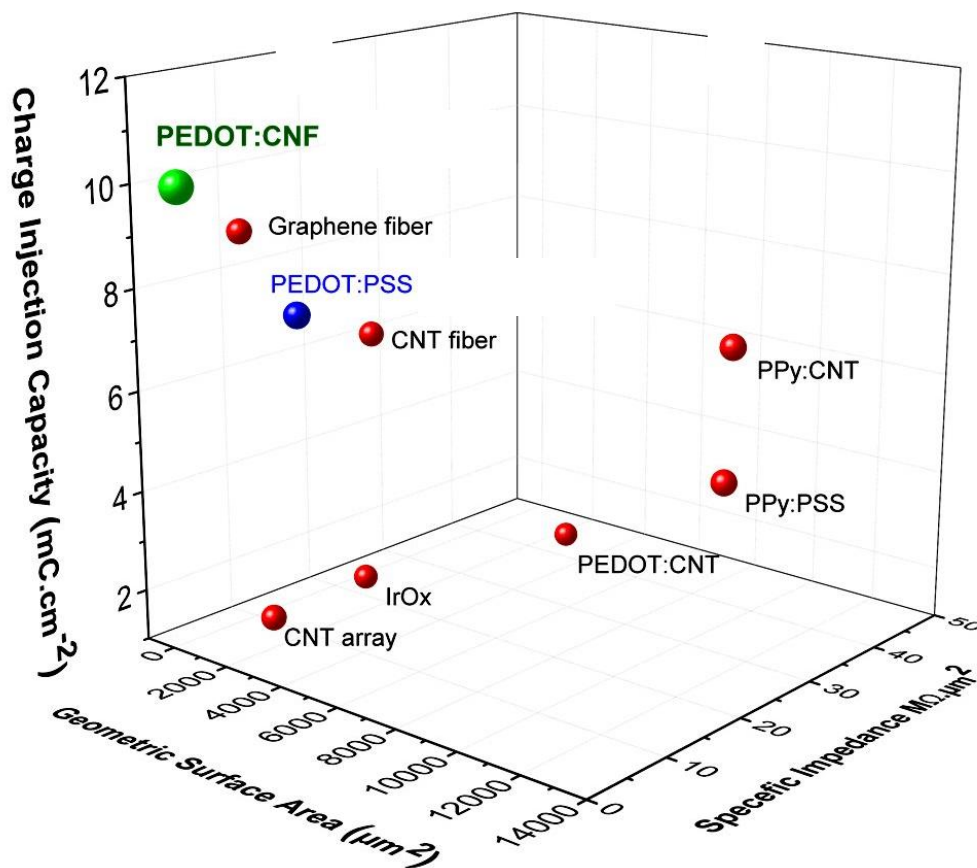


**Fig. 11: Comparison of the stimulation and impedance performances of our CP-modified microelectrodes with relevant literature references, in terms of CIL, geometric surface area and specific impedance plotted in a 3D graph.**

### 3.4 In-vitro cell culture assay

#### 3.4.1 MTT assay

As the electrical and electrochemical properties of PEDOT-CNF microelectrodes have been demonstrated, this composite needs to be further characterized in terms of biocompatibility. The PEDOT-CNF composite material should be free of toxic elements, to be used as an in-vivo neural interface. PEDOT-based materials on gold microelectrodes are commonly used for neural cell culturing and have been proven to be a biocompatible material with living systems usable to design neural interfaces [20].

Through cell viability assay, we set the preliminary objective to establish the non-cytotoxicity of the produced composite, after the electrochemical deposition. For that purpose, cytotoxicity was investigated with the MTT cell viability assay (ISO 10993-5 norm). The MTT assay is a colorimetric assay, used to measure cell metabolic activity. A tetrazolium dye MTT is added to the cell culture media, which (under precise conditions) is reduced by certain enzymes (NADH-dependent cellular oxidoreductase) into formazan, a purple molecule (insoluble in water), in a proportional manner to cell metabolic activity.

MEAs used for the MTT assay were sterilized by chemical treatment (ethanol 70%/DIW 30%). Two populations of cells were cultured for 24h and then one population was exposed for 24h to culture media containing PEDOT-CNF material extracts. After 48h, cell media is replaced by DMSO, to break the cells and solubilize formazan. Absorbance at 570nm is then measured by spectroscopy in both the control and the experiment group. The ratio between the absorbance obtained (viability percentage) determines if the material displays a cytotoxicity. The results show that the population of living SH-SY5Y cells increases over time in a similar fashion for controls and experiment, demonstrating that no cytotoxicity could be observed as viability percentage highly exceeds 75% (>99%).

### 3.4.2 Cell growth assay

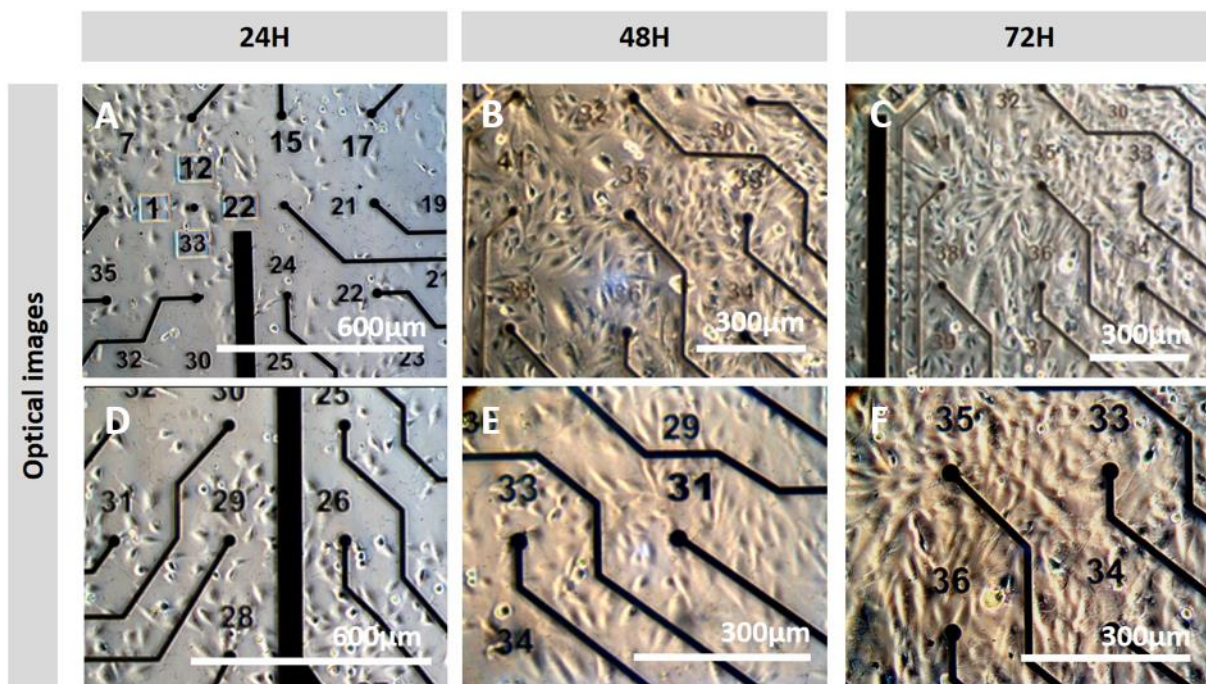


**Fig. 12: Optical pictures of cell growth on PEDOT-CNF modified MEAs.** A & D) Optical images showing SH-SY5Y cultivated on top of the PEDOT-CNF coated microelectrodes array after 24h of cell culture. B & C & E & F) Optical images showing SH-SY5Y cultivated on top of the PEDOT-CNF coated microelectrodes array after 72h of cell culture.

To complete the MTT assay, a cell growth and interfacing assay is performed. To this purpose, human neuroblastoma SH-SY5Y cells were cultivated on PEDOT-CNF-modified MEAs to investigate the cell adhesion and neurite outgrowths on the modified microelectrodes. At 24h (**Fig. 12 A&D**), 48h (**Fig. 12 B&E**) and 72h (**Fig. 12 C&F**), SH-SY5Y cells were monitored by microscopy and it can be seen that they grew uniformly and spread homogeneously, demonstrating a good viability on the MEA substrate, even at 24h. No cell repulsion was found around coated electrodes.

To further investigate the state of SH-SY5Y cells cultured in detail, as optical imaging is not sufficient, an additional study was conducted by immunofluorescent staining. At 24h (**Fig. 13 A&D**), SH-SY5Y cells were evenly distributed on the entire MEA surface, and some neurites were clearly observed on the composite

materials. At 72h (**Fig. 13 B&C, E&F**), the MEA was fully covered, with no necrotic zones observed. These results indicate that PEDOT-CNF composite is a favorable material for the adhesion and neurite outgrowth of SH-SY5Y cells.

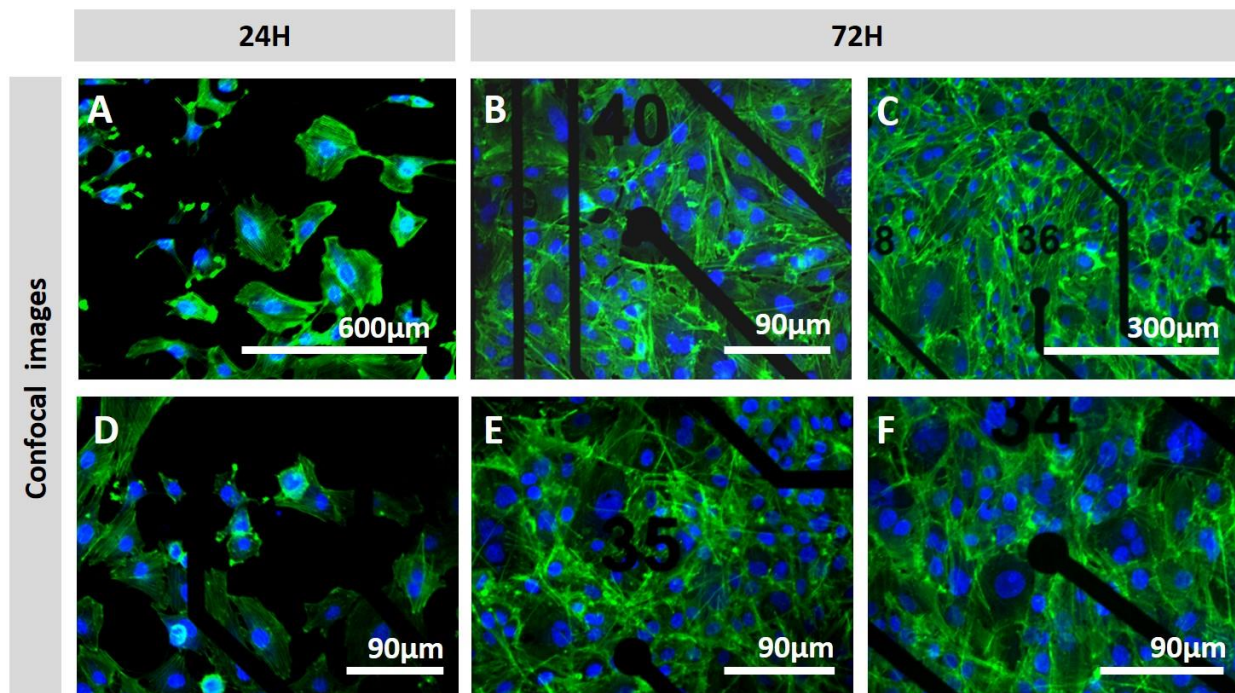


**Fig. 13: Confocal pictures of cell growth on PEDOT-CNF modified MEAs.** A & D) Optical images showing SH-SY5Y cultivated on top of the PEDOT-CNF coated microelectrodes array for 24h and 72h. The corresponding Phalloidin-AM fluorescent images showing SH-SY5Y cultivated on top of the PEDOT-CNF coated microelectrodes array for B&C) 24h and E&F) 72h.

### 3.4.3 Morphology and interfacing study

Finally, the morphology of the cells on the PEDOT-CNF microelectrodes was also assessed through SEM. SH-SY5Y cells were seeded in the MEA and cultured for 48 h. The fixation procedure was then performed before proceeding to the SEM observation.

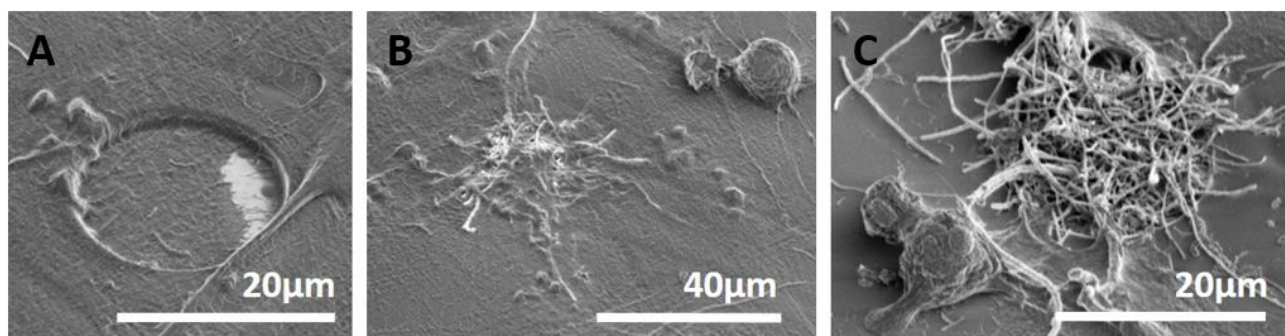


**Fig. 14: Cells morphology and interfacing with PEDOT-CNF assessment.** SEM images of SH-SY5Y cells cultured 48 hours on functionalized PEDOT-CNF microelectrodes surface. A) Bare microelectrode interfaced with the cultivated cells, B) Cell completely interfaced in 3D-manner with a PEDOT-CNF modified microelectrodes, with clear interfacing with fiber network of the electrode, C) PEDOT-CNF microelectrode being colonized by a cell.

Individual cells can be clearly recognized on top of both bare microelectrode (**Fig. 14A**) and PEDOT-CNF microelectrodes (**Fig. 14 B&C**). The SH-SY5Y cells display extensive processes and appear to be well attached on the surface of the PEDOT-CNF material. It is worth mentioning that the cells do not show any particular preference for different materials i.e. gold, MEA passivation layer or PEDOT-CNF and, as can be observed, they spread homogeneously on the surface of the MEA. The attachment of cells on PEDOT-CNF coated microelectrode shown in SEM images means that it is possible to get direct, reliable and functional contact with the target tissue required for interfacing purposes. For example, when precise electrophysiology recordings are required, a single unit can be detected and recorded when the recording device is very close from the targeted single neuron.

### 3.5 Electrophysiological recordings and stimulation on implants

In order to validate the capability of PEDOT-CNF microelectrodes to be used for neural interfacing, they were transferred from MEAs to flexible implants. After characterization, these electrodes were used for recording and stimulation of neural activity in mouse hippocampal brain slices, prepared and recorded at the Brain and Cognition Research Center (CerCo) in Toulouse, in Lionel NOWAK's lab, who we thank very much for his help and time working with us.

#### 3.5.1 Implant preparation

To perform electrophysiology on brain slices with our modified microelectrodes, implants were fabricated using protocols developed by A.Lecomte in a previous PhD thesis. The four microelectrodes present on these implants were modified following the chronoamperometry deposition protocol described in Chapter II of this thesis. To adapt this deposition protocol to implant electrode that are bigger (40 $\mu$ m vs 20 $\mu$ m diameter on MEAs), the current density and the deposition charge density were kept the same, respectively at 10pA/ $\mu$ m<sup>2</sup> and 3.822nC/ $\mu$ m<sup>2</sup>.

The modified electrodes went through the same set of characterizations we described on MEAs (EIS, CV, SEM, optical imaging, CIL determination) in Artificial CerebroSpinal Fluid (aCSF), the media used for brain slices preparation and experiments. These electrodes did present the same morphology (cf. **Fig. 15**) than the one on MEAs, with a clearly fibrous 3D structure confined on the microelectrodes. Their characteristics were also similar, with low impedance at 1kHz (even in aCSF, which is less conductive than other buffer and solutions that can be used for microelectrode characterization), high charge storage capacity and high stimulation capability (cf. **Table 1**).

<i>Parameters</i>	<i>Impedance at 1kHz</i>	<i>Charge storage</i>	<i>Charge injection limit</i>
<i>Protocol</i>	<i>EIS in aCSF between 10Hz and 7MHz (N=4).</i>	<i>CV in aCSF, between -0.8 and 0.5V (N=4).</i>	<i>Current pulse injection in aCSF (N=4).</i>
<i>Value</i>	<i>9970<math>\pm</math>268<math>\Omega</math></i>	<i>99.6<math>\pm</math>6.1mC/cm<sup>2</sup></i>	<i>7.6<math>\pm</math>1.3mC/cm<sup>2</sup></i>

**Table 1: Summary of the PEDOT-CNF characterization on flexible implants in aCSF.**

As can be seen in **Fig. 14**, PEDOT-CNF deposition leads to modified electrode without bridges (CNF that could overhang toward other electrodes and create short circuits) and clean implant with no residues on the implant that could be released later in experiments with brain slices.

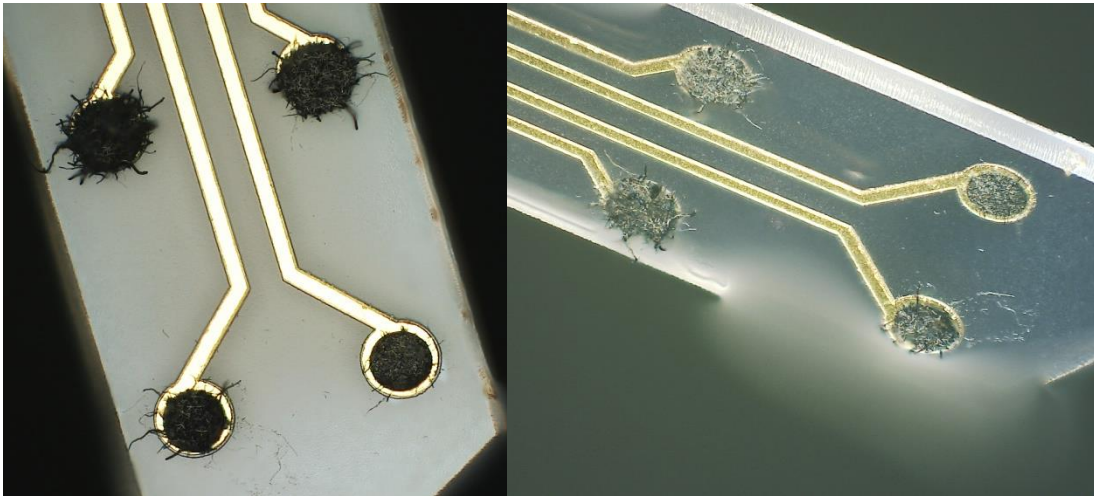


**Fig. 15:** 3D multi-focus optical images of implants with a tilt angle of A) 0° and B) 52°, after PEDOT-CNF deposition with varying deposition charge (1200nC, 2400nC and 7200nC). Images obtained by 3D tilling using the RX-100 microscope, under a A) semi-annular light and B) annular light. Aberration on B) is due to software reconstruction of the multi-focus image.

### 3.5.2 Setup and brain slice preparation

The targeted zone for recording with PEDOT-CNF modified implants was the hippocampus (**Fig 16**). To allow recording from the four microelectrodes on the implant, brain slices were cut to 400µm-thick by Pr. Lionel NOWAK, leading to 2-3 slices presenting hippocampus cells.

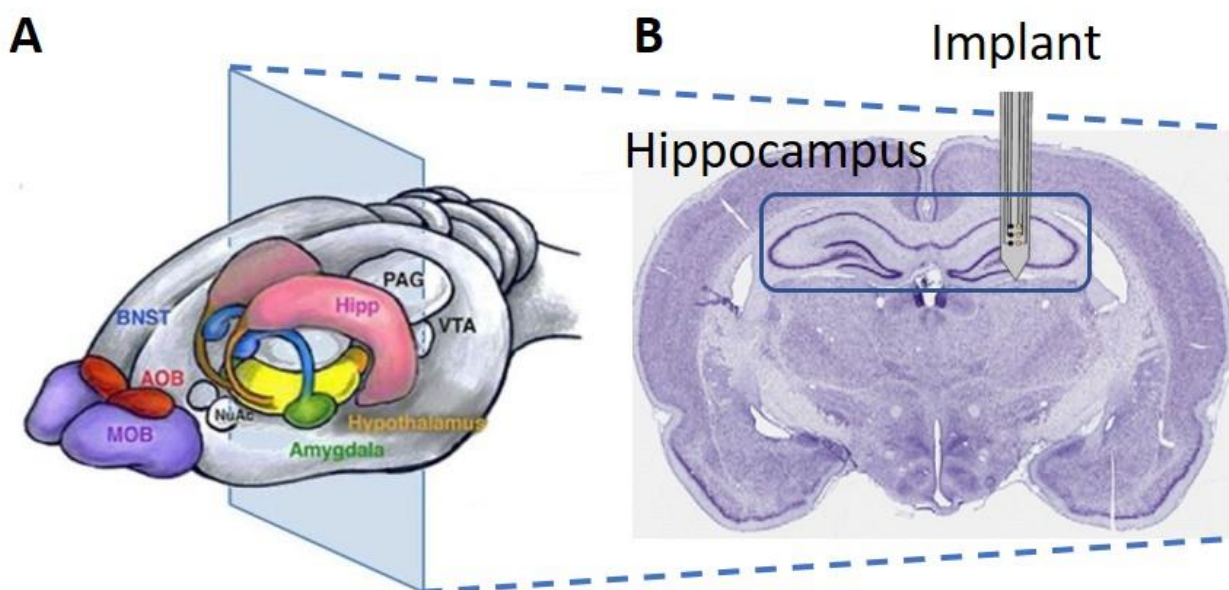


**Fig.16: Brain slice anatomy.** A) Scheme of a rat brain in 3D, with specific brain regions colored, B) Optical picture a brain slice [21] with the hippocampus highlighted, where the implant was inserted for recordings.

After preparation, brain slices were kept in a modified aCSF, without calcium and enriched in magnesium ions (10mM). This prevents brain slices degradation, by blocking calcium entry in the neurons. The aCSF was continuously oxygenated and pH buffered through bubbling of 5% CO<sub>2</sub> / 95% O<sub>2</sub>. For recordings in slice, slices were transferred in the chamber and immersed in an in-vivo like aCSF (**Fig. 17A**) to restore calcium concentrations necessary for neuronal activity. Recordings were performed inside a homemade Faraday cage, with a continuous flow of oxygenated aCSF provided from both side to the brain slice and electrodes were implanted in targeted zones (**Fig. 17B**). The total time of our experiments did not exceed 3h/slice after the first implantation.

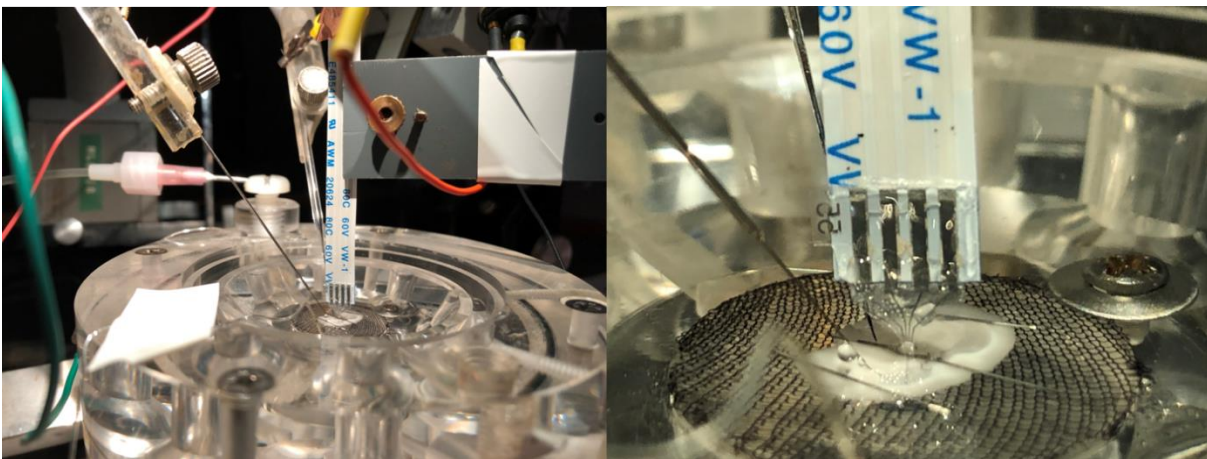


**Fig. 17: Setup for electrophysiology recording in brain slices.** A) Global view of the setup, with brain slice placed in the center of the chamber, with the implant and a reference, high impedance, electrode being hold in place in the brain slice by micromanipulators, B) Zoom in on the implant and electrodes placed in the brain slice.

### 3.5.3 Brain slices recordings

It is worth pointing out that due to variations in experiments (brain slice slight thickness variation, slice activity variation, electrode placement in the slice both in depth and on the XY axis), results are hard to compare in between batches, even in between electrodes from the same implant. Hence, no statistical treatment is given in the following paragraphs, only meant as proof of concept for PEDOT-CNF microelectrodes for high performance neural electrodes. Statistical analysis of the electrophysiological signals will be the object of further studies.

Recordings were first performed in standard conditions of filtering using a bandpass 300-3000Hz, parameters provided by Lionel NOWAK. Then high pass filter was removed to record low frequency signals.

Targeted signals were sharp waves – ripples (SWRs) complexes and neuronal spikes. SWR are events consisting of a propagating synchronized neuronal activity in the entire slice, generating amplitudes of several 100s of  $\mu$ V, with time span of several ms. On the other hand, spikes are quick spontaneous firing of single neurons,

with amplitudes revolving around 10s of  $\mu\text{V}$  (depending of the electrode-neuron distance and the electrode impedance mainly) and duration of less than a millisecond.

### 3.5.3.1 Bandpassed recordings (300-3000Hz)

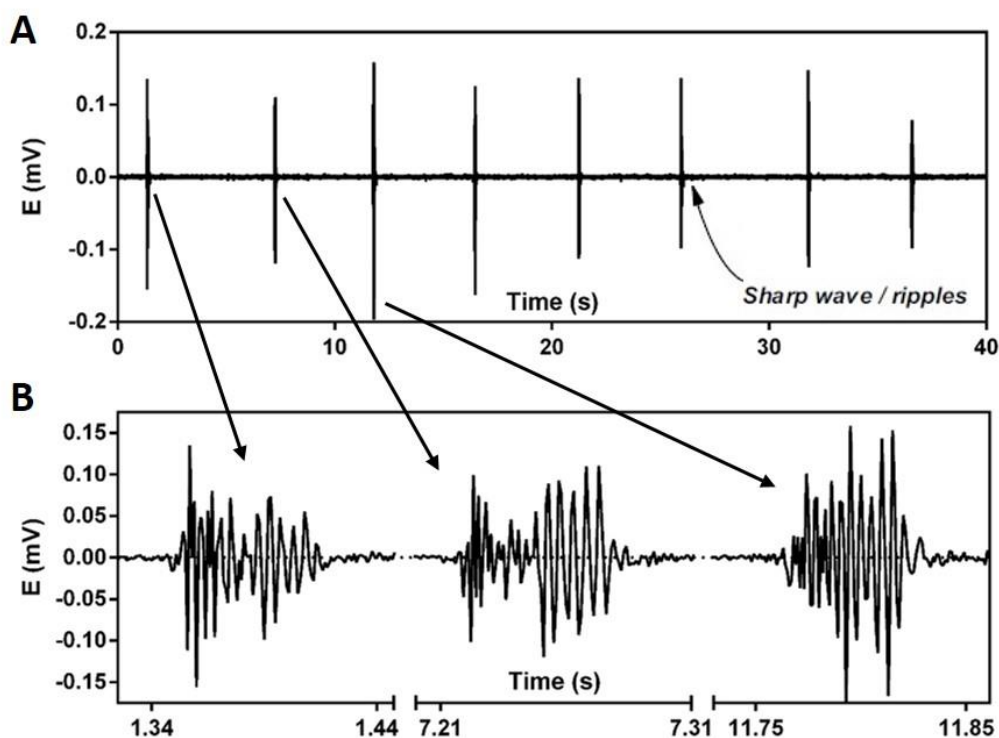


**Fig. 18: Band passed brain slice recordings** on a  $40\mu\text{m}$ -diameter microelectrode, modified with PEDOT-CNF deposited at  $12.56\text{nA}$  ( $10\text{pA}/\mu\text{m}^2$ ) with a deposition charge equal to  $4800\text{nC}$ . Activity recorded is spontaneous and filtered with bandpass filter (300-3000Hz). A) 40s-long sample of a recording showing regular SWRs, with amplitudes in the  $100\text{-}200\mu\text{V}$  range, B) Zoom in on the first three SWRs on the sample, showing shape and amplitudes variability among SWR recorded on the same electrode from the same brain slice.

Bandpassed recordings are standard electrophysiological practice to record spontaneous spiking activity, with multiple examples published in the literature. Due to this filtering, SWRs only appear under the form of a 100ms long event (**Fig. 18A**), presenting high amplitude oscillations ( $150\mu\text{V}$ , **Fig. 18B**) but with almost no baseline variation. This is only the high frequency component of SWRs that is recorded. Spikes were also recorded with these parameters (data not shown).

### 3.5.3.2 Wideband recordings (bandpass 0,1Hz-3000Hz)

As our modified electrodes have higher charges storage capacities and lower impedances in low frequencies ( $<1\text{ M}\Omega$  at frequencies  $<1\text{kHz}$ ), high pass filtering the recordings at  $300\text{Hz}$  might remove low frequency signals that could be recorded by PEDOT-CNF modified electrodes (usual metallic microelectrodes display very high impedance,  $>10\text{M}\Omega$ , in this frequency frequency).

Removal of this filter was operated during recording session with everything else kept the same (setup, electrode, implant, brain slice, recording time). These recordings are called wideband recordings for the rest of



this manuscript. Wideband recordings were actually filtered between 0.1Hz and 3000Hz, the 0.1Hz filter is imposed by the amplifier used to record electrophysiological signals.

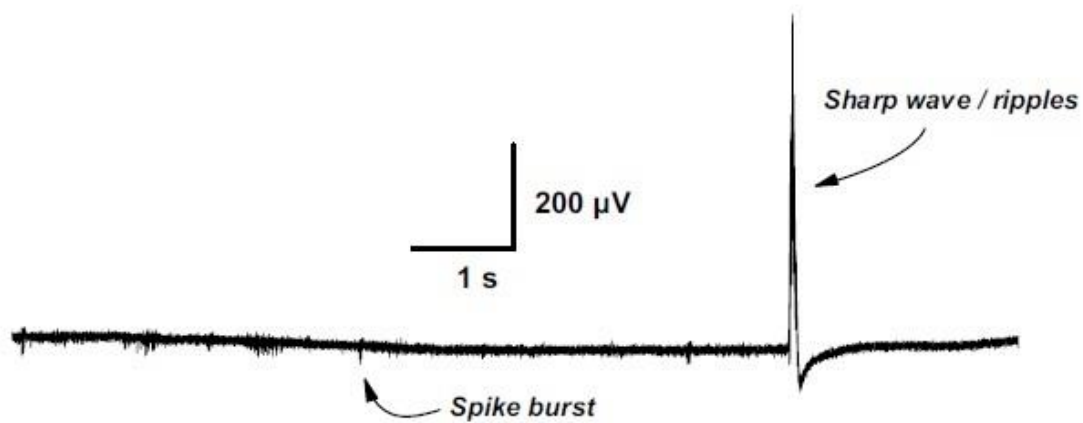


**Fig. 19: Wide band brain slice recordings** on a  $40\mu\text{m}$ -diameter microelectrode, modified with PEDOT-CNF deposited at  $12.56\text{nA}$  ( $10\text{pA}/\mu\text{m}^2$ ) with a deposition charge equal to  $4800\text{nC}$ . Activity recorded is spontaneous and filtered with bandpass filter (0.1-3000Hz). Both spikes and one SWR are recorded.

As can be seen in **Fig. 19**, removal of the high pass filter drastically changes the profile of SWR recorded with modified electrodes, revealing the massive synchronized activity in SWRs, encompassed in their low frequency component. SWR amplitude in these conditions can reach more than  $600\mu\text{V}$ , up to almost  $1\text{mV}$  (cf. **Fig. 23**).

It is important to note that different types of SWRs were observed, according to what type of cellular entities were interfaced with the electrodes (cellular bodies, dendrites, etc.). For example, SWRs presenting potential changes toward negative potentials are supposed to be interfaced with dendrites, while SWR going toward positive potentials (like in **Fig. 20**) are supposed to be interfaced with cellular bodies. In these conditions, spikes burst like the ones depicted in **Fig. 21** were recorded.

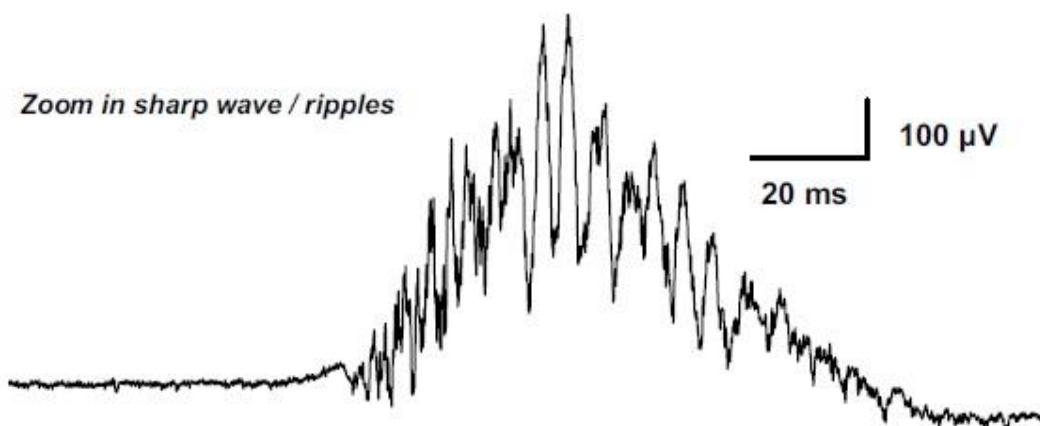


**Fig. 20: Zoom in on the SWR** presented in Fig. 21, clearly displaying a rise of the baseline, reaching a maximum and then getting back to its starting value. Higher frequency is superposed on this baseline change, constituted from the ripples and single neuron activities.

Zoom in spike burst

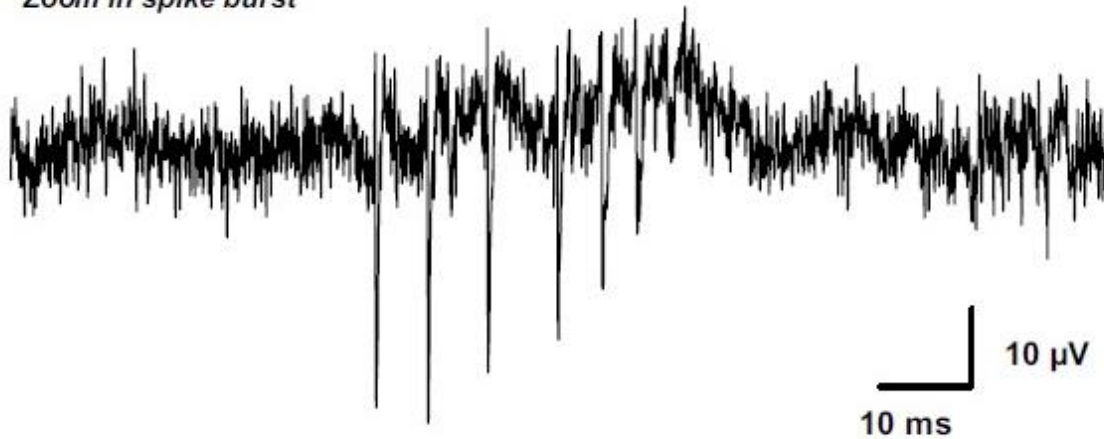


**Fig. 21:** Zoom on a spike burst observed during brain slice recordings on a 40 $\mu$ m-diameter microelectrode, modified with PEDOT-CNF deposited at 12.56nA (10pA/ $\mu$ m<sup>2</sup>) with a deposition charge equal to 4800nC. Activity recorded is spontaneous and filtered with bandpass filter (0.1-3000Hz).

### 3.5.3.3 SWRs frequency analysis and decomposition

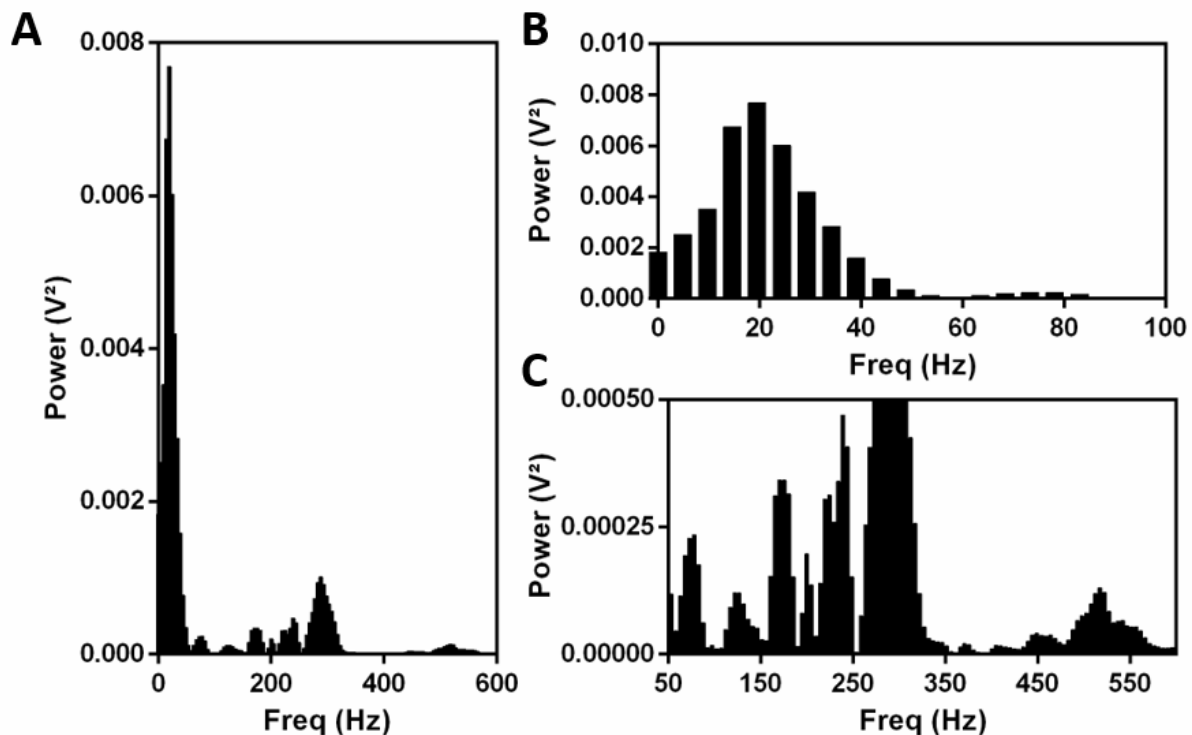


**Fig. 22:** FFT analysis of a sampled SWR. A) Overall power density spectrum obtained after FFT analysis, B) Zoom in on the 0-100Hz range, showing the respective density difference between the activity centered at 20Hz and 75Hz (first and second activity bands), C) Zoom in on the 50-675Hz range, showing the multiple harmonics in the spectrum.

The signals that have been presented are visibly composed of multiple signals temporally stacked. Isolation of SWR from electrophysiological recordings can be realized by analysis through Fast Fourier Transform

(FFT), to decompose it in the frequency domain. After FFT analysis, signals can be deconstructed into several signals, each on a specific frequency window, to observe relevant electrophysiological activity like ripples (cf. later). Here, signals were analyzed by FFT with sample size set at 8192 (time sample of the signal of 0.4096s) and using a Hanning window to prevent distortions. This results in a resolution of 2.441Hz in the FFT analysis presented in **Fig. 22A**.

The low frequency component, in the 1-50Hz range, represents the majority of the signal in terms of power density (**Fig. 22B**), while it can be easily observed that other frequency ranges encompass interesting activity bands (75Hz, 130Hz, 165Hz, 240Hz, 270Hz, 450Hz and 480Hz, **Fig. 22C**).

Through digital filtering post-recording, it is possible to obtain the isolated components composing the raw signal from the bench. In the case of sharp waves (ripples), this procedure has already been described elsewhere [22]. The methodology presented proposes to decompose SWRs into three distinct signals (**Fig. 23**):

- 1) 500Hz-3kHz, where lies the spiking activity (from which single unit activity can be extracted);
- 2) 150Hz-300Hz, where the ripples are present (centered around 200Hz, it is important to note that pathological ripples can extend until 400Hz, which, in light on the important density in the 250-350Hz range in the data presented, could be interesting to consider for future research);
- 3) 1Hz-50Hz, the typical range in which sharp waves are found (partially on the theta band 5-10Hz and the gamma band 30-80Hz).

The decomposition results in signals consistent with data found in the literature, with ripples displayed as spindle-shaped oscillations in the 150-300Hz range, that are similar in shape and amplitude with other references. However, low impedance of PEDOT-CNF modified electrodes allowed recording of high SNR of a wider range of signals composing SWR, frequency-wise. This demonstrates the high performances of these electrodes for recording neural activity of interest.

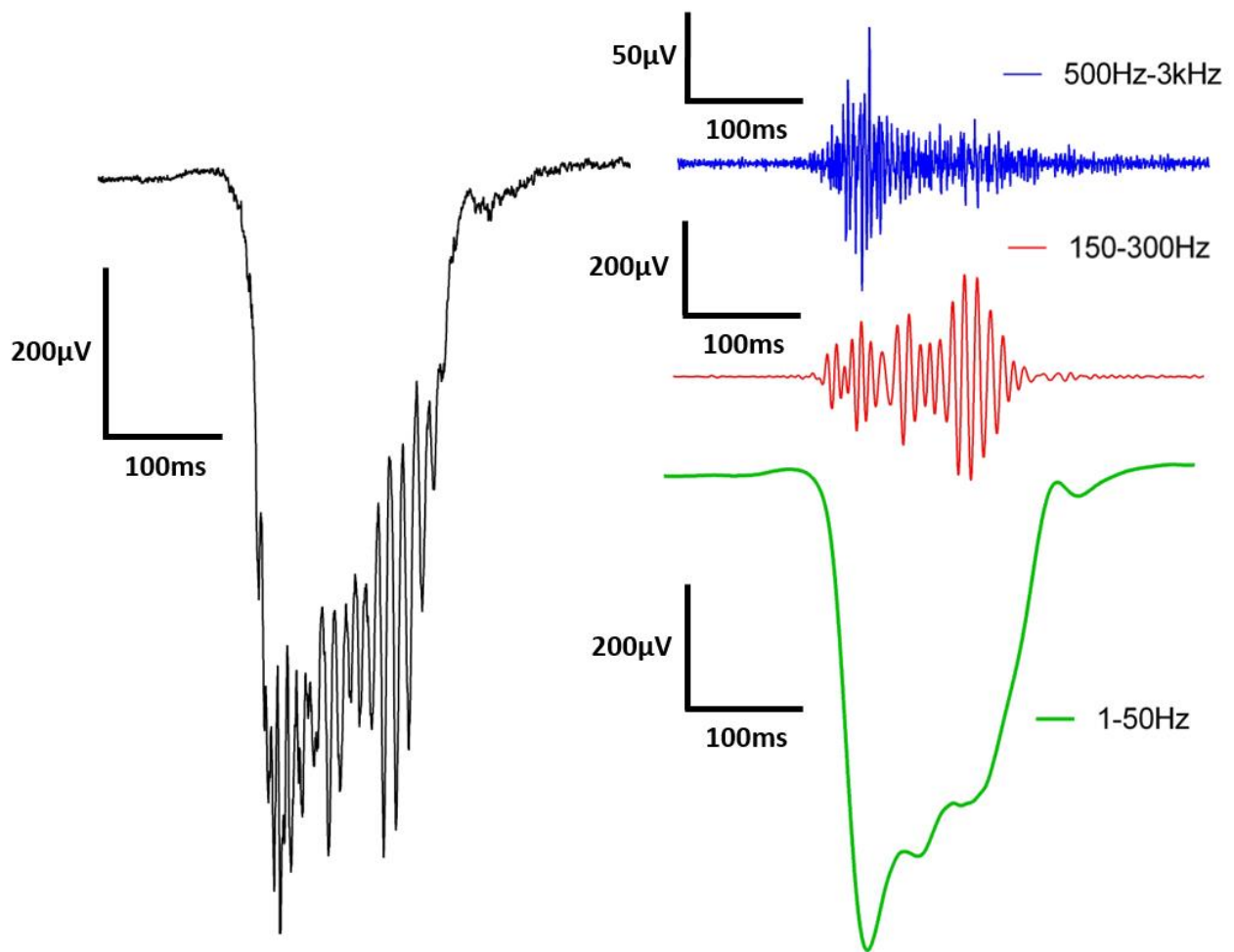


**Fig. 23: SWR decomposition through digital filtering.** Order 8 butterworth FIR bandpass filters were used to extract single-unit activity (blue trace), the ripple (red trace) and the sharp wave (green trace) from the black trace, which the raw signal recorded at the bench.

### 3.5.4 Stimulation performances

Stimulation using PEDOT-CNF was tested in brain slices and recorded with unitary metallic microelectrodes. These experiments confirmed the possibility to reliably inject charge in brain slices and produce a measurable reaction, with low current.

However, this data is still under treatment and will be the object of further studies and developments.

### 3.6 Conclusion & Perspectives

We described the characterization of the PEDOT-CNF microelectrodes on MEA described in the Chapter II of this thesis, through in-vitro EIS, CV and current injection. Then the best candidates for electrodedetection were selected and successfully transferred on flexible implants and used for neural recordings and stimulation in brain slices.

Taken together, all the characterizations performed (impedance, phase, charge storage, charge injection) and the profiles of the electrodes (geometric surface area) showed the high-performance capability of PEDOT-CNF and PEDOT-PSS microelectrode deposited by CP. They also tended to show the incompatibility of CV-deposited microelectrodes with electrodedetection (diameter and charge storage too high).

The microelectrodes deposited by CP displayed very low impedance at 1kHz, likely coming from their high 3D-structured conductive surface, while having a relatively small base microelectrode and preserving a small spatial footprint, making them extremely good candidate for electrophysiological measurements. They also display state-of-the art charge injection limit, while still having a low specific impedance and geometric surface area, that would allow them to be used for very high interest stimulation experiments, while preserving a good degree of stability toward electrical stimulation.

These modified electrodes were then successfully transferred from MEAs (on which they were developed) to flexible implants, to test them in brain slices. They allowed the recording of sharp-waves/ripples on a wider frequency range and a higher SNR compared to standard electrodes used in electrophysiology recordings. They could also be used for stimulation (data under treatment). This proves their capacity to be high-performance bidirectional neural electrodes for electrophysiology.

Further work in stimulation stability will be performed, to optimize long-term charge injection in function of pulses width and electrodes deposition charge. The electrodes on flexible implants will also be redesigned to match their diameter on MEA (20 $\mu$ m), thus allowing finer interfacing in future electrophysiological and electrodedetection.

Finally, to prove the multifunctional aspect of these electrodes, they need to be evaluated as sensing electrodes, using electrodedetection through chronoamperometry and fast-scan cyclic voltammetry, which is developed in the next chapter of this thesis.

1. Baranauskas, G., et al., *Carbon nanotube composite coating of neural microelectrodes preferentially improves the multiunit signal-to-noise ratio*. J Neural Eng, 2011. **8**(6): 066013.
2. Ganji, M., et al., *Scaling Effects on the Electrochemical Performance of poly(3,4-ethylenedioxythiophene (PEDOT), Au, and Pt for Electrocorticography Recording*. Advanced Functional Materials, 2017. **27**(42): 1703018.
3. Urbanová, V., et al., *Macroporous microelectrode arrays for measurements with reduced noise*. Journal of Electroanalytical Chemistry, 2011. **656**(1-2): p. 91-95.
4. Seker, E., et al., *The fabrication of low-impedance nanoporous gold multiple-electrode arrays for neural electrophysiology studies*. Nanotechnology, 2010. **21**(12): 125504.
5. Mandal, H.S., et al., *Improved Poly(3,4-Ethylenedioxythiophene) (PEDOT) for Neural Stimulation*. Neuromodulation, 2015. **18**(8): p. 657-63.
6. Luo, X., et al., *Highly stable carbon nanotube doped poly(3,4-ethylenedioxythiophene) for chronic neural stimulation*. Biomaterials, 2011. **32**(24): p. 5551-7.
7. Nimbalkar, S., et al., *Ultra-Capacitive Carbon Neural Probe Allows Simultaneous Long-Term Electrical Stimulations and High-Resolution Neurotransmitter Detection*. Sci Rep, 2018. **8**(1): p. 6958.
8. Aryan, N.P., H. Kaim, and A. Rothermel, *Stimulation and Recordin Electrodes for Neural Prostheses*. SpringerBriefs in Electrical and Computer Engineering. Vol. 78. 2015: Springer.
9. Donahue, M.J., et al., *Tailoring PEDOT properties for applications in bioelectronics*. Materials Science and Engineering: R: Reports, 2020. **140**: 100546.
10. Zhou, H., et al., *Poly(3,4-ethylenedioxythiophene)/multiwall carbon nanotube composite coatings for improving the stability of microelectrodes in neural prostheses applications*. Acta Biomater, 2013. **9**(5): p. 6439-49.
11. Xu, G., et al., *Electrodeposited conducting polymer PEDOT doped with pure carbon nanotubes for the detection of dopamine in the presence of ascorbic acid*. Sensors and Actuators B: Chemical, 2013. **188**: p. 405-410.
12. Kozai, T.D., et al., *Chronic In Vivo Evaluation of PEDOT/CNT for Stable Neural Recordings*. IEEE Trans Biomed Eng, 2016. **63**(1): p. 111-9.
13. Abidian, M.R. and D.C. Martin, *Experimental and theoretical characterization of implantable neural microelectrodes modified with conducting polymer nanotubes*. Biomaterials, 2008. **29**(9): p. 1273-83.
14. Alba, N.A., et al., *In Vivo Electrochemical Analysis of a PEDOT/MWCNT Neural Electrode Coating*. Biosensors (Basel), 2015. **5**(4): p. 618-46.
15. Volkov, A.V., et al., *Understanding the Capacitance of PEDOT:PSS*. Advanced Functional Materials, 2017. **27**(28): 1700329.
16. Gerwig, R., et al., *PEDOT-CNT Composite Microelectrodes for Recording and Electrostimulation Applications: Fabrication, Morphology, and Electrical Properties*. Front Neuroeng, 2012. **5**: 8.
17. Hudak, E.M., et al., *Electron transfer processes occurring on platinum neural stimulating electrodes: calculated charge-storage capacities are inaccessible during applied stimulation*. J Neural Eng, 2017. **14**(4): 046012.
18. Carli, S., et al., *Single walled carbon nanohorns composite for neural sensing and stimulation*. Sensors and Actuators B: Chemical, 2018. **271**: p. 280-288.
19. Wang, K., et al., *High-Performance Graphene-Fiber-Based Neural Recording Microelectrodes*. Adv Mater, 2019. **31**(15): e1805867.
20. Asplund, M., et al., *Toxicity evaluation of PEDOT/biomolecular composites intended for neural communication electrodes*. Biomedical Materials, 2009. **4**(4).
21. Rohan, J.G., et al., *Modulating Hippocampal Plasticity with In Vivo Brain Stimulation*. The Journal of Neuroscience, 2015. **35**(37): p. 12824-12832.

22. Maier, N., V. Nimrich, and A. Draguhn, *Cellular and network mechanisms underlying spontaneous sharp wave-ripple complexes in mouse hippocampal slices*. *J Physiol*, 2003. **550**(Pt 3): p. 873-87.





## *Chapter IV*

---

# *Toward neurotransmitter electro detection on PEDOT-microelectrodes*

## **4.1 Introduction**

This chapter deals with the last part of the efforts undertaken in developing and characterizing the multifunctional electrodes, presented in chapter II and characterized as neural electrodes in chapter III. These electrodes were proven to be high-performance neural electrodes capable of bidirectional interfacing with brain slices in chapter III. These electrodes are meant as multifunctional electrodes and this last chapter addresses the development of electro detection on these same electrodes (on MEAs). As said in Chapter I, this electro detection is envisaged by the use of two complementary techniques: chronoamperometry (CA) and fast-scan cyclic voltammetry (FSCV).

First, the advantages and drawbacks of both these techniques will be explored, then both CV and CP-deposited PEDOT-coatings will be evaluated in chronoamperometry (CA) for dopamine detection. Next, the FSCV setup is validated with well-known electrodes, carbon-fiber microelectrodes (CF $\mu$ Es), for dopamine detection, an electroactive neurotransmitter that has a highly documented signature in FSCV on such microelectrodes. This setup is then used with PEDOT-modified electrodes to test their performances in FSCV.

### **4.1.1 Technical requirements**

As described in Chapter I, to realize electro detection, a potentiostat is required to generate potential differences/currents and measure the resulting response of the system (constituted of the electrodes and the solution in which they are immersed) studied. The potentiostat choice is crucial according to the application targeted. Here we used two different ones: the Biologic VMP3 and the VSP240, which are a multipurpose, multichannel research potentiostat (also used for electrodeposition and characterization) and a high speed analog ramping potentiostat (used for FSCV, and stimulation for Chapter III) respectively.

### **4.1.2 Electro detection technique choice**

#### **4.1.2.1 Possible techniques for electro detection**

In the literature, multiple techniques for molecular electro detection have been developed according to the applications targeted and the sensor used in conjunction with the considered technique.

These techniques all manipulate the potential at an electrode to generate chemical reactions that produce or consume electrons, generating a current. However, they all differ by the way they manipulate this potential and their resulting inherent performances. Here, we will focus on the main four techniques that can be found in publications: cyclic voltammetry (CV), chronoamperometry (CA), differential pulse voltammetry (DPV) and fast-scan cyclic voltammetry (FSCV).

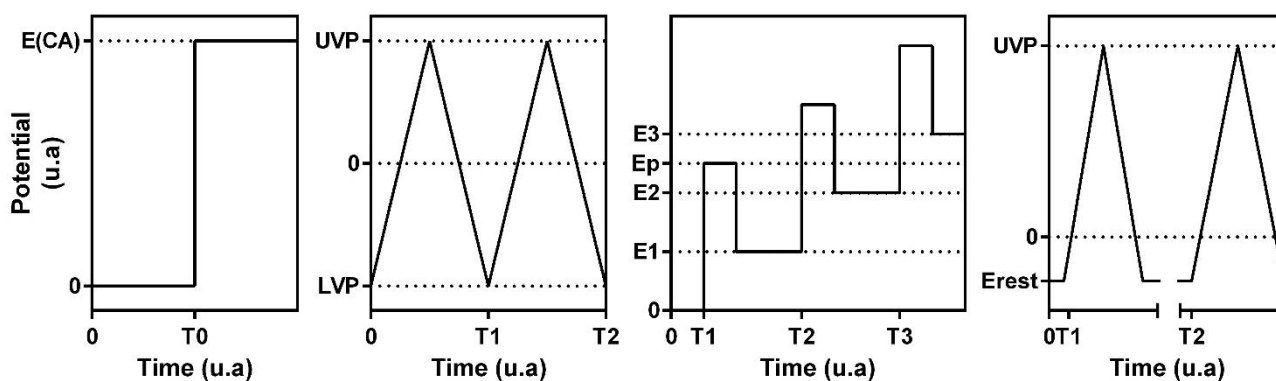


**Fig. 1: Electrode detection techniques potential waveforms.** A) Potential step applied for chronoamperometry (CA). B) Cyclic potential sweep used for CV. C) Pulsed potential sweep used for DPV (or Square-Wave Voltammetry, SWV). D) Triangular sweep spaced with rest period used for FSCV.

Chronoamperometry uses a single potential value manipulation (**Fig. 1A**), fixing it at a strategical value to trigger some reactions. This technique has multiple advantages, mainly ease of use and analysis in combination with high temporal resolution. Indeed, the current frequency sampling during CA experiments is limited only by the potentiostat used (the VSP240 in LAAS, when used in conjunction of EC-Lab Express has a maximum sampling frequency of 1MHz). However, this technique lacks selectivity, as all the reactions that can be triggered due to their activation potential being lower than the electrode energy will be unselectively triggered. The current observed will then be a sum of the currents generated.

Cyclic voltammetry uses a cyclic potential ramp (**Fig. 1B**) that will cross activation potentials at distinctive moment during the ramp (the oxidation potential of each compound) and generate a current function of the electroactive compound concentration, usable to quantify it. Also, the access to both a forward and a reverse scan allows to probe both oxidative and reductive processes separately, creating a more exhaustive foot print for each considered compound. This technique displays good selectivity and sensitivity (influenced by the ramp speed mostly) but is limited by its scan rate, as completing a cycle can take time varying from 100ms to 10s depending of the scanned window and the scan rate, making its temporal resolution low.

Differential pulse voltammetry combines the ramping potential of CV but adds a pulsing potential (**Fig. 1C**). This technique allows, by subtracting at each step the capacitive current (measured at the end of each pulse), to isolate the faradaic peak of each compound in the solution. The selectivity of this technique is then very high, as well as its sensitivity (due to the use of pulses) but like standard CV, it lacks temporal sensitivity.

Fast-scan cyclic voltammetry differs from CV only by its scan rate raised to few 100s of V/s to 1000s of V/s, while these cycles are spaced with rest period at a specific potential (**Fig. 1D**). This decreases the time necessary to complete cycles to few ms, highly increasing the temporal resolution of this technique. The effect of this increased scan rate on other parameters in electrodedetection is discussed later.

The advantages and drawbacks of all these techniques are summarized in **Table 1**.

**Table 1: Electrodedetection techniques advantages and drawbacks in terms of sensitivity, selectivity and temporal resolution. NB: Table partially adapted from [1].**

<i>Techniques</i>	<i>Sensitivity</i>	<i>Selectivity</i>	<i>Temporal resolution</i>
<i>Amperometry (CA)</i>	<i>Low (10-100 nM LOD, depends on the potential value)</i>	<i>Lowest (no selectivity under the oxidation potential)</i>	<i>Highest (sampling rate limited by electronics only)</i>
<i>Cyclic Voltammetry (CV)</i>	<i>Low (slow scan reduce current produced during redox reactions)</i>	<i>Highest (slow cyclic scanning induces high peak separation between molecules type, and reduction peak detection)</i>	<i>Low (depends on the scan rate)</i>
<i>Pulse Voltammetry (PV)</i>	<i>High (around 10nM LOD, depending on the pulse height and scan rate)</i>	<i>High (100mV resolution achievable)</i>	<i>Low (due to pulse time increasing scan duration up to mins)</i>
<i>Fast-Scan cyclic voltammetry (FSCV)</i>	<i>High (lower than 10nM LOD, depends on the adsorption/scanning frequency/vertex potentials and the scan rate)</i>	<i>Highest (as for CV, peak signature allows to identify and separate class of molecules, even similar molecules)</i>	<i>High (1-10Hz most of the time)</i>

#### 4.1.2.2 Association of FSCV and CA

In order to obtain the best combination of sensitivity/selectivity and frequency sampling, an association of FSCV and CA is proposed. This allows to follow rapid sub-milliseconds events using CA while still taking advantage of the sensitivity and selectivity of FSCV to follow changes of low concentrations of electroactive molecules selectively on the same implantable platform. The PEDOT-modified electrodes presented in Chapters II and III will be evaluated as “sensing electrodes” (meant as electrode performing electrochemical detection) using both CA and FSCV.

## 4.2 Electrodedetection Chronoamperometry

### 4.2.1 Electrochemical characterization for faradaic currents

Both CP- and CV-deposited PEDOT-PSS and PEDOT-CNF were evaluated as electrodedetection electrodes. As chronoamperometry is a technique monitoring currents, electrodes must be characterized toward electron transfers. The previous characterizations set deployed in Chapter III are thus inadequate for this application.

To realize this, our modified microelectrodes were characterized toward faradaic transfers using a combination of EIS and CV in conjunction with a standard one-electron electrochemical probe,  $\text{Fe}(\text{CN})_6^{3-/4-}$ . This probe is a surface-sensitive inner sphere probe, which response is known to be a better evaluation of the surface electrochemical properties of an electrode, as it considers the surface defects on top of the electroactive area.

First, CV in 100mM KCl as supporting electrolyte is performed to measure the electroactive area (function of the one-electron transfer wave), then EIS is performed in the same medium at the half-wave potential of both materials (defined as the median potential of the oxidation and reduction potentials or of the inflexion points of the wave), to be in the same electron transfer conditions for both materials.

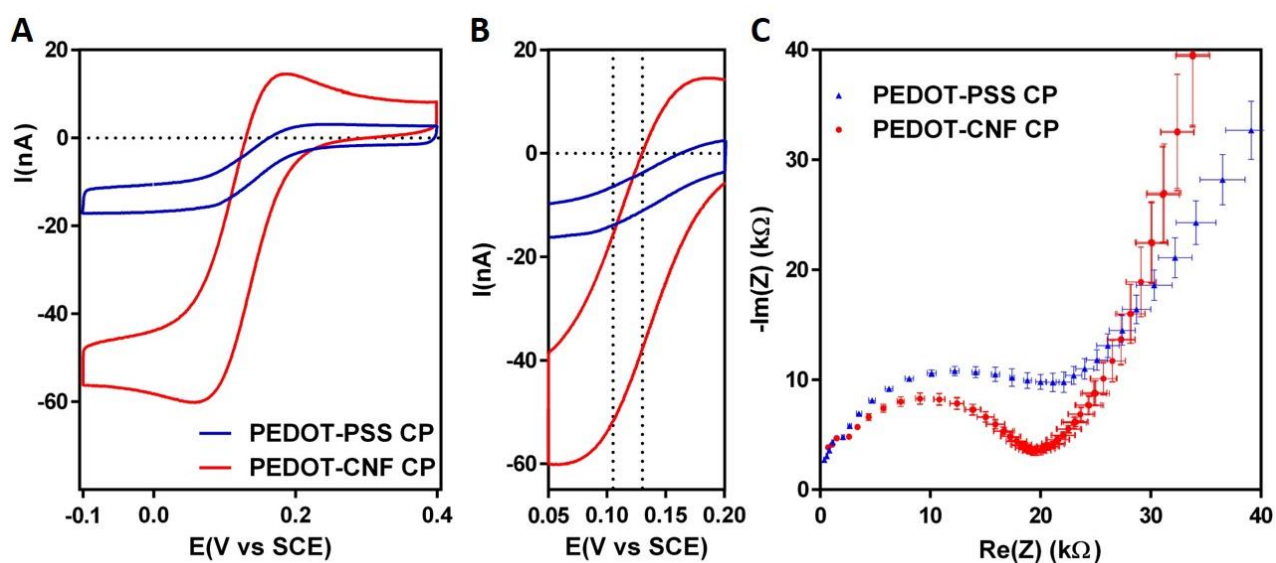


**Fig. 2: Electron transfer characterization with ferri-ferrocyanide probes.** (A) Cyclic voltammetry between -0.1 and 0.4V vs SCE at 50mV/s of PEDOT-PSS and PEDOT-CNF-modified microelectrode in 5mM  $\text{K}_3\text{Fe}(\text{CN})_6$ , 100mM KCl. (B) Zoom in on the wave region. (C) Nyquist plot of modified microelectrodes at 105mV vs SCE (PEDOT-CNF) and 130mV vs SCE (PEDOT-PSS) of PEDOT-PSS and PEDOT-CNF-modified microelectrodes ( $N=3$ ) in 5mM  $\text{K}_3\text{Fe}(\text{CN})_6$ , 100mM KCl. Frequency sweep between 10Hz and 7MHz, 10mV sinus, at 0V vs SCE.

As we can see in **Fig. 2A**, the wave height for PEDOT-CNF is bigger than PEDOT-PSS, with a higher reductive current of -60nA for PEDOT-CNF-modified microelectrodes compared to the reductive current of -18nA for PEDOT-PSS modified microelectrodes, showing a higher electron transfer capability from the electrode to the electrolyte. Both microelectrode types display voltammograms with both pretty important widths forming a hysteresis between the forward and backward cycle parts, likely coming from the microelectrode capacitances. On top of these features, PEDOT-CNF showed a pair of redox peaks, with a profile closer to what is obtained due to semi-infinite planar diffusion at macroelectrodes, while PEDOT-PSS presents no such peaks presenting a sigmoidal profile, closer to voltammograms due to semi-infinite hemispheric diffusion to microdisk electrodes. These observations are coherent with the developed surface of PEDOT-CNF microelectrodes being much higher than the one of PEDOT-PSS microelectrodes, which clearly have repercussions on the electrode performance.

Then, the half-wave potentials for both electrode types were determined, 105mV vs SCE for PEDOT-CNF and 130mV vs SCE for PEDOT-PSS (**Fig. 2B**). EIS measurements at these potentials (to be in electrochemically equivalent situation for electron transfer on both materials) displayed typical profiles, with semi-circles appearing at high frequencies in the Nyquist plots (**Fig. 2C**). It is interesting to note that a constant-phase element (CPE) is present in the Nyquist plot of the probed PEDOT-PSS microelectrodes, implying a heterogeneity of surface perturbing electron transfers. As the diameter of these semi-circles is smaller (while still being in the same magnitudes) for PEDOT-CNF (19.6k $\Omega$ ) than for PEDOT-PSS (21.1k $\Omega$ ), this confirmed that electron transfer resistance is lower for PEDOT-CNF and PEDOT-PSS. Also, a clear difference in the slope of low frequency tails can be observed, with a slope lower for PEDOT-PSS (slope of 1.3613,  $R^2=0.9949$ ) than for PEDOT-CNF (slope of 3.5757,  $R^2=0.9941$ ). By analogy between the difference between a standard Warburg element and T element Warburg, it would suggest that charge carriers in the solution can diffuse easier in PEDOT-CNF than in PEDOT-PSS.

These features directly impact positively the electro detection performances of the PEDOT-CNF composite compared to the PEDOT-PSS, with a better diffusion and a lower resistance, which will less limit the detected currents. Also, the electrons generated during electro detection are less prone to be absorbed by the material and to generate undesired reactions in its bulk. Taken together, these characterizations highlight that PEDOT-CNF microelectrodes are them better candidates as for use as sensing electrodes.

#### 4.2.2 Chronoamperometric detection of dopamine

First, CVs at low scan rate (to be closer to CA, which can be considered to a null scan rate CV after the potential step which would be an infinite scan rate potential sweep) were performed in a physiological-mimicking media (here Tris buffer 1X), with and without DA, to determine its oxidation potential on both PEDOT-CNF and PEDOT-PSS electrodes. Then, CA at the potential determined by CV was performed and the current responses were processed for calibration.

For PEDOT-CNF electrodes (CV- and CP-deposited), after subtraction of the two CVs (CV with DA – CV without DA), a double oxidation peak (111mV and 173mV) and a single reduction peak (-23mV) could be observed of PEDOT-CNF (**Fig. 3A**).

Then, CA at the potential of the highest peak (173mV) was performed under successive injection of DA freshly diluted in Tris buffer (concentrations from 100nM to 9 $\mu$ M). The reference electrode actually used during the experiments was a chlorinated silver wire, in order to prevent hours-long exposition of SCE to dopamine containing solutions and possible pollutions. The potential of this wire was compared back-to-back to the potential of the SCE used for CV experiment and corrected to prevent detection potential drift.

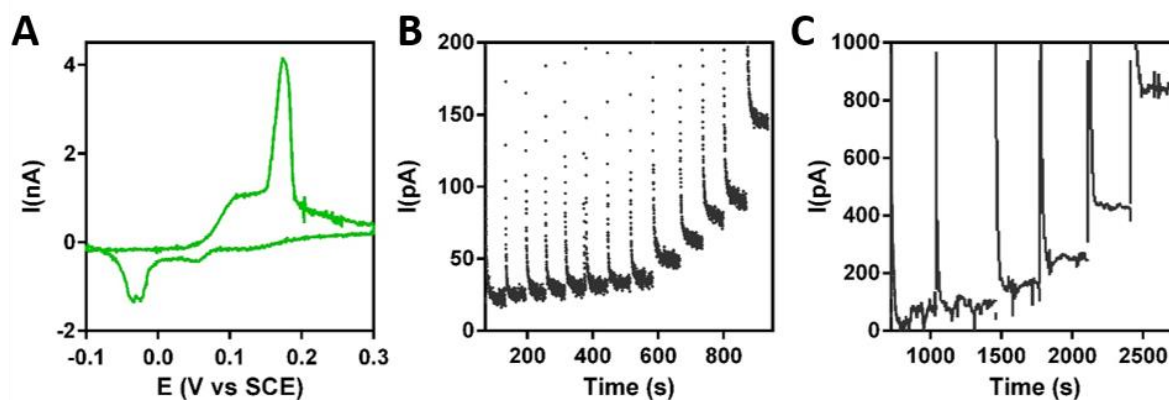


**Fig. 3: In-vitro DA sensing on PEDOT-CNF.** (A) Subtracted CV of  $1\mu\text{M}$  DA in Tris buffer 1X at  $200\text{mV/s}$  between  $-0.6$  and  $0.6\text{V}$  vs SCE (zoom between  $-0.1$  and  $0.3\text{V}$  for readability). Typical chronoamperometric response of a (B) CP-modified and (C) CV-modified microelectrode PEDOT-CNF to DA injections. The currents steps in the figure correspond to (B)  $100, 200, 300, 400, 600, 800\text{nM}$  and  $1, 2, 3, 4, 5, 9\mu\text{M}$  and (C)  $100, 400\text{nM}$  and  $1, 2, 4, 9\mu\text{M}$  injections.

CP-deposited PEDOT-CNF electrodes resulted in very stable responses, quickly reaching current values corresponding to concentrations (Fig. 3B). CV-deposited PEDOT-CNF electrodes however displayed responses that were less stable (particularly at concentrations lower than  $1\mu\text{M}$ ), which needed higher times to reach stable current values (Fig. 3C), possibly due to DA diffusion in the electrode with 3D porous structure. The same procedure (CV for oxidation potential determination + CA) reproduced on PEDOT-PSS did not yield any oxidation or reduction peak (data not shown) after CV subtraction. However, CA detection of DA was even though tried on PEDOT-PSS microelectrodes, at the same potential used for PEDOT-CNF microelectrodes.

The current responses to DA injections resulted in linear regressions with good confidence for PEDOT-CNF electrodes (Fig. 4,  $R^2=0.9964$  for CV and  $R^2=0.999$  for CP) while PEDOT-PSS could not reliably detect DA concentrations ( $R^2=0.4085$  for CV and  $R^2=0.7352$  for CP). PEDOT-PSS unreliability to sense DA can be explained by its surface chemistry, as it is heavily negatively charged (pending PSS chains), preventing negatively-charged entities (like DA at the experiment pH) to reach the electrode, causing the absence of oxidation peak (leading to no detection capability).

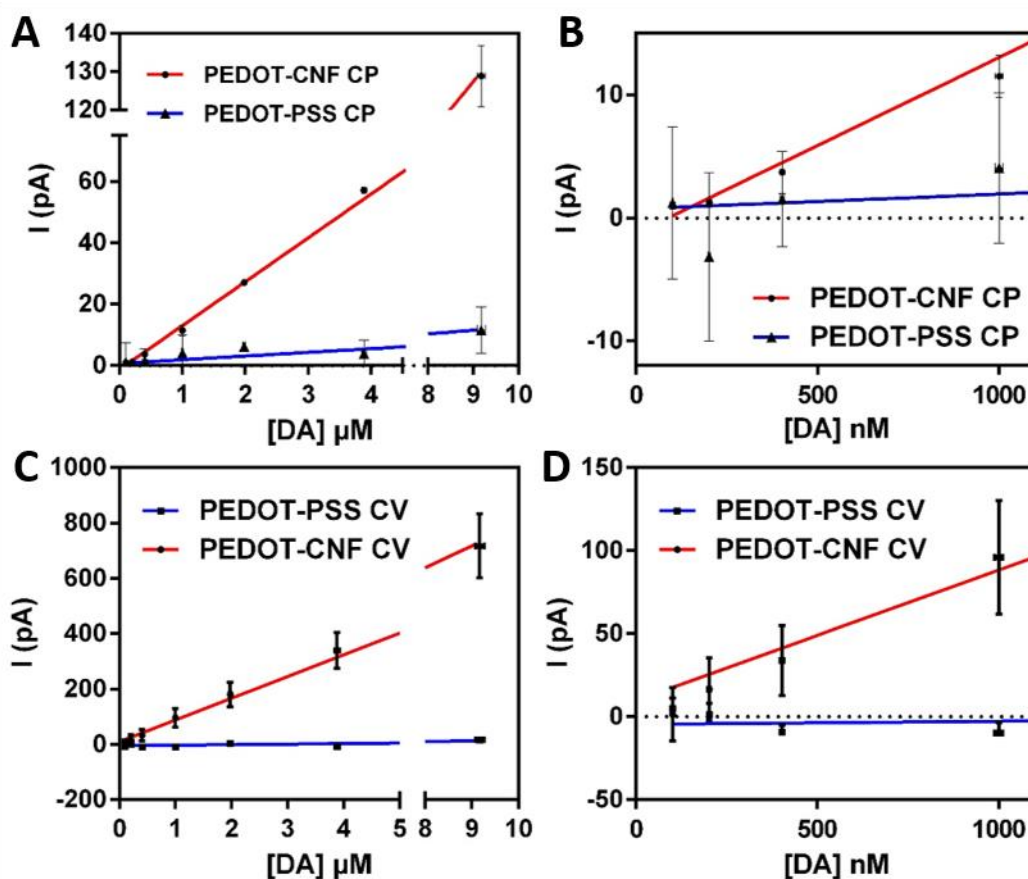


**Fig. 4: In-vitro calibration of DA sensing.** Linear regression curve of (A) CP-modified and (B) CV-modified PEDOT-CNF electrode response to DA in Tris buffer, (C&D) Zoom in on the region between 0 to 1 $\mu$ M for both electrode types.

Sensitivities of  $78.6 \pm 2.1 \text{ pA}/\mu\text{M}$  and  $14.3 \pm 0.2 \text{ pA}/\mu\text{M}$  were respectively achieved for CV- and CP-modified electrodes. Analysis of the RMS noise during the chronoamperometry experiments leads to LOD equal to 45nM for CP-deposited PEDOT-CNF electrodes and 55nM for their CV-deposited counterparts. LOD is calculated by dividing the RMS Noise obtained (in pA) divided by the sensitivity (in  $\text{pA}/\mu\text{M}$ ). Higher LOD for this latter electrode type despite its higher sensitivity is explained by a higher noise, compensating the higher sensitivity. All these parameters are gathered in **Table 2** for clarification and comparison between the different microelectrode types in this manuscript. As the lowest concentration tested (100nM) is higher than some LOD announced, which have to be considered theoretical, it would be necessary to confirm these LODs experimentally.

**Table 2: Comparison of chronoamperometry performances of the four microelectrode types presented, in terms of  $R^2$ , sensitivity and LOD.**

Parameters	PEDOT-PSS (CV)	PEDOT-PSS (CP)	PEDOT-CNF (CV)	PEDOT-CNF (CP)
$R^2$	0.4085	0.7352	$R^2=0.9964$	0.999
Sensitivity ( $\text{pA}/\mu\text{M}$ )	$1.9 \pm 1.0$	$1.2 \pm 0.3$	$78.58 \pm 2.1$	$14.3 \pm 0.2$
LOD	2838nM	322nM	55nM	45nM

As a final summary, all parameters quantifying the performances of the PEDOT-CNF microelectrodes in CA electrodedetection of DA are summarized in **Table 3** for comparison with a few relevant references from the literature.

**Table 3: Comparison of the PEDOT-CNF performance for DA electrodedetection by chronoamperometry in terms of potential, linear range, sensitivity and LOD with relevant literature references. Parameters highlighted in dark green are the one incompatible with the requirements for neural interfacing at the single cell level. Blue ones show the use of a different technique/technology. Green ones show better performances of the published sensors compared to ours.**

Modified electrode	Geometric area ( $\mu\text{m}^2$ )	Detection technique	Target	E(mV)*	Linear range	Sensitivity ( $\text{pA/nM}\cdot\mu\text{m}^2$ )	LOD ( $\mu\text{M}$ )	Ref
CNT	7068583	CA	DA	-50	10-100 $\mu\text{M}$	46.053	10	[2]
Pt-rGo	1100	CA	DA	150	10nM-350 $\mu\text{M}$	1.698	0.01	[3]
PtNPs-Nafion	314	CA	DA	500	0-160 $\mu\text{M}$	43.95	0.02	[4]
Ox-PPy	5000	CA	DA	700	100nM-45 $\mu\text{M}$	325	0.062	[5]
OPPy/Nafion /GlutOx	5000	CA	Glut	700	0-18 $\mu\text{M}$	1.256	2.1	[5]
Pt-Nafion	450	CA	DA	500	100nM-10 $\mu\text{M}$	22.31	0.1	[6]
nsPt-GluOx-MPD	7500	CA	L-Glu	700	5-30 $\mu\text{M}$	7.47	0.5	[7]
rGO-PtNPs	2827	DPV	NE	100	5-250 $\mu\text{M}$	364.34	0.08	[8]
PEDOT-CNT	1963	SWV	DA	100	200nM-5 $\mu\text{M}$	370	0.2	[9]
PEDOT-CNF	314	CA	DA	130	100nM-9 $\mu\text{M}$	44.54	0.045	LAAS

\*=potential reported with different reference electrodes.

As can be seen in **Table 3**, the PEDOT-CNF microelectrodes display high normalized sensitivities (well above than enzymes-based sensors), with a quite low LOD compared to relevant literature references. Higher sensitivities could be achieved using DPV or SWV, while also having a better selectivity. Without the use of an enzyme or of a scanning technique, no selectivity for dopamine over other electroactive molecules is ensured. However, the use of a low potential limits interferences from other oxidizable molecules, as few molecules are redox-active at low potential (generating less of a selectivity issue compared to CA realized at 700mV for example).

#### 4.2.3 Conclusions for electrodedetection using chronoamperometry

Taken together, the performances and characterizations of PEDOT-CNF and PEDOT-PSS microelectrodes show the modularity of such microelectrodes for electrodedetection. By changing the deposition technique, different morphologies and performances can be reached.



CP-deposited PEDOT-CNF are the better candidate as sensing electrodes (using CA) for chronoamperometry, with quick and stable response to DA injection, while having a low spatial fingerprint, allowing measurements at a single-cell level. CV-deposited PEDOT-CNF the deposition and characterization results showed that for electrodedetection, CP-deposited electrodes were more indicated, as they have lower impedances and capacitances (hence, lower response time), displayed more stable response to DA injections than their CV-modified electrodes counterparts. Moreover, CV-deposited electrodes display an equivalent diameter too high (50 $\mu$ m) to still take advantages of microelectrodes, which is detrimental to electrodedetection performance of these electrodes, even though they have higher sensitivity. In the light of these points, only PEDOT-PSS and PEDOT-CNF deposited by CP are kept for further characterization and use in our experiments.

## 4.3 FSCV: Validation and deployment

The next part on this chapter deals with the efforts to develop a FSCV setup and validate it in the LAAS lab, starting by an overview of FSCV features, modularity and scope, followed by the experimental validation of FSCV. Finally, the CP-deposited PEDOT microelectrodes are evaluated as if they are FSCV-compatible.

### 4.3.1 Focus on FSCV

#### 4.3.1.1 Technique presentation

As quickly described in Chapter I of this manuscript, FSCV works by applying a triangle-shaped waveform to a microelectrode at high scan rate (higher than 100V/s). The electrode is typically a Carbon Fiber Microelectrode (CF $\mu$ E), with a scan rate (SR) around 400 V/s (but can be up to 1200V/s or even 2400V/s [10]), and scan limits of -0.4 V to 1.3 V. The scans are typically applied every 100ms with the electrode holding at -0.4 V (being the lower vertex potential) in between scans (**Fig. 5A**).

The current collected from a triangle scan is displayed as a cyclic voltammogram  $I=f(E)$ . This current is the sum of the capacitive currents (charging of the electrical double layer, created by ions movements for example) and faradaic currents (the current created by electrons produced by redox reactions from interest species), as can be seen in **Fig. 5B** (black trace). To obtain the electrochemical signature of a targeted molecule, the non-faradaic currents (currents not produced by the target reaction, called background) must be subtracted, which is the differential aspect of this technique. These currents are measured before exposure of the electrode to the molecule(s) of interest.

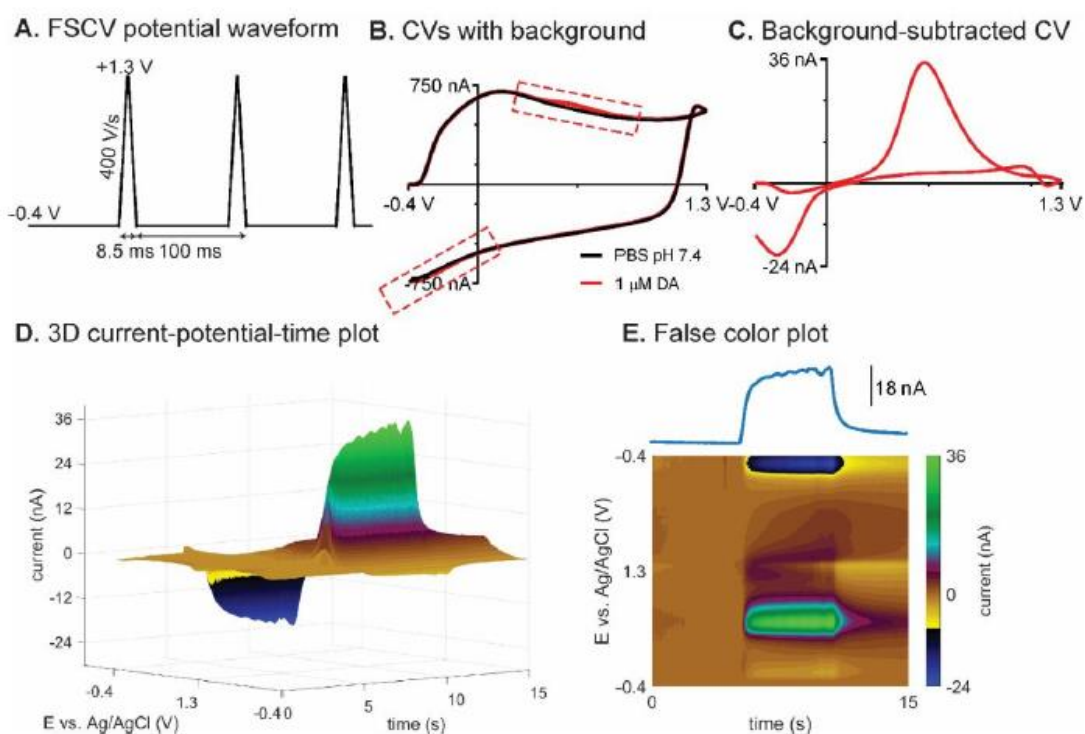


**Fig. 5: FSCV realization steps exemplified with dopamine.** A) FSCV potential waveform, showing the temporal progression of the potential during FSCV at 10Hz. B) CV of a CF $\mu$ E with (red trace) and without (black trace) 1 $\mu$ M DA in PBS (pH=7.4), with the redox peaks from DA. C) Background-subtracted voltammograms, revealing the faradaic component from DA in the raw signal. D) 15s-long FSCV data set plotted in a 3D-color plot showing the rise of the DA peaks. E) Same data set as a 2D-color plot. Adapted from [1].

As presented in Chapter I, an increase in dopamine (a common redox active neurotransmitter) in the electrode surrounding space yields to the apparition of a current peak in the voltammogram at certain potentials (depending of the pH, the media, the scan rate, the electrode material, etc.), as pictured in **Fig. 5B** (red trace). A cyclic voltammogram of the current change due to this addition of dopamine is obtained by digitally subtracting the background current [11] from the signal with the dopamine (**Fig. 5C**). These measurements are realized overtime at a given frequency (10Hz) and to display changes in concentration overtime, the CVs are plotted in 3D (**Fig. 5D**) or in color maps (**Fig. 5E**) where the y-axis is potential, x-axis is time, and current is in false color [12]. A trace taken along the x-axis (at one signature potential) indicates the changes in concentration of the corresponding analytes over the measurement time.

Thanks to high scan rates, FSCV displays a high sensitivity compared to other electrodedetection techniques (higher than CA for example, being a “0V/s scan rate” technique) and the possibility to follow subsecond-transients. Also, the presence of a reverse scan allows to identify multiple molecules reacting at different potentials through both their oxidation and reduction peaks. This leads to a very high selectivity.

These characteristics make FSCV a very effective technique for in-vivo electrochemical detection of neurotransmitters [13, 14]. On top of that, FSCV is a very versatile tool in the neuroscientist toolbox, as the FSCV waveform can be manipulated to analyze new molecules, differentiate analytes and alleviate fouling.

However, FSCV also have many disadvantages, mainly due to its differential nature. The need for background measurements done prior to implantation and then used to background subtract all data along the FSCV experiment makes this technique very sensitive to any background drift, making calibration obsolete. This drawback has been the major motivation for research to overcome it by in-vivo calibration [15], recalibration [16] or post-measurement data detrending [17] for example. This also impedes FSCV to be easily used for long-term measurements (to detect slow-changing concentrations of some molecules for example) but it can be adapted to it [18]. And finally, transients quicker than the time between two scans cannot be accurately followed with FSCV. Some strategies to address these issues are discussed in the following paragraphs to give an idea of how one can take advantage of this technique modularity for practical application.

#### 4.3.1.2 Background current (BC) management

- **Background prediction for subtraction**

One strategy to handle BC change overtime is to probe this BC during measurements to detect any change and correct background subtraction.

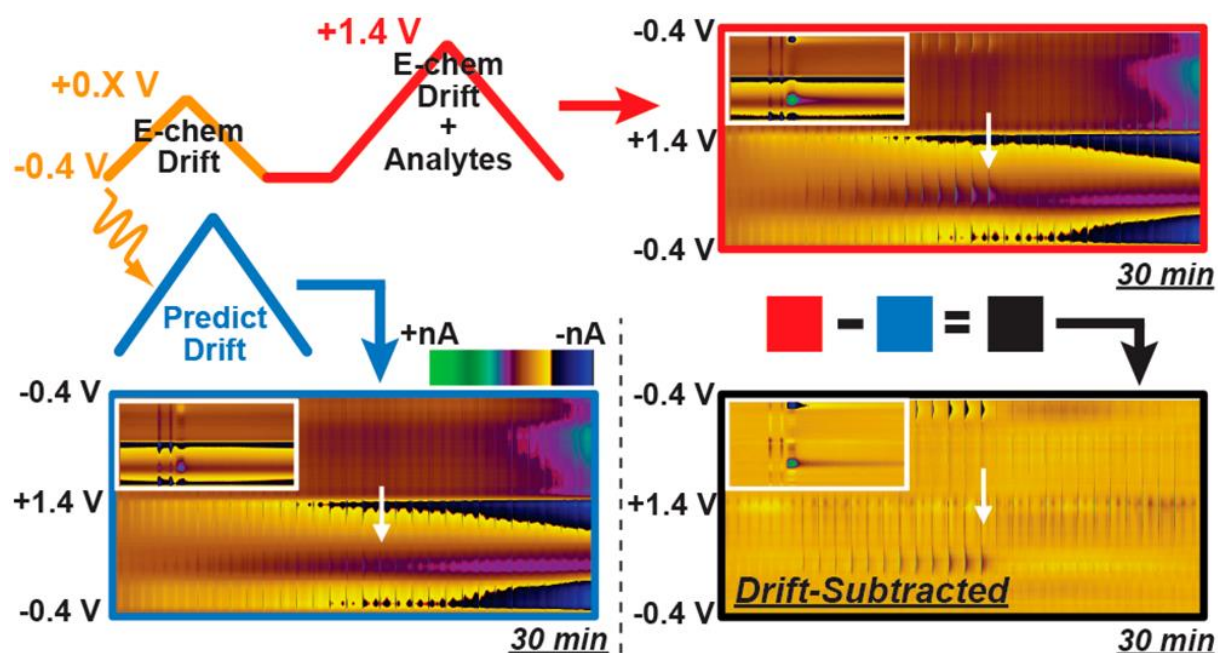


**Fig. 6: Drift prediction and subtraction using a double triangular waveform.** A first cycle is used to measure part of the drift and predict the rest (blue framed data), that is subtracted after to the data from full scans (red framed data) to correct a 30min-long data set (black framed data) [20].

Two different methodologies have been published in this spirit, the first probing the BC by an additional incomplete scan placed before measurements [19, 20]. This probe a part of the BC and capture information of its drift. This probing scan is then used as a predictor of the electrochemical drift of the entire drift through partial-least squares regression (PLSR) that is later subtracted to the data (Fig. 6).

This technique has been proved to improve quantification of adenosine, dopamine and hydrogen peroxide for both rapid and gradual (minutes) changes.

The second methodology uses a small potential step placed before the actual FSCV scan to probe the BC [16] and uses the current decrease during this step to build and fit a standard electronic RC-model. This is used to predict a non-neglectable part of the background current that will be generated during the FSCV scan and subtract it from the data.

- **Baseline drift management by post-filtering**

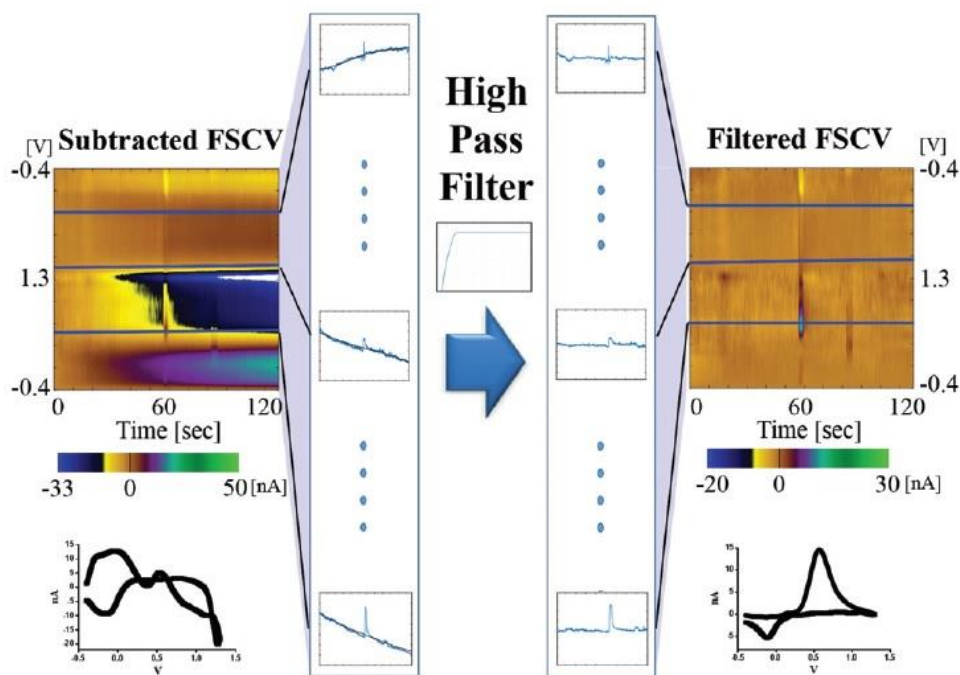


**Fig. 7: Drift removal by high pass filtering.** A zero-phase IIR Butterworth HPF was applied to current= $f(\text{time})$  data recorded at each voltage (horizontal blue lines). In this illustration, a  $1 \mu\text{M}$  bolus of dopamine in a Tris buffer was injected in a flow cell and the background drift was removed by the filter leaving only the signal due to the presence of dopamine. [17]

Another approach to improve FSCV measurements after background-subtraction is the use of filtering to detrend drift in data.[17] This approach is based on the idea that drift happens on a much slower time scale than relevant events detected by FSCV.

Based on this consideration, one published article used a zero-phase IIR (Infinite Impulse Response) Butterworth High-Pass Filter (HPF) on a minute to hour-long data sets, to remove drift and extract a cleaner data. This way the voltammograms obtained after HPF filtering are reconstructed using data exempt of drift, leading to better identification of compounds like pictured in Fig. 7.

#### 4.3.1.3 FSCV modularity: Waveform manipulation

In order to adapt FSCV to certain application/target, the waveform can be modified to achieve better stability, selectivity, sensitivity, etc. or detect new targets and separate similar molecules. This is discussed in the

following paragraphs, that deal with Upper Vertex Potential (UVP) and Lower Vertex Potential (LVP) modification and scan rate adaptation.

- **UVP increase**

Increasing the UVP induces multiple effects on the electrode: i) surface renewal during electrochemical etching of surface residues and etching of a very thin layer of the electrode surface, ii) electro-modification of the electrode surface by oxidation, potentially inducing sensitivity increase, as exemplified in **Fig. 8A** with dopamine.

But contrary to dopamine or other catechol-based molecules, some key compounds are not highly electro-reactive, meaning that their inherent redox reactions need higher potentials (in absolute values) to be triggered.

For example, for adenosine a higher UVP of 1.5V vs Ag/AgCl is required to trigger its oxidation (**Fig. 8B**) as the molecule is highly delocalized, thus stabilized, making electron withdrawal more energetically demanding.

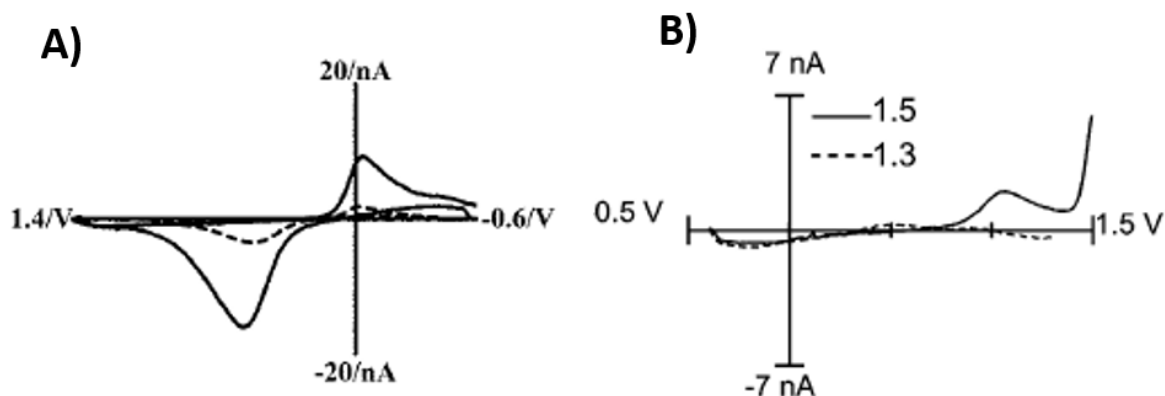


**Fig. 8: UVP increase effect on sensitivity and targeting.** A) Background-subtracted cyclic voltammograms for 1  $\mu\text{M}$  dopamine in Tris buffer solution, pH 7.4, when the traditional waveform (-0.4 V to 1.0 V, 300  $\text{V/s}^{-1}$ , dashed line) or an extended waveform (-0.6 V to 1.4 V, 400  $\text{V/s}^{-1}$ ) is applied [21], B) Cyclic voltammograms of 5  $\mu\text{M}$  adenosine when the switching potential is 1.3V (dashed line) and 1.5V (solid line) [22].

It is important to note that higher UVP will induce a more important etching of the electrode, decreasing its surface and in the end making it fail. It might also trigger electro-oxidation in the solvent in which the electrode is placed.

- **LVP**

As with UVP, extending the possible oxidation reactions array on the electrode, lowering the LVP has the same effect on the possible reduction reactions. Lowering the LVP has been published in an article, in conjunction with the use of two waveforms to detect reducible compounds like oxygen [23], as pictured in **Fig. 9**. However, like for UVP increase, LVP decrease will modify the electrode surface chemistry and might trigger electro-reduction on the solvent.

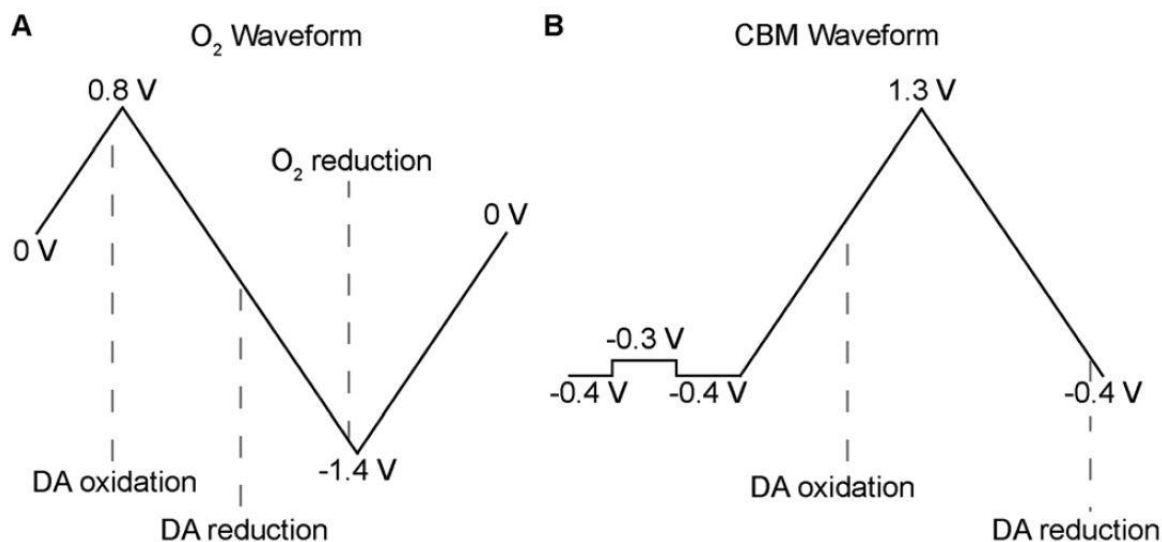


**Fig. 9: Dual FSCV waveform for simultaneous oxygen and dopamine detection.** A) Oxygen-sensitive waveform having a lower vertex potential of -1.4V to reach O<sub>2</sub> reduction at -1.3V. B) Dopamine waveform using background prediction with a potential step before the scan [23].

- Scan rate

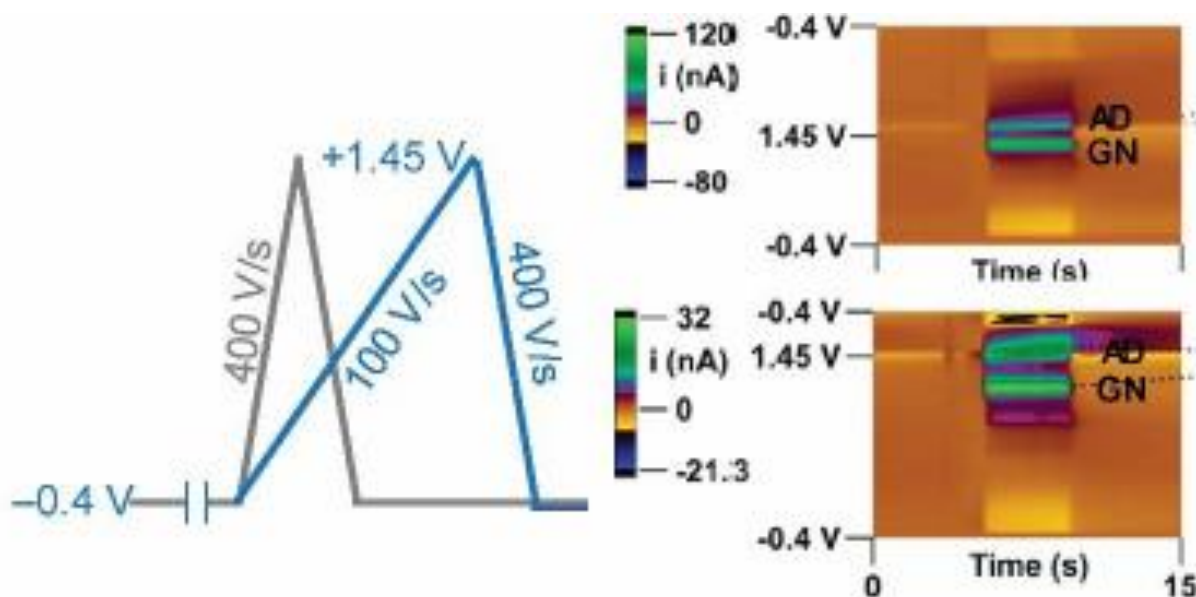


**Fig. 10: "Scalene" FSCV waveform with asymmetrical scan rates for guanosine detection.** A) Potential versus time curves of the waveform, showing the temporal difference between this waveform and a symmetrical one. B) Color plots with the standard waveform (top) and the "scalene" waveform (bottom) with enhanced peak separation [24].

Another parameter that can be adapted is the scan rate used during FSCV experiments, to play on the targeted compounds differences in electro-reactions kinetics. By increasing the scan rate, the potential at which takes place the redox reactions will also increase (in potential value). The increase will be different for each compound according to its structure, diffusion kinetics, reactions kinetics, etc.

A more advanced approach to scan rate engineering has been published [24], using different scan rates on both the forward and reverse scan inside a FSCV cycle (**Fig. 10**). This “scalene” waveform was shown to increase peak separation between adenosine and guanosine peaks, two molecules having very similar structures.

- **Conclusion**

As was just described, FSCV has a high potential as a versatile, modular electroanalytical technique, adapted to both in-vitro and in-vivo studies. It is capable to target multiple molecules of interest, with high selectivity and sensitivity.

It is important to note that multiple strategies developed around FSCV like the use of training sets [25, 26] or the use of regression algorithms to resolve multiple compounds [27-29]. These have not been discussed here as they are additional techniques used on FSCV data and not FSCV adaptations, hence being out of the scope of this manuscript. They are however very important and present in the literature linked to FSCV.

In the FSCV parameters, the potential rest value has also shown to have a great influence on the viability of the technique [30] and has been let out of the preceding paragraphs to prevent information overcharge. Even though, it is an important parameter to consider.

#### 4.3.1.4 Experimental plan

To be able to exploit all the FSCV features, it is necessary to verify that the setup used for it is capable of producing usable FSCV data, fitting the requirements to be exploitable.

#### 4.3.2 FSCV sur CF $\mu$ E: Validation of the experimental setup and method

As previously mentioned, in-vivo neurotransmitter electrodedetection is mostly performed by FSCV on single carbon fiber microelectrodes (CF $\mu$ Es) [31] as they are quite easily fabricated, have high surface and high surface electron transfer kinetics, making them the gold standard for this kind of study. However, these electrodes suffer several limitations making them inadequate for long-term use in-vivo. Even though, they constitute a prime electrode choice to develop FSCV from the ground.

Here, we used a Biologic VSP240 potentiostat running EC-LAB Express to run and produce high speed voltage ramps, CF $\mu$ E (100 $\mu$ m length, 10 $\mu$ m diameter, bought from World Precision Instrument, **Fig. 11**) were used as known electrodes, to test this setup expecting a known output. The molecular target for these preliminary tests was dopamine as it is the most referenced electroactive neurotransmitter in the literature.

Tests were realized in pH-controlled PBS (1X). pH was verified and if necessary rectified to 7.2 using 0.1M HCl or NaOH. The electrochemical cell used for these tests was constituted of three electrodes: the

microelectrode ( $\mu\text{E}$ ) as working electrodes (WE), a chlorinated silver wire ( $\text{Ag}/\text{AgCl}$ ) as a pseudo reference electrode (RE) and a Pt wire as a counter electrode (CE).

#### 4.3.2.1 First tests: high DA concentrations

To confirm that the commercial microelectrode used here can be used in FSCV, they must be able to reach a stable FSCV signature (called background current BC) with a given set of parameters: scan rate (SR), upper vertex potential (UVP), lower vertex potential (LVP), waveform frequency (WF) and rest potential ( $E_{\text{rest}}$ ).

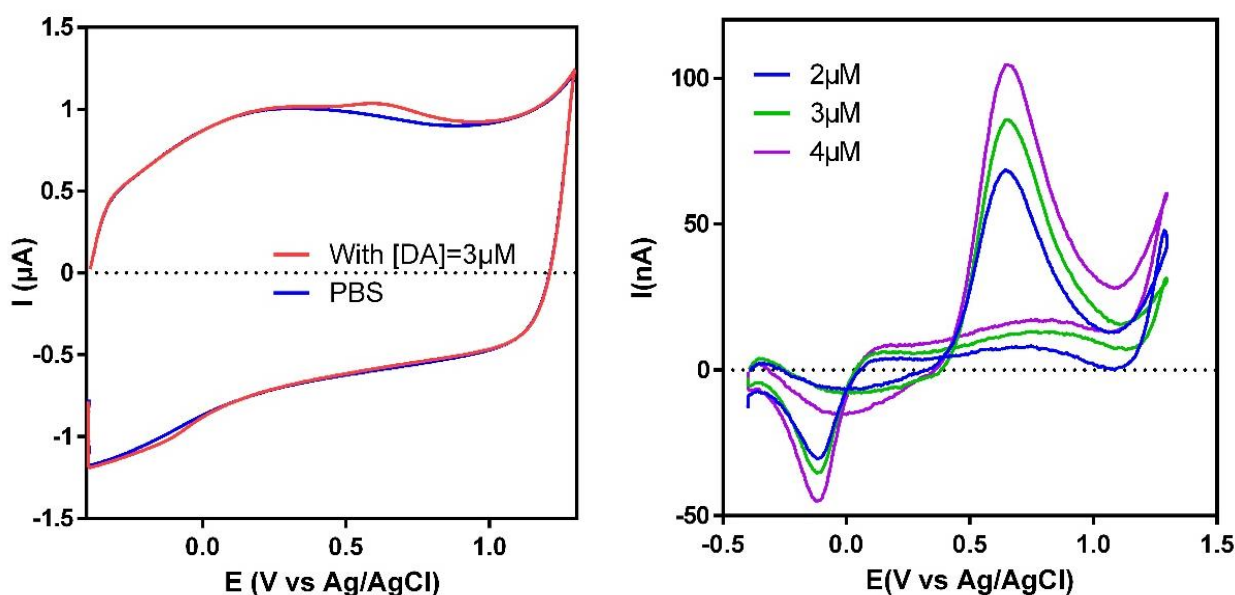


**Fig. 12:** FSCV electro detection of dopamine on carbon fiber microelectrodes (CF $\mu\text{Es}$ ). A) Voltammograms of a CF $\mu\text{E}$  in PBS (pH=7.2) without (blue trace) and with 3 $\mu\text{M}$  of dopamine (red trace), B) Background subtracted voltammograms of 2-4 $\mu\text{M}$  of dopamine in PBS (pH=7.2) on CF $\mu\text{Es}$  (FSCV parameters: scan rate=1200V/s, UVP=1.3, LVP=-0.4, WF=10Hz,  $E_{\text{rest}}$ =-0.4V).

Here, these parameters were first chosen accordingly to [32] with SR = 1200V/s, UVP = 1.3V, LVP = -0.4V, WF=10Hz and  $E_{\text{rest}}$  = -0.4V. Electrodes were cycled at least 20min to verify their intrinsic capability to reach a stable FSCV response with this set of parameters. Each electrode incapable to reach such stable profile was discarded. Before cycling, electrodes were soaked in unstirred VLSR isopropanol (IPA) for 20min and then rinsed by immersion in DIW for 2min. Electrodes were stored dry between tests. All neurotransmitters were freshly dissolved in PBS for measurement and these solutions were discarded after 20min. Neurotransmitters were injected in PBS to reach to desired concentration value for measurements.

Voltammograms were recorded using the VSP240 from Biologic, using a sampling time of 1 $\mu\text{s}$  (sampling frequency of 1MHz), to generate 2800 points during each cycle (lasting 2.833ms) without any hardware filtering. A home-written MATLAB code is used to subtract blank (Fig. 12A, blue trace) to measurement with dopamine (Fig. 12A, red trace) and obtain the typical dopamine redox signature on CF $\mu\text{Es}$  (Fig. 12B). This MATLAB code uses an interpolation to subtract accurate BC value at each point in measurements.



For the first tests, high concentrations of dopamine (compared to physiological concentrations of this molecule in the brain) in the  $\mu\text{M}+$  range were used to calibrate our setup and find adequate settings and conditions for reproducible detection. After background subtraction, the very well-known FSCV signature of dopamine on CF $\mu\text{E}$ s can be clearly seen, with a redox peak couple at around 0.75V and -0.1V respectively. This confirms the capability of our setup and our MATLAB code to generate usable background-subtracted voltammograms.

#### 4.3.2.2 Further calibration: physiological concentrations

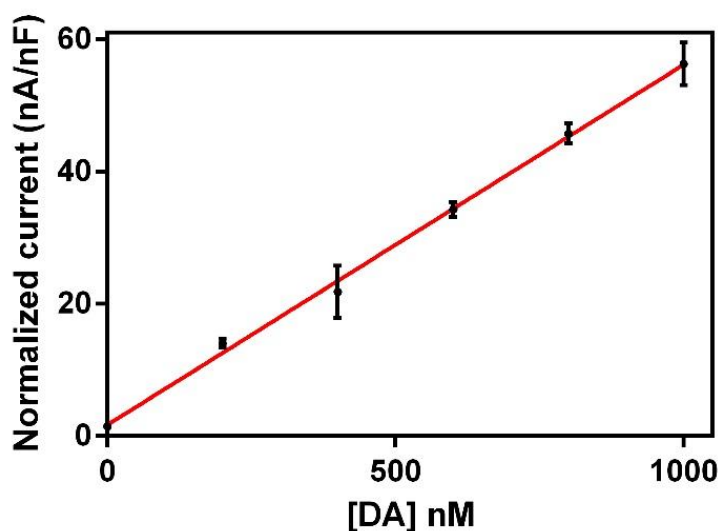


**Fig. 13: Calibration curve of FSCV electro detection dopamine on carbon fiber microelectrodes (N=3).** Current measured at the oxidation peak maximum and normalized by the integration of the current in the CF $\mu\text{E}$  voltammogram on the measured cycle. Dopamine concentrations: 200, 400, 600, 800 and 1000nM. Same FSCV parameters.  $R^2=0.9975$  and  $S=54.49$  nA/ $\mu\text{M}$ .

To obtain a valuable calibration of FSCV electro detection of dopamine with these electrodes, concentrations inferior to  $1\mu\text{M}$  must be detectable and calibrated. Hence, concentrations from 0 to  $1\mu\text{M}$  were tested with 200nM step, with three different electrodes. As CF $\mu\text{E}$ s are manually fabricated and manually trimmed to a certain length, which is thus variable, the currents observed were different. To compensate for this variation, these currents were normalized against the integral of the current in the CF $\mu\text{E}$ s CVs. This integral is roughly equivalent to a surface measurement, which allows to compensate for size difference of the electrodes. This way, the calibration curve presented in **Fig. 13** was obtained.

#### 4.3.2.3 First tests conclusions

The setup developed has been validated for FSCV measurements, giving results similar to already existing data in the literature in terms of dopamine FSCV signature and sensitivity.

The possibility to reach 1MHz in frequency sampling during FSCV measurements allows to obtain a high density of points for each voltammograms, leading to high fidelity BC subtraction through MATLAB interpolation.

## 4.4 PEDOT for FSCV: Validation and dopamine electrodedetection

### 4.4.1 Electrode requirement for FSCV

#### 4.4.1.1 Limitations of Carbon fiber microelectrodes

As FSCV was rising, electrodes requirements to perform FSCV were drawn out. From an electrochemical point of view, small CF $\mu$ Es (<10 $\mu$ m diameter) allow low RC constant, low background current/capacitance and negligible ohmic drop which make them adequate candidate for high speed scanning. Having low RC constant induced fast response time during cycling, limiting electronic lag. Having low background current/capacitance induces low electrochemical noise, which allows for better LOD. Finally, having low ohmic drop limits electrochemical distortion during cycling.

From a material point of view, the carbon constituting the CF $\mu$ Es is good material for FSCV electrode because of its edge planes and defects, responsible of surface electron exchange, and oxygen functions, responsible for analyte adsorption like dopamine for example. And even though these electrodes have been used for decades, some analytical challenges are still remaining:

- 1) Sensitivity: blocked in the low nanomolar range, which is not enough for neuropeptides for example;
- 2) Selectivity: many neurotransmitters have similar CVs (same electroactive moieties like DA, Nor, DOPAC and epinephrine) or similar peak potentials (H<sub>2</sub>O<sub>2</sub>, Adenosine, Histamine)
- 3) Fouling and etching: CF $\mu$ Es are easily fouled by biological species during experiments if not cycled at high UVP, which in return induces electrode etching.
- 4) Temporal resolution: most experiments are capped to 10Hz max as WF, due to the signal being too low at higher WF (time allowed for analyte adsorption too low).

#### 4.4.1.2 Translation to PEDOT requirements to perform FSCV

By analogy with the requirements for FSCV on CF $\mu$ Es presented just before, here are their translation to PEDOT-modified microelectrodes. To perform FSCV on PEDOT coatings, one must:

- 1) Lower the capacitance of the electrode by both having an optimal dopant/EDOT moieties ratio in the polymer and an adequate deposition charge (to tailor the electrode thickness). [\[32\]](#) . This will lower the noise (and the LOD) and allow for good BC subtraction.

- 2) Keep low diffusion times [33, 34], this implies to keep coating thin and uniform to prevent molecules and ions diffusion in the coating (trapping effect that will create electrodedetection artifacts) while also keeping the electronic lag (and thus the electrode response time) low.
- 3) Keep the UVP at an adequate value to prevent electrode damaging [32, 35] during cycling.
- 4) Keep the scan rate at a value where the coating resistance is low enough [35] to be used.

In regards of these requirements and as said before, CV-modified microelectrodes were not tested in FSCV as their charge storage and spatial footprint is too high to get a FSCV signature leading to a SNR possibly usable for electrodedetection of low concentrations (and so low currents) of neurotransmitters.

As CP-modified microelectrodes have a controllable thickness due to control over deposition charge/time, two types of electrodes were tested (with deposition charge of 1200nC and 80nC respectively) to verify that the electrodes described in Chapters II & III are not already meeting the requirements described before, particularly in terms of thickness/electronic lag. 80nC was chosen as the minimal deposition charge to obtain viable electrodes, while reducing a lowest value possible the deposition charge, after try-and-error method. This is meant to reduce at the maximum the electronic lag of these electrodes during FSCV.

## 4.4.2 In-vitro calibration of FSCV on PEDOT-modified electrodes

### 4.4.2.1 Methodology

There is only a small number of publications treating of FSCV on PEDOT microelectrodes, with multiple configurations (different PEDOT dopants from Nafion to rGO, different deposition techniques, etc.). Most of these are featuring PEDOT-modified CF $\mu$ Es, the electrode used before for dopamine detection in this chapter. This configuration is difficult to relate to the one presented in this manuscript (PEDOT deposited on a planar gold microelectrode) as CF $\mu$ Es are inherently capable, in their bare state, to perform neurotransmitters detection.

To overcome this issue, advantage was taken of part of the methodology already published by Vreeland [32], as it is the only totally relevant reference on PEDOT-modified electrodes to compare our electrode with (PEDOT on gold microelectrodes) even though it presents multiple differences (PEDOT deposited by vapor phase deposition vs electrochemical deposition, band vs circular microelectrodes).

The electrochemical methodology followed consisted in the following steps: verification that electrodes could reach a stable FSCV response without analytes by cycling them for 20min, FSCV measurements with ferrocene and then with dopamine (DA). Finally, a calibration study is completed to obtain sensitivity of the electrodes.

### 4.4.2.2 Stable FSCV signature

As for CF $\mu$ Es, to confirm that PEDOT-modified microelectrode can be used in FSCV, they must be able to reach a stable FSCV signature (the background current). Here, these parameters were first chosen accordingly

to [32] with SR=100V/s, LVP = -0.4 V, WF=1Hz and  $E_{\text{rest}} = -0.4$  V, except the UVP chosen to be equal to 0.5V to prevent electrode degradation.  $E_{\text{rest}}$  was kept at -0.4V for all results presented after.

Same than for CF $\mu$ Es, electrodes were soaked in VLSR IPA and rinsed in DIW before cycling. Electrodes were cycled at least 20min to verify their intrinsic capability to reach a stable FSCV response with this set of parameters.

First, the electrodes electron transfer properties were studied, using a ferrocene-based probe. Then, detection of dopamine was tried on these electrodes.

#### 4.4.2.3 Fast electron transfer evaluation with Ferrocene-methanol

Detection of ferrocene-methanol (FcMeOH) with the parameters described just before was first tested. This test was meant to verify that PEDOT-modified microelectrodes were capable to perform rapid faradaic transfers with a known electrochemically-active molecule. Electrodes BC were measured in PBS (pH=7.2) like specified before and then, the media was changed to PBS containing 1mM FcMeOH and the FSCV signature of both was recorded. The same MATLAB code was used to subtract the BC to the measurement with FcMeOH. The obtained subtracted-voltammograms (SVs) are displayed in Fig. 14A for 1200nC electrodes and **Fig. 14 A&B** for 80nC.

Artifacts at switching potentials (after UVP and LVP, shaped as sharp peaks) come from the MATLAB code used to obtain subtracted voltammograms and will be the subject of future optimisation of this code to remove them. Even though, the SVs clearly display the typical reversible redox peak couple attributed to ferrocene-based probes, showing the possibility to perform electrodedetection based on fast electron transfers.

Lower peak separation was observed on 80nC deposits compared to 1200nC ones, meaning the overpotential appearing on these deposits during redox reaction of FcMeOH are lower due to lower electronic lag during electron transfer. This is consistent with a thinner, less capacitive electrode.

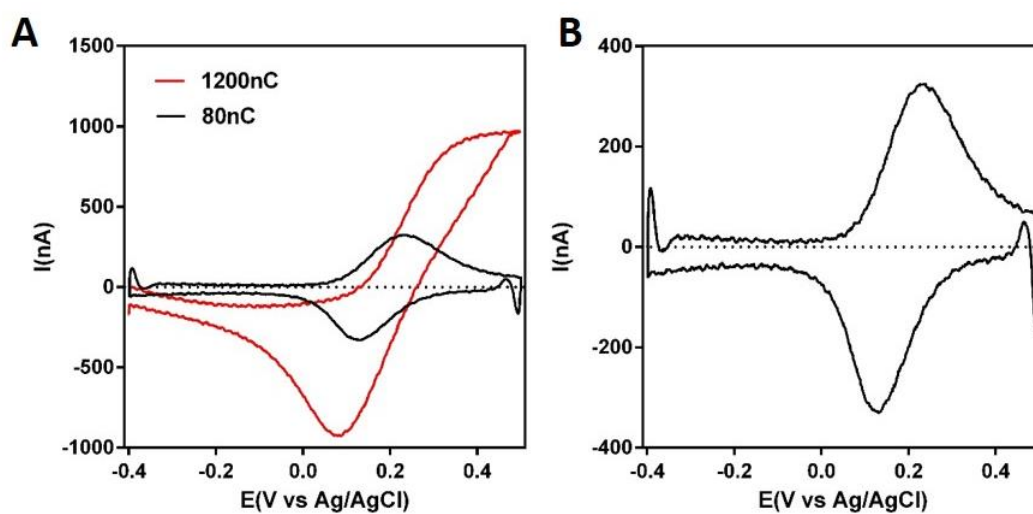


**Fig. 14: FSCV electrodedetection of FcOH on PEDOT-PSS microelectrodes.** Background subtracted voltammograms of 1mM FcOH in PBS (pH=7.2) on PEDOT-PSS deposited on gold microelectrodes (20 $\mu$ m-diameter) by chronopotentiometry at 3.14nA with a deposition charge of A) 1200nC (red trace) and 80nC (black trace) and B) 80nC only.

However, less current is measured on 80nC electrodes compared to their 1200nC counterparts (300nA vs 1000nA), which is also consistent with the charge difference, as the 80nC electrodes have a lower surface and so a lower electrochemically active surface.

Hence, according to the objective balance targeted between sensitivity and selectivity, the right value for the charge deposition should be explored.

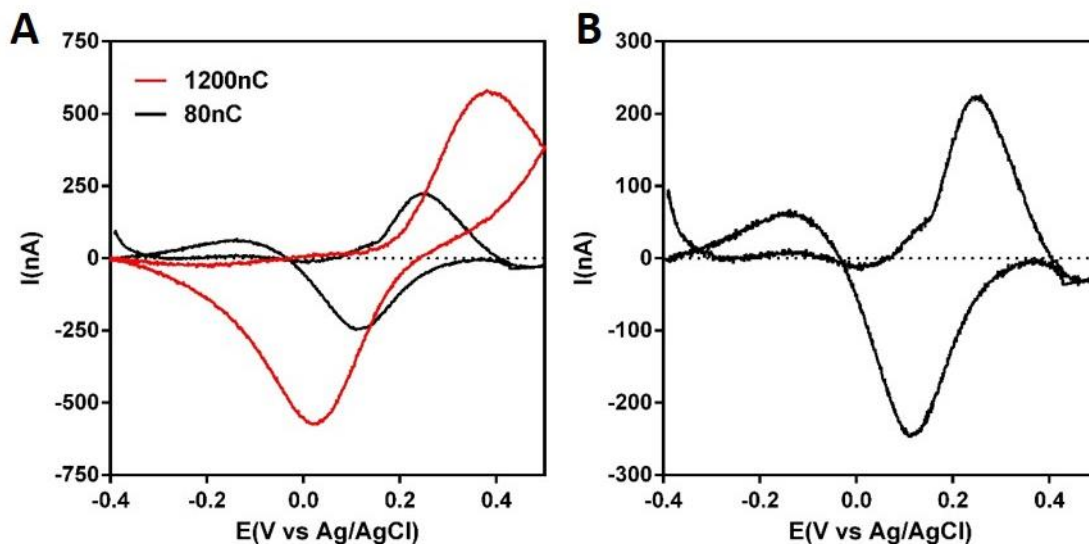


**Fig. 15: FSCV electrodedetection of FcOH on PEDOT-CNF microelectrodes.** Background subtracted voltammograms of 1mM FcOH in PBS (pH=7.2) on PEDOT-CNF deposited on gold microelectrodes (20 $\mu$ m-diameter) by chronopotentiometry at 3.14nA with a deposition charge of A) 1200nC (red trace) and 80nC (black trace) and B) 80nC only.

In the same conditions, PEDOT-CNF also displayed the typical ferrocene signature (**Fig. 15A**). The same trends can be observed in terms of peak separation and current when compared with PEDOT-PSS microelectrodes, with lower peak separation and current on PEDOT-CNF (80nC, **Fig. 15B**) than on PEDOT-CNF (1200nC).

However, as can be seen in **Fig. 14A** (red trace) the oxidation peak of FcMeOH was incomplete on PEDOT-PSS (1200nC), it would be interesting to increase the UVP of the FSCV waveform to at least 0.6V, to increase peak definition. To verify that this UVP increase could be done without degrading the electrodes (PEDOT is very sensitive to oxidation by potential manipulation), study of BC stability was realized by successively cycling electrodes for 20min with an increasing UVP (0.1V step). All microelectrodes could withstand a UVP of up to 0.9V at 100V/s. At higher UVP, the BC starts slowly degrading, without reaching a stable profile. Thus, these data show that a UVP of 0.6V could be used for further FSCV experiments to improve peak definition.

#### 4.4.2.4 FSCV electrodedetection of dopamine on PEDOT-PSS

On a second hand, detection of dopamine was tested with the same FSCV parameters, setup and protocol except that the concentration and UVP were set to 100 $\mu$ M DA and 0.6V respectively to match other work published [32].

It is important to note that dopamine is a very reactive molecule, that polymerizes with itself very quickly in basic media and/or under UV exposure. Even at pH=7.2 (neutral physiological condition), a concentrated solution of DA in PBS will darken quickly (around 20 min for mM ranged concentrations).

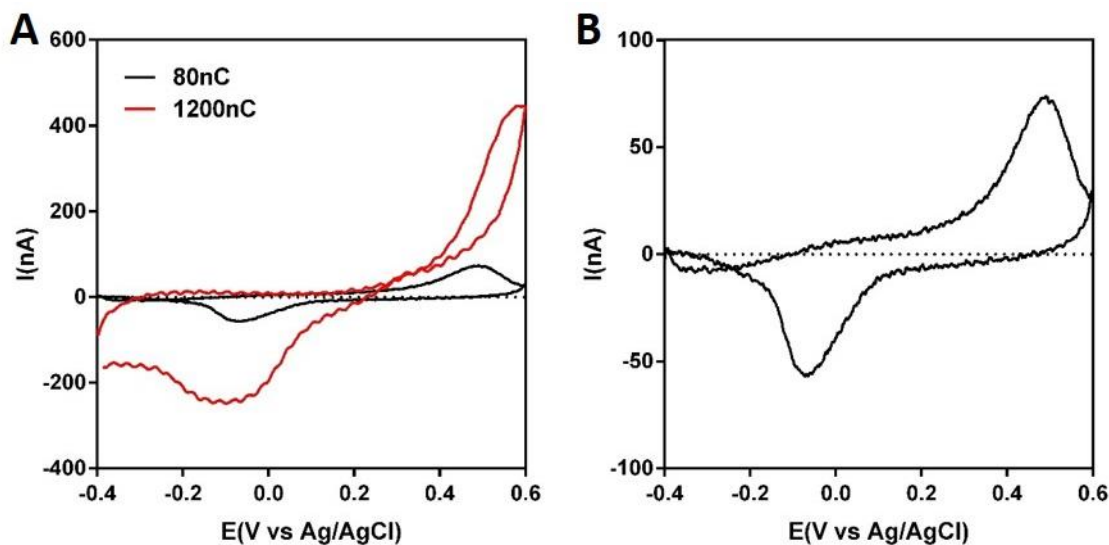


**Fig. 16: FSCV electrodedetection of DA on PEDOT-PSS microelectrodes.** Background subtracted voltamograms of 100 $\mu$ M DA in PBS (pH=7.2) on PEDOT-CNF deposited on gold microelectrodes (20 $\mu$ m-diameter) by chronopotentiometry at 3.14nA with a deposition charge of A) 1200nC (red trace) and 80nC (black trace) and B) 80nC only.

Dopamine on PEDOT-PSS microelectrodes displayed a coherent FSCV signature with a couple of redox peaks on both microelectrode types. However, the oxidation peak detected at 0.596V (**Fig. 16A**, red trace) on PEDOT-PSS (1200nC) is incomplete and very close to the UVP set at 0.6V. A wide reduction peak centered at -0.106V is also observed. On the other hand, a clearly defined couple of peaks is observed on PEDOT-PSS (80nC) at 0.507V and -0.072V, though the current measured is lower (**Fig. 16B**). These observations tend to show that the redox reactions of DA are more difficult on the first electrode type than on the second one, with a peak separation of 702mV vs 579mV, which is coherent with the electrode being thinner, less capacitive and developing less electronic lag/overpotentials. New tests with higher UVP to obtain a complete FSCV signature (complete peaks) will be performed in further studies.

#### 4.4.2.5 FSCV electrodedetection of dopamine on PEDOT-CNF

Following the behaviour of dopamine on the PEDOT-CNF microelectrodes did not deviate in terms of trend compared with PEDOT-PSS: i) Higher peak separation on PEDOT-CNF (1200nC) than on PEDOT-CNF (80nC) with 516mV vs 362mV respectively, ii) Higher current on PEDOT-CNF (1200nC) than on PEDOT-CNF (80nC) with 1170nA vs 346nA.

Even though, several differences can be observed between PEDOT-PSS and PEDOT-CNF  $\mu$ Es. The DA oxidation peak on PEDOT-CNF (1200nC) was not complete, it was still a little further away from the UVP

(Fig. 17A, red trace). The DA reduction peak on the other hand was sharper than on PEDOT-PSS (1200nC), with broad base, which would tend to show the DA oxidation products (dopamine quinone DQ) reduction is slower than its oxidation. This is not true on PEDOT-CNF (80nC), which displays a couple of well-defined peaks (Fig. 17B), with the oxidation and reduction peak respective width much smaller.

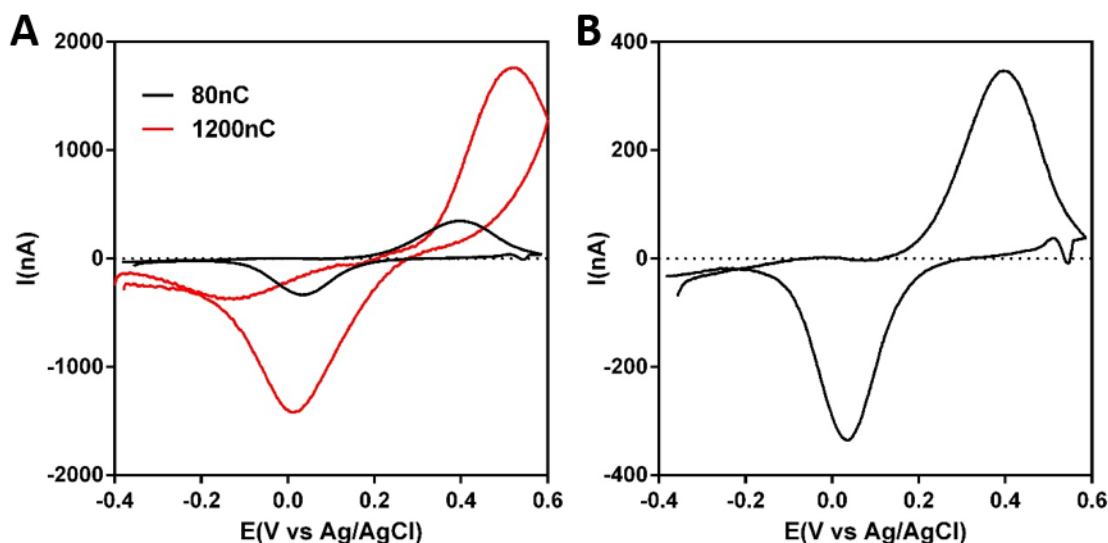


**Fig. 17: FSCV electrodetectors of DA on PEDOT-CNF microelectrodes.** Background subtracted voltammograms of 100 $\mu$ M DA in PBS (pH=7.2) on PEDOT-CNF deposited on gold microelectrodes (20 $\mu$ m-diameter) by chronopotentiometry at 3.14nA with a deposition charge of A) 1200nC (red trace) and B) 80nC only.

Unfortunately, no calibration could be realized with these parameters/electrodes due to lack of time from CoVid-19 crisis, lockdowns and experimental time restrictions.

#### 4.4.2.6 Performance comparison

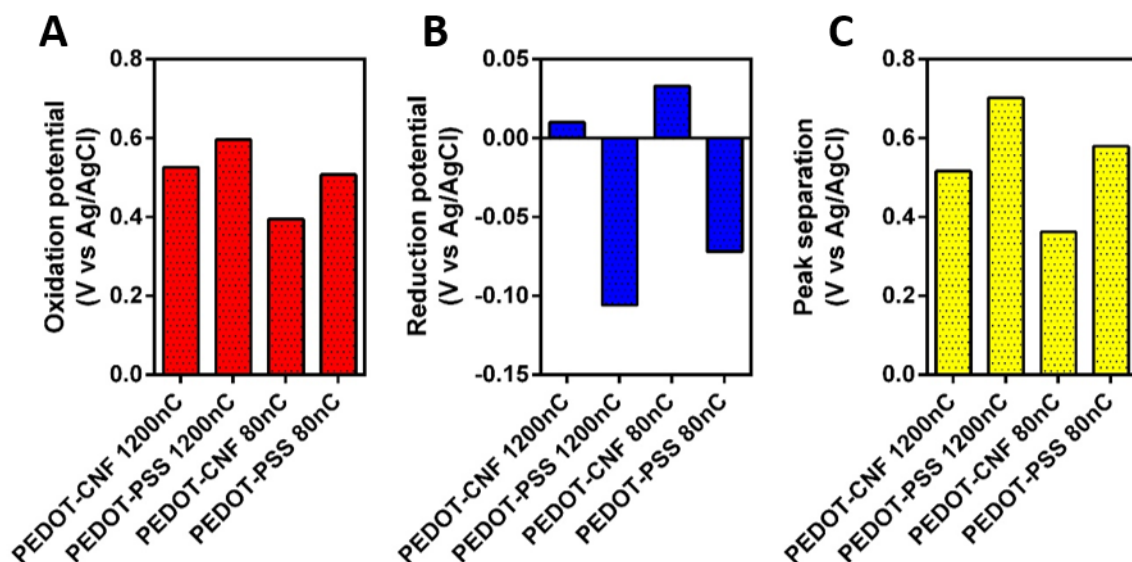


**Fig. 18: Dopamine peak separation on PEDOT-PPS and PEDOT-CNF microelectrodes.** A) Oxidation potential and B) Reduction potential of dopamine on the different types of microelectrodes, detected at the peak maximum. C) Total peak separation on the different types of microelectrodes.

Compared to PEDOT-PSS, the PEDOT-CNF microelectrodes displayed lower peak separation (**Fig. 18C**) and higher current (**Fig 19**) than their PEDOT-PSS counterparts. A 29.8% peak separation reduction was realized by decreasing the deposition charge from 1200nC to 80nC for PEDOT-CNF while it produced a lower reduction of 17.5% with PEDOT-PSS.

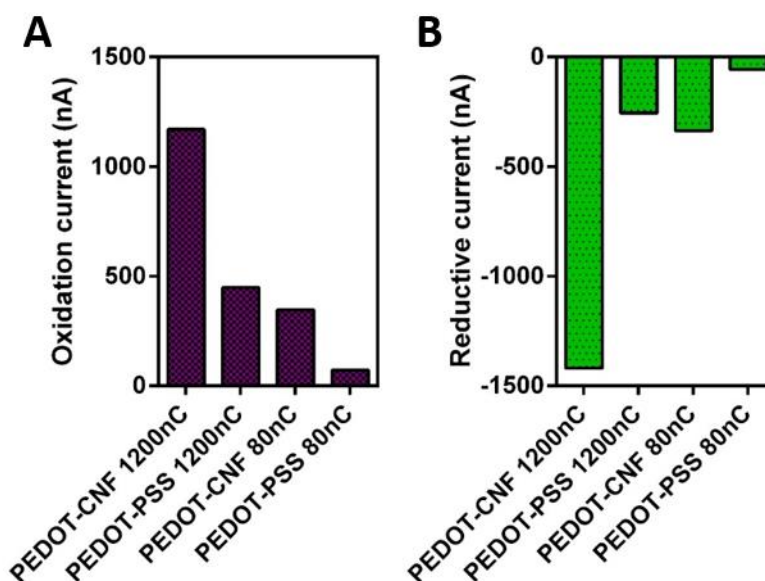


**Fig. 19: Dopamine redox currents on PEDOT microelectrodes.** A) Oxidation currents and B) Reduction currents of dopamine on the different types of microelectrodes, detected at the peak maximum.

Finally, PEDOT-CNF 80nC displayed current in the same order of magnitude of PEDOT-PSS 1200nC, showing the higher surface electro-activity compared to PSS (**Fig. 19**).

#### 4.4.2.7 Conclusions & Comparison for FSCV electrodedetection

We demonstrated the possibility to use FSCV on PEDOT-modified planar microelectrodes, on both PEDOT-PSS and PEDOT-CNF. PEDOT

As this technology is MEA-compatible, it opens the way to realizing FSCV on multiple coplanar electrodes on the same device, like MEAs or implants fabricated in clean room. This will lead to simultaneous multisite FSCV electrodedetection of neurotransmitters both in-vitro and in-vivo at the single-cell level, which is currently impossible with CF $\mu$ Es. Even though some software platforms are available and array-compatible [36], FSCV on arrays is still a challenge to realize, particularly in terms of construction of FSCV-compatible arrays. This also opens a new array of possible electrodes, that can be used for neural interfacing, stimulation and CA or FSCV electrodedetection of neurotransmitters. Moreover, the use of electrodeposited PEDOT to create these electrodes allows a high degree of modularity, in terms of dopant, electrode surface, electrode surface chemistry etc. allowing for electrode engineering.

Even though, due to the Covid crisis, it was impossible to realize a complete calibration of dopamine detection which prevents a total comparison with the literature. However, it is possible to extrapolate a sensitivity out of the data presented before, that will need to be confirmed in further studies. These results are gathered in **Table 4**, for comparison matters.



Ref	Material	Base $\mu E$	Protocol	Target	Sensitivity
LAAS	PEDOT-PSS*	Au 20 $\mu m$ - $\emptyset$	100V/s, -0.4 to 0.6V, 1Hz	DA	0.713 <sup>a</sup> or 4.49 <sup>a</sup> nA/ $\mu M$
LAAS	PEDOT-CNF* <sup>2</sup>	Au 20 $\mu m$ - $\emptyset$			3.46 <sup>a</sup> or 11.7 <sup>a</sup> nA/ $\mu M$
[32]	PEDOT:OTs* <sup>3</sup>	Au 150x50 $\mu m$	100V/s, -400mV to 0.6V, 1Hz	DA	3.7 nA/ $\mu M$
[37]	PEDOT-Nafion	CF $\mu Es$	400V/s, -0.4 to 1.3V, rest at -0.4V, 10Hz	DA	46 nA/ $\mu M$
[35]	PEDOT:ClO <sub>4</sub> * <sup>4</sup>	Pt 50 $\mu m$ - $\emptyset$	100V/s, -0.2 to 1.1V, rest at -0.2V, 10Hz	DA	1.5 nA/ $\mu M$
[34]	PEDOT:GrO* <sup>5</sup>	CF $\mu Es$ 7 $\mu m$ - $\emptyset$ L=400 $\mu m$	400V/s, from 0 to 1V, down to -0.5V back to 0V. 10Hz	DA	50nA/ $\mu M$
*PSS=PolyStyreneSulfonate    * <sup>2</sup> CNF=Carbon nanofiber    * <sup>3</sup> OTs=Tosylate    * <sup>4</sup> ClO <sub>4</sub> =Chlorate * <sup>5</sup> GrO=Graphene Oxide <sup>a</sup> =sensitivity extrapolated from the current described before					

**Table 4: Comparison of the PEDOT-modified microelectrodes with other microelectrodes from the literature used for FSCV electro-detection in terms of material, base microelectrode, FSCV protocol and sensitivity, all detecting dopamine.**

Based on this extrapolation in **Table 4**, it can be seen that the performance of the PEDOT-microelectrodes presented in this manuscript are either comparable or better than other coplanar PEDOT-microelectrodes used with FSCV, developed by Heien *et al.* (PEDOT:OTs on gold [32] or PEDOT:ClO<sub>4</sub> on platinum [35]).

When compared to CF $\mu Es$ -based PEDOT microelectrodes developed by Heien *et al.* (PEDOT-Nafion on CF $\mu Es$ ) and Cui *et al.* (PEDOT:GrO on CF $\mu Es$ ), these display better sensitivity, 5 to 10 times higher, due to their higher surface and cylindrical shape. Also, the use of higher UVP and scan rates encounters for part of these better performances.

For comparison sakes, the performance of our PEDOT-microelectrodes could be enhanced by using higher scan rates, higher UVP, allowing to bridge their performances with those of the CF $\mu E$ -based microelectrodes. Hence our microfabricated microelectrodes are well placed in the literature against other PEDOT-modified microelectrodes.

## 4.5 Conclusion for multifunctionality and perspectives

This chapter proves the capacity of PEDOT-CNF microelectrodes (deposited by CP) to electro-detect dopamine through a relevant combination of techniques (CA and FSCV) for in-vivo monitoring. On top of this capability to electro-detect dopamine in-vitro, these CP-deposited PEDOT-CNF electrodes showed in Chapter III a well-placed mix of performances (impedance, charge storage and CIL).

The proof-of-concept of this functionality combination makes them promising multifunctional electrodes for multi-level bidirectional neural interfacing and monitoring. These electrodes are compared to other relevant references of multifunctional materials in **Table 5**.

<i>Ref</i>	<i>Geometric area (<math>\mu\text{m}^2</math>)</i>	<i>Material</i>	<i>Impedance (<math>M\Omega \cdot \mu\text{m}^2</math>)</i>	<i>CIL (<math>\text{mC}/\text{cm}^2</math>)</i>	<i>Potential (mV)</i>	<i>Sensitivity (<math>\text{pA}/\text{nM} \cdot \mu\text{m}^2</math>)</i>
[2]	7068583	CNTs	NA	NA	-50	46.053
[3]	380	Pt-rGo	53899	NA	150	1.698
[4]	314	PtNPs-Nafion	3454	NA	500	43.95
[5]	5000	Ox-PPy	NA	NA	700	325
[6]	450	Pt-Nafion	724.95	NA	500	22.31
LAAS	314	PEDOT-CNF	1.287	10.11	130	44.54

**Table 5: Comparison of the multifunctionality performances of our CP-modified microelectrodes against relevant literature references, in terms of geometric microelectrode area, impedance, CIL and electrodedetection performances of dopamine by chronoamperometry represented by detection potential and normalized sensitivity.**

#### 4.5.1.1 Perspectives for FSCV at PEDOT microelectrodes

On a first hand, the PEDOT-CNF microelectrodes have to be placed among newly-developed microelectrodes for FSCV [1] which are meant to tackle the new challenges in FSCV. These are some of these challenges in FSCV that have been pinpointed recently: i) Measurement in nm-sized discrete regions using nanoelectrodes (Flame-etched CF $\mu$ E's capable of monitoring individual vesicular exocytosis at a single synapse by amperometry), ii) Multisite measurements, with several of producing carbon MEAs have been reported (PPF, multiple CF $\mu$ E's assembled in MEA), iii) Coupling with other techniques.

How the PEDOT-CNF electrodes answer these challenges? The PEDOT-modified microelectrodes allow multisite FSCV without CF $\mu$ E assembly or pyrolysis during microfabrication, which make them flexible device-compatible. As PEDOT can be doped with a wide array of molecules, like antibody, aptamers, etc. allowing to deploy different interactions for molecular detection. The only downside of these electrodes in regards of these challenges is their inherent incompatibility with diameters needed to match CF $\mu$ E and diamond nanoelectrodes, as the CNFs have length and diameters that are not compatible with such dimensions.

On a second hand, the work presented in this chapter about FSCV used specific FSCV parameters (extracted from literature). A lot of work remains to bridge these results with FSCV on CF $\mu$ E's and bring them at the same level of knowledge and applicability:

##### 1) FSCV with a higher scan rate/wider potential window/lower DA concentration

In the presented results, scan rate was kept at 100V/s, which is the bare minimum to consider being in FSCV territory. However, publications with SR up to 2400V/s have been published and showed the interest to reach these higher SR, to improve sensitivity and LOD, while generating a higher background current that will have to be efficiently subtracted. This approach would have to consider the higher electrochemical stress applied to the electrode that would possibly lead to delamination, as observed with stimulation. Also, FSCV with a wider window would be an interesting technique to explore, as more compounds of interest could be targeted,

with better peak resolution. However, the electrodes would have to withstand FSCV on this wider window, without degradation of their electrochemical signature. Finally, the electrodes performances in FSCV were tested only at 100 $\mu$ M DA, which is a concentration much higher than the one encountered in the brain. Concentrations would have to decrease to the 0-1 $\mu$ M range to be representative of in-vivo conditions. Preliminary tests have been conducted in these directions and are presented in **Annex 7**.

## 2) FSCV in biomimetic media containing interferents

Another aspect to explore before translating the results presented in more relevant conditions for in-vivo FSCV would be to test the influence of common interferents like DOPAC, Ascorbic Acid, Uric Acid, etc. on the performances presented in FSCV.

These molecules are known to be present with concentration ratio 100 to 1000 to neurotransmitters like DA, and their possible interference with target molecules must be carefully considered. Multiple strategies have already been published to take into account their interference, through charge exclusion using Nafion [[3](#), [38](#), [39](#)] for example.

## 3) FSCV in brain slices

Finally, these electrodes will be tested in brain slices for electrodedetection. As the implants microfabricated in LAAS clean room have already been used for electrophysiology, they would be redesigned to have 20 $\mu$ m-diameter and used in such experiments. They will be modified using the same protocol described all along this manuscript. A particular care to the electrochemical cell used for these experiments, as they are usually conducted with an Ag/AgCl reference that drifts overtime and is toxic [[40](#)].

1. Puthongkham, P. and B.J. Venton, *Recent advances in fast-scan cyclic voltammetry*. *Analyst*, 2020. **145**(4): p. 1087-1102.
2. Wooten, M. and W. Gorski, *Facilitation of NADH Electro-oxidation at Treated Carbon Nanotubes*. *Anal Chem*, 2010. **82**: p. 1299-1304.
3. Yang, L., et al., *A Platinum/reduced Graphene Oxide nanocomposites modified Nafion coated implantable microelectrode array intent on neural dopamine and electrophysiological recordings*. 8th International IEEE EMBS Conference on Neural Engineering, 2017: p. 227-230.
4. Zhang, S., et al., *Real-time simultaneous recording of electrophysiological activities and dopamine overflow in the deep brain nuclei of a non-human primate with Parkinson's disease using nano-based microelectrode arrays*. *Microsystems & Nanoengineering*, 2018. **4**: 17070.
5. Tseng, T.T. and H.G. Monbouquette, *Implantable Microprobe with Arrayed Microsensors for Combined Amperometric Monitoring of the Neurotransmitters, Glutamate and Dopamine*. *J Electroanal Chem (Lausanne)*, 2012. **682**: p. 141-146.
6. Johnson, M.D., et al., *Implantable microelectrode arrays for simultaneous electrophysiological and neurochemical recordings*. *J Neurosci Methods*, 2008. **174**(1): p. 62-70.
7. Wei, W., et al., *An implantable microelectrode array for simultaneous L-glutamate and electrophysiological recordings in vivo*. *Microsystems & Nanoengineering*, 2015. **1**(1).
8. Wang, L., et al., *A microelectrode array electrodeposited with reduced graphene oxide and Pt nanoparticles for norepinephrine and electrophysiological recordings*. *Journal of Micromechanics and Microengineering*, 2017. **27**(11): 115001.
9. Samba, R., et al., *Application of PEDOT-CNT Microelectrodes for Neurotransmitter Sensing*. *Electroanalysis*, 2014. **26**(3): p. 548-555.
10. Keithley, R.B., et al., *Higher sensitivity dopamine measurements with faster-scan cyclic voltammetry*. *Anal Chem*, 2011. **83**(9): p. 3563-71.
11. A. Hermans, R.B.K., J.M. Kita, L.A. Sombers, and R. Mark Wightman, *Dopamine Detection with Fast-Scan Cyclic Voltammetry Used with Analog Background Subtraction*, *Analytical Chemistry*, 2008. **80**(11): p. 4040-4048.
12. Michael, D., E.R. Travis, and R.M. Wightman, *Color Images for Fast-Scan CV*. *Analytical Chemistry News & Features*, 1998: p. 586-592.
13. Schmidt, A.C., et al., *Multiple scan rate voltammetry for selective quantification of real-time enkephalin dynamics*. *Anal Chem*, 2014. **86**(15): p. 7806-12.
14. Park, J., P. Takmakov, and R.M. Wightman, *In vivo comparison of norepinephrine and dopamine release in rat brain by simultaneous measurements with fast-scan cyclic voltammetry*. *J Neurochem*, 2011. **119**(5): p. 932-44.
15. Roberts, J.G., et al., *In situ electrode calibration strategy for voltammetric measurements in vivo*. *Anal Chem*, 2013. **85**(23): p. 11568-75.
16. Johnson, J.A., C.N. Hobbs, and R.M. Wightman, *Removal of Differential Capacitive Interferences in Fast-Scan Cyclic Voltammetry*. *Anal Chem*, 2017. **89**(11): p. 6166-6174.
17. DeWaele, M., et al., *A baseline drift detrending technique for fast scan cyclic voltammetry*. *Analyst*, 2017. **142**(22): p. 4317-4321.
18. Dengler, A.K. and G.S. McCarty, *Microfabricated Microelectrode Sensor for Measuring Background and Slowly Changing Dopamine Concentrations*. *J Electroanal Chem (Lausanne)*, 2013. **693**: p. 28-33.
19. *Supporting information : Drift Subtraction for FSCV Using Double-Waveform Partial-Least-Squares Regression*.
20. Meunier, C.J., G.S. McCarty, and L.A. Sombers, *Drift Subtraction for Fast-Scan Cyclic Voltammetry Using Double-Waveform Partial-Least-Squares Regression*. *Anal Chem*, 2019. **91**(11): p. 7319-7327.
21. Heien, M.L., et al., *Overoxidation of carbon-fiber microelectrodes enhances dopamine adsorption and increases sensitivity*. *Analyst*, 2003. **128**(12): p. 1413-9.
22. Swamy, B.E.K. and B.J. Venton, *Subsecond Detection of Physiological Adenosine Concentrations Using Fast-Scan Cyclic Voltammetry*. *Anal Chem*, 2007. **79**: p. 744-750.
23. Hobbs, C.N., et al., *An implantable multimodal sensor for oxygen, neurotransmitters, and electrophysiology during spreading depolarization in the deep brain*. *Analyst*, 2017. **142**(16): p. 2912-2920.
24. Cryan, M.T. and A.E. Ross, *Scalene Waveform for Codetection of Guanosine and Adenosine Using Fast-Scan Cyclic Voltammetry*. *Anal Chem*, 2019. **91**(9): p. 5987-5993.

25. Rodeberg, N.T., et al., *Construction of Training Sets for Valid Calibration of In Vivo Cyclic Voltammetric Data by Principal Component Analysis*. Analytical Chemistry, 2015. **87**(22): p. 11484-11491.
26. Johnson, J.A., N.T. Rodeberg, and R.M. Wightman, *Failure of Standard Training Sets in the Analysis of Fast-scan Cyclic Voltammetry Data*. ACS Chem Neurosci, 2016.
27. Henao-Escobar, W., et al., *Resolution of quaternary mixtures of cadaverine, histamine, putrescine and tyramine by the square wave voltammetry and partial least squares method*. Talanta, 2015. **143**: p. 97-100.
28. Johnson, J.A., et al., *Multivariate Curve Resolution for Signal Isolation from Fast-Scan Cyclic Voltammetric Data*. Anal Chem, 2017. **89**(19): p. 10547-10555.
29. Heien, M.L.A.V., M.A. Johnson, and R.M. Wightman, *Resolving Neurotransmitters Detected by Fast-Scan Cyclic Voltammetry*. Anal. Chem., 2004. **76**: p. 5697-5704.
30. Oh, Y., et al., *Monitoring In Vivo Changes in Tonic Extracellular Dopamine Level by Charge-Balancing Multiple Waveform Fast-Scan Cyclic Voltammetry*. Anal Chem, 2016. **88**(22): p. 10962-10970.
31. Lama, R.D., et al., *Ultrafast detection and quantification of brain signaling molecules with carbon fiber microelectrodes*. Anal Chem, 2012. **84**(19): p. 8096-101.
32. Meier, A.R., et al., *Rapid Voltammetric Measurements at Conducting Polymer Microelectrodes Using Ultralow-Capacitance Poly(3,4-ethylenedioxythiophene):Tosylate*. Langmuir, 2016. **32**(32): p. 8009-18.
33. Taylor, I.M., et al., *Direct in Vivo Electrochemical Detection of Resting Dopamine Using Poly(3,4-ethylenedioxythiophene)/Carbon Nanotube Functionalized Microelectrodes*. Anal Chem, 2019. **91**(20): p. 12917-12927.
34. Taylor, I.M., et al., *Enhanced dopamine detection sensitivity by PEDOT/graphene oxide coating on in vivo carbon fiber electrodes*. Biosens Bioelectron, 2017. **89**(Pt 1): p. 400-410.
35. Meier, A.R., *PEDOT Electrodes for Improving Multiple Facets of Neurochemical Measurements*, in *Department of chemistry and biochemistry*. 2017, University of Arizona.
36. Bucher, E.S., et al., *Flexible software platform for fast-scan cyclic voltammetry data acquisition and analysis*. Anal Chem, 2013. **85**(21): p. 10344-53.
37. Vreeland, R.F., et al., *Biocompatible PEDOT:Nafion composite electrode coatings for selective detection of neurotransmitters in vivo*. Anal Chem, 2015. **87**(5): p. 2600-7.
38. S. Demuru, H.D., *Surface PEDOT:Nafion Coatings for Enhanced Dopamine, Serotonin and Adenosine Sensing*. Journal of The Electrochemical Society, 2017. **164**(14): p. G129-G138.
39. Yanga, L., et al., *A Platinum/reduced Graphene Oxide nanocomposites modified Nafion coated implantable microelectrode array intent on neural dopamine and electrophysiological recordings*, 8th International IEEE EMBS Conference on Neural Engineering, 2017.
40. Hashemi, P., et al., *Chronically Implanted, Nafion-Coated Ag/AgCl Reference Electrodes for Neurochemical Applications*. ACS Chem Neurosci, 2011. **2**(11): p. 658-666.

# *Conclusions and Perspectives*

## **Outcome of the thesis**

The detection of neurochemical signals constitutes an important complementary source to electrophysiological signals, to correlate these two linked signals and study their interaction help study both the healthy and diseased brain. This would mark a new major step forward for neuroscience and help advance treatment research for neurological disorders like epilepsy and neurodegenerative diseases like Parkinson's or Alzheimer's.

To realize this, it is necessary to achieve easy widespread access to combined electrophysiology and neurochemical detection, thus it is necessary to have electrodes capable of both without sacrificing performances on both brain study modes. To answer this unmet need, we proposed to combine electrophysiological recording with neurotransmitter electro detection at the single-electrode level.

In this thesis, this is realized by a first-time demonstration of deposition of CNFs on microelectrodes through co-electrodeposition with PEDOT. These PEDOT-CNF microelectrodes proved to be multifunctional electrodes, capable of in-vitro low impedances and high charge injection limit. These electrodes also showed the capacity to electro detect dopamine, a key neurotransmitter, in-vitro through a combination of two complementary techniques: chronoamperometry, which lack selectivity but allow to follow sub-millisecond concentrations transients, and fast-scan cyclic voltammetry, which is limited to 10Hz sampling (in this thesis) but have high sensitivity and high selectivity.

On top of these properties, these electrodes display a low spatial profile, allowing them to interface at the single-cell level. Their synthesis protocol is also compatible with flexible polymer substrates and multi-electrode array modification, making them a high-potential new tool for neuroscience research, capable of simultaneously recording in real-time the electrophysiological and neurochemical activities of neuron networks. We hope this new electrode type will benefit other research teams and topics in neuroscience.

Brain slices experiments were performed to confirm the capability to realize bidirectional electrophysiology and produced high signal-to-noise ratio (SNR) recordings on a wider frequency range than standard microelectrodes used for such electrophysiology. These electrodes could also be used to electrically stimulate brain slice tissues, producing measurable responses with injection of low charge compared to standard microelectrodes.

Taken together, all these results show encouraging results in the fabrication of a flexible implant capable of real-time simultaneous recording of the electrical and neurochemical activities of the brain.

## Immediate to Short-term perspectives

In this thesis, we have carried out the synthesis and validation of a new multifunctional electrode type *in-vitro*. Its capacity to perform bidirectional electrophysiology was also validated *in-vivo* in brain slices. The first next milestone to reach would be to perform electrodedetection (using both CA and FSCV) in the same brain slices, using PEDOT-CNF microelectrodes. For that, several sub-steps could be envisaged.

- It would be possible to use PEDOT-CNF modified CF $\mu$ Es as first tests for electrodedetection in brains slices, to then move to flexible implants [1, 2]. These CF $\mu$ Es-based PEDOT-CNF  $\mu$ Es would constitute a first easy preliminary test for FSCV on PEDOT-CNF in brain slices, without the need of implant fabrication and with base electrodes inherently capable of FSCV (contrary to gold microelectrode). It will be also necessary to evaluate the electrode resistance to FSCV cycling [3] on the long-term, to be able to go further in *in-vivo* experiments (up free-moving animals and patients).

- An improvement of the FSCV instrumentation and setup would also be beneficial to gain access to quicker and more reliable experimental workflow, while also giving access to more advanced FSCV strategies (couple waveforms, asymmetric waveforms...). For that, a fully automated fluidic instrumentation should be developed for FSCV experiments, while the acquisition of a FSCV-specialized potentiostat should be done, to supplement the VSP240. This potentiostat should have the ability to accurately produce complex waveforms and waveform sequences while taking into account the need for combination with electrophysiology [4].

- Improvement of the FSCV calibration of electrodes meant for *in-vivo* operation should also be considered, by adding interferents *in-vitro* (AA, UA, DOPAC). FSCV detection of dopamine for example has been shown to possibly be tricky in presence of these interferents (while it is easier with other techniques [5]). An interesting lead to improve un-interfered detection of interest neurotransmitters by FSCV is engineered electrodes, particularly through tailored surface chemistry [6].

## Futures developments: toward combined electrophysiology and electrodedetection

The next big step in further work would be to perform combined electrophysiology and electrodedetection simultaneously in the same study. This could be done by either alternating recording and electrodedetection on the same electrodes or dedicating a number of electrodes to recording and another to electrodedetection. This could be also facilitated by the integration of an internal reference/counter electrode for enhanced electrophysiology [7, 8] as showed in **Fig. 1**, and for on-chip integrated electrodedetection [5, 8] by using 2-electrode electrochemical microcells (**Fig. 2**).

Also, it will be necessary to work out the crosstalk between electrodedetection and recordings (current bleeding) and to decorrelate the foretold neurostimulation effect of electrodedetection, as electrode potential manipulation will trigger neuron depolarizations.

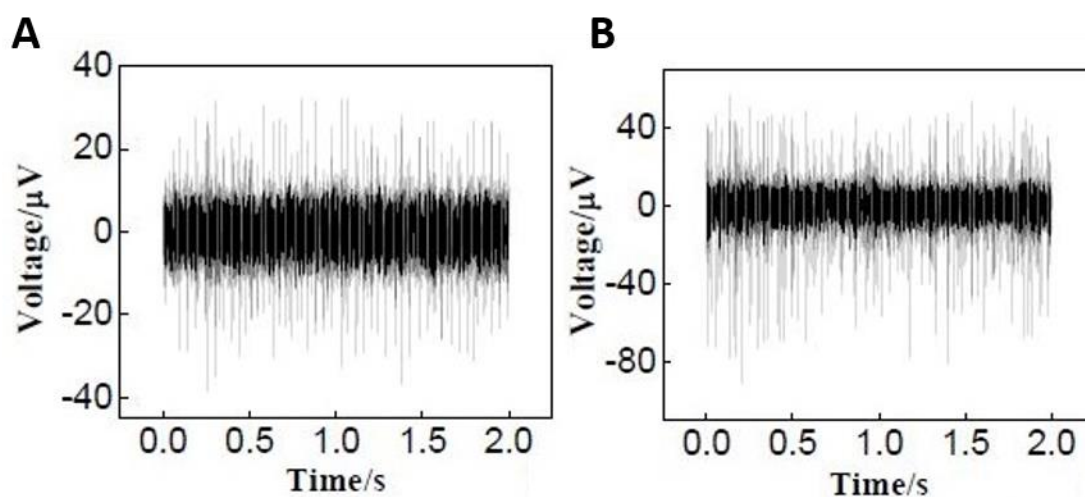


**Fig. 1: Electrophysiological recordings** with (A) an external and (B) an internal, showing a lower noise and signals with higher amplitudes [7].

The distance between this working electrode and the reference electrode could be tailored according to the role chosen for the cell (recording or electrodedetection), as can be shown in **Fig. 2**, depicting preliminary results in microfabrication of integrated 2-electrodes cells, with controlled working and reference electrodes surfaces, and different distances.

In these 2-electrodes cell, the use of an electrochemical cell using an IrOx electrode both as CE and RE could open the possibility to use it both for referencing and for pH detection (not simultaneously), through EIS for example [9, 10] or potential recording. pH detection has already proved to be interesting, particularly with implantable device. The wound from the implantation induce BBB leakage can modify the local pH at the implantation site. Thus, monitoring the pH at this site is one key measurement of the interface state [11]. Some encouraging preliminary results have already been obtained at LAAS in terms of IrOx electrode modification and pH detection (**Annex n°8**).



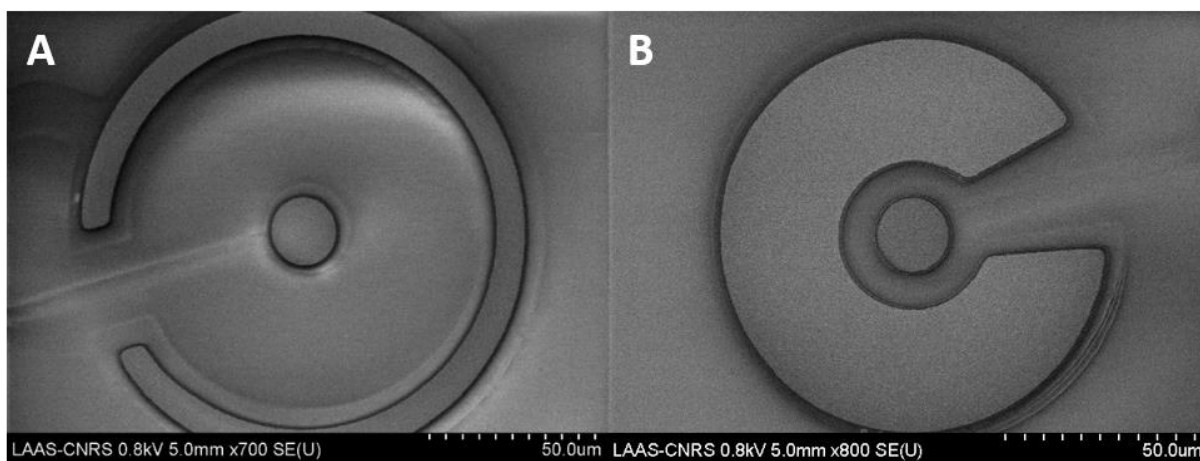


**Fig. 2:** *Integrated 2-electrodes microcells before electrode modification with (A) a large WE/RE interdistance, more tailored to electrodedetection (to prevent diffusion of molecules generated at the RE/CE toward the WE), and (B) a close WE/RE interdistance, to minimize noise during recordings.*

## Opportunities

A collaboration with ESIEE to develop FSCV on diamond microelectrodes [12] as multifunctional electrodes (stimulation on diamond [13]) would be an interesting lead for further research. Diamond has a higher safe electrochemical window [14], allowing for more molecules to be targeted during electrodedetection. For example, UVPs higher of 1.5 to detect molecules like adenosine are easy to achieve on diamond without triggering water electrolysis. Also, diamond is more durable toward FSCV cycling than CF $\mu$ E [12] as can be seen in **Fig. 3**. However, this material is not necessarily indicated for stimulation.

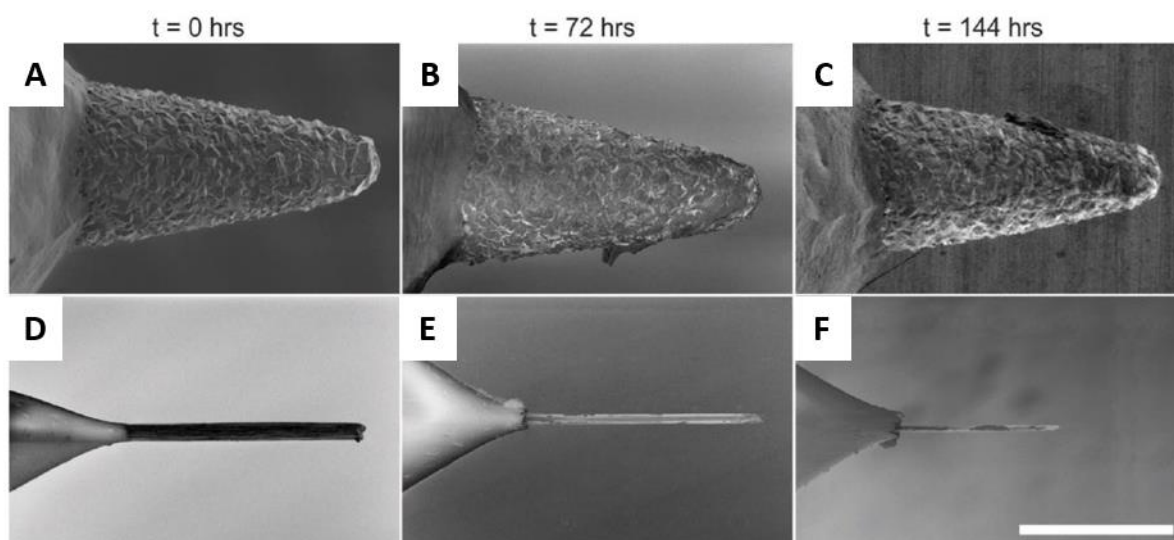


**Fig. 3:** SEM images of diamond (A-C) and carbon fiber electrode (D-F) after 0H (A-D), 72H (B-E), 144H (C-F) of continuous FSCV use. Diamond electrodes clearly withstand this test without critical failure while CF $\mu$ Es clearly degraded to the point to almost be completely etched [12].

Also, a new topic to develop in conjunction with CIRIMAT could be proposed. CIRIMAT was already part of this thesis, through their expertise in carbon nanomaterial (CNM) functionalization, which could be further used to develop a new type of doping nanomaterials for PEDOT-coating. As depicted in **Fig. 4**, connecting EDOT moieties to CNMs through functionalization by organic chemistry, using a conductive linker, the delocalization of electrons or holes on the CNM would be made possible during recording or electrodedetection. That way, the CNM acts as an active part of the PEDOT-coating, creating a new hybrid material, having multiple conductive domains and heterogeneous properties, taking advantage of the CNM doping at a new level.

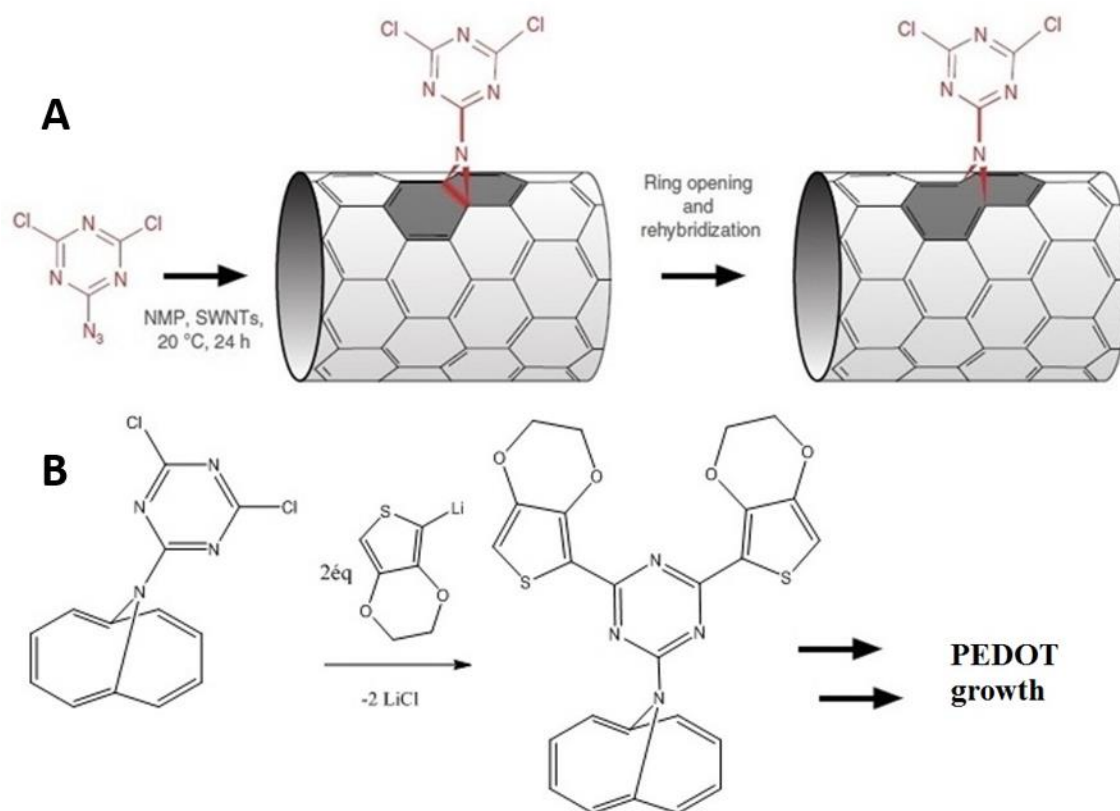


Fig. 4: Functionalization pathway of a carbon nanomaterial (here SWNTs as model for representation) to covalently graft EDOT moieties on its surface by using a delocalized spacer, to connect PEDOT chains to the carbon nanomaterial and take advantage of its conductive skeleton for electron/hole transfer and potential recording.

## Technical and technological challenges toward long-term operation

Finally, as a long-term operation of our implants and microelectrodes is targeted, multiple barriers to this long-term in-vivo operation will have to be addressed. Here are a few of these that can be foreseen:

- The RE drift and degradation. The drift of the reference is one of the major challenges to tackle with device operating electrodedetection, as it basically impedes the accurate use of potential manipulation. It also impedes the identification of redox compounds through their reaction potential in FSCV for example. It is important to note that if the drift is constant, it could be compensated but if it is inconsistent and/or oscillating, it is impossible to compensate for.

- Fouling is another of the major challenging issue with long-term in-vivo operation. Fouling happens because of biological compounds accumulation on the electrode, creating a layer with decreased (even blocked) diffusion and conductivity. Fouling resistance studies would have to be conducted. Multiple strategies to prevent or minimize fouling have been already developed and could be deployed on implants [6, 15].

- Robust operation of electrodedetection. One raising topic is the handling of artifacts generated by electrode movement in electrophysiology and electrodedetection in free-moving animals and patients [16]. For CA, an operational mode inspired from “sentinel modes” or self-referencing in biodetection would be an interesting lead to remove artifacts from data [17-19] (Fig. 5A). For FSCV for example, a FSCV operational mode inspired of Paired Pulse Voltammetry (PPV, Fig. 5B) [20-23] would be interesting lead to explore, as it removes the need of background subtraction, making FSCV much more drift-resistant (Fig. 5C&D) but could also remove the contribution of artifacts from the final data. Finally, research in signal filtering might also a good lead to enhance electrodedetection reliability [24] and LOD.

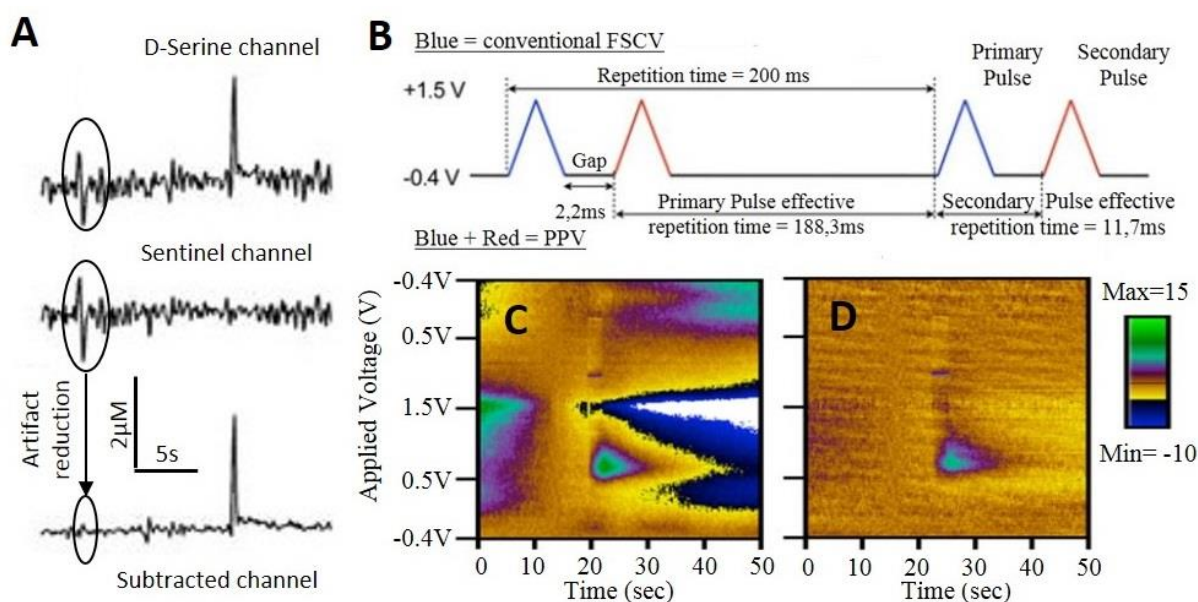


**Fig. 5: Robust operational modes for electrodedetection.** (A) Amperometric detection of D-serine, with two electrodes, one modified, the other unmodified, used to detect unspecific events (artifacts) and subtract them from the signal (also reducing the noise) [17], (B) Paired pulse Voltammetry vs conventional FSCV waveforms, (C) Color plot of a FSCV experiment using a CFμE as working electrode, with a dopamine injection at 20s, (D) Same dataset but treated with PPV, with most of the drift removed [23].

- Finally, operation on arrays of combined electrophysiology and electrodedetection will be one of the biggest challenges in the future. This comes from multiple locks, from the data transfer as FSCV has been shown to be wireless-compatible [25, 26], which will later prevent the need for cables connecting the patient to instrumentation (making our device compatible with patient free movement in the end) but requiring new instrumentation to convert the data produced. Also, data management will have to be addressed as recordings, CA and FSCV produce high volumes of data content and require high calculation power for real-time analysis and data acquisition. Finally, the need for waveform (WV) production, in an addressable and customized way demands new instrumentation (potentiostat and headstage) to realize such WV production.

1. Taylor, I.M., et al., *Enhanced dopamine detection sensitivity by PEDOT/graphene oxide coating on in vivo carbon fiber electrodes*. *Biosens Bioelectron*, 2017. **89**(Pt 1): p. 400-410.
2. S. Demuru, H.D., *Surface PEDOT:Nafion Coatings for Enhanced Dopamine, Serotonin and Adenosine Sensing*. *Journal of The Electrochemical Society*, 2017. **164**(14): p. G129-G138.
3. Yakushenko, A., et al., *On-chip fast scan cyclic voltammetry for selective detection of redox active neurotransmitters*. *physica status solidi (a)*, 2014. **211**(6): p. 1364-1371.
4. al., T.e., *Instrumentation for Fast-Scan Cyclic Voltammetry combined with electrophysiology for behavioral experiments in freely moving animals*. *Review of Scientific Instruments*, 2011. **82**(074302).
5. Belaidi, F.S., et al., *PEDOT-modified integrated microelectrodes for the detection of ascorbic acid, dopamine and uric acid*. *Sensors and Actuators B: Chemical*, 2015. **214**: p. 1-9.
6. Chen, C.H. and S.C. Luo, *Tuning Surface Charge and Morphology for the Efficient Detection of Dopamine under the Interferences of Uric Acid, Ascorbic Acid, and Protein Adsorption*. *ACS Appl Mater Interfaces*, 2015. **7**(39): p. 21931-8.
7. Wei, W.J., et al., *A Novel Microelectrode Array Probe Integrated with Electrophysiology Reference Electrode for Neural Recording*. *Key Engineering Materials*, 2013. **562-565**: p. 67-73.
8. Li, C., et al., *Single probe for real-time simultaneous monitoring of neurochemistry and direct-current electrocorticography*. *Biosensors and Bioelectronics*, 2016. **77**: p. 62-68.
9. Dengler, A.K., R.M. Wightman, and G.S. McCarty, *Microfabricated Collector-Generator Electrode Sensor for Measuring Absolute pH and Oxygen Concentrations*. *Analytical Chemistry*, 2015. **87**(20): p. 10556-10564.
10. Folkertsma, L., et al., *Reference-Electrode Free pH Sensing Using Impedance Spectroscopy*. *Proceedings*, 2018. **2**(13): 742.
11. Johnson, M.D., O.E. Kao, and D.R. Kipke, *Spatiotemporal pH dynamics following insertion of neural microelectrode arrays*. *J Neurosci Methods*, 2007. **160**(2): p. 276-87.
12. Bennet, K.E., et al., *A Diamond-Based Electrode for Detection of Neurochemicals in the Human Brain*. *Front Hum Neurosci*, 2016. **10**: 102.
13. Garrett, D.J., et al., *Ultra-nanocrystalline diamond electrodes: optimization towards neural stimulation applications*. *J Neural Eng*, 2012. **9**(1): 016002.
14. Torz-Piotrowska, R., et al., *Electrochemical properties of undoped CVD diamond films*. *Journal of Physics and Chemistry of Solids*, 2011. **72**(11): p. 1225-1229.
15. Wang, G., et al., *Zwitterionic peptide anchored to conducting polymer PEDOT for the development of antifouling and ultrasensitive electrochemical DNA sensor*. *Biosens Bioelectron*, 2017. **92**: p. 396-401.
16. Nicolai, E.N., et al., *Design Choices for Next-Generation Neurotechnology Can Impact Motion Artifact in Electrophysiological and Fast-Scan Cyclic Voltammetry Measurements*. *Micromachines (Basel)*, 2018. **9**(10).
17. Campos-Beltran, D., et al., *Amperometric Self-Referencing Ceramic Based Microelectrode Arrays for D-Serine Detection*. *Biosensors (Basel)*, 2018. **8**(1).
18. J.J. Burmeister, G.A.G., *Self-Referencing Ceramic-Based Multisite Microelectrodes for the Detection and Elimination of Interferences from the Measurement of L-Glutamate and Other Analytes*. *Anal Chem*, 2001. **73**: p. 1037-1042.
19. McLamore, E.S., et al., *A self-referencing glutamate biosensor for measuring real time neuronal glutamate flux*. *J Neurosci Methods*, 2010. **189**(1): p. 14-22.
20. Jang, D.P., et al., *Paired pulse voltammetry for differentiating complex analytes*. *Analyst*, 2012. **137**(6): p. 1428-35.
21. Kim, D.H., et al., *Investigation of the reduction process of dopamine using paired pulse voltammetry*. *J Electroanal Chem (Lausanne)*, 2014. **717-718**: p. 157-164.
22. Oh, Y., et al., *Optimization of Paired Pulse Voltammetry Using Sawhorse Waveform*. *International Journal of Electrochemical Science*, 2015. **10**: p. 10061-10073.

23. Paek, S.B., et al., *Dopamine measurement during prolonged deep brain stimulation: a proof-of-principle study of paired pulse voltammetry*. Biomed Eng Lett, 2013. **3**(1): p. 22-31.
24. DeWaele, M., et al., *A baseline drift detrending technique for fast scan cyclic voltammetry*. Analyst, 2017. **142**(22): p. 4317-4321.
25. Chang, S.Y., et al., *Wireless fast-scan cyclic voltammetry to monitor adenosine in patients with essential tremor during deep brain stimulation*. Mayo Clin Proc, 2012. **87**(8): p. 760-5.
26. Garris, P.A., et al., *Wireless transmission of fast-scan cyclic voltammetry at a carbon-fiber microelectrode: proof of principle*. J Neurosci Methods, 2004. **140**(1-2): p. 103-15.

---

## *Annexes*

---



### Annex 1: Published Microfabricated devices used for combined electrophysiology and electrochemistry in-vivo

Ref	Architecture						Operation		Electrophysiology				Electrochemistry				
	Insulation Layer(s)		Flexible	Base $\mu$ E mat	Number of WE		Dual mode	Animal & location	Base $\mu$ E surface ( $\mu\text{m}^2$ )	Final $\mu$ E material	RE	Target Signal	Base $\mu$ E surface ( $\mu\text{m}^2$ )	Final $\mu$ E material	Target molecule	Tech	RE
	Type	Thick.			Ephy	Echem											Type Surface
[1]	Polyimide	6 $\mu\text{m}$	Yes	Au	2	2	3	Rat cerebral cortex	45000 <sup>c</sup>	IrOx	IrOx (0.045mm <sup>2</sup> )	SD*	45000 <sup>d</sup>	PtNPs/mPD	Oxygen	CA at -0.75V	IrOx (0.45 mm <sup>2</sup> )
														PtNPs/GOD-CO-GA-Ch/mPD	Glucose	CA at 0.45V	
[2]	SiN	800nm	No	Pt	6	8	3	SD rats – cortex	176.7	PtNPs	Ext Ag/AgCl	LFP* <sup>2</sup> Spikes	7500	GlutOx-GA/mPD	Glutamate	CA at 0.7V	Ext Ag/AgCl
[3]	SU8	NA	No	Pt	2	2	3	Rhesus macaque – Primary visual cortex	225	Pt	Ext Ag/AgCl	LFP* <sup>2</sup>	4500	ChOx-BSA-GA/mPD	Choline	CA at -0.7V	Ext Ag/AgCl
[4]	Epoxy	NA	No	CF $\mu$ E	1* <sup>3</sup>		1	SD rats – motor cortex and NAc**	1178 <sup>b</sup>	NA	Ext Ag/AgCl	SD*	1178 <sup>b</sup>	NA	DA	FSCV	Ext Ag/AgCl
														O <sub>2</sub>	CA at -1V		
[5] [6]	Polymidie	1.5 $\mu\text{m}$	No	Pt	4		2	Mistar rats – Dorsal hippocampus	4995	NA	Ext Ag/AgCl	LFP-currents	4995	NA	O <sub>2</sub>	CA at -0.6V	Ext Ag/AgCl
[7]	NA	NA	No	CF $\mu$ E	1		1	Nuclues accumbens	1020	NA	NA	Cell firing	1020	NA	AA, DOPAC 5HIAA	DPV, CV	NA
[8]	SiO <sub>2</sub> /Si <sub>3</sub> N <sub>4</sub>	300nm/500nm	No	Pt	16		3	Rats Striatum (Cortex, White Matter)	314	PtNPs-Nafion	Ext Ag/AgCl	Spikes LFP	314	PtNPs-Nafion	DA	CA at 0.5V	Ext Ag/AgCl
[9]	SiO <sub>2</sub> /Si <sub>3</sub> N <sub>4</sub>	300nm/500nm	No	Pt	8	8	3	Rats Hippocampus	490	PtNPs	Ext Ag/AgCl	Spikes	490	PtNPs/GlutOx-BSA-GA/mPD	Glutamate	CA at 0.6V	Ext Ag/AgCl
[10]	SiO <sub>2</sub> /Si <sub>3</sub> N <sub>4</sub>	300nm/500nm	No	Pt	8	8	3	Male machin monkey* <sup>4</sup> - Putamen	490	PtNPs	Ext Ag/AgCl	Spikes	490	PtNPs/GlutOx-BSA-GA/Nafion	Glutamate	CA at 0.5V	Ext Ag/AgCl
[11] [12]	SiO <sub>2</sub> /SiN/SiO <sub>2</sub>	NA	No	Pt or Ir	8	8	3	SD rats - Striatum	177	Ir-Nafion	Ext Ag/AgCl	Spikes LFP	450	Pt-Nafion	DA	CA at 0.5V	Ext Ag/AgCl
[13]	SiO <sub>2</sub> /Si <sub>3</sub> N <sub>4</sub>	300nm/500nm	No	Pt	8	8	3	Sd rats – Temporal lobe	314	PtNPs-Nafion	Ext Ag/AgCl	Spikes LFP	314	PtNPs/GlutOx-BSA-GA/mPD	Glutamate	CA at 0.6V	Ext Ag/AgCl
[14]	SiO <sub>2</sub> /Si <sub>3</sub> N <sub>4</sub>	300nm/500nm	No	Pt	8	4	3	PD rats – Caudate Putamen, Motor cortex (M1, CPu)	314	PtNPs-Nafion	Ext Ag/AgCl	Spikes LFP	314	PtNPs-Nafion	DA	Ca at 0.5V	Ext Ag/AgCl
[15]			No	Pt	8	8	3	SD rats – Striatum	176	PtNPs	Ext Ag/AgCl	Spikes LFP	7500	GluOx-BSA-GA/mPD	Glucose	CA at 0.7V	Ext Ag/AgCl
[16]	SiO <sub>2</sub> /Si <sub>3</sub> N <sub>4</sub>	300nm/500nm	No	Pt	12	4	3	Mouse – Cortex & Striatum	78	PtNPs	Ext Ag/AgCl	Spikes LFP	78	GlutOx-BSA-GA/mPD	Glutamate	CA at 0.7V	Ext Ag/AgCl
[17]	NA	NA	No	CF $\mu$ E	1		1	SD rats – Nac, Cortex	605	NA	Ext Ag/AgCl	Spikes SD	605	NA	DA	FSCV	Ext Ag/AgCl
														O <sub>2</sub>			
[18]	SI <sub>3</sub> N <sub>4</sub>	800nm	No	Pt	60	3	1	Bran slices of SD rats	706	rGO-PtNPs	Ext Ag/AgCl	Spikes	706	rGO-PtNPs	NE	DPV	Ext Ag/AgCl
LAA S	ParyleneC	1,3 $\mu\text{m}$	Yes	Au	4	4	1	Brain slices of mouse	314	PEDOT-CNF	Ext Ag/AgCl	Spikes SWR	314	PEDOT-CNF	DA	CA, FSCV	Ext Ag/AgCl

\*=Spreading depolarization (induced with a needle prick). \*\*Nucleus Accumbens. \*<sup>2</sup>=Local field potential. \*<sup>3</sup>=The RE is used as CE, in a two-electrode configuration. \*<sup>4</sup>=animals in a Faraday Cage during measurements. \*<sup>5</sup>=Non-implantable MEA fabricated on glass wafer. \*<sup>3</sup>=Same electrode used for both electrophysiology and electrochemistry. \*<sup>c</sup>=not specifically. \*<sup>d</sup>=calculated from electrode measurements (75 $\mu\text{m}$  length with 5 $\mu\text{m}$  diameter).

Mode 1: successive on the same electrode, Mode 2: simultaneous on the same electrode, Mode 3: Simultaneous on different electrodes.

1. Li, C., et al., *Single probe for real-time simultaneous monitoring of neurochemistry and direct-current electrocorticography*. Biosensors and Bioelectronics, 2016. **77**: p. 62-68.
2. Wei, W., et al., *An implantable microelectrode array for simultaneous L-glutamate and electrophysiological recordings in vivo*. Microsystems & Nanoengineering, 2015. **1**(1).
3. Disney, A.A., et al., *A multi-site array for combined local electrochemistry and electrophysiology in the non-human primate brain*. J Neurosci Methods, 2015. **255**: p. 29-37.
4. Hobbs, C.N., et al., *An implantable multimodal sensor for oxygen, neurotransmitters, and electrophysiology during spreading depolarization in the deep brain*. Analyst, 2017. **142**(16): p. 2912-2920.
5. Ledo, A., et al., *Combined in Vivo Amperometric Oximetry and Electrophysiology in a Single Sensor: A Tool for Epilepsy Research*. Anal Chem, 2017. **89**(22): p. 12383-12390.
6. Ledo, A., et al., *Ceramic-Based Multisite Platinum Microelectrode Arrays: Morphological Characteristics and Electrochemical Performance for Extracellular Oxygen Measurements in Brain Tissue*. Anal Chem, 2017. **89**(3): p. 1674-1683.
7. Crespi, F., et al., *Carbon fibre micro-electrodes for concomitant in vivo electrophysiological and voltammetric measurements : no reciprocal influences*. Neurosci Lett., 1995. **188**: p. 33-36.
8. Zhang, S., et al., *Real-time simultaneous recording of electrophysiological activities and dopamine overflow in the deep brain nuclei of a non-human primate with Parkinson's disease using nano-based microelectrode arrays*. Microsystems & Nanoengineering, 2018. **4**: p. 17070.
9. Xiao, G., et al., *A high-sensitive nano-modified biosensor for dynamic monitoring of glutamate and neural spike covariation from rat cortex to hippocampal sub-regions*. J Neurosci Methods, 2017. **291**: p. 122-130.
10. Zhang, S., et al., *A silicon based implantable microelectrode array for electrophysiological and dopamine recording from cortex to striatum in the non-human primate brain*. Biosens Bioelectron, 2016. **85**: p. 53-61.
11. Drake, K.L., et al., *Performance of planar multisite microprobes in recording extracellular single-unit intracortical activity*. IEE Transactions on Biomedical Engineering, 1988. **35**(9): p. 719-732.
12. Johnson, M.D., et al., *Implantable microelectrode arrays for simultaneous electrophysiological and neurochemical recordings*. J Neurosci Methods, 2008. **174**(1): p. 62-70.
13. Li, Z., et al., *Bio-electrochemical microelectrode arrays for glutamate and electrophysiology detection in hippocampus of temporal lobe epileptic rats*. Anal Biochem, 2018. **550**: p. 123-131.
14. Zhang, Y., et al., *High frequency stimulation of subthalamic nucleus synchronously modulates primary motor cortex and caudate putamen based on dopamine concentration and electrophysiology activities using microelectrode arrays in Parkinson's disease rats*. Sensors and Actuators B: Chemical, 2019. **301**: p. 127126.
15. Wei, W., et al., *Simultaneous recording of brain extracellular glucose, spike and local field potential in real time using an implantable microelectrode array with nano-materials*. Nanotechnology, 2016. **27**(11): 114001.
16. Fan, X., et al., *In Situ Real-Time Monitoring of Glutamate and Electrophysiology from Cortex to Hippocampus in Mice Based on a Microelectrode Array*. Sensors (Basel), 2016. **17**(1).
17. Hobbs, C.N., et al., *Comparison of Spreading Depolarizations in the Motor Cortex and Nucleus Accumbens: Similar Patterns of Oxygen Responses and the Role of Dopamine*. ACS Chem Neurosci, 2017. **8**(11): p. 2512-2521.
18. Wang, L., et al., *A microelectrode array electrodeposited with reduced graphene oxide and Pt nanoparticles for norepinephrine and electrophysiological recordings*. Journal of Micromechanics and Microengineering, 2017. **27**(11): 115001.



## Annex 2: MEA microfabrication process sheet

Process step	Parameter	Type or Value	Additional information	Equipment/Manufacturer
Substrate	Type	4" glass wafer (AF32)	Thickness 525 $\mu$ m	
		Plasma cleaning (800W, 15 min, 400 sccm O <sub>2</sub> )	Remove dust, clean the wafer and enhance resin adhesion	
Photolitho for lift-off	Coating	AZ-nLOF 5 $\mu$ m	a=5000rpm=sec, v=1350rpm, t=30sec V=3mL - soft bake 216s at 110°C	PR: MicroChemicals Coater: Gyrset SUSS Microtec or PIST
	UV exposure	$\lambda$ =405nm (CH <sub>2</sub> )	HARD CONTACT, 90mJ/cm <sup>2</sup> , PEB 216s at 110°C (recipe saved)	SUSS Microtec MA6GEN4
	Development	MF CD-26	t =120 sec, don't fear to overdevelop a little to get good inverted resin profiles	
Metallization & Lift-off	Metallization	Ti 50nm/Au 200nm	PVD	Alliance EVA 600
	Lift-off	Acetone (5-6h to overnight) then DMSO (10min)	Lift-off 5-6h, Room Temperature (option US at 135kHz) with orbital agitation. Replace Acetone by DMSO for 10min when lift-off is finished to remove resin residues. Rinse with DIW. Heat at 90°C to dehydrate before plasma.	
	Cleaning	Plasma cleaning (400W, 5 min, 1000 sccm O <sub>2</sub> ) with Faraday cage	Remove resin residues after lift-off, enhance the SU8 adhesion and prevent dust to be encapsulated between the wafer/SU8. Use of a faraday cage is primordial to prevent damages to the metal electrodes. To do just before SU8 coating, one wafer by one wafer.	
SU8 pasivation (1.5 $\mu$ m)	Coating	SU8 3005	Recipe "SU8 2 $\mu$ m". The resin must be spread until 1cm of its edge, and the (coater cover must close <u>before</u> the spin-coating).	PR: MicroChemicals Coater: Obducat QSC200BM with RCCT cover
	PSB		PSB 5min 110°C.	
	UV exposure PEB	Recipe	HARD CONTACT PEB 5min 110°C	SUSS Microtec MA6GEN4
	Development	SU8 developer	1'30 to complete development, 2'30-3' to remove residues	
Hard bake	Recipe	Pg 10 (125°C)	Aim at removing solvent traces and mechanical strengthen the passivation	SU8 hotplate (F-FRAI) Suss Microtech
Wafer dicing	Coating	AZ-4562 « découpe » 10 $\mu$ m	To prevent any silicon dust from dicing to stick on the final MEA	Avisa Technology Omega 201
	Dicing	Saw dicing in assembly	Follow dicing paths	
	Stripping	Acetone	Double bath, t(first bath)=15min then 1h in a new bath (upside down to prevent re-deposit)	Sigma-Aldrich

### *Annex 3: MEA design evolution for multiple applications*

- **MEA GEN1: Electrophysiologic recordings and PEDOT deposits**

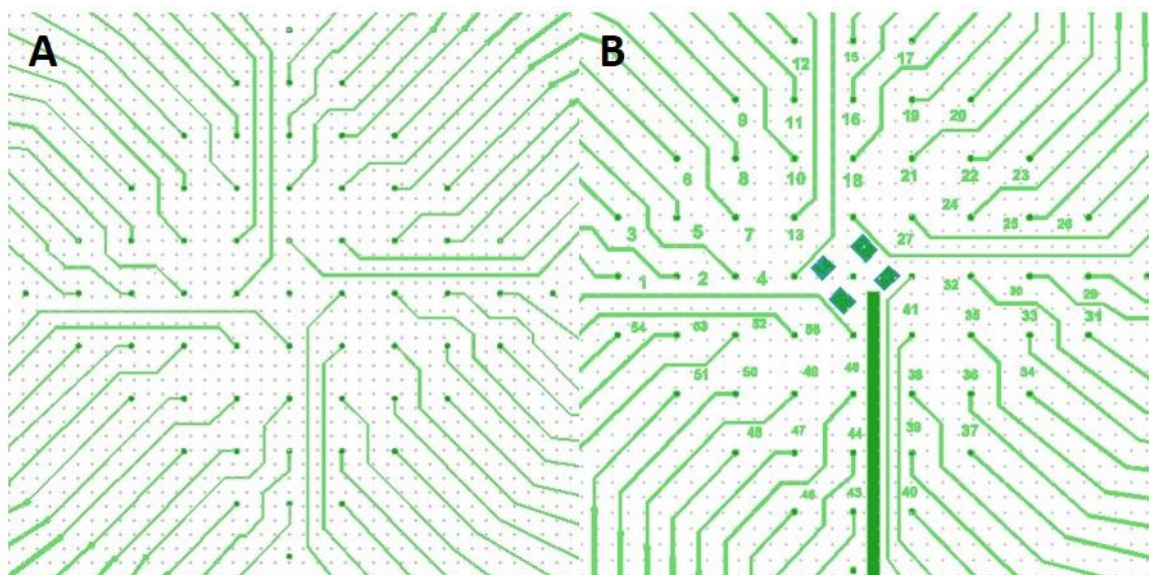


**Fig. 1: MEA GEN1 et 2 matrix.** A) Microelectrode matrix of the first MEA generation, containing 56 microelectrodes and 5 unconnected  $\mu$ Es, B) Microelectrode matrix of the second MEA generation, with the added SEM markers,  $\mu$ E numeration and drain electrode.

First generation of MEA consisted of 56 gold microelectrodes, 20 $\mu$ m in diameter with 10 $\mu$ m large tracks (in the center part of the  $\mu$ E matrix) and 50 $\mu$ m minimum between tracks (**Fig. 1A**). Interelectrode distance was 200 $\mu$ m and 300 $\mu$ m (on 2 different MEA on the same wafer). It was based on a design generously provided by L. ROUSSEAU from ESIEE, Paris. This generation was already integrating two couples of supplementary electrodes, used as REs (cross shaped) and CEs (disk shaped).

- **MEA GEN2: Design modification for PEDOT-CNF deposition**

The second MEA generation (GEN2) was a redesign of GEN1 to better fit the need of PEDOT-CNF experimentations, namely, ease of optical/SEM imaging, prevention of deposits contaminating other unused microelectrodes and ease of use with CNF containing solutions. This resulted in the integration of SEM markers (uncovered gold numbers in the center of the matrix), microelectrodes numeration, thicker tracks, 300 $\mu$ m interelectrode distance edge to edge (enough to prevent interelectrode contamination) and of a drain electrode. This latter addition consisted in a bigger electrode uncovered in the

middle of  $\mu\text{E}$  matrix, with larger track and contact pad connectable to the SEM imaging support, meant to drain electrons during SEM imaging and prevent charging effects during imaging (**Fig. 1B**).

This generation also integrated, electrode-wise, a ground electrode (near the  $\mu\text{E}$  for better electrophysiological recordings), 3 rectangular electrodes for REs and one bigger electrode for CE, and feature-wise, part of the passivation were removed on unused zones, to allow direct exposition of glass, creating contact zones for liquid injection with pipettes without the risk of damaging the passivation.

- **MEA GEN3: Design modification for IrOx deposition**

The third generation (GEN3) was designed for IrOx deposition, having 56 all- rectangular microelectrodes with varying surface ( $4000, 9000, 16000\mu\text{m}^2$ ), still integrating all other electrode and features of the precedent generations (drain electrode, CE, RE, numeration, SEM markers, pipetting zones). These electrodes shapes/surfaces were extracted from literature, and meant to have big surfaces to be used as stable integrated REs after IrOx deposition (**Fig. 2A**).

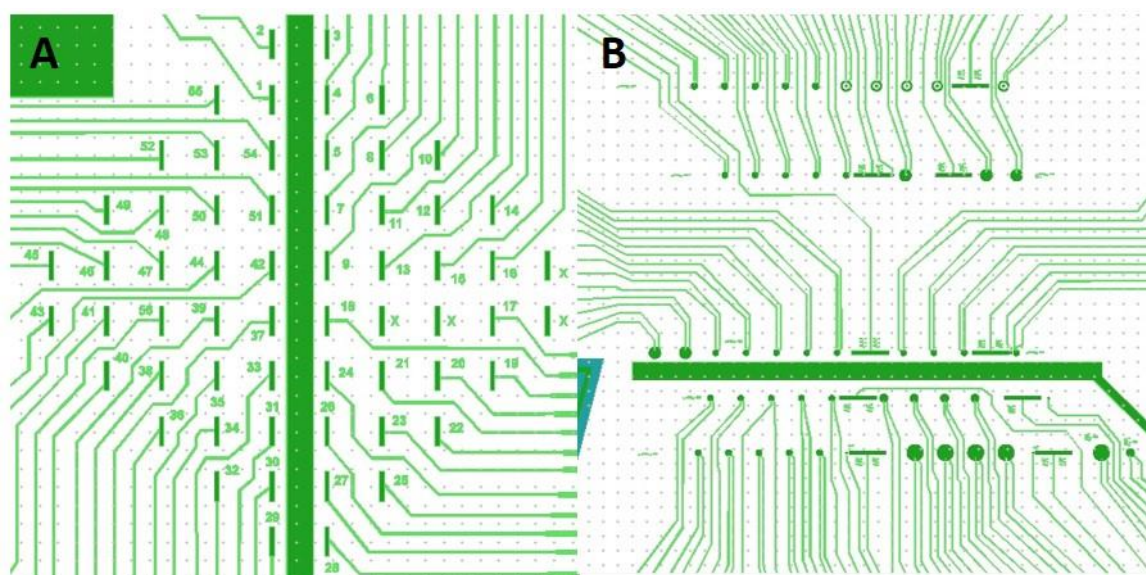


**Fig. 2 : MEA GEN3 et 4 matrix.** A) Microelectrode matrix of the third MEA generation, containing 56 rectangular microelectrodes, B) Microelectrode matrix of the fourth MEA generation, showing electrode couples meant to test WE/CE or WE/RE parameters.

- **MEA GEN4: Design for microcell configuration optimization**

The fourth and last generation of MEAs (GEN4), depicted in **Fig. 2B**, was designed to test the effect of distance and surface parameters on the performances of integrated two- and three-electrode micro-electrochemical cells, as no guidelines for such integration do exist to the best of our knowledge. These

cells are meant to be tested with both CA and FSCV, unmodified and modified (PEDOT-PSS/PEDOT-CNF).

Guidelines to design all-in-on addressable MEAs (all  $\mu$ Es polarized together) do exist [1, 2], to prevent diffusion volumes overlap and maximize MEA performance and thus, can help find the interelectrode distance necessary to prevent crosstalk between microcells

Integrated, in plane, electrochemical cells have been published [3] but no guidelines exist to our knowledge about the influence of its geometry, particularly for FSCV scans, even though the influence of some parameters among published designs have been sometimes discussed on slow scan rate CVs [4].

The design of working electrode is kept as a disk, even though other base electrode shapes have shown promising properties for neural applications like stimulation for example [5]. This is to keep continuity with modification protocols (PEDOT-PSS...) already developed at LAAS.

**Table 1: Parameters meant to be tested with the GEN4, to test microelectrochemical cell construction through planar microfabrication.**

WE	CE	Distance ( $\mu\text{m}$ )	WE/CE surface ratio
Disk ( $\varnothing=20\mu\text{m}$ )	CRE* ( $S=3140\mu\text{m}^2$ )	3, 5, 7, 10, 15, 50	10, 20, 50, 100
Disk ( $\varnothing=20\mu\text{m}$ )	Rectangular	50, 100, 150, 200, 400, 800, 1200, 1600, 2000	13, 29, 50
* = Conformal ring Electrode			

As it can be seen in the **Table 1**, two types of counter electrodes are envisaged, one rectangular, with parameters to match other publications where such electrodes are described, and one conformal ring-shaped (CRE), with small WE/CE distance, to create electrode configurations that are optimal to decrease as much as possible uncompensated resistance.

### • Transition from MEA GEN1 to GEN4

From the first to the fourth and last generation of MEAs, multiple advances have been developed and integrated on the MEA and on the wafer (**Fig. 3**), to optimize production costs (more MEAs produced on the same wafer, with less unused space) and characterization efficiency and time (resolution marker etc...). These advances accompanied the design change (**Table 2**) and are summarized in **Table 3**.

**Table 2: Summary of all designs produced during this thesis and their targeted applications.**

MEA (TiAu/SU8) GEN1: Electrophysiology GEN2: PEDOT-CNF deposit GEN3: Iridium Oxide deposition GEN4: Integrated electrochemistry	Implant (TiAu/ParyleneC) GEN1: Aziliz design
---	---

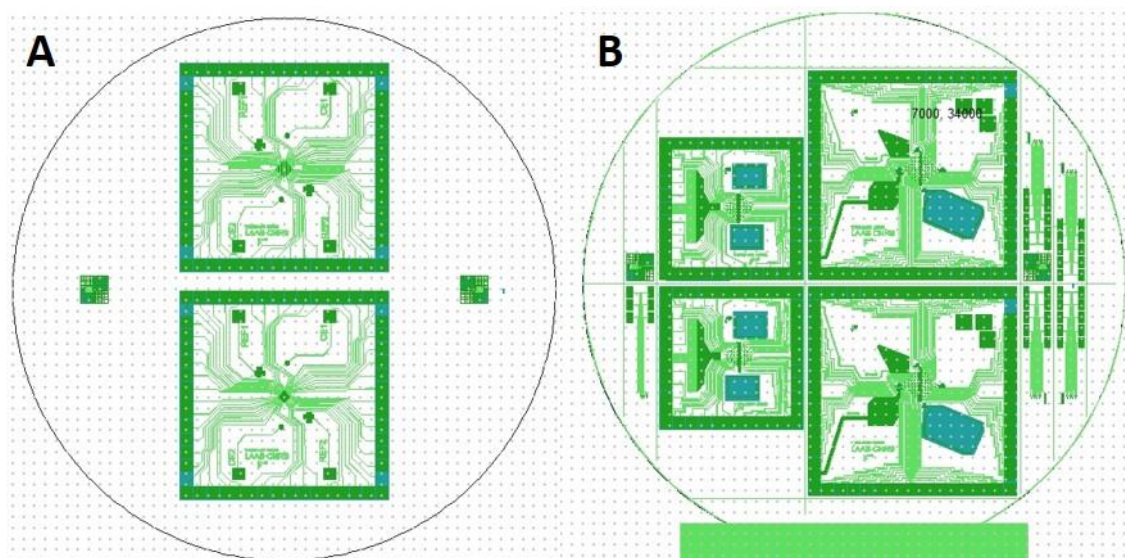


**Fig. 3: Masks of the first and fourth generation of MEA.** A) First generation MEA wafer design, with only 2 MEAs and alignment mires, B) Fourth generation MEA wafer design, with 9 MEAs, dicing guides and flattened section metallization.

**Table 3: Features overview from GEN 1 to GEN4.**

Features	Aim	GEN1	GEN4
Total number of MEA	Lower microfabrication costs	2	9 (x4.5)
$\mu$ Es repartition	Increased experimental adaptability	2x56	2x116 / 2x40 / 5x10
Total number of $\mu$ Es	Increased electrode mass	112	352 (+214%)
Counter electrode	Make MEAs compatible with electrochemistry	Yes	Yes
Ground electrode	Make MEAs compatible with electrophysiology	No	Yes
Drain electrode	Make MEAs easier to image with SEM	No	Yes
Pipetting areas	Make MEAs passivation easier to protect during in-vitro experiments	No	Yes
Dicing guides	Make MEA dicing more reproducible	No	Yes
Resolution markers	Make process easier to characterize	No	Yes

As a conclusion on the evolution of our MEA designs, it can be seen on the **Fig 3** that wafer coverage largely increased, due to the optimization of device density on the wafer (for microfabrication yield increase). The other features added are gathered and explained in Table 3.



1. Said, N.A.M., et al., *Fabrication and characterization of microfabricated on-chip microelectrochemical cell for biosensing applications*. 2017. **1808**: 020032.
2. Huang, X.J., A.M. O'Mahony, and R.G. Compton, *Microelectrode arrays for electrochemistry: approaches to fabrication*. *Small*, 2009. **5**(7): p. 776-88.
3. Twomey, K., et al., *Fabrication and characterization of a miniaturized planar voltammetric sensor array for use in an electronic tongue*. *Sensors and Actuators B: Chemical*, 2009. **140**(2): p. 532-541.
4. Moujahid, W., et al., *Microelectrochemical Systems on Silicon Chips for the Detection of Pollutants in Seawater*. *Electroanalysis*, 2011. **23**(1): p. 147-155.
5. Park, H., P. Takmakov, and H. Lee, *Electrochemical Evaluations of Fractal Microelectrodes for Energy Efficient Neurostimulation*. *Sci Rep*, 2018. **8**(1): 4375.

## Annex 4: Flexible implant microfabrication process sheet

Step	Substeps	Parameters	Aim & Additional informations	Post-characterization	Equipment
Substrate preparation		4" Si wafer	Thickness 525µm	none	Chemistry bench TEPLA Dehydration oven in photolitho zone
	Piranha cleaning (optional for recycling)	2min	Remove dust on the wafer to minimize pC bursting from dust extraction by vacuum		
	Plasma cleaning	TEPLA, Pg 02 (800W, 400 sccm O <sub>2</sub> , 5min)	Etch the remaining absorbed molecules from the wafer surface		
	Dehydration	>200°C, overnight	Remove any volatile organic/aqueous residues from the wafer surface		
Parylene 1st layer deposition (23µm)	Dust removal	Spray nitrogen front and back side Isopropanol can be used on the backside of wafers to ensure dust removal.	Remove fresh dust from the wafer surface	Visual check for any visible dust	Nitrogen blower from the hood near the PaC deposition system
	Deposition	m(dimer)=46g, t(deposit)=5hours, P(consign)=55µbar, T(pyrolysis)=670°C, T(prepyrolysis)=T(postpyrolysis)=220°C, T(deposit)=80°C (stable value)	Deposition carried out at 55µbar to lead to quasi-amorphous layer in a reasonable time considering the thickness to deposit	DRX → Verify the crystallinity of the deposited PaC FTIR → Compositional analysis of the PaC to detect any pollution in its bulk Profilometry and SEM → Quantify PaC thickness and rugosity Optical imaging → Qualify optical properties of the PaC, its surface state	DPX-C, Special Coating System / Comelec C-30-S
Thermal annealing (optional)	Temperature Ramp Up	From room temperature to 110°C at 1°C/min. N <sub>2</sub> (flux)=8L/min.	Ramp up & down must be slow to prevent to induce stress in the PaC and the oven must be purged with high nitrogen flux (8L/min) before ramping up the temperature to prevent parylene oxidation.	DRX → Verify that the maximum crystallinity <u>has not</u> been reached FTIR → Verify that no bulk oxidation of the parylene has occurred Profilometry → Verify the PaC thickness variation after annealing Optical imaging → Qualify optical properties of the PaC, its surface state (oxidation lead to yellowing the polymer)	AET 4" Furnace, Tube BG (Recuit Polyimide)
	Annealing	110°C for 4h. N <sub>2</sub> (flux)=4L/min.			
	Temperature Ramp Down	Return to RT by cutting the heating (overnight preferably). N <sub>2</sub> (flux)=2L/min.			
Plasma surface preparation	Plasma cleaning	P=200W, t=2min, 1000 sccm O <sub>2</sub> metallic support (plasma treatment of the wafers one by one)	Pg 04, samples must be placed in the back of the reactor, metallic support must be cleaned with isopropanol before being used	Profilometry → Ensure that the rugosity of the PaC is compatible with further photolithographic steps	PVA Tepla 300
Photolithography for lift-off - AZ-nLOF 5µm	Spin-Coating	Recipe "NLoF 5µm", 1300rpm, 5000 rpm/s (acceleration), 30s	Spray nitrogen on the wafer before spin-coating to remove dust and ensure proper uniform coating	Profilometry → Verify the resin thickness Optical imaging → Verify the inverted profiles of the NLoF (AD=1, x50)	Gyrset SUSS Microtec
	PSB	110°C, 90s	Remove the solvent from the resin		Hotplate
	UV exposure	I-Line on the MA6 GEN4, 150mJ/cm <sup>2</sup>	Initiate the polymerization of the resin. Mask must be dehydrated for 15min at least before exposition.		SUSS Microtec
	PEB	110°C, 90s	Propagate the polymerization		Hotplate
	Development	t=90sec in MFCD-26	Remove unexposed resin		Photolitho bench + Glassware
Metallization & Lift-off	Metallization	PVD Ti 50nm/Au 150nm	Slow deposition protocol to prevent PaC smashing	Profilometry → Verify metal thickness Optional: EDS → Verify metal composition Optical imaging → Verify the metal patterns shapes SEM imaging → Verify the metal surface state/rugosity	Alliance EVA 600 (ask for Ludo)
	Lift-off	Lift-off in Acetone 1-2h, Room temperature, orbital agitation  DMSO, 5min	Lift-off is to be as short as possible, and can be shortened using spraying acetone on the wafer after every 10-15min in the bath, to accelerate removal of the resist  Remove NLoF residues, rinsing with DIW for at least 30s after this step completion is necessary		
Wafer cleaning	Dehydration	90°C, 1'30	Dehydration helps remove most of the volatile residues before plasma cleaning and must be conducted at PA on a hot plate (no vacuum)	Profilometry → Ensure that the rugosity of the PaC is compatible with further photolithographic steps	PVA Tepla 300
	Plasma cleaning	P=200W, t=2min, 1000 sccm O <sub>2</sub> with Faraday cage + metallic support			
ParyleneC 2 <sup>nd</sup> layer (1,3µm)	Dust removal	Spray nitrogen front and back side Isopropanol can be used on the backside of wafers to ensure dust removal.	Remove fresh dust from the wafer surface	Visual check for any visible dust	Nitrogen blower from the hood near the PaC deposition system
	Deposition	m(dimer)=3g, t(deposit)=1hour (max), P(consign)=30µbar, T(pyrolysis)=670°C, T(prepyrolysis)=T(postpyrolysis)=220°C, T(vaporisator)=80°C	As the initial dimer mass is lower, the deposition is required to be conducted at lower work pression to obtain a clean even PaC layer	DRX → Verify the crystallinity of the deposited PaC FTIR → Compositional analysis of the PaC to detect any pollution in its bulk Profilometry and SEM → Quantify PaC thickness and rugosity/surface state (particularly on top of microelectrodes) Optical imaging → Qualify optical properties of the PaC, its surface state	DPX-C, Special Coating System / Comelec C-30-S
Annealing	Temperature Ramp Up	From room temperature to 150°C at 1°C/min. N <sub>2</sub> (flux)=8L/min.	Ramp up & down must be slow to prevent to induce stress in the PaC and the oven must be purged with high nitrogen flux (8L/min) before ramping up the temperature to prevent parylene oxidation.	DRX → Verify that the maximum crystallinity <u>has</u> been reached FTIR → Verify that no bulk oxidation of the parylene has occurred	AET 4" furnace, Tube BG (Recuit Polyimide)
	Annealing	150°C for 16h. N <sub>2</sub> (flux)=4L/min.			

	Temperature Ramp Down	Return to RT by cutting the heating (overnight preferably). N <sub>2</sub> (flux)=2L/min.		Profilometry → Verify the PaC thickness variation after annealing Optical imaging → Qualify optical properties of the PaC, its surface state (oxidation lead to yellowing the polymer)	
Wafer cleaning	Plasma cleaning	P=200W, t=1min, 1000 sccm O <sub>2</sub> Faraday cage + metallic support	Pg 04, samples must be placed in the back of the reactor, metallic support must be cleaned with isopropanol before being used	Profilometry → Ensure that the rugosity of the PaC is compatible with further lithographic steps	PVA Tepla 300
Photolithography for passivation etching - AZ-4562 5μm	Spin-Coating	Recipe "AZ-4562 5μm", 5000rpm, 5000 rpm/s, 30s	Spray nitrogen on the wafer before spin-coating to remove dust and ensure proper uniform coating	Profilometry → Verify the resin thickness in resin openings Optical imaging → Verify the placement of the resin openings	Gyrset SUSS Microtec
	PSB	105°C, 60s	Remove the solvent from the resin		Hotplate
	UV exposure	I-line, 300mJ/cm <sup>2</sup>	Initiate and propagate the polymerization of the resin. Mask must be dehydrated for 15min at least before exposition.		SUSS Microtec
	Development	MFCD-26	Remove unexposed resin		Photolitho bench + Glassware
Passivation etching by ICP-RIE O <sub>2</sub> plasma	Plasma Etching	T = 10°C, O <sub>2</sub> =20sccm, Pr=20 mTorr, P <sub>ICP</sub> =500W, P <sub>bias</sub> =10W, t=according to thickness/etching rate, Fomblin oil	DFA during RIE (on ICP3) to follow etching progress and stop the etching at the most adequate moment (+10s to ensure complete etching wafer-wide).	Profilometry → Verify the resin thickness after etching and the etched PaC thickness after stripping to quantify the etching rates for both the resin and the PaC Conductimetry → Verify that the passivation etching is completed SEM → Verify the state of the microelectrode openings (etching residues, completed etching etc...)	ICP3 - Avisa Technology Omega 201 Or Alcatel P4
	Stripping	1min in Acetone + 1min in DMSO + dehydration (1min on 90°C on hotplate)	Remove the AZ resin thoroughly (acetone plus DMSO like for the NLoF). Rinsing with DIW for at least 30s after this step completion is necessary, the dehydration prevent further damage		Chemical bench Fluidair
Wafer cleaning	Plasma cleaning	P=200W, t=1min, 1000 sccm O <sub>2</sub> Faraday cage + metallic support	Pg 04, samples must be placed in the back of the reactor, metallic support must be cleaned with isopropanol before being used	Profilometry → Ensure that the rugosity of the PaC is compatible with further lithographic steps	PVA Tepla 300
Photolithography for DRIE - BPN 50μm	Spin-Coating	Recipe "BPN 50μm", 1350rpm, 5000 rpm/s, 30s	Spray nitrogen on the wafer before spin-coating to remove dust and ensure proper uniform coating	Profilometry → Verify the resin thickness Optical imaging → Verify the placement of the resin openings	Gyrset SUSS Microtec
	PSB	120°C, 6'30	Remove the solvent from the resin		Hotplate
	UV exposure	SOFT CONTACT, 2,55J/cm <sup>2</sup> , Big Circle Frame	Initiate and propagate the polymerization of the resin. Mask must be dehydrated for 15min at least before exposition. No PEB required as BPN is photopolymerized and not photoinitiated.		SUSS Microtec
	Development	t=3'30 in MF-CD26	Remove unexposed resin		Photolitho bench + Glassware
Implant DRIE & release	ICP-DRIE O <sub>2</sub> plasma (P4)	T = 4°C, O <sub>2</sub> =200sccm, Pr=20 mTorr, P <sub>ICP</sub> = 2500W, P <sub>bias</sub> =40W, t≈18 (O <sub>2</sub> ) +1(He, C <sub>4</sub> F <sub>8</sub> ) +7 (O <sub>2</sub> ) min	Etch the entire parylene thickness, etching can be followed by a camera.	Profilometry (pre-stripping) → Verify the resin thickness after etching and the etched PaC thickness after stripping to quantify the etching rates for both the resin and the PaC --- SEM (post-stripping) → Verify the state of the microelectrode and of the etching trenches (etching feet/filaments, delamination...) DRX (post-stripping) → Verify the crystallinity of the PaC after the fabrication process end (measure frontside and backside) FTIR (post-stripping) → Verify the compositional state of the PaC after the fabrication process end (measure frontside and backside)	Alcatel P4
	BPN Stripping & Implant release	Intervia Stripper BP (NF52) bath, at 60°C (90°C on the hotplate) under orbital agitation. 10 rinse cycles (1h) in DI water.	Remove the remaining BPN and release the implants. To determine the optimal stripping time and prevent damage to the gold surfaces, release the implants in DIW. Then strip one implant separately from the others in NF52, to find the optimal minimal time of stripping.		Chemical stripping bench

## ***Annex 5: Critical issues during flexible implant microfabrication - plasma cleaning & adhesion promotor***

- **Plasma cleaning during microfabrication**

To ensure adhesion between photoresists and parylene layers at each photolithographic step and adhesion between parylene layers, it is critical to have a clean surface state of the receiving surface (the parylene layer). In our process, it is particularly critical for the deposition of the second PaC layer, which serves as passivation layer, and the following etching steps for passivation opening and implant release.

For that purpose, the best technique is plasma cleaning at low power, which enhance the surface wettability and porosity [1] while descumming the surface by destruction of residual organic pollutions (resist residues, solvent residues...). However, as the plasma is etching the surface, a thinning of the paC layer is to be anticipated. For that, a calibration of the etching rates is necessary. The results of this calibration are presented in Fig. 1.

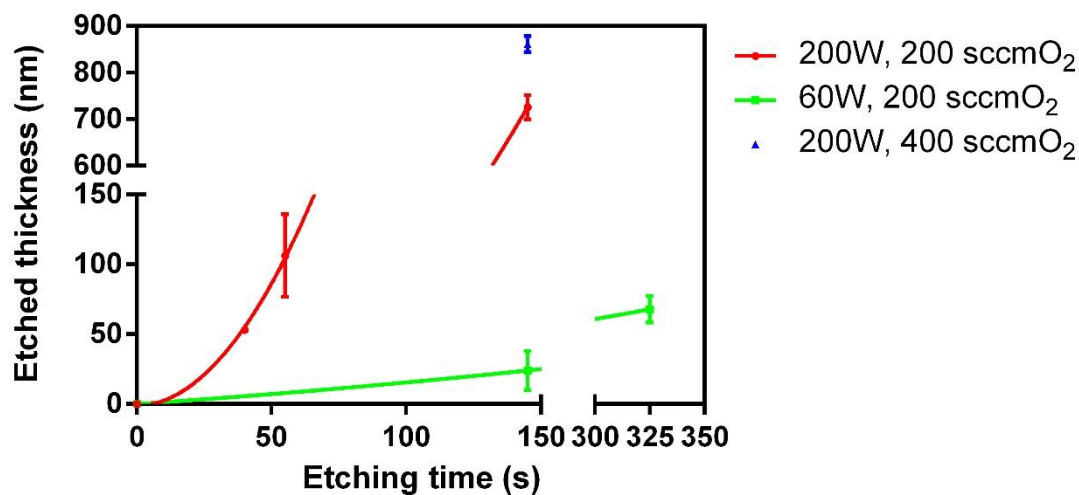


**Fig. 1: Thickness etched as a function of etching time.** Time scales extracted from data in the PhD of Aziliz LECOMTE [2]. Tests realized before metallization with thicknesses measured three times on different locations of the wafer (PaC deposited on a SiP wafer at 55 $\mu$ bar and annealed 4h at 150°C in a nitrogen atmosphere). Etching is realized in the TEPLA reactor (CCP plasma), without cage. Data were fitted with second order polynomial regression ( $R^2=0.9966$  for 200W, 200sccm,  $R^2=0.9256$  for 60W, 200sccm).

The calibration in **Fig. 1** was realized before metallization, on a wafer deposited with a thick parylene layer, patterned through etching beforehand and then passed through multiple etching times (at 200W, 200sccm O<sub>2</sub>, without cage) to measure the thickness of the etched PaC (N=3). A polynomial regression was fitted on each data set, which led to think that etching rates were not constant during the all duration of the plasma cleaning (as the etching rate tends to be lower at low etching times). This is probably due to temperature increase in the reactor during plasma generation.

A cleaning time of 60s was chosen according to these results, which leads to a 120nm loss of the passivation layer, which is then anticipated by increasing the deposited thickness of PaC.

However, the etching rates measured by this calibration protocol were not followed after metallization when this plasma cleaning protocol was used. A 60s plasma cleaning resulted in the complete etching of the 1.3 μm-thick passivation layer after passivation opening. The etching of the passivation was inhomogeneous, happening only on the electrode openings. This is due to the use of a microwave plasma, in conjunction with exposed metal. As the microwaves hit the metal, they also heat it which in return dramatically increases the temperature locally at the electrode/pads openings, making the plasma more energetic, increasing the etching rates, up to values high enough to result in a complete etching of the second PaC layer in 60s (**Fig. 2**). To limit such troublesome issue, the use of a Faraday cage is necessary. A Faraday cage confines the MW field outside of its structure, preventing heating of the sample. However, it also impacts the nature of the plasma cleaning as it prevents charged species to reach the sample. The calibration of this plasma cleaning is still to be completed, as for time constraints, it could not be finished.

For long-term resolution of this problem, the use of a RF-plasma (currently under maintenance by T. CORBIN) would be recommended as such plasma would not theoretically induce any heating of the sample. As this problem only appears after passivation opening, the plasma cleaning of the wafer to ensure BPN adhesion could either be removed (then the BPN adhesion would only rely on its viscosity and thickness) or replaced by a Piranha cleaning (to be tested).

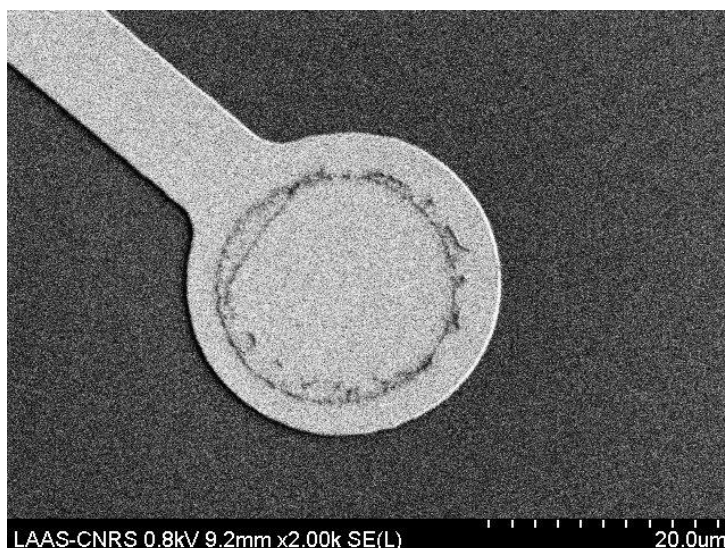


**Fig. 2: SEM image of a microelectrode after a 55s plasma cleaning (total etching of the passivation layer) on a MEA (same phenomenon on implant was too risky to image by SEM, as PaC pieces could delaminate and fall inside the SEM chamber). The ring on the electrode is made of etching filaments produced during the etching of the passivation and could be removed by further Piranha cleaning.**

- **ParyleneC Adhesion Promotor (AP) use and interference with electro-chemistry**

The A-174 AP is a molecule meant to help parylene adhere to hydroxylated surfaces ( $\text{SiO}_2$ , glass, other oxides, see **Fig. 3A**)[\[3, 4\]](#) by creating a covalent link between these surfaces and the depositing polymer (**Fig. 3**). This is to palliate the poor adhesion of parylene to other surfaces, even to itself (it is important to note that other molecules/strategies can be used for such adhesion issue [\[5, 6\]](#)). This molecule is added into the deposition chamber and vaporize onto the entire chamber and the samples in it.

However, when too many AP are added into the chamber, part of it stays unreacted in bubbles in the parylene deposited in the chamber and in the parylene deposited on the samples. This unreacted AP will then diffuse in the chamber during the next depositions until it is exhausted, leading to adherent/polluted parylene even though AP has not been added to the chamber.

The unreacted AP will also diffuse back from deposited parylene on the samples in the solutions in/with which the samples are used (for example in  $\text{H}_2\text{SO}_4$  for electrochemical experiments). As the AP is electroactive, it reacts on microelectrodes when they are polarized, for example during electrochemical activation, which makes the electrodes become black/brown and passivate them. This is believed to come from the AP molecules polymerizing, creating an unreactive plug of carbon chains bearing inorganic moieties.

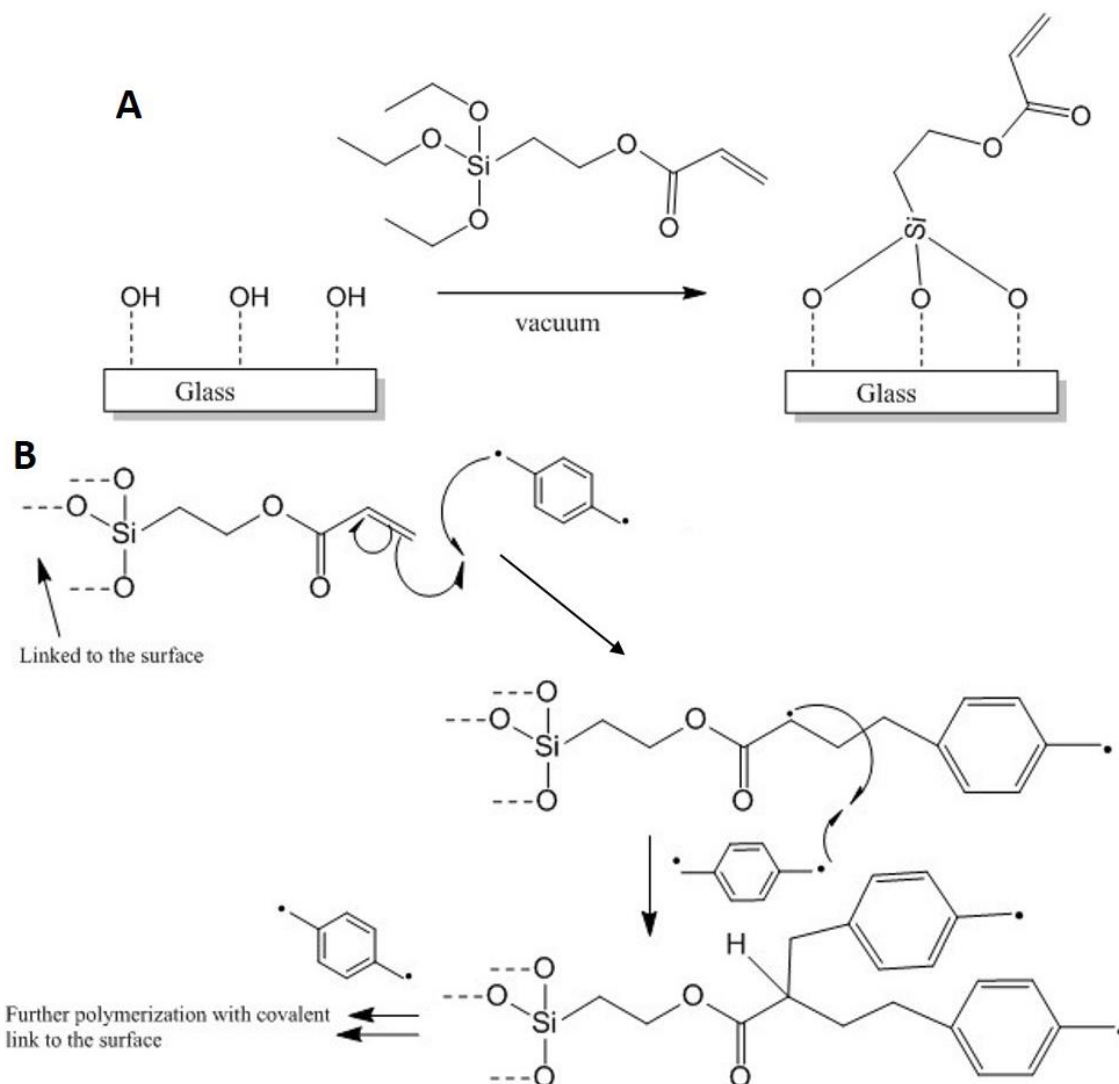


**Fig 3: Adhesion promotor condensation and covalent linking with parylene molecular mechanisms.**  
 A) AP condensation on a hydroxylated glass surface (with the release of 3 ethanol molecules, B) Covalent linking of the AP with two gaseous parylene radicals.

The solution to prevent any trouble with the AP is to keep an exhaustive tracking of its use in the chamber, clean the chamber by removing all PaC in it and make a blank deposition before any sensitive deposition, to test for residual presence of the AP. The AP should probably be introduced at a rate of one drop/deposition in the chamber to prevent overcharge. Another pathway, excluding the use of the AP inside the deposition chamber, could also prevent any trouble. Such a pathway has been published by other groups [3, 6, 7].

It is important to note that AP release during electrochemistry is not the only trouble linked to AP overcharge. As AP is designed to condensate to hydroxylated surfaces like glass, the REs glass tubing also gets polluted and then transfer the AP into other solutions and on other devices, which spread the pollution and oblige to discard any polluted REs/devices.

## Annex 6: SU8 electrochemical degradation during microelectrode activation

SU8 exact formulation is actually not known, but information about its polymerization system can be found in the literature. A description of the photopolymerization mechanisms is proposed in the **Fig. 1**, where only a part of the Novalac-base molecule of SU8 (which has an average of 8 epoxides per unit) is used to illustrate this polymerization.

Briefly, a arylsulfonium salt eliminates one of its aryl groups under UV irradiation, following either a ionic or radical path, which recombines with this salt to form an acid in-situ (**Fig. 1A**). This acid then triggers the chain-opening of epoxides bore by the Novalac resin (**Fig. 1B**), the reaction being amplified by baking of the resin (thermo-amplification).

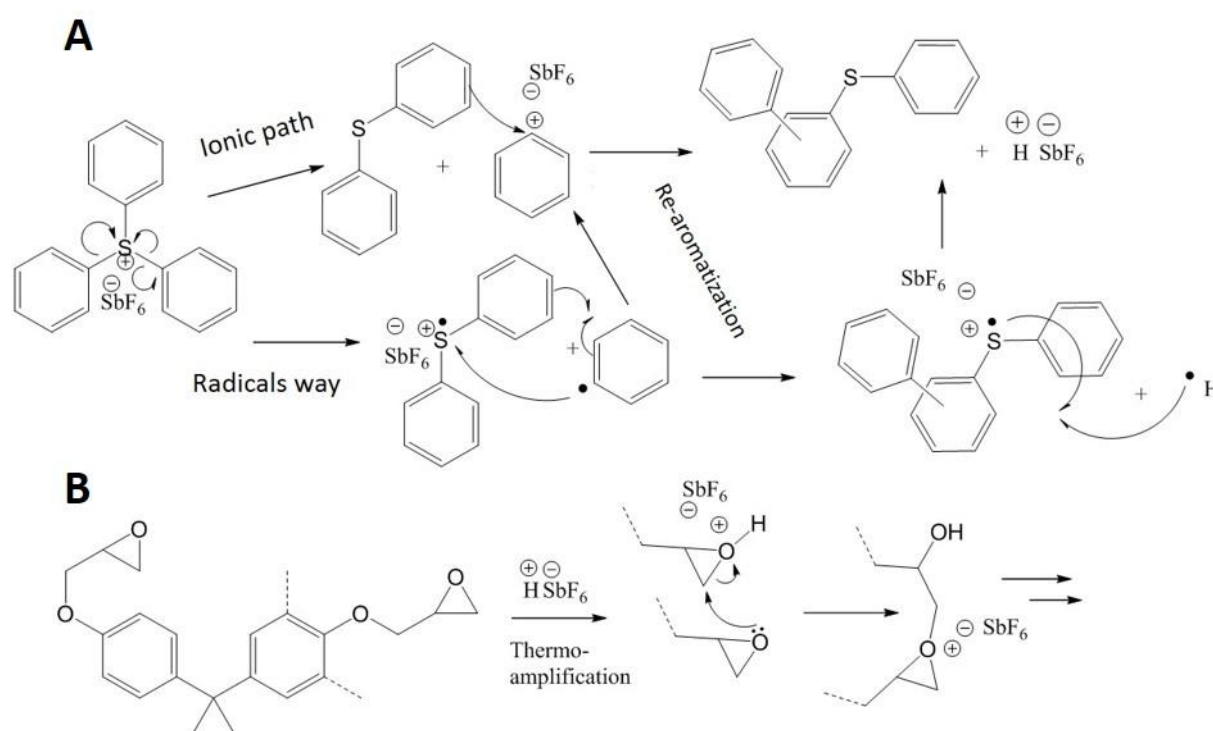


**Fig. 1: Photo-initiation and polymerization mechanism of SU8.** A) Generation of a photo-acid through both ionic and radical pathways, converging toward the same acid upon UV irradiation; B) Thermo-amplification of the polymerization through cationic chain growth generated by the use of the photoacid and increased temperature.  $pK_a(HSbF_6) = -20$  to  $-23$ .

SU8 is used routinely for passivation in microfabrication. We observed that SU8 coatings could be degraded by electrochemical oxidation when high positive potentials ( $>1.75V$ ) were used for electrochemical cleaning of microelectrodes for example. Such degradation has been observed previously in



the literature [7]. However, SU8 was still adequate for our experiment as passivation degradation could be prevented by using only short pulses (<500ms) of high potentials when needed. This also prevented bubble formation (as such high potential are far over the water electrolysis potential and so generate reactive oxygen species and oxygen, which turn into bubbles).

A possible explanation of the SU8 degradation mechanism is illustrated in **Fig.2**, relying on an analogy with the oxidation of phenol, applied to the phenolic moieties in the polymer chains and being degraded in radicals under electro-oxidation.

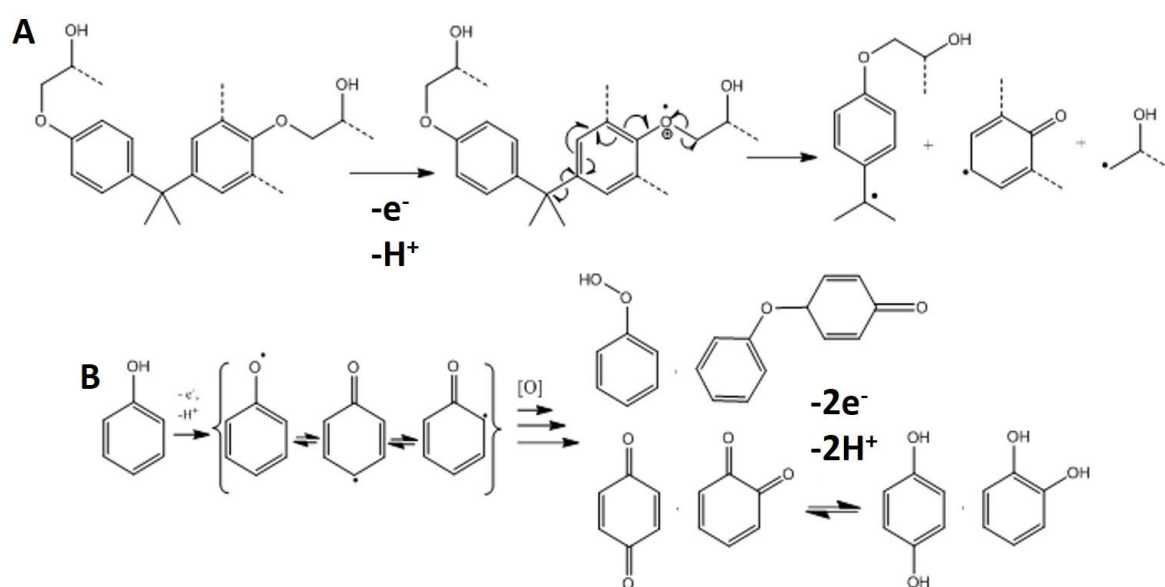


**Fig. 2: Hypothesized SU8 chains fragmentation** through A) electron withdrawing under oxidative potential application, leading to radicals similar to the ones produced by B) electro-oxidation of phenol.

1. Golda, M., et al., *Oxygen plasma functionalization of parylene C coating for implants surface: nanotopography and active sites for drug anchoring*. Mater Sci Eng C Mater Biol Appl, 2013. **33**(7): p. 4221-7.
2. Lecomte, A., *Conception and characterization of flexible microelectrodes for implantable neuroprosthetic development*. 2016, Université Fédérale de Toulouse Midi-Pyrénées.
3. Hassler, C., et al., *Characterization of parylene C as an encapsulation material for implanted neural prostheses*. J Biomed Mater Res B Appl Biomater, 2010. **93**(1): p. 266-74.
4. Gao, J., et al., *Adhesion promoter for a multi-dielectric-layer on a digital microfluidic chip*. RSC Advances, 2015. **5**(60): p. 48626-48630.
5. Zeniieh, D., et al., *ParyleneC thin film for biocompatible encapsulations with very strong adhesion and superior barrier properties*. 21st International Symposium on Plasma Chemistry (ISPC 21), 2013.
6. Driesche, S.v.d., et al., *A Simple Method to Allow Parylene-C Coatings on Gold Substrates*. Proceedings, 2017. **1**(4): 299.
7. Temiz, Y., et al., *A comparative study on fabrication techniques for on-chip microelectrodes*. Lab Chip, 2012. **12**(22): p. 4920-8.

## Annex 7: High-performance FSCV on PEDOT-microelectrodes

It was discovered that PEDOT-PSS deposited by chronoamperometry at 3.14nA, with a deposition charge of 1200nC, could reach a stable FSCV signature at 1200V/s, with  $E_{rest} = -400\text{mV}$ , LVP and UVP equal to  $-0.6\text{V}$  and  $1.2\text{V}$  respectively and  $WF = 10\text{Hz}$ . Detection of DA was tried from  $50\text{nM}$  to  $10\mu\text{M}$  in PBS (pH 7,2) to try to detect very low concentrations of DA. Subtracted-voltammograms of these tests are displayed in **Fig. 1** and calibration in **Fig. 2**.

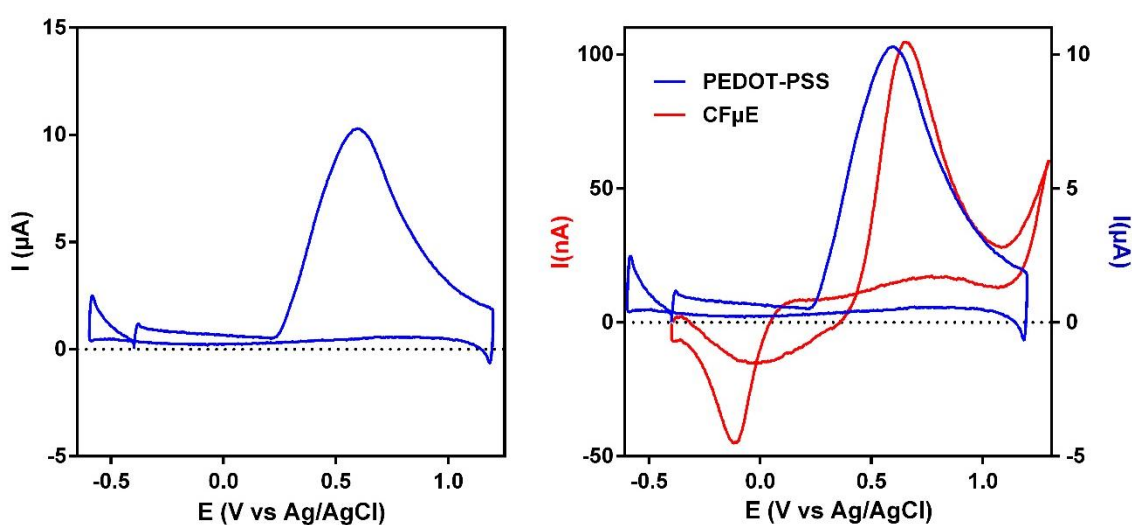


**Fig. 1:** Background-subtracted voltammograms (BS-V) of DA on PEDOT-PSS and CF $\mu\text{E}$ . A) BS-V of  $50\text{nM}$  of DA on a PEDOT-PSS microelectrode. B) Comparison of DA FSCV signature on CF $\mu\text{E}$  (red trace) and PEDOT-PSS (blue trace).

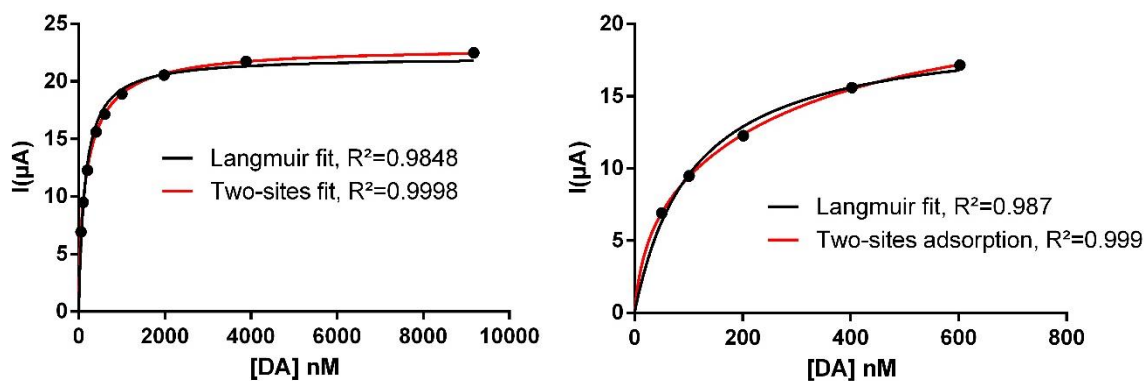


**Fig. 2:** Calibration curve of DA on PEDOT-PSS microelectrodes. A) Calibration plot of DA on PEDOT-PSS with two fits, by standard Langmuir plot (black trace) and by two-sites Langmuir fit (red trace). B) Zoom in on the  $0\text{-}800\text{nM}$  range.

As can be seen in **Fig. 1A**, DA have a FSCV signature that is very different than the typical, double-peaked profile obtained on CF $\mu$ E (**Fig. 1B**, red trace). A single oxidation peak is observed centered at 0.6V with a sharp increase at 0.2V, and no reduction peak. These features make this profile strikingly different from the one obtained on CF $\mu$ E (**Fig. 1B**, red trace).

This reduction peak absence could be explained by the surface negative charges on the pending PSS chains, inducing a desorption of the DA oxidation products, phenomenon known at charged electrodes [1].

By plotting the oxidation currents obtained (**Fig. 2A**), the currents showed a profile clearly involving a contribution of adsorption, with a quick increase of the current, reaching a plateau above 2 $\mu$ M. These data were fitted with both a Langmuir isotherm adsorption curve and a two-sites adsorption model, which is fitting better, leading to think that DA can adsorb on both PEDOT and PSS [2] chains for example (constituting two different adsorption site types). This would explain why a plateau is reached above 2 $\mu$ M and why such a high current is produced (**Fig. 2B**), due to a small electrode with a high density of adsorption sites [3, 4].

It is interesting to note that to calculate LOD with FSCV, it must be estimated through RMS noise at the oxidation peak location [5].

1. Taylor, I.M., et al., *Direct in Vivo Electrochemical Detection of Resting Dopamine Using Poly(3,4-ethylenedioxythiophene)/Carbon Nanotube Functionalized Microelectrodes*. *Anal Chem*, 2019. **91**(20): p. 12917-12927.
2. Meier, A.R., W.A. Bahureksa, and M.L. Heien, *Elucidating the Structure–Function Relationship of Poly(3,4-theylenedioxythiophene) Films to Advance Electrochemical Measurements*. *The Journal of Physical Chemistry C*, 2016. **120**(37): p. 21114-21122.
3. Samba, R., et al., *Application of PEDOT-CNT Microelectrodes for Neurotransmitter Sensing*. *Electroanalysis*, 2014. **26**(3): p. 548-555.
4. Meier, A.R., et al., *Rapid Voltammetric Measurements at Conducting Polymer Microelectrodes Using Ultralow-Capacitance Poly(3,4-ethylenedioxythiophene):Tosylate*. *Langmuir*, 2016. **32**(32): p. 8009-18.
5. Vreeland, R.F., et al., *Biocompatible PEDOT:Nafion composite electrode coatings for selective detection of neurotransmitters in vivo*. *Anal Chem*, 2015. **87**(5): p. 2600-7.

## ***Annex 8: Iridium oxide electrodeposition and characterization***

- **Iridium Oxide (IrO<sub>x</sub>)**

Iridium oxide a very well-known material, used to build (micro)reference electrodes [1-4] and pH sensors [5-8] for a long time. These applications come from a very particular property of this oxide: the presence at its surface of a mix oxides that can be easily protonated/deprotonated, leading to change in the surface electronic density of the material and thus in its potential. Furthermore, this property has been shown to be quite selective, with minimal interference of other ions. It is important to note that IrO<sub>x</sub> can also be used for stimulation [9, 10]. Here, the deposition and characterization of IrO<sub>x</sub> is presented and discussed.

- **Electrochemical deposition**

Iridium oxide is electrodeposited from a solution containing IrCl<sub>4</sub>, H<sub>2</sub>O<sub>2</sub>, and oxalic acid at pH=10.4. This formulation of the deposition solution has first been developed by Yamanaka [11] and then improved and used by other groups [8, 12]. After preparation the solution needs to let age for 48h and can then be used reproductively for 2-3months if kept at 4°C in the dark.

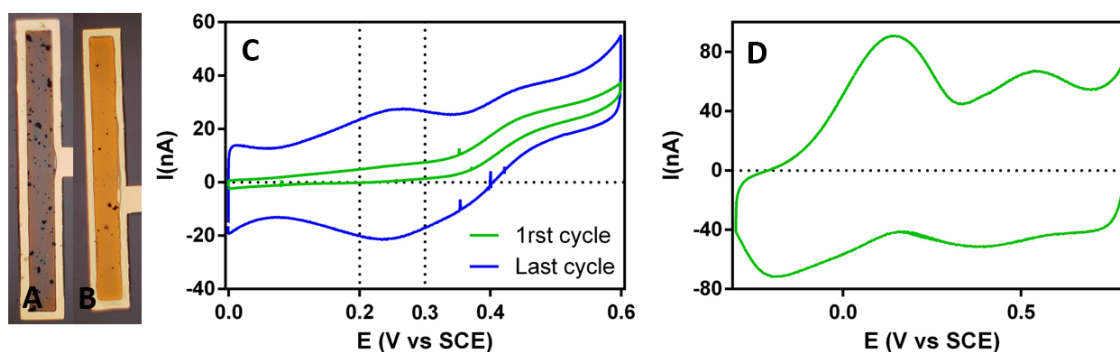


**Fig. 1: Iridium Oxide deposition and characterization.** A) mat orange-iridized blue (25µC) and B) bright pastel orange (50µC) IrO<sub>x</sub> deposits obtained by CV deposition; C) Voltammograms obtained during deposition by CV between 0 and 0.6 vs SCE, at 10mV/s, with the first and last cycles displayed, showing the oxide growth; D) CV characterization of the deposit in PBS pH=7.4, between -0.3 and 0.8V, at 50mV/s.

CV deposition by cycling between 0 and 0.6V vs SCE for 20 to 50 cycles. To obtain a reproducible deposit, in terms of pH sensitivity and CV signature in PBS, the key parameter is the integral of the

peak centered at 0.25V, which must be in the same range for all deposit. In this thesis, the integral between 0.347 and 0.058V (the beginning and the end of the first oxidation peak) was 4.532nA.V and between 0.3 and 0.2V was 1.886nA.V. Deposits had deposition charge between 25 and 50 $\mu$ C and varied from a bright pastel orange to a mat orange-iridized blue as can be seen in **Fig. 2**.

Even though a variation of color and deposition time is observed, the CV of the deposits in PBS 1X (pH=7.4) and the properties in terms of pH sensitivity were similar from deposit to deposit, at the condition to follow the protocol on oxide growth presented before and to keep the deposition solutions in the dark at 4°C when unused. Depositions runs of up to 6 deposits were performed. IrOx could clearly be identified through its typical CV signature, with two couples of redox peaks, corresponding to Ir(II)/Ir(III) and Ir(III)/Ir(IV) transition.

- **pH sensing**

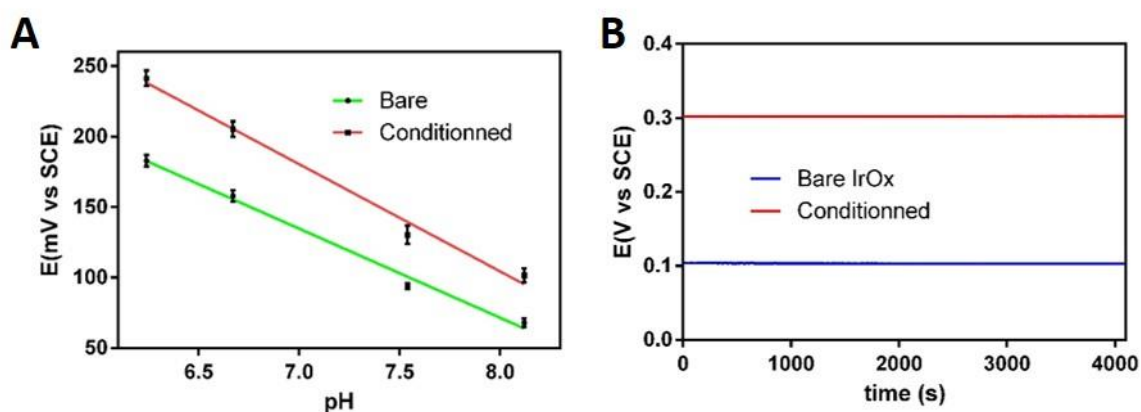


**Fig. 2: Iridium oxide pH sensing characterization as a function of the oxide conditioning.** A) Potential vs pH measurements with bare (N=3) and electrochemically conditioned (N=3) IrOx electrodes, with linear regression of the obtained values. B) Potential values of both bare and conditioned oxides after 60h of stabilization in PBS.

pH sensing tests were realized 48h after deposition, with the IrOx deposits kept in DIW to keep them hydrated. Before measurements, an electrochemical conditioning of the material through CV cycling in PBS 1X (pH=7.4) was performed on half of the electrodes, to stabilize the material.

pH detection was possible for up to 2h with little to no drift in sensitivity. However, after 2h, the electrode potential drifts too much to have a good quality monitoring of pH changes. Conditioned IrOx deposits showed a higher sensitivity to pH, probably due to change of the oxide mix on the electrode surface.

To circumvent that, it is necessary to let the IrOx electrode stabilize in a pH buffered medium, here PBS 1X. After 60h in PBS, the electrode potentials reached stable values. **Fig. 2B** shows the stability of these values in-vitro for more than 1h, making our deposits adequate reference for such time scales. For further work, only stabilized electrode should be considered for referencing purposes. It is important to note that electrochemical conditioning of the oxides could not prevent the need for a stabilization as drift still appeared in our measurements. However, it did decrease its importance and increase the time at which it appeared compared to bare oxides.



1. Shinwari, M.W., et al., *Microfabricated reference electrodes and their biosensing applications*. Sensors (Basel), 2010. **10**(3): p. 1679-715.
2. K., F.R., et al., *A Comparison of Fabrication Methods for IrOx Reference Electrodes*, IEE SENSORS 2009 Conference, 2009: p. 1086-1089.
3. Yang, H., et al., *An iridium oxide reference electrode for use in microfabricated biosensors and biochips*. Lab Chip, 2004. **4**(1): p. 42-6.
4. Tolosa, V.M., et al., *Electrochemically deposited iridium oxide reference electrode integrated with an electroenzymatic glutamate sensor on a multi-electrode array microprobe*. Biosens Bioelectron, 2013. **42**: p. 256-60.
5. Ges, I.A., et al., *Thin-film IrOx pH microelectrode for microfluidic-based microsystems*. Biosens Bioelectron, 2005. **21**(2): p. 248-56.
6. Sayed A. M. Marzouk, S.U., and Richard P. Buck, Timothy A. Johnson, Larry A. Dunlap, and Wayne E. Cascio, *Electrodeposited Iridium Oxide pH Electrode for Measurement of Extracellular Myocardial Acidosis during Acute Ischemia*, Anal Chem, 1998. **70**: p. 5054-5061.
7. Ges, I.A., et al., *Differential pH measurements of metabolic cellular activity in nl culture volumes using microfabricated iridium oxide electrodes*. Biosens Bioelectron, 2007. **22**(7): p. 1303-10.
8. Elsen, H.A., C.F. Monson, and M. Majda, *Effects of Electrodeposition Conditions and Protocol on the Properties of Iridium Oxide pH Sensor Electrodes*. Journal of The Electrochemical Society, 2009. **156**(1).
9. S.C. Mailley, M.H., P. Mailley, J.M. McLaughlin, E.T. McAdams, *Electrochemical and structural characterizations of electrodeposited Iridium Oxide thin-film electrodes applied to neurostimulating electrical signal*. Materials Science and Engineering C, 2002. **21**: p. 167-175.
10. Zeng, Q., et al., *Electrodeposited Iridium Oxide on Platinum Nanocones for Improving Neural Stimulation Microelectrodes*. Electrochimica Acta, 2017. **237**: p. 152-159.
11. Yamanaka, K., *Anodically Electrodeposited Iridium Oxide Films (AEIROF) from alkaline solutions for electrochromic display devices*. Japanese Journal of Applied Physics, 1989. **28**(4): p. 632-637.
12. M.A. Petit, V.P., *Anodic electrodeposition of iridium oxide films*. Journal of Electroanalytical Chemistry, 1998. **444**: p. 247-252.